Estimation of trigger rates, data rates and data volumes for CTA and observations of SNR RX J0852.0−4622 with H.E.S.S.

DISSERTATION
zur Erlangung des akademischen Grades
doctor rerum naturalium (Dr. rer. nat.)
im Fach Physik
Spezialisierung: Experimentalphysik
eingereicht an der
Mathematisch-Naturwissenschaftlichen Fakultät
der Humboldt-Universität zu Berlin
von

Herrn Licenciado Manuel Paz Arribas

Präsidentin der Humboldt-Universität zu Berlin:
Prof. Dr.-Ing. habil. Dr. Sabine Kunst
Dekan der Mathematisch-Naturwissenschaftlichen Fakultät:
Prof. Dr. Elmar Kulke

Gutachter/innen:
1. Prof. Dr. Thomas Lohse
2. Prof. Dr. Elisa Bernardini
3. Prof. Dr. Nukri Komin

eingereicht am: 19.09.2016
Tag der mündlichen Prüfung: 15.12.2016

Dedico este trabajo a
Bruno, Alisa y
Dr. Mama.

Abstract

This work focuses on two different aspects of γ-ray astronomy. On the one hand, it studies the instrumental challenge posed by the future CTA Observatory by estimating the amount of data to be collected. On the other hand, it studies supernova remnants, by presenting analysis results of the γ-ray data of the RX J0852.0−4622 supernova remnant measured with the operating H.E.S.S. experiment and interpreting them in order to check the plausibility of RX J0852.0−4622 being a cosmic ray accelerator. In addition, an outlook on the capabilities of CTA for studying supernova remnants is also presented, using RX J0852.0−4622 as an example.

With its improved sensitivity, CTA will face a background rate unprecedented in Cherenkov telescope systems. The first part of this work evaluates the amount of data that needs to be handled by the detectors, the read-out system and the storage system of CTA. Based on an analysis of simulated data, the more demanding southern array is expected to have an array trigger rate of $\sim 13\,\mathrm{kHz}$, a data rate of up to $2500\,\mathrm{MB/s}$ and a data volume after 15 yr of operation and assuming a duty cycle of 15% of up to 165 PB. The design of the data acquisition and storage systems will be a challenge but should be manageable with existing technologies.

More than 100 yr after their discovery, the origin of cosmic rays is still a mystery. Supernova remnants are believed to be the accelerators of Galactic cosmic rays, although no definite proof exists as of today. The second part of this work presents detailed morphological and spectral analysis of γ-ray data from the supernova remnant RX J0852.0−4622 measured with the H.E.S.S. experiment in order to evaluate the γ-ray emission on the perspective of hadronic and leptonic emission models. The more precise measurements permit a better determination of the parent particle population properties with respect to previous publications. More precisely, a clear curvature of the spectrum of RX J0852.0−4622 is measured with an exponential energy cut-off at 7.2 TeV. Finally, the analysis of simulated data shows that CTA should be able to significantly improve the determination of the spectral energy cut-off of RX J0852.0−4622, which should help in identifying the nature of the γ-ray emission.

Zusammenfassung

Die vorliegende Arbeit beschäftigt sich mit zwei Aspekten der Gammastrahlungsastronomie. Einerseits studiert sie die Anforderungen an das zukünftige CTA-Observatorium für Gammastrahlung und präsentiert insbesondere Abschätzungen der Datenmengen, die während des Betriebs des Observatoriums anfallen werden. Andererseits befasst sie sich mit dem Supernovaüberrest RX J0852.0−4622, präsentiert die Ergebnisse einer Analyse von Daten, die mit dem H.E.S.S.-Experiment genommen wurden, und geht der Frage nach, ob RX J0852.0−4622 ein kosmischer Teilchenbeschleuniger ist. Ferner wird ebenfalls am Beispiel von RX J0852.0−4622 die Leistungsfähigkeit von CTA bei der Beobachtung von Supernovaüberresten untersucht.

Die für das CTA-Observatorium angestrebte Verbesserung des Flusssensitivität um einen Faktor 10 zieht Raten von Untergrundschauern mit sich, die weit größer sind als die Raten, die bei den derzeitigen Tscherenkow-Experimenten (H.E.S.S., MAGIC, VERITAS) anfallen. Der erste Teil der Arbeit präsentiert Ergebnisse von Monte-Carlo-Simulationen zu den Ereignis- und Datenraten, die vom Datenerfassungssystem ausgelesen, transportiert und gespeichert werden müssen. Für das größere CTA-Teleskopfeld auf der Südhalbkugel werden demnach eine Triggerate von $\sim 13\,\mathrm{kHz}$ und Datenraten von bis zu $2500\,\mathrm{MB/s}$ erwartet. Unter der Annahme, dass 15% der Zeit für Beobachtungen genutzt werden können, ergibt sich in 15 Jahren ein Datenvolumen von bis zu 165 PB. Die Implementation eines entsprechenden Systems zur Datenerfassung und -speicherung stellt eine Herausforderung dar, die jedoch mit existierenden Technik bewältigt werden kann.

Mehr als 100 Jahre nach der Entdeckung der Kosmischen Strahlung sind ihre Quellen noch nicht eindeutig identifiziert. Es wird davon ausgegangen, dass Supernovaüberreste geeignete Beschleuniger für den galaktischen Anteil der Kosmischen Strahlung sind, ein endgültiger Nachweis steht jedoch noch aus. Das zweite Teil der vorliegenden Arbeit stellt eine detaillierte Analyse der Morphologie und des Spektrums der Gammastrahlung des RX J0852.0−4622-Supernovaüberrestes vor. Die Analyse basiert auf Daten des H.E.S.S.-Experimentes und verfolgt das Ziel, anhand der Gammastrahlungsemission die Plausibilität hadronischer und leptonischer Emissionsmodelle zu prüfen. Dabei erlauben die präzisen Messungen eine im Vergleich zu früheren Veröffentlichungen verbesserte Bestimmung der Eigenschaften der emittierenden Teilchenpopulation. Es ergibt sich, dass das Energiespektrum von RX J0852.0−4622 ein Potenzgesetz ist, das zu hohen Energien hin mit einer Abschneideenergie von 7.2 TeV exponentiell unterdrückt wird. Abschließend wird anhand von Simulation gezeigt, dass CTA die Abschneideenergie von RX J0852.0−4622 signifikant besser bestimmen können wird. Diese genauere Vermessung des Energiespektrums sollte dazu beitragen, den hadronischen oder leptonischen Charakter der Emission aufzuklären.

Resumen

Este trabajo trata dos aspectos de la astronomía de rayos γ. Por una parte trata el desafío instrumental que supone el futuro observatorio CTA, poniendo especial hincapié en la cantidad de datos que tendrá que manejar durante su operación. Por otra parte trata sobre el remanente de supernova RX J0852.0−4622 presentando los resultados del análisis de los datos de rayos γ tomados con el experimento H.E.S.S., y usándolos para argumentar sobre la posibilidad de que RX J0852.0−4622 sea un acelerador de rayos cósmicos.

La mejora sustancial de la sensibilidad que se espera para los detectores de CTA supondrá un incremento de la tasa de eventos de fondo sin precedente en la historia de los sistemas de telescopios de efecto Cherenkov. La primera parte de este trabajo se encarga de evaluar la cantidad de datos que tendrán que procesar los detectores y los sistemas de adquisición y de almacenamiento de datos de CTA. Un análisis de datos simulados revela que el sistema de telescopios más exigente, previsto para el hemisferio sur, estará expuesto a tasas de disparo de $\sim 13\,\mathrm{kHz}$ y tasas de datos de hasta 2500 MB/s. Asumiendo que la fracción de tiempo utilizable para observaciones sea del 15 %, se espera un volumen de datos de hasta 165 PB tras 15 años de servicio. El diseño de los sistemas de adquisición y almacenamiento de datos supondrá un reto, salvable no obstante con tecnología existente.

Tras más de 100 años del descubrimiento de los rayos cósmicos, su origen sigue siendo un misterio. Se piensa que los remanentes de supernova son los aceleradores de la componente galáctica de los rayos cósmicos aun cuando no exista una prueba irrefutable. La segunda parte de este trabajo presenta un análisis de los datos de rayos γ procedentes del remanente de supernova RX J0852.0−4622 medidos con el experimento H.E.S.S. Los resultados de los detallados estudios morfológicos y espectrales son usados para evaluar la naturaleza de la emisión de rayos γ de este remanente de supernova en perspectiva de modelos hadrónicos y leptónicos. La mayor precisión de estas medidas permite una mejor determinación de los parámetros de la población de partículas emisoras con respecto a las publicaciones precedentes. Concretamente, este análisis revela una curvatura prominente en el espectro, con una energía de corte de 7,2 TeV. Finalmente, un análisis de datos simulados demuestra que CTA será capaz de mejorar de manera significativa la determinación de la energía de corte de RX J0852.0−4622. Esto a su vez ayudará a esclarecer la naturaleza de la emisión de rayos γ que se origina en esta fuente.

Résumé

Le sujet de cette thèse sur l'astronomie des rayons γ est double. D'une part elle étudie le défi instrumental posé par le futur observatoire CTA en estimant de la quantité de données qui devra être processée pendant son service. D'autre part elle présente les résultats de l'analyse des données des rayons γ du rémanent de supernova RX J0852.0−4622 mesurées avec l'expérience H.E.S.S., et leur interprétation pour évaluer si RX J0852.0−4622 est un accélérateur de rayons cosmiques.

L'amélioration de la sensibilité prévue pour CTA entraîne un taux d'évènements de fond sans précédent dans l'histoire des systèmes de télescopes Tcherenkov. En se basant sur l'analyse de données simulées, la première partie de cette thèse s'occupe d'évaluer la quantité de données à processer par les détecteurs et les systèmes d'acquisition et stockage de donées de CTA. Pour le plus grand réseau de télescopes de l'hémisphère sud, un taux de trigger de $\sim 13\,\mathrm{kHz}$ et un taux de données jusqu'à $2500\,\mathrm{MB/s}$ sont attendus. Dans l'hypothèse d'une fraction de temps employable pour observations de 15%, un volume de donées jusqu'à $165\,\mathrm{PB}$ est prévu après 15 ans de service. La conception des systèmes d'acquisition et stockage de données entraînera un défi, cependant faisable avec des technologies actuelles.

Plus de 100 ans après leur découverte, l'origine des rayons cosmiques est toujours inconnue. L'hypothèse a été émise que les rémanents de supernova pourraient être les accélérateurs de rayons cosmiques galactiques. Néanmoins, une preuve indiscutable n'existe pas. La deuxième partie de cette thèse présente les analyses morphologiques et spectrales des données de rayons γ en provenance du rémanent de supernova RX J0852.0−4622 mesurées avec l'expérience H.E.S.S. Le but est d'évaluer la nature de l'émission des rayons γ en testant la compatibilité des données avec des modèles hadroniques et leptoniques. Les mesures plus précises permettent une meilleure détermination des paramètres des populations de particules émettantes par rapport aux publications précédentes. Particulièrement, l'analyse révèle une claire courbure dans le spectre avec une coupure en énergie à $7.2\,\mathrm{TeV}$. Finalement, l'analyse de données simulées démontre que CTA sera capable d'améliorer significativement la caractérisation de l'énergie de coupure de RX J0852.0−4622. Ceci aidera à identifier la nature de l'émission des rayons γ.

Contents

Introduction

With only a few decades of history, γ-ray astronomy is a fairly new field in the realm of science. The field is experiencing a rapid growth, with new generations of instruments exceeding the previous ones in sensitivity and resolution. Cherenkov telescopes are amongst the most successful instruments for the observation of the sky in γ-rays.

γ-ray astronomy studies light at the highest possible frequencies, in order to study a variety of phenomena. Amongst them, the study of the origin of cosmic rays is one of the most important ones. Supernova remnants are believed to be the origin of Galactic cosmic rays. Spanning 2° in diameter, with a γ-ray luminosity of the same order as the Crab nebula and its well defined shell morphology, RX J0852.0−4622 is one of the best examples of TeV shell supernova remnants.

About this work

This work focuses on γ-ray astronomy, concentrating on two different aspects. This work studies the instrumental challenge posed by the future CTA Observatory by estimating the amount of data to be collected. Likewise, this work studies supernova remnants, by presenting analysis results of the γ-ray data of the RX J0852.0−4622 supernova remnant measured with the operating H.E.S.S. experiment and interpreting them in order to check the plausibility of RX J0852.0−4622 being a cosmic ray accelerator. In addition, an outlook on the capabilities of CTA for studying supernova remnants is presented, using RX J0852.0−4622 as an example.

This work is organized as follows. An introduction about γ-ray astronomy and Cherenkov telescopes is given in chapter 1. The future CTA Observatory is introduced in chapter 2. This chapter contains detailed estimates of the trigger rates, data rates and data volumes expected for CTA, based on the analysis of Monte Carlo simulations. An introduction to supernova remnants is presented in chapter 3. The H.E.S.S. instrument is described in chapter 4, together with an introduction to the RX J0852.0−4622 supernova remnant. The analysis of the H.E.S.S. data on this object is presented in the same chapter and in chapter 5. The last part of the chapter is dedicated to an overview of the capabilities of CTA in observing supernova remnants, using RX J0852.0−4622 as an example. Finally, a synopsis of the findings of this work is given in a short summary chapter.

Additional material supporting the results of the main chapters are appended to this work. Results of the trigger rates, data rates and data volumes for all possible CTA array layouts of the first official production of simulated data for CTA is presented in appendix A. The telescope connection scheme for a next-neighbors array trigger for one

of the possible CTA array layouts is presented in appendix B. The H.E.S.S. data sets used for the analysis of RX J0852.0−4622 are listed in appendix C. The results of the crosscheck analyses for the derivation of the RX J0852.0−4622 spectrum are presented in appendix D. A description of the muon correction necessary for the correct event energy reconstruction and its effects on spectral calculations is presented in appendix E.

1. γ-ray astronomy and the imaging atmospheric Cherenkov technique

γ-ray astronomy is the branch of astronomy that studies photons at the largest possible energies: $E \gtrsim 100\,\mathrm{keV}$. This is a large energy band, studied with different techniques. The best studied band, where the experimental techniques are quite mature and the achieved sensitivity is largest, is from $E \sim 30\,\mathrm{MeV}$ to $E \sim 100\,\mathrm{TeV}$. This work focuses on the latter energy range, with special emphasis in the so called very high energy (VHE) domain: energies from $E \sim 100\,\mathrm{GeV}$ to $E \sim 100\,\mathrm{TeV}$.

This chapter introduces the basic concepts of γ-ray astronomy and the imaging atmospheric Cherenkov telescope (IACT) technique, one of the most successful techniques to observe the sky in the VHE domain. The concepts introduced here are necessary to discuss the results presented in the rest of this work. They are particularly important for the subsequent chapter 2. First, a brief introduction to γ-ray astronomy and a list of source types is presented in section 1.1. Then, the observation techniques used in γ-ray astronomy are reviewed in section 1.2. The chapter ends with a more detailed review of the IACT technique and its sources of signal and background in section 1.3.

1.1. The violent universe

The *visible* universe, i.e. the part of the universe that can be directly detected and measured, is composed of regular (baryonic) matter. In the universe, baryonic matter represents only a mere $\sim 4-5\%$ of the total energy budget. The rest is dark matter and dark energy. The visible universe is dominated by thermal processes characterized by the emission of radiation following the black body spectrum. However, outshined by these *ordinary* processes, a much richer variety of phenomena exists: the so called *violent universe*. This term serves to group a variety of relativistic (i.e. non-thermal) processes resulting in some cases from sudden releases of large amounts of energy (for instance supernova explosions), hence its name.

These processes are very interesting for different branches of modern physics, like astrophysics, cosmology and particle physics. The latter domain benefits from the fact that energies measured in the universe can be far greater than in any man-made experiment ever built.

At γ-ray energies the universe is mostly non-thermal. Many of the non-thermal processes can be characterized by the emission of radiation following power-law spectra with fluxes slowly decaying with increasing energy, when compared to the black body spectra of the thermal processes. Therefore, even if the fluxes are low, these processes are better

studied at high energies (hard X-rays or γ-rays), where the thermal radiation does not play a role as important as in other wavebands. The power-law spectrum is given by

$$\frac{\mathrm{d}\Phi}{\mathrm{d}E} = \Phi_0 \left(\frac{E}{E_0} \right)^{-\Gamma}, \tag{1.1}$$

where Φ is the photon flux, E the photon energy, Φ_0 the flux normalization, E_0 the reference energy and Γ the spectral index.

One example of these processes is the spectrum of cosmic rays: a constant flux of charged particles bombarding the upper layers of the atmosphere that follows a power-law spectrum decaying in energy with a spectral index close to 2.7. More details about the cosmic rays are given in chapter 3 in section 3.2.

Further details on γ-ray astronomy and the violent universe can be found in the chapter 1 of both Longair [2011] and Weekes [2003].

1.1.1. Source classes

There are numerous types of γ-ray sources. However, in many cases they share a common pattern: first charged particles are accelerated via different means to large energies, followed by the emission of highly energetic photons in a variety of processes involving the interaction of the accelerated particles with the surrounding medium (either baryonic matter, typically from the interstellar medium (ISM) or gas clouds (i.e. molecular clouds), or photon fields, typically from the cosmic microwave background (CMB) or from nearby stars). More details about particle acceleration and subsequent γ-ray emission are given in chapter 3 in sections 3.5 and 3.6, with focus on the important processes for supernova remnants. Focusing on the VHE regime, a list of TeV γ-ray source types according tho the TeVCat catalog (TeVCat Team [2016]) follows:

SNR : supernova remnants are the structures resulting from the bright and violent supernova explosions that mark the end of the regular life cycle of many stars. An SNR is bounded by a fast shock wave expanding into space and consists of expanding material ejected from the progenitor star during the explosion and the material swept up and shocked in its expansion. In their shocks, SNRs can accelerate particles that emit photons at γ-ray energies, when interacting with material and photon fields in the surrounding medium. Moreover, the interaction of the accelerated particles from the SNR shocks with the particles in nearby molecular clouds can also produce photons at γ-ray energies. More details about SNRs are given in chapter 3.

PWN : pulsar wind nebulae are the interstellar clouds (nebulae) formed when the winds of relativistic particles (mostly electrons e^- and positrons e^+) powered by a pulsar interact with surrounding material to produce radiation. The accelerated particles can upscatter low energy photons of surrounding photon fields, like the CMB, up to γ-ray energies.

PSR : pulsars are fast rotating neutron stars. They have strong magnetic fields. The rotation of the magnetic fields produce strong electric fields at the poles of the neutron star that can accelerate electrons with subsequent emission of photons via curvature radiation and inverse Compton scattering. Pulsed emission has been observed up to γ-rays.

Binary : binary systems of a compact object (a neutron star (often in the form of a pulsar) or a black hole) rotating around a massive star with an eccentric orbit can produce radiation when accelerated particles from the compact object interact with photons or matter (i.e. particle winds, or stellar disk) from the massive star. A modulation of the γ-ray signal with respect to the orbital phase of the compact object is often measured.

AGN : active galactic nuclei are compact regions at the center of galaxies with a much higher than usual luminosity, that often dominates the optical emission of the entire galaxies where they are hosted. Each AGN is believed to host a super massive black hole in its center with an accretion disk of matter around it and relativistic jets of particles emerging from it. These accelerated particles, interacting with material and photon fields in the surrounding medium or even with other (slower) parts of the jet can produce photons at γ-ray energies.

Globular cluster : globular clusters are very old stellar systems with high densities of stars in their cores. They contain many millisecond pulsars: pulsars with rotating periods of the order of ms. They are believed to produce γ-rays by the interaction of high energy electrons accelerated by the millisecond pulsars with stellar and CMB radiation fields.

Massive star cluster : massive star clusters, also known as super star clusters, are very massive young open clusters thought to be the precursor of globular clusters. They contain large numbers of young massive stars. These stars evolve fast and usually end their lives in supernova explosions close yo their birth places. Collective effects of interacting SNRs and stellar winds in these systems are believed to accelerate particles that can produce γ-rays by their interactions with material and photon fields in the surrounding medium.

Starburst galaxy : starburst galaxies are galaxies with an exceptionally high rate of star formation. They are characterized by a boosted formation rate of massive stars and an increased rate of supernovae in localized regions. They are believed to produce γ-rays by the interaction of high energy particles accelerated in SNRs with material and photon fields surrounding the SNRs.

Superbubble : superbubbles are cavities filled with gas blown into the interstellar medium by multiple supernovae and stellar winds. They are believed to produce γ-rays by the interaction of accelerated particles with material and photon fields in the surrounding medium.

Some sources remain unidentified. For instance the γ-ray source detected towards the Galactic center (GC, HESS J1745−290 as named by H.E.S.S.) is believed to be associated to the black hole postulated to exist in the center of the Milky Way (Sgr A*), but it could also be explained as the PWN of a PSR close to the GC.

1.2. Observation techniques

Current experiments follow two different approaches:

Direct measurements : since γ-rays are absorbed in the upper atmosphere they can be directly detected only in outer space using satellite experiments. A good example is the *Fermi* telescope (Fermi Collaboration [2016]), sensitive in the 8 keV to 300 GeV energy band. A very successful technique is the use of the γ-ray conversion into an e^+/e^- pair. The e^+/e^- pairs can be well measured using trackers and calorimeters, as is the case for the *Fermi*-LAT (large area telescope) instrument (30 MeV to 300 GeV). For lower energies, other techniques are applied. For instance the photoelectric effect, or photon to electron conversion at a photocathode, and the subsequent measurement of the resulting electron using photomultiplier tubes (PMTs), as is the case for the *Fermi*-GBM (γ-ray burst monitor) instrument (8 keV to 30 MeV). Other instruments in the past used also the Compton effect of photons passing through matter upscattering electrons, that are measured using scintillator detectors. Direct measurements are limited by the size of the satellite and are well suited for measuring low and medium energy γ-rays.

Indirect measurements : Earth-bound experiments can detect the secondary products of the interactions of the γ-rays occurring in the upper atmosphere. A very successful method is the IACT technique that uses the Earth atmosphere as a calorimeter and detects the Cherenkov light from the interactions of the γ-rays using Cherenkov telescopes. The most successful experiments currently in operation are H.E.S.S. (HESS Collaboration [2016b]), MAGIC (MAGIC Collaboration [2016]) and VERITAS (VERITAS Collaboration [2016]). Another example is the future CTA Observatory (CTA Consortium [2016]). This technique has proven to be very successful in the 100 GeV to 100 TeV energy band. Other techniques in use involve similar effects but measuring Cherenkov light in water instead of the atmosphere: the water-Cherenkov technique is used by HAWC (HAWC Collaboration [2016]).

Since this work focuses on ground-based IACT experiments, following discussions will concentrate on the IACT technique.

1.3. The IACT technique

Space γ-rays interact with the matter of the Earth atmosphere. The dominant process is e^+/e^- pair production in the presence of the nuclear Coulomb field of the atoms in the upper atmosphere. The e^+ and e^- loose energy via Bremsstrahlung, creating new γ-rays

susceptible to creating new e^+/e^- pairs. The process is repeated on average after each radiation length ($X_0 \simeq 36.5\,\mathrm{g/cm^2}$ for particles traveling in the atmosphere) creating an electromagnetic particle shower (also known as air shower). The shower develops until the energy of the e^+ and e^- particles is so low (about 10 MeV) that ionization losses dominate. At this point the e^+ and e^- particles are rapidly cooled and thermalized. The whole process takes about 10^{-4} s.

Very few energetic particles from the air shower arrive at the ground (for primary γ-rays of about 100 GeV). Nevertheless, the shower is still visible for optical telescopes sensitive to the Cherenkov radiation[1] emitted by the relativistic e^+ and e^- particles in the air shower. Each of them emits a cone of Cherenkov light along its path that reaches the ground without being absorbed. The collective effect leads to a uniformly illuminated light pool on the ground for each primary γ-ray that can extend over a few hundred meters in diameter and is centered at the shower core (point in the ground that the primary γ-ray would have hit if no interaction had occurred). The amount of light in the light pool is directly related to the energy of the primary γ-ray (more energy means more particles are produced in the air shower, hence more Cherenkov light). Thus, by measuring the properties of the Cherenkov light pool, the properties of the primary γ-ray can be inferred, specifically its direction and energy. This is the working principle of IACT systems. A schematic is shown in figure 1.1.

The largest disadvantage of the IACT technique is the faintness of the Cherenkov light, that reduces the observation time available to the dark hours (ideally moonless) of the night, and requires quite large light collection devices. Another challenge is the brief duration of the Cherenkov light signal (a few ns). In order to record the signal without integrating too much noise (which is dominant even at night) fast recording devices are required.

IACT systems consist typically of arrays of Cherenkov telescopes with large mirrors ($5 - 30$ m diameter) that focus the light into fast PMT cameras sensitive to Cherenkov light (typically electromagnetic wavelengths in the range from 300 nm to 600 nm; orange to near UV bands) that record the light with fast electronics.

The images of γ-ray air showers recorded by the cameras are typically elliptical. An image of a γ-ray induced shower is shown in the left panel of figure 1.2. The amount of light recorded (typically measured in photo-electrons, p.e.) is proportional to the energy of the primary and can be calibrated. The major axis of the ellipses and the gradient of arrival times of the signal at each part of the ellipse carry information about the direction and distance of the primary: for instance the major axis points to the arrival direction of the primary, and images from showers falling closer to the telescopes develop faster in the cameras than those from showers falling further away. It is usual to require at least two images per event (i.e. stereoscopic view of the shower) in order to enhance the quality of the reconstruction. In stereoscopic events, the intersection of the major axis of the projections of all images of all telescopes in a common plane marks the direction

[1] The Cherenkov light is the electromagnetic radiation emitted by charged particles traveling faster than the speed of light in a dielectric medium. The spectrum of Cherenkov radiation is continuous and peaks in the blue-ultraviolet (UV) band.

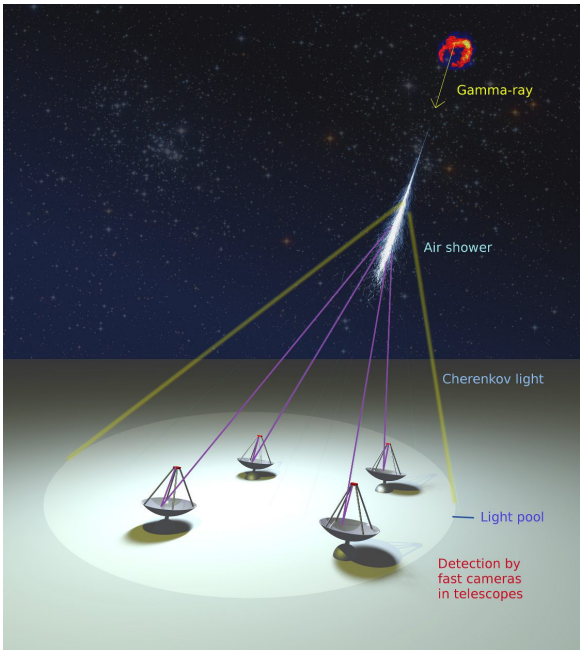

Figure 1.1.: IACT system imaging an air shower originated from a γ-ray from an SNR. Figure taken from Völk and Bernlöhr [2009].

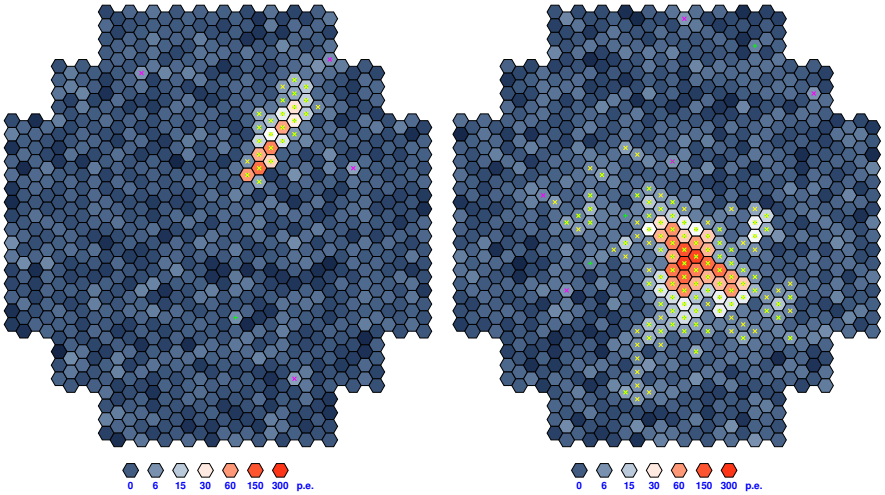

Figure 1.2.: Camera images of a γ-ray initiated shower (left) and a proton initiated shower (right). Figure taken from Völk and Bernlöhr [2009].

of the primary particle, pinpointing the source of the γ-ray. A schematic of how the stereoscopic technique works is shown in figure 1.3. Thus the properties of the γ-ray (its energy and direction) can be reconstructed.

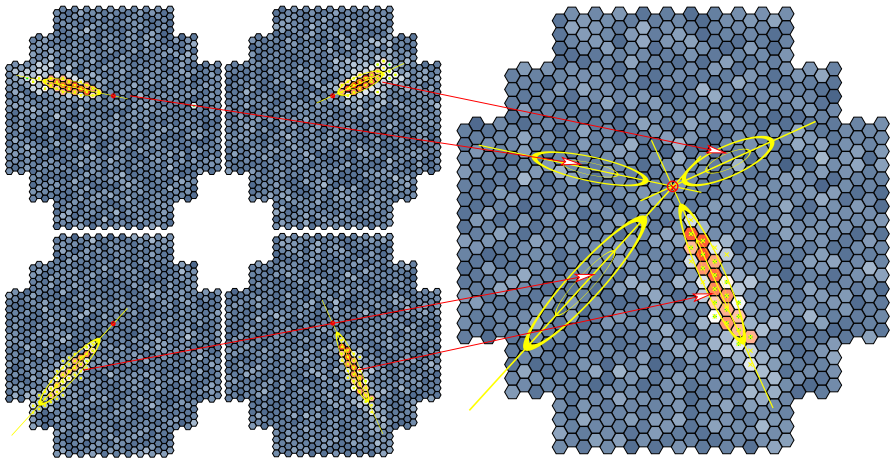

Figure 1.3.: Left: shower images of an event recorded with several cameras in a stereoscopic system. Right: projection of the different views of the shower from the left into a common camera plane to determine the direction of the primary particle producing the shower. Figure taken from Völk and Bernlöhr [2009].

Further details on the IACT technique can be found in Völk and Bernlöhr [2009].

1.3.1. Signal and noise sources

The PMT cameras used as detectors of IACT systems are very sensitive in order to record the faint and fast glow of the Cherenkov light of the particle showers from the γ-ray signal that is the subject of the measurements. Therefore they record many other non interesting sources of light (noise or background). The imprints of γ-ray events in the cameras are compact elliptical images that develop in a few nanoseconds. IACT systems are typically built such that images of the γ-ray showers are detected in more than one telescope. The difference in arrival times between the images of different telescopes depends on the geometry of the array and the zenith angle of the telescopes. A typical value for non-zenith observations is a few tens of nanoseconds.

The major noise sources for IACT systems are listed in the following:

Bright stars : stars in the field of view of a telescope are typically imaged into one pixel in the camera. A bright star can cause the PMT into which it is imaged to be constantly above the threshold, hence give false triggers. Therefore, pixels imaging a star are typically switched off and their intensity is later on estimated by interpolating the signal in the neighboring pixels.

NSB : night sky background is a diffuse emission with different sources (diffuse light reflected in the atmosphere, nearby human lights, diffuse scattered star lights, etc.) that produce randomly triggered pixels, blurring the images of air showers. To minimize this effect, read-out windows are kept as short as possible. In addition,

multiple NSB triggered pixels can produce a false camera trigger. The camera trigger is tuned in order to minimize such NSB triggers.

Muons : relativistic muons from hadronic cascades traveling through the atmosphere produce Cherenkov light cones very low in the atmosphere and leave ring-shaped images in the camera, typically triggering only one telescope. The requirement of stereoscopy (multiple camera (i.e. telescope) triggers for each event) minimizes the effect of muons.

Hadrons : hadrons produce air showers very similar to the ones initiated by γ-rays, and hence leave signatures in the cameras very similar to the images of γ-rays. Cosmic ray hadrons are very numerous and are continuously entering the atmosphere, dominating over any γ-ray signal by a factor of $\sim 10^3$. Hadrons interact with matter in the upper atmosphere producing a large variety of products mostly π-mesons) that decay into other particles, among them γ-rays, producing hadronic showers that also contain electromagnetic components. Hadronic showers tend to be more spread (due to the large transverse momentum transfer in hadronic interactions) and irregular (due to the mixture of hadronic and electromagnetic components and the vast number of different possible hadronic interactions) compared to γ-ray showers. An image of a proton induced shower is shown in the right panel of figure 1.2.

Electrons : electrons[2] produce air showers almost indistinguishable from the ones initiated by γ-rays. Hence, their suppression is very challenging. Essentially, the only difference is the location of the first interaction in the atmosphere and thus, the depth of the shower maximum (atmospheric depth at which the number of particles generated by the shower reaches its maximum value), which occurs on average half a radiation length higher in the atmosphere for electrons.

Ultimately, the cameras rely on a precise triggering system and a thorough calibration in order to best extract the γ-ray signal and its properties. There is always a large number of noise events (mostly hadronic showers and electrons) as well as random NSB pixels in the images that cannot be filtered online (at the time of observation and data acquisition) because their signature in the camera is very similar to that of γ-rays. This noise that is recorded together with the γ-ray images has to be suppressed offline by means of the so called image cleaning process and the so called γ/hadron separation techniques. The former suppresses the random NSB pixels and the latter makes use of the morphological differences between electromagnetic and hadronic air showers to reduce the hadronic events. Still, many hadronic events that are indistinguishable from γ-rays, as well as electron initiated electromagnetic shower events, survive the filters: the so called γ-like background. In order to reduce its impact in the analysis this background has to be modeled and subtracted.

[2]Here *electrons* is used as a generic term to denote both, electrons and positrons, which are indistinguishable for IACT systems.

Further details on how Cherenkov telescope system triggers work to suppress the noise are given in section 2.2. In addition, more details about the operation of IACT systems and the processing of the data are given in sections 4.3 and 4.4 using H.E.S.S. as an example.

2. Estimation of trigger rates, data rates and data volumes for CTA

In this chapter, estimations of the trigger rates, data rates and data volumes for the CTA project are presented. Such estimations are very important in the design phase of a new project, especially for its data acquisition and archival systems: while the trigger and data rates will determine the required speed and processing power of the data acquisition system, the data volume will determine the storing capacity of the archival system.

The results in this chapter are obtained by studying detailed simulations of possible array configurations based on the experience gathered from current instruments. For this purpose, some input regarding the camera electronics and some assumptions about the information that should be stored are necessary. The reliability of the results depends on the accuracy of these "a priori" assumptions.

This chapter is organized as follows. The CTA project is be presented in section 2.1. Then, the trigger systems of IACT experiments are introduced in section 2.2. The details about the simulation chain and the properties of the simulated telescope array and the simulated trigger system are included in section 2.3. The results about effective areas, trigger rates, data rates and data volumes for a specific candidate array are presented in section 2.4. The results for all candidate arrays are summarized in appendix A. The next-neighboring scheme for the candidate array used to derive the results in the main text is presented in appendix B. Finally, the results of all candidate arrays are compared in section 2.5, and put in the perspective of the data acquisition and archival systems.

2.1. The CTA project

The Cherenkov Telescope Array (CTA) is a project for a future ground-based γ-ray experiment. It will represent the next generation of imaging atmospheric Cherenkov telescope (IACT) experiments, aiming at improving the sensitivity and angular resolution by a factor of 10, compared to current experiments, in the energy range from a few tens of GeV to a hundred TeV. In addition, the energy resolution will be as good as 10%, and the field of view (FoV) as wide as 10° in diameter for the highest energies. Scientists from all major current experiments H.E.S.S. (HESS Collaboration [2016b]), MAGIC (MAGIC Collaboration [2016]) and VERITAS (VERITAS Collaboration [2016]) are working in the project, to achieve these goals. An artist view of one possible CTA array layout is shown in figure 2.1.

The superior sensitivity and energy resolution of CTA will allow the exploration of the origin of cosmic rays and acceleration of particles, as well as the indirect search

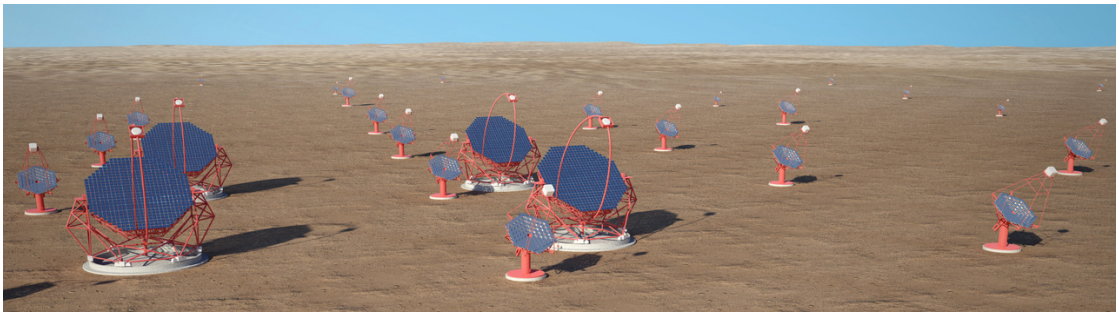

Figure 2.1.: CTA artist view. Copyright G. Pérez, IAC (SMM).

of dark matter over a large parameter space. The wider FoV and improved angular resolution will enable deeper and more detailed surveys of the sky. CTA will be able to reach sub minute time variability resolutions, making possible more detailed studies of transient events. More than 1000 sources will be detectable with CTA, allowing both, detailed studies of particular sources, as well as population studies of source classes, and eventually the discovery of new source classes and new physics.

CTA will be operated as an open observatory, allowing the whole scientific community to profit from its capabilities. The observatory is planned to be deployed in two different sites, one in the northern and a second one in the southern hemisphere, allowing a full coverage of the sky.

Each site will host an array of several tens of telescopes, covering an area of several square kilometers. CTA will be the first experiment of its kind, where the Cherenkov light pool will be fully contained within the array for a wide energy range. This will allow each shower to be simultaneously mapped by several telescopes at the same time, improving the energy and angular resolution of the reconstructed events. The improvement in energy coverage and sensitivity is achieved by using different kinds of telescopes across the array (see table 2.1):

- Large size telescopes (LST) densely packed in the center of the array for low energy coverage with a modest FoV. They should cover an area of $\mathcal{O}(0.01\,\mathrm{km}^2)$, from which $\sim 10\%$ should be covered by reflectors.

- Medium size telescopes (MST) around the LSTs for medium energy coverage with a wide FoV. They should cover an area of $\mathcal{O}(0.1\,\mathrm{km}^2)$, from which $\sim 1\%$ should be covered by reflectors.

- Small size telescopes (SST) spread around the MSTs for high energy coverage with the widest FoV. They should cover an area of $\mathcal{O}(1\,\mathrm{km}^2)$, from which $\sim 0.05\%$ should be covered by reflectors.

The design of the cameras foresees the use of more sensitive Cherenkov light detectors and fast electronics. This will improve the sensitivity and the timing resolution of CTA.

For the optical design of the telescopes, several possibilities are under consideration:

	D/ m	D_{FoV} / °	F/D
LST	23	3-5	~ 1.35
MST	12	8-10	1.3-1.4
SST	6-7	10	~ 1.7

Table 2.1.: Approximate specifications for the different telescopes: diameter of the dish D, diameter of the FoV covered by the cameras D_{FoV} and ratio of the focal length to the diameter of the dish F/D. These numbers are taken from CTA Consortium [2016] and CTA Consortium [2011].

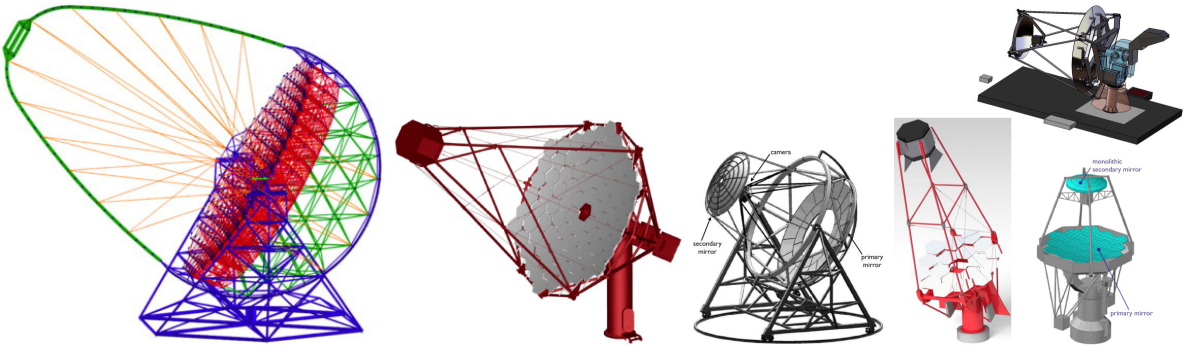

Figure 2.2.: CTA telescope designs. From left to right: LST, Davies-Cotton MST, Schwarzschild-Couder MST and various designs for the SST. Figures taken from Acharya et al. [2013] (not to scale).

- Parabolic mirror design: the reflector consists of a large parabolic mirror, which can be built from smaller spherical mirrors with varying focal length. This design has the advantage, that it preserves the intrinsic timing of the shower in the imaging process. This is especially important for low energy events, because they do not produce much light, so it is important to reduce the time integration gate for the photomultiplier tubes (PMTs), in order to avoid integrating too many night sky background (NSB) photons. Another advantage is the small on-axis point spread function (PSF). The disadvantage is that the PSF worsens rapidly with increasing off-axis angle. Moreover, off-axis images have an asymmetric PSF due to coma aberration. This design is used by the MAGIC 17 m telescopes, and the new 28 m telescope in H.E.S.S. This is the preferred design for LSTs in CTA, in order to lower the energy threshold of the system.

- Modified Davies-Cotton (DC) design: the reflector consists of a large spherical mirror composed of small identical spherical mirrors. The individual facets have a radius of curvature which is different from twice the radius of curvature of the dish, which is the main difference with respect to a pure DC design. DC designs have the advantage of having a circular PSF across the whole surface, which remains quite stable for a reasonable range of off-axis angles. The disadvantage is that the

on-axis PSF is not as small as for the parabolic mirror. In addition, the timing within the shower is not preserved. The pure DC design has been used for most of the IACTs, for instance the four 12 m telescopes in both H.E.S.S. and VERITAS. Because of the small on-axis PSF and the preservation of the timing within the shower, the modified DC represents an improvement of the technique and is the preferred design for MSTs in CTA. Moreover, it is considered also as an option for some designs of the SSTs.

- Schwarzschild-Couder (SC) design: the telescope holds a secondary optics reflector with two aspherical mirrors. This is a more complex design that presents a few technical challenges. It was never used for γ-ray astronomy, so it needs prototyping and testing. It has the advantage of imaging the showers into a small area and having a very small PSF, that could benefit from a new camera with smaller and cheaper detectors (i.e. silicon photomultipliers). Moreover, the secondary optics allows for a large FoV with a relatively small camera. The disadvantages are the high precision needed for the mirror construction and alignment, as well as the non-planar focal plane of the camera, that increase the cost of the telescope. This design is being taken into account for some designs for the SSTs in CTA and maybe for a second set of MSTs, that should work in parallel to the DC MSTs.

A performance comparison between parabolic and DC telescopes is given in Akhperjanian and Sahakian [2004]. An overview of the design of DC and SC SSTs for CTA can be found in White et al. [2011]. The current designs for each type of telescope is shown in figure 2.2.

As mentioned above, the observatory is planned to be built in two different sites. Each site will have access to a different region of the sky, with different properties. The inner part of the Milky Way, where most of the Galactic sources reside, is only observable from the southern hemisphere of the Earth. The Galactic sources are characterized by a hard spectrum and are expected to present spectral cut-offs at high energies. Most of them are spatially extended beyond the PSF of the instrument. The density of sources in the Galactic plane is very high. From the northern hemisphere of the Earth, only a small fraction of the Galactic plane is visible, so most of the sources are expected to be extragalactic: their spectra are softer due to the effects of absorption of high energy photons by the extragalactic background light, so a signal is only expected at low energies, and the sources are mostly point-like. Therefore, the southern site will be dedicated to both Galactic and extragalactic physics, whereas the northern site will concentrate mostly on extragalactic physics. For this reason, the southern array should cover a wider energy range, have better sensitivity at medium to high energies, a larger FoV and a better angular resolution. The northern site should have a good sensitivity and angular resolution at low energies. A list with the requirements for each site is given in table 2.2. The expected integral sensitivity and angular resolution curves as determined from Monte Carlo (MC) simulations for the southern site are shown in figure 2.3.

After the design phase, the project has entered its preparatory phase, in which proto-

	Southern array
energy range:	$\sim$ some 10 GeV ... $\sim$ 100 TeV
angular resolution:	0.2° ... 0.02° per event
flux sensitivity:	$\mathcal{O}$(few 10 mCrab) above $\sim$ 30 GeV (10 h)
	$\mathcal{O}$(1 mCrab) above 200 GeV (50 h)
	Northern array
energy range:	$\sim$ some 10 GeV ... $\sim$ 1 TeV
angular resolution:	0.2° ... 0.05° per event
flux sensitivity:	$\mathcal{O}$(few 10 mCrab) above $\sim$ 30 GeV (10 h)
	$\mathcal{O}$(4 mCrab) above 100 GeV (50 h)

Table 2.2.: Requirements for the northern and southern sites. These numbers are taken from CTA Consortium [2016] and CTA Consortium [2011].

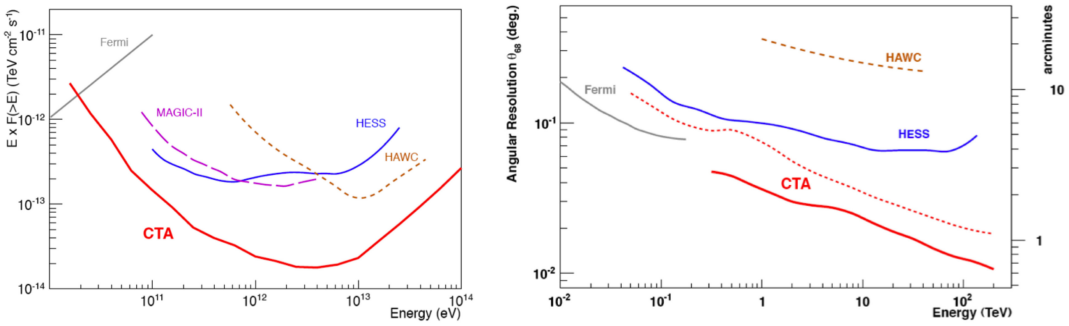

Figure 2.3.: CTA performance curves determined from MC simulations for the southern site, compared to other existing experiments. Left: integral sensitivity for a 50 h observation in the case of IACT experiments and one year for *Fermi* and HAWC. Right: angular resolution. The red solid line represents the angular resolution for events with ten or more images, whereas the red dashed line shows the angular resolution for events with only two images. Figures taken from Acharya et al. [2013].

typing of the different parts of the detectors is one of the main goals.

More details about CTA are given in CTA Consortium [2016], CTA Consortium [2011] and Acharya et al. [2013].

2.2. Trigger levels

IACT systems are background-dominated particle detectors. For this reason, an efficient trigger system is essential for the selection of interesting events. In the case of CTA, the large effective area of $\mathcal{O}(10^7\,\mathrm{m}^2)$ expected for arrays of $\mathcal{O}(50)$ telescopes presents a challenge for the trigger, which needs to suppress the abundant background processes,

in order to keep the dead time of the system as low as possible.

As already discussed in subsection 1.3.1, for ground-based IACT arrays, the major sources of background are night sky background, single muons and hadronic showers, the latter mostly induced by protons. The first two sources of background can be heavily suppressed by an online trigger system. Hadronic showers, however, produce telescope images that are quite similar to the images induced by γ-ray showers and it is therefore preferred to separate hadrons and photons offline.

IACT systems have in general a 3 level trigger system:

- Level 0 ($L0$) or pixel threshold: the threshold on the voltage level of the PMTs of the cameras is adjusted in order to reduce the NSB rate.
- Level 1 ($L1$) or telescope level trigger: a spatial and temporal coincidence of triggered pixels of one camera is required in order to select shower images and avoid random NSB triggers.
- Level 2 ($L2$) or array level trigger: the information of different telescopes is combined in order to reject muons and hadrons.

The purpose of the camera trigger ($L0$ and $L1$) is to provide an energy threshold as low as possible, while keeping a low rate of NSB. The number of pixels for $L1$ is selected in order to have compact (γ-like) images. The length of the gate for pixel coincidences for $L1$ is adjusted in order to correctly trigger showers with large impact parameter: these far away showers produce images in the camera that develop more slowly, and hence cannot produce a trigger unless the allowed gate is long enough.

For the array trigger ($L2$), in order to avoid triggering on single muons, a minimum telescope multiplicity is requested within a certain time window. This requirement increases the energy threshold, but suppresses most of the muon rings. Another advantage of having stereoscopic events is that the quality of the shower reconstruction is improved significantly. Especially the direction of the primary can be determined with better accuracy, as well as the impact distance, which helps in solving the ambiguity between a low energy event at a small impact parameter and a high energy event at a large impact parameter. In addition, the images of the cameras could be parametrized in real time during the $L1$ trigger and combined in the $L2$ trigger in order to reject the most obvious hadronic events, thus reducing the trigger rate. This possibility is discussed in Schroedter et al. [2009].

Another possibility for the camera trigger is the so called sum trigger concept used by MAGIC for lowering the threshold of the system in special observations. For this trigger concept, overlapping triggering sectors of the camera are predefined.The signals of the PMTs are clipped to avoid afterpulses, and summed for all pixels belonging to the same sector. If the summed signal of a sector exceeds a predefined value, a trigger is issued and the event is read out. This possibility is not further discussed in this work. For more details, refer to Haefner et al. [2011] and references therein.

For more details about IACT arrays triggering systems, refer to the references of the current experiments: H.E.S.S. (Funk et al. [2004], Schlenker [2001]), MAGIC (Aleksić et al. [2012]) and VERITAS (Weinstein [2008], Schroedter et al. [2009]).

2.3. Simulation chain and data sets

In this section, first the simulation chain used to produce the data sets for the analysis is described in detail. Afterward, the benchmark array implementations CTA-97 and CTA-ULTRA3 are introduced, followed by a description of the trigger parameters. Finally the simulated data sets are introduced.

2.3.1. Simulation software

The simulations used for the studies in this thesis where produced with the official software tools prepared for CTA. The generation process is based on a full MC simulation divided into two steps: the generation of air showers in the atmosphere with `CORSIKA` and the detector simulation with `sim_telarray`:

- `CORSIKA`: the name is an acronym from COsmic Ray SImulations for KAscade. This program was initially developed for the KASCADE experiment (KASCADE Collaboration [2014]), and was adapted for IACT experiments. As a result, it was used for HEGRA (HEGRA Collaboration [2006]), it is being used for H.E.S.S. and now for CTA.

  This program simulates the air showers produced when a γ-ray or a cosmic ray particle enters the atmosphere, and the propagation of the particles created in the shower. Simulations of a variety of primary particles are possible. In particular, both electromagnetic (i.e. γ-ray or electron induced) and hadronic showers (i.e. proton or heavier-nuclei induced) can be simulated. For this work, simulations of γ-ray- (proton-) induced showers were used as signal (background).

- `sim_telarray`: this program was developed mainly by Konrad Bernlöhr, first for the HEGRA experiment, later for H.E.S.S. and now for CTA. This program simulates a detailed response of an IACT system: mirror reflection of the Cherenkov light generated in the shower, PMT response[1], trigger system and read-out electronics.

More details about `CORSIKA` and `sim_telarray`are given in Bernlöhr [2008b] and references therein.

The output of the above described software chain is similar to that of a real detector: one data file per run, where the data is stored on an event-by-event basis, with the raw information of the PMT signals: integrated signal over the allowed time window (typically a few nanoseconds) with a few parameters that allow the rough estimate of the pulse shape[2]. The files are saved in the so called eventio format, which is a data format developed to be machine independent, in order to be as flexible as possible. For more details, refer to Bernlöhr [2001].

[1] At this point, random triggering of pixels is added to the simulation, in order to emulate the detector response in presence of NSB.

[2] The storage of fully digitized pulse shapes are not implemented to the date of the generation of the simulation files used for this work.

These files can be converted to a different (experiment specific) data format in order to use specific tools to analyze them. For this work, the files were downloaded from the central storage platform for CTA MC simulations and converted to the root-based `SASH` (Storage and Analysis Software at H.E.S.S.) format used by the H.E.S.S. experiment to analyze real data. In order to properly read the CTA simulated data, some modifications of the code, especially regarding the number of telescopes and the size of the field of view of the telescopes had to be performed. In addition, new classes and modules were developed and integrated into the regular H.E.S.S. analysis software chain in order to simulate the different trigger cases and read-out scenarios that are presented in section 2.4.

2.3.2. CTA-97

There have been many previous studies of benchmark arrays in order to limit the enormous parameter space that has to be explored for CTA. The first simulated array that matched the physics requirements was the CTA-97 array (Bernlöhr [2008a]). This was a 97 telescope array with telescopes of 2 different sizes.

The array was not optimized in all technical aspects, but it showed that the project is possible, and served as starting point for further designs. In particular, it would have been too expensive to build the CTA-97 array. Regarding the trigger rates, this topic was already studied in Paz Arribas [2008] for the CTA-97 array.

2.3.3. CTA-ULTRA3

The first official CTA MC mass production (production-1) started in 2009. Under the name CTA-ULTRA3, a super-array of 275 telescopes of 5 different kinds[3] was simulated (see figure 2.4). From these 275 telescopes, different subsets were selected in order to emulate the response of the actual candidate arrays for CTA. The candidate arrays were selected for different purposes (i.e. best performance for low energy events, or high energy events, or high angular resolution, etc.) and optimized in terms of costs, in order not to exceed the estimated budget. Dedicated candidate arrays were selected for the northern and southern sites. Some of the telescopes are used by several candidate arrays, sometimes with a different field of view[4]. The results of this chapter are based on the analysis of the CTA-ULTRA3 simulations.

A description of the simulated telescopes is shown in table 2.3. The values of the NSB rates in the PMTs are adapted to represent the NSB when pointing away from the Galactic plane and zodiacal light according to Preuß et al. [2002].

There are 13 candidate arrays in total: 11 for the southern site (A-K) and 2 for the northern site (NA, NB). Additionally, for this work, a subset of 4 MSTs organized as a H.E.S.S.-like telescope array (designated as subarray HESS) is also studied for

[3] One type of LST, three of MSTs and one of SST. The third type of MST is not relevant for this study, since it was not used in any of the candidate arrays, so it is ignored.

[4] The limitation of the FoV for some of the telescopes in some arrays is motivated by the cost optimization between number of telescopes in the array and size of the cameras.

	LST	MST	SST	MST_{LFoV}
F / m	31.20	15.60	11.20	16.80
D / m	23.0	12.0	6.7	12.0
mirror shape	parab.	DC	DC	DC
D_{C} / m	2.800	2.200	1.970	2.970
D_{FoV} / °	5.14	8.07	10.05	10.10
N_{P}	2841	1765	1417	1417
D_{P} / cm	4.900	4.900	4.900	7.400
$D_{\text{P}_{\text{FoV}}}$ / °	0.090	0.180	0.251	0.252
$L0$ trigger	102 mV	107 mV	103 mV	180 mV
$L1$ trigger	3 pix	3 pix	3 pix	3 pix
Δt_{disc} / ns	3.0	6.0	16.0	16.0
$\mathcal{R}_{\text{NSB}}$ / MHz	122	120	85	274

Table 2.3.: Specifications for the different telescopes in the simulations: focal length of the telescope F, diameter of the dish D, shape of the reflecting surface (parabolic or Davies-Cotton), diameter of the camera D_{C}, diameter of the field of view covered by the cameras D_{FoV}, number of pixels of the camera N_{P}, pixel size D_{P}, pixel angular size $D_{\text{P}_{\text{FoV}}}$, $L0$ and $L1$ trigger requirements, allowed gate for pixel coincidence for a camera trigger Δt_{disc} and rate of photo-electrons generated by NSB photons at the photo cathode of an individual PMT $\mathcal{R}_{\text{NSB}}$.

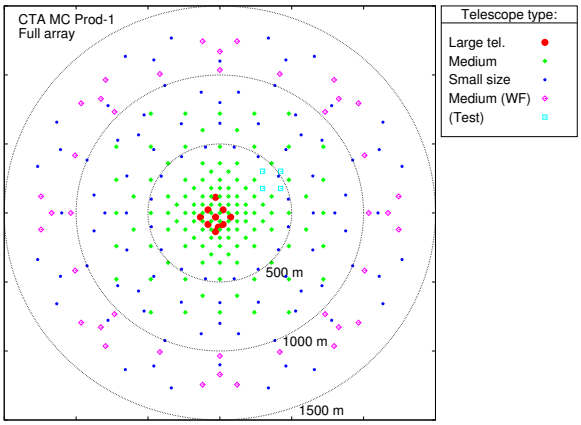

Figure 2.4.: Simulated telescope array used for the CTA MC production-1. Figure taken from Bernlöhr et al. [2013].

comparison to current IACT experiments[5]. The subarray HESS is also interesting in the case of a possible operation mode, where the CTA array would be split into subarrays of telescopes, each one observing one region of the sky. A description of the purpose and properties of each of the candidate arrays is given in appendix A. For more details on the simulations and performance of the CTA-ULTRA3 candidate arrays, refer to Bernlöhr et al. [2013].

For the purpose of readability, further discussions will concentrate on the so called candidate array E. The results of all configurations are included in appendix A. The candidate array E has been selected as example, for being a multipurpose array foreseen for the southern site of CTA with a balanced performance across the whole energy range. Moreover, this candidate array has been used extensively as a test array within the MC working package of CTA. Other candidate arrays with similar characteristics and performance are I and J, included in appendix A.

In the process of transforming the simulation files from the eventio format to the `SASH` format, two aspects had to be taken into account:

1. The number of telescopes were limited from the original 275 from the super-array to match the candidate arrays proposed for CTA.

2. The camera FoV was reduced for some of the telescope in the different candidate arrays, according to the cost optimization between the number of telescopes and the size of the cameras, in order to fit the estimated budget.

The particular selection of telescopes for the candidate array E is presented in table 2.4. If a specific parameter is not specified, its value remains unchanged, to the value

[5]The comparison will not be perfect, since the subarray HESS is simulated with improved PMTs and electronics, compared to current experiments, but it still agrees in the order of magnitude (i.e. the trigger rate of the subarray HESS is $\sim 400\,\mathrm{Hz}$ versus $300\,\mathrm{Hz}$ for the real H.E.S.S. experiment (Funk et al. [2004]).

indicated in table 2.3. The array layout is displayed in figure 2.5.

	N_T	D_{FoV} / °	N_P
LST	4	4.6	2275
MST	23	8	1735
SST	32	10	1393

Table 2.4.: Properties of the simulated telescopes for the candidate array E: number of telescopes of each kind N_T, diameter of the FoV covered by the camera D_{FoV} and number of pixels of the camera N_P.

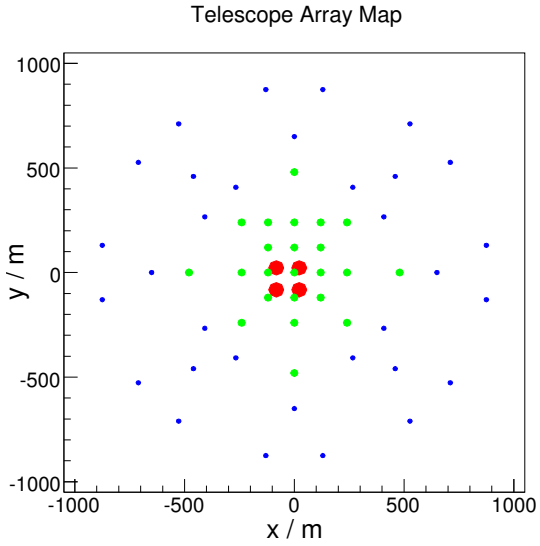

Figure 2.5.: Telescope map for the candidate array E. Each circle represents a telescope on the ground. The sizes of the circles are scaled to represent the size of the mirror dishes of the telescopes scaled by a factor three in radius for better visibility. Each color represents a different telescope type.

2.3.4. Simulated trigger system

The trigger simulated is a particular implementation of the three level structure described in section 2.2:

$L0$: the voltage of one pixel of the camera has to exceed a certain threshold, which is different for each telescope type, as denoted in table 2.3.

$L1$: each camera has to have 3 fired pixels (one pixel and two of its neighbors) within a certain allowed time gate, as denoted in table 2.3. The 3 fired pixels should form a compact image as depicted in figure 2.6.

The camera trigger ($L0$ and $L1$) is optimized accordingly, in order to keep the random telescope trigger rate due to NSB bellow 100 Hz.

$L2$: a coincidence of at least 2 triggered telescopes of the whole array is required within an unlimited time window[6].

The concept of the simulated camera trigger for CTA is depicted in figure 2.6. Figure 2.7 shows the trigger level scheme of IACT experiments, together with the particular numbers derived in this work for CTA.

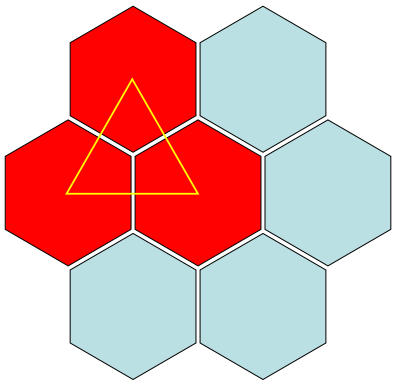

Figure 2.6.: CTA camera trigger concept. Depicted is a drawer of 7 PMTs. The red hexagons represent fired pixels. The triangle depicts the allowed topology for pixel coincidence for a $L1$ camera trigger.

Three different cases for the array trigger seem plausible:

Case 1: *central* trigger. There is a central trigger module connected to all the telescopes of the array, responsible for the $L2$ decision. When a camera trigger ($L1$) occurs, the corresponding telescope sends a signal to the central module and waits for a decision whether the event is accepted (and needs to be read out) or discarded. The read-out process could take place in parallel to the array triggering. In this case, a natural choice is to merge the events online, but the telescopes need large temporary storage memories, since the array is vast compared to current experiments and the trigger signals have to travel a long way.

Case 2: *local* trigger. Instead of a central trigger box, there are several local trigger modules distributed over the array, linking several neighboring telescopes. In this case, the temporary storage memories in the telescopes do not have to be very large, but the events have to be merged offline. In addition, inconsistencies could emerge between close-by telescopes that belong to different local triggers. If no

[6]The $L2$ trigger condition was applied to the 275 telescope array in the simulations, so this step had to be applied again for each particular candidate array in the analysis.

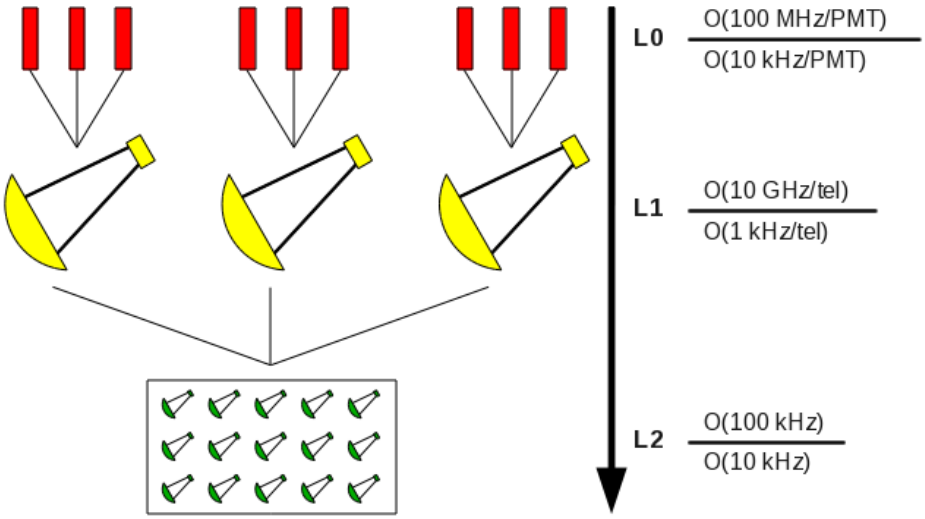

Figure 2.7.: IACT trigger levels. The numbers represent the values for CTA before and after each trigger level.

overlap among different local triggers is implemented, some events are lost. If it is implemented, some telescopes have a higher chance of triggering than others.

Case 3: *no* trigger. The telescopes act in stand alone mode: whenever a camera trigger occurs, the telescope starts the read-out. This way the telescope does not depend on an array trigger, so the array triggering and event merging have to be performed offline. The problem is that the trigger and data rates can become unbearable.

In the following, the results and discussions will concentrate on case 1 (*central* trigger), but numbers for the other 2 cases will be presented as well.

2.3.5. Data sets

For this work, simulations of γ-ray and proton showers are used. The γ-rays are simulated to emulate the signal coming from a point-like source, and the protons are simulated to emulate the diffuse background coming from cosmic rays. A continuum power-law spectrum $\propto E^{-2}$ was used for generating particles. However, more realistic particle flux spectra are considered in the analysis for deriving the results of this study. More details are given in subsection 2.4.2.

The results on the trigger rates and data rates depend of course on the pointing direction of the telescopes, especially on the zenith angle θ_{zen}. There are two competing processes. On the one hand, the low energy showers produce less Cherenkov light in the atmosphere. The light is partially absorbed and hence the events may not leave enough light in the telescope to be detected. Therefore, at zenith, where the thickness of the atmosphere layer that the light needs to cross is minimal, low energy particles are more

likely to produce a trigger. This effect increases the trigger rate at low energies and low zenith angles. On the other hand, high energy showers produce enough light to be detected at high zenith angles. In this case, since the thickness of the atmosphere layer is larger, the first interaction of the primary particle occurs at a larger distance from the ground (as measured along the shower axis), enlarging the area of the ground illuminated by the Cherenkov light cone, so showers with a larger impact parameter are also visible for the telescopes. This effect increases the trigger rate at high energies and high zenith angles. But since the particle spectra are represented by power-law functions in energy with a negative index, more particles are expected at low energies, so the first effect dominates over the second one. For this study, regarding the trigger rates, a worst-case scenario is simulated, with the telescopes pointing only 20° away from the zenith[7].

For point-like emission, as for the simulated γ-rays, the offset (off axis angle) from the center of the camera θ_{off} plays an important role as well. The acceptance of the camera has a radial dependence with a maximum in the center of the camera, therefore, events falling close to the camera center are more likely to be detected than if they fall close to the edge. In this respect, for γ-rays, a point source is simulated in the center of the camera ($\theta_{\text{off}} = 0°$), where both the acceptance and the trigger rate are maximal.

The values used for the pointing in the simulations are displayed in table 2.5, together with the number of showers and energy ranges of each data set. For the estimation of the single telescope rates, a different data set was used, where no array level trigger condition was requested. For this case, no γ-ray showers were simulated. The number of proton showers simulated is $N_{\text{sim}} = 8 \times 10^6$, equivalent to an observation time of $t_{\text{sim}} \sim 0.1\,\text{s}$. The rest of the parameters remain unchanged.

	θ_{zen}	θ_{az}	θ_{off}	R_{sim}	θ_{sim}	N_{sim}	t_{sim}	E_{min}	E_{max}
γ-rays	20°	90°	0°	2.5 km	—	4.8×10^6	17 min	3 GeV	300 TeV
protons	20°	90°	—	3.0 km	10°	3.0×10^7	0.5 s	5 GeV	500 TeV

Table 2.5.: Properties of the simulated data sets used for the analysis: zenith angle θ_{zen}, azimuth angle (measured from the north towards the east) θ_{az}, offset angle θ_{off}, radius for simulating particles around the pointing direction at the center of the array R_{sim}, angle for simulating particles around the pointing direction θ_{sim}, number of simulated showers N_{sim}, corresponding observation time t_{sim} and minimum E_{min} and maximum E_{max} energies of the primaries. For γ-rays, a point source was simulated, so the angle θ_{sim} is not defined in this case. In the case of protons, diffuse emission was simulated, so the angle θ_{off} is not defined in this case. For t_{sim}, a spectrum has to be assumed. In the case of γ-rays the spectrum of the Crab nebula measured by H.E.S.S. is used, and for protons a combination of the HEGRA and *BESS* spectra is assumed (more details are given in subsection 2.4.2).

[7] According to the figure 8 of Funk et al. [2004], the the trigger rates at zenith angles $\theta_{\text{zen}} = 0°$ and $\theta_{\text{zen}} = 20°$ are very similar, so 20° is a good value for the extreme case.

2.4. Results

In this section, results for effective areas, trigger rates, data rates and data volumes will be presented, for the different array trigger cases discussed above in section 2.3.4. Some of the results presented here have already been described in Paz Arribas et al. [2012]. The aim of this chapter is to give an update and extend the scope of the work already presented.

As already mentioned, the results will be derived for the candidate array E. For a summary of the results of each candidate array, refer to appendix A. A comparison among all candidate arrays is presented in subsection 2.5.1. The discussion will be centered on the case of a *central* trigger, but results of the other 2 cases are also shown. In particular, the mean trigger and data rates of each telescope type in each candidate array in stereoscopic mode will be shown for the case of a *local* array trigger[8,9], and the mean values for each telescope type for the 275-telescope super-array will be shown as an estimate of the amount of data generated for each telescope in the case of *no* array trigger at all.

In the case of a *central* array trigger, the results of a simple stereoscopic trigger (at least 2 cameras from the whole array should have triggered) will be contrasted to the case of requesting that the triggered telescopes should be next-neighbors (NN). This is motivated by the fact that most proton induced showers are very scattered, producing a quite inhomogeneous light pool at the ground, whereas γ-ray induced showers tend to be more compact, producing more homogeneous light pools. Therefore, with a next-neighbor system, some of the proton showers could be filtered away already at an early stage. The gray lines in figure 2.8 show the allowed connections between telescopes. The connections were chosen between pairs of close-by telescopes in a three step process:

1. First as many four-telescope cells with a (quasi)square shape as possible were defined using only MSTs and SSTs. Each telescope of the cell is connected to all members of the cell. In some cases in the zones of transition between MSTs and SSTs (transition between a square and a circular geometry) cells with five or three telescopes had to be defined.

2. Then, the telescopes at the boundaries of the SST four-telescope cells (circular geometry) are interconnected for neighboring cells in order to fill the gaps with three telescope cells.

3. Finally, the LSTs were interconnected as in step one, and each of them was interconnected to the telescopes of the MST-cell by which they are surrounded.

The exact definitions of the neighboring connections is given in appendix B.

[8] These values should be seen as upper limits of the case of a *local* array trigger, since the event stereoscopy request was not limited to close-by telescopes.

[9] This case is also interesting for the case of a *central* array trigger, since it will determine the amount of data to manage for each telescope.

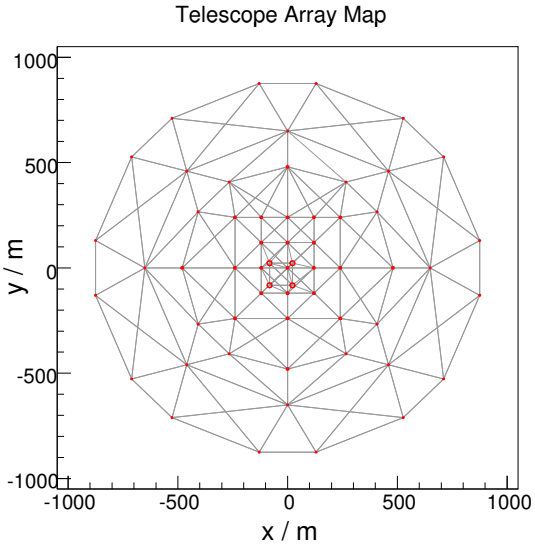

Figure 2.8.: Telescope map for the candidate array E for the case of a next-neighbors *central* array trigger. Each circle represents a telescope on the ground. The sizes of the circles are scaled to represent the size of the mirrors of the telescopes. The lines represent the allowed connections between telescopes.

2.4.1. Effective areas

For fixed zenith and offset angles, the effective area $A_{\text{eff}}(E)$ of the array for point source observations can be calculated using

$$A_{\text{eff}}(E) = \pi R_{\text{sim}}^2 \frac{N_{\text{sel}}(E)}{N_{\text{sim}}(E)} \tag{2.1}$$

where R_{sim} is the radius, measured in a plane perpendicular to the pointing direction of the array, within the showers are simulated; N_{sim} is the number of simulated showers with energy E; N_{sel} is the number of showers with energy E that are selected by the array trigger. This formula is used for the data set of simulated γ-ray events. In the case of diffuse emission the equation 2.1 needs to be multiplied by the solid angle Ω used in the simulations. This is the case for the data set of simulated proton events. The actual values for R_{sim} and Ω are given in table 2.5. They are selected big enough to cover the whole sensitive area and solid angle of the detector.

Figure 2.9 shows the effective areas as function of the energy for γ-rays (left) and for protons (right) for the candidate array E for the stereoscopic array trigger. The curves rise from zero at low energies ($E < 100\,\text{GeV}$), where the showers produce so little light that detection is subject to shower fluctuations, until they reach a plateau at high energies ($E > 10\,\text{TeV}$). In the case of γ-rays, the plateau slightly below $10^7\,\text{m}^2$, a factor 10 higher than for current experiments. Visible are also abrupt changes in the slope of the imaginary curve connecting the points that mark the transitions between regimes of

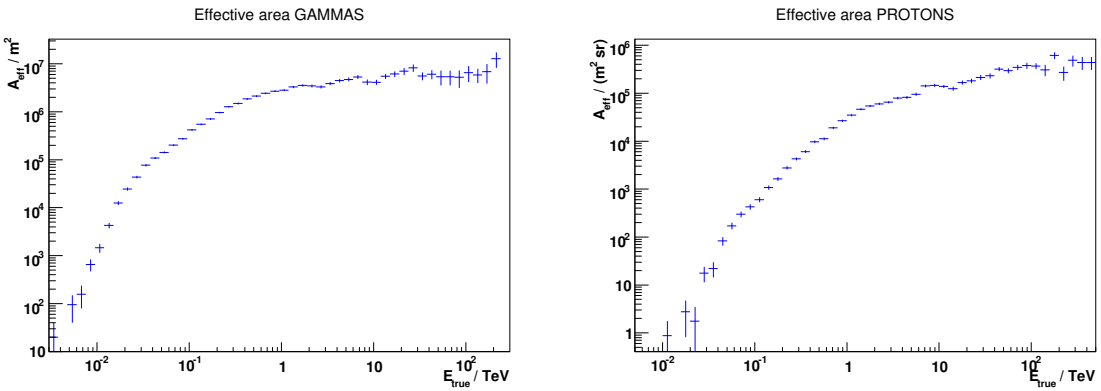

Figure 2.9.: Effective areas for the candidate array E for γ-rays (left) and protons (right) for the stereoscopic array trigger. The error bars represent 1σ statistical uncertainties.

different telescope types: at $\sim 100\,\mathrm{GeV}$ for the transition between LSTs and MSTs, and at $\sim 10\,\mathrm{TeV}$ for the transition between MSTs and SSTs.

2.4.2. Trigger rates

Once the effective area curves are known, the trigger rates $\mathcal{R}_{\mathrm{tr}}$ can be calculated by folding them with realistic spectra and integrating over all energies, using

$$\mathcal{R}_{\mathrm{tr}} = \int_0^\infty \mathrm{d}E \; A_{\mathrm{eff}}(E) \; \frac{\mathrm{d}\phi}{\mathrm{d}E} \tag{2.2}$$

where $\frac{\mathrm{d}\phi}{\mathrm{d}E}$ represents the particle spectrum. The emission of sources in γ-rays is highly non-thermal, and spectra often follow power-law functions.

In the case of γ-ray showers, the spectrum of the Crab nebula as measured by H.E.S.S. in (Aharonian et al. [2006a]) is used. The Crab nebula is the "standard candle" for γ-ray astronomy, and one of the brightest TeV sources in the sky. The spectrum is well described by a power-law function with an energy cut-off at high energies at 14 TeV. In this study the energy cut-off seen by H.E.S.S. is ignored for simplicity. Since the spectrum follows a power-law function and the cut-off affects only the high energies (where the flux is already very small), this will not modify the results significantly. The resulting spectrum is

$$\frac{\mathrm{d}\phi}{\mathrm{d}E} = 3.76 \times 10^{-7} \Big(\frac{E}{1\,\mathrm{TeV}}\Big)^{-2.39} \; 1/(\mathrm{s\,m^2\,TeV}). \tag{2.3}$$

The uncertainties in flux measurements is a source of uncertainties for the estimation of the trigger rate. For this reason, a quadratic combination of the statistical uncertainty in the spectrum normalization and the systematic uncertainty on the flux determination of the H.E.S.S. measurements (1.9% and 20% respectively) is used for the determination

of the systematic uncertainty of the trigger rates. This results in a 20% combined uncertainty[10].

In the case of proton showers, a combination of the *BESS* (Sanuki et al. [2000]) and the HEGRA (Aharonian et al. [1999]) proton spectrum measurements is used. HEGRA measured a pure power-law spectrum from 1.5 TeV to 3 TeV, whereas the *BESS* spectrum, measured from 1 GeV to 120 GeV, has a cut-off at low energies at $E = 4$ GeV due to the magnetic field of the Earth. Both spectra, if extrapolated, connect very well at the overlapping energies, resulting in the spectrum

$$\frac{\mathrm{d}\phi}{\mathrm{d}E} = 0.099 \, \frac{(E\,[\mathrm{TeV}])^{-2.70}}{1 + (0.004/E\,[\mathrm{TeV}])^{1.75}} \; 1/(\mathrm{s\,sr\,m^2\,TeV}). \tag{2.4}$$

The *BESS* measurement is reported with a total uncertainty (statistical and systematic) of 5%, whereas the HEGRA spectrum is reported with 18% statistical uncertainty in the normalization constant and 35% systematic uncertainty in flux measurements, leading to a combined uncertainty of 39%. Therefore, the spectrum from Eq. 2.4 is used with 5% systematic uncertainty below 120 GeV and 39% above 120 GeV.

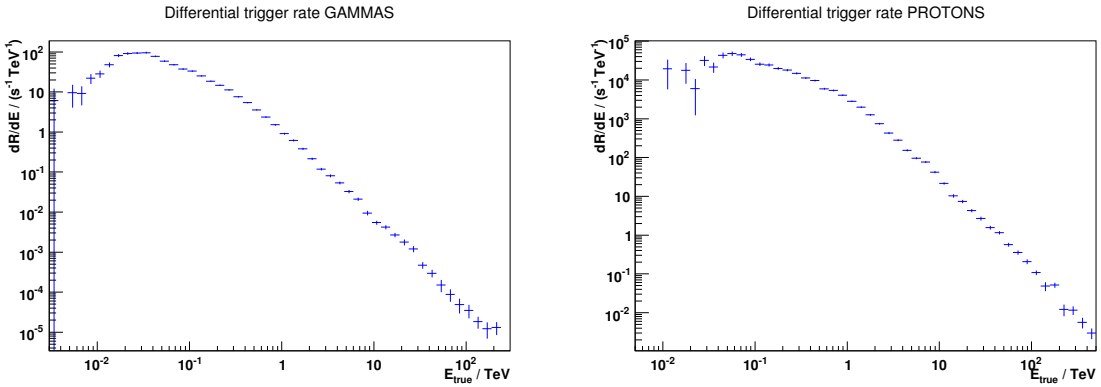

Figure 2.10.: Differential trigger rates for the candidate array E for γ-rays (left) and protons (right) for the stereoscopic array trigger. The error bars represent 1σ statistical uncertainties. The spectrum of the Crab nebula measured by H.E.S.S. is used for γ-rays and a combination of the *BESS* and HEGRA spectra is used for protons, as stated in the text.

Figure 2.10 shows the differential trigger rate as function of the energy for γ-rays (left) and for protons (right) for the candidate array E for the stereoscopic array trigger. The curves rise at low energies due to the small effective areas until they reach a maximum between 10 GeV and 100 GeV and fall afterward following the corresponding power-law spectrum. The transitions between telescope types are also visible here at the same energies as for the effective areas in figure 2.9. The trigger energy threshold E_{th} is

[10] The uncertainties in the behavior of the final trigger electronics is larger than the 20% mentioned here, but this contribution is very hard to estimate, since at the time of this study still new ideas are being presented.

defined as the energy for which the differential trigger rate curve has a maximum. For the candidate array E the values of E_{th} for γ-rays and protons are

$$\begin{aligned} E_{\mathrm{th}_\gamma} &= (34 \pm 4)\,\mathrm{GeV} \\ E_{\mathrm{th}_\mathrm{p}} &= (56 \pm 7)\,\mathrm{GeV}. \end{aligned}$$

The indicated uncertainties represent the width of the bin where the maximum is located.

The total trigger rates of the system are estimated by integrating the differential trigger rates from figure 2.10 over all energies. They amount to

$$\begin{aligned} \mathcal{R}_{\mathrm{tr}_\gamma} &= (12.32 \pm 0.12_{\mathrm{stat}} \pm 2.46_{\mathrm{syst}})\,\mathrm{Hz} \\ \mathcal{R}_{\mathrm{tr}_\mathrm{p}} &= (13.2 \pm 0.3_{\mathrm{stat}} \pm 1.2_{\mathrm{syst}})\,\mathrm{kHz}. \end{aligned}$$

These numbers represent the rates of events to read out in the case of a *central* array trigger. From the numbers it is clear that the trigger rate is dominated by proton showers: the signal to noise ratio is $\sim 1/10^3$. This represents a factor 40 higher trigger rates than that of H.E.S.S., with 300 Hz (Funk et al. [2004]).

For the results for the rest of the candidate arrays, refer to table A.15 in appendix A.

Comparing the numbers of the simple stereoscopic trigger to the results for the next-neighbor trigger

$$\begin{aligned} \mathcal{R}^{\mathrm{NN}}_{\mathrm{tr}_\gamma} &= (11.94 \pm 0.12_{\mathrm{stat}} \pm 2.39_{\mathrm{syst}})\,\mathrm{Hz} \\ \mathcal{R}^{\mathrm{NN}}_{\mathrm{tr}_\mathrm{p}} &= (11.7 \pm 0.3_{\mathrm{stat}} \pm 1.1_{\mathrm{syst}})\,\mathrm{kHz} \end{aligned}$$

the difference is a 10% gain in proton rejection, with only a 3% loss in γ-ray efficiency.

In the case of a *local* array trigger, the global trigger rates of each type of telescopes, when requesting stereoscopy, can be interpreted as an upper limit to the values of the local trigger rates. These local trigger rates should be smaller than the global trigger rates because in the case of a *local* array trigger, the telescopes connected to each array trigger unit should be close to each other and hence cover a smaller area in the ground, resulting in a smaller effective area. The values, shown in table 2.6, are calculated by averaging the trigger rate of all telescopes of a certain kind assuming the candidate array E. As expected, the highest rates come from the LSTs with ~ 2.6 kHz, though the MSTs also contribute significantly with ~ 1.0 kHz. These rates are generated from triggers coming from the central part of the array, where the density of telescopes (LSTs and MSTs) is quite large, as shown in figure 2.5. This higher density of telescopes and their large mirror area enable the triggering of low energy showers, that are very numerous, due to the power-law energy spectrum of incoming particles.

With the values of table 2.6 and using

$$\mathcal{R}^{\mathrm{tot}}_{\mathrm{tr}} = \sum_i N^i_{\mathrm{T}} \langle \mathcal{R}_{\mathrm{tr}} \rangle_i \,, \quad i = \mathrm{LST,\ MST,\ SST,\ MST_{LFoV}} \tag{2.5}$$

where N^i_{T} represents the number of telescopes of type i, the rates of telescope triggers

	$\mathcal{R}_{\mathrm{tr}_\gamma}$ / Hz	$\mathcal{R}_{\mathrm{tr}_\mathrm{p}}$ / kHz
LST	$4.908 \pm 0.018_{\mathrm{stat}} \pm 0.982_{\mathrm{syst}}$	$2.570 \pm 0.040_{\mathrm{stat}} \pm 0.257_{\mathrm{syst}}$
MST	$0.989 \pm 0.033_{\mathrm{stat}} \pm 0.198_{\mathrm{syst}}$	$1.025 \pm 0.062_{\mathrm{stat}} \pm 0.103_{\mathrm{syst}}$
SST	$0.282 \pm 0.016_{\mathrm{stat}} \pm 0.056_{\mathrm{syst}}$	$0.277 \pm 0.014_{\mathrm{stat}} \pm 0.028_{\mathrm{syst}}$

Table 2.6.: Mean trigger rates, when requesting stereoscopy, for each type of telescopes for the candidate array E for γ-rays and protons. The statistical errors are overestimated, because the samples are not statistically independent when calculating the mean value. In order to have uncorrelated samples a dedicated data set per telescope would have been necessary. This is not done because in that case, the MC production would have been large.

that need to be read out across the whole array in the case of either a *central* or a *local*[11] array trigger are estimated as $\mathcal{O}(40\,\mathrm{kHz})$. This is not equivalent to the rate of triggered events, since the same event can be triggered by several local triggers, and needs to be merged offline.

The dependence of the stereoscopic telescope trigger rate on the distance of the telescope to the center of the array is shown in figure 2.11. From the figure it is clear that not all telescopes of each kind behave equally: the telescopes closer to the center (where the telescope density is bigger) have a higher trigger rate. For instance, MSTs have a proton rate of $\sim 1.5\,\mathrm{kHz}$ up to 100 m away from the center, but afterward, the rate falls down exponentially with the distance up to $\sim 0.5\,\mathrm{kHz}$ at 500 m. In comparison, the mean value given in table 2.6 is $\sim 1\,\mathrm{kHz}$. This dependence can be interesting since some telescopes could have cheaper electronics (i.e. less local storage capacity), according to their position in the array.

In the case of *no* array trigger, the single telescope trigger rates represent the total trigger rate of each telescope of a certain type. The values, listed in table 2.7, are calculated by averaging the trigger rate of all telescopes of a certain kind. For this calculation, all telescope from the simulations were used, without assuming any particular candidate array. Therefore, no field of view reduction was applied to any of the telescopes. The rates were calculated using the dedicated proton simulations indicated in subsection 2.3.5, and they vary from 5 kHz for the LSTs to 2 kHz for both types of MSTs and 1 kHz for SSTs. If the field of view reduction of the candidate array E is applied, the rates of the LSTs go down to 4 kHz.

With the values of the single trigger rates and using the equation 2.5, the total telescope rate that an array trigger should process, or the telescope read-out rate in the case of *no* array trigger for the candidate array E is estimated as $\mathcal{O}(100\,\mathrm{kHz})$. The single telescope rates are roughly a factor 2 higher than the stereoscopic ones.

[11] As already mentioned, in the case of a *local* array trigger, the number has to be interpreted as an upper limit.

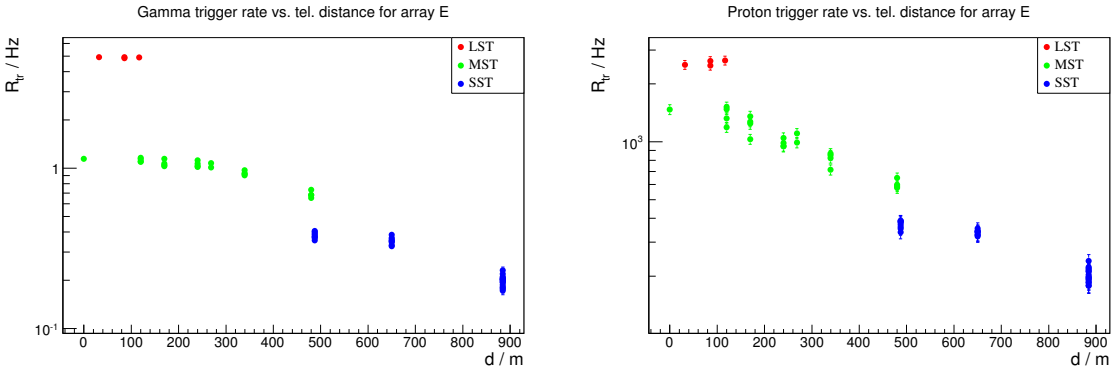

Figure 2.11.: Stereoscopic telescope trigger rates as function of the distance of the telescope to the center of the array for the candidate array E for γ-rays (left) and protons (right). The different telescope types are represented by different colors: red for LSTs, green for MSTs and blue for SSTs. The error bars represent 1σ statistical uncertainties.

tel type	$\mathcal{R}_{\mathrm{tr_p}}$ / kHz
LST	$4.652 \pm 0.103_{\mathrm{stat}} \pm 0.465_{\mathrm{syst}}$
MST	$2.180 \pm 0.020_{\mathrm{stat}} \pm 0.218_{\mathrm{syst}}$
SST	$0.918 \pm 0.026_{\mathrm{stat}} \pm 0.092_{\mathrm{syst}}$
$\mathrm{MST_{LFoV}}$	$1.655 \pm 0.031_{\mathrm{stat}} \pm 0.166_{\mathrm{syst}}$

Table 2.7.: Mean single telescope trigger rates for the four different telescope types. Like in table 2.6, the statistical errors are slightly overestimated.

Dead time implications

The dead time of a particle detector, such as the camera of an IACT, is the time after each event during which the system is unable to record another event. Using the single telescopes trigger rates and the array geometry, the dead time of the system can be estimated for CTA. The estimate of the dead time can help in deciding which camera electronics and trigger system should be used.

The dead time of the system is given by the read-out process of the PMT signals from the camera, and hence depends on the specific implementation of the electronics of the camera and the trigger modules[12]. The electronics of the H.E.S.S. cameras are used as starting point (Funk et al. [2004]). In this case, the PMTs are sampled using analog samplers and, when a camera trigger occurs the ring buffers of the PMTs are frozen while the digitization of the read-out process takes place, interrupting the data taking of the telescope. This process can be interrupted by a reset signal if the $L2$ trigger condition is not fulfilled. For the H.E.S.S. experiment, the dead time amounts to $450\,\mu$s for an

[12]The options for the electronics for CTA are not discussed, since they are beyond the scope of this work.

accepted event and 6 μs for a discarded one. These values can be considered as upper limits for CTA.

For CTA, in the ideal case of no time losses due to the generation and processing of triggering signals in the camera and the trigger module[13], there are only 2 contributions to the time delay of the trigger decision: the time delay for the signal to go from the telescope to the trigger module (*central* or *local*) and back, plus the central trigger processing time (which in this ideal case is just the allowed time window for telescope coincidence). These values can be interpreted as the lower limits to the dead time.

The extreme case of a *central* trigger (long distances between telescopes and trigger module, and long time window) is considered in this paragraph. In this case, if the trigger module is at the center of the array, the maximum distance between a telescope and the trigger module is ~ 1 km. This distance has to be counted twice for the array trigger decision to come back. If optical fibers are used for the communications of trigger signals, the speed of the signal is $\sim 2/3\,c$, so the contribution to the time delay of the trigger signal is $\sim 10\,\mu$s. The time window for telescope coincidence is typically a small fraction of this time (a couple of 100 ns), so it can be ignored. In the case of a *local* trigger, the distances are one order of magnitude smaller, so the time delay is $\sim 1\,\mu$s. In this case, the time window for telescope coincidence can represent an important fraction of the time delay, so it should be considered, increasing the time delay to $\lesssim 2\,\mu$s.

Comparing these times to the values from the H.E.S.S. experiment it is clear that the time delay in the case of a *central* trigger with ideal electronics (10 μs) is already higher than the dead time of discarded events by almost a factor 2. Therefore, in order not to significantly increase the dead time, CTA should either use a distributed array trigger (such as a *local* or *no* array trigger) or use a camera electronics concept that does not need to interrupt the data taking process, when a camera trigger occurs, i.e. fully digital electronics, with sampling buffers that cover at least 10 μs (typical ones are on the order of a few μs).

Moreover, the probability of an event arriving within the time delay of the signal for the case of a *central* array trigger is not negligible. The probability density function (PDF) of an event triggering the camera as a function of time t (counted from the time of the previous event) can be described using the following Poisson distribution

$$p(t) = \frac{1}{\tau}\, e^{-t/\tau} \tag{2.6}$$

where τ represents the characteristic time of the camera trigger ($\tau = 1/\mathcal{R}_{\mathrm{tr}}$). The probability of a second event triggering the camera, while the first one is being read out, is given by the integral of the previous PDF over a time interval Δt equal to the dead time produced by the read-out of the first event. In the extreme case of an LST with $\mathcal{R}_{\mathrm{tr}} = 5$ kHz, $\tau = 200\,\mu$s and $\Delta t \leq 10\,\mu$s, the probability is larger than 5%. In the case of a *local* array trigger, $\Delta t \sim 2\,\mu$s, so the probability is 1%. These values are quite high already, without introducing the effects produced by the electronics: the delays

[13] These effects are specific to the implementation of the electronics of the camera and the trigger modules, so their estimation is beyond the scope of this work.

coming from signal creation/interpretation and the read-out process, suggesting that an asynchronous trigger may be a good option for CTA, as suggested by Hermann et al. [2008]. Another possibility would be to fully digitize the PMT signal, so the buffers do not need to be frozen. In this case, the buffers need to be long enough to wait for the array trigger decision, increasing the current buffer sizes from a few μs to tens of μs. The use of analog buffers in not foreseen for CTA because they would need to be too long compared to that of existing experiments and hence too expensive; analog buffers are able to handle a few μs); digital ones could handle u to a few seconds.

2.4.3. Data rates

For the estimation of the data rates a plausible scenario of the amount and kind of information to be stored for one event has to be considered. In the case of H.E.S.S. (Funk et al. [2004]), the individual PMTs are sampled at 1 GHz and, when an array trigger occurs, all cameras that have triggered will store the integrated signal over the allowed time window of 16 ns for each and every pixel in the camera, for each of the two pixel channels (high gain and low gain). In the end this is translated into 2 bytes of information for each channel. In the case of MAGIC (Aleksić et al. [2012]), more resolution is needed, so the time profile of the PMT signal is sampled at 2 GHz and stored to disk. This technique has proven to be very useful for lowering the thresholds of the image cleaning and for the γ-hadron separation, especially when operating the telescopes in single mode. Both contributions help in lowering the energy threshold of the system. Assuming a 1 GHz sampling for a time window of 15 ns and 2 bytes/sample/channel, the amount of data per channel to be stored for each event is 30 bytes.

At this point, assuming only one channel per pixel[14] and that only triggered telescopes are read out, the data rate $\mathcal{R}_\mathrm{d}$ can be estimated via

$$\mathcal{R}_\mathrm{d} = \int_0^\infty dE \, \frac{\mathrm{d}\Phi}{\mathrm{d}E} \int_0^\infty \mathrm{d}d \, \frac{\mathrm{d}n}{\mathrm{d}d}\Big|_E S_\mathrm{ev}(E, d) \tag{2.7}$$

where S_ev is the typical size for events of energy E and distance to the center of the array d. This quantity is determined in the form of a 2D-lookup from the MC sample.

The equation 2.7, assumes that the particle distribution $\frac{\mathrm{d}N}{\mathrm{d}E\,\mathrm{d}d}$ can be separated into 2 distributions: $\frac{\mathrm{d}\Phi}{\mathrm{d}E}$ (normalized to the flux Φ) and $\frac{\mathrm{d}n}{\mathrm{d}d}$ (normalized to 1 for each energy bin). The latter one can be interpreted as a probability density function $\mathcal{P}(d)$ for d in a particular energy bin E, and thus the equation can be rewritten as

$$\mathcal{R}_\mathrm{d} = \int_0^\infty \mathrm{d}E \, \frac{\mathrm{d}\Phi}{\mathrm{d}E} \langle S_\mathrm{ev} \rangle \Big|_E \tag{2.8}$$

where $\langle S_\mathrm{ev} \rangle \Big|_E$ is the mean value of the event size in a particular bin of energy E.

[14] Here it is assumed, that pixels with a single non-linear amplification channel will be used. In the case of more than one channel, the resulting data rate has to be multiplied by the total number of channels per pixel.

For the estimation of the data rate of specific telescopes, in the case of a *local* or *no* array trigger, a different approach is taken. Again, assuming only one channel per pixel and that only triggered telescopes are read out, the data rate $\mathcal{R}_\mathrm{d}$ of a specific telescope can be estimated via

$$\mathcal{R}_\mathrm{d} = \mathcal{R}_\mathrm{tr}\, N_\mathrm{P} \Big[\eta\, 30 \text{ bytes} + (1-\eta)\, 2 \text{ bytes}\Big] \tag{2.9}$$

where $\mathcal{R}_\mathrm{tr}$ is the trigger rate of the specific telescope, N_P is the total number of pixels in the camera and η is the fraction of pixels to be read with timing information: the average of this quantity over all images triggered by the specific telescope is calculated. Afterward, the average of $\mathcal{R}_\mathrm{d}$ is calculated among all telescopes of a certain kind.

The simulations do not take into account "busy triggers", where a telescope could be still transferring data from a previous event, and hence would not be able to deliver data for a new event (no dead time of the instrument is simulated), and the time window for telescope coincidence is not limited. As a result, the values derived for the event sizes and data rates are somehow conservative, from the point of view of the planning of the data acquisition system, and can be interpreted as upper limits of the real values.

For the estimation of the data rates, 3 different read-out scenarios were considered, depending on the values for S_ev and η:

Scenario 1: read-out without waveform sampling. Only the integrated signal over the allowed time window is saved for all pixels. For this simple scenario, $\eta = 0$.

Scenario 2: read-out with waveform sampling for selected pixels. A selection of pixels important for the image reconstruction is read with full waveform information, while the rest of the camera is read as in scenario 1. This scenario relies on the feasibility of an online algorithm that could perform a rough and quick estimate of the image topology. As an estimate for the number of important pixels for the image, the mean number of pixels per image that survived the image cleaning $N_{\mathrm{P_{cl}}}$ was taken[15] and multiplied by three in order to take into account that the cleaning process has removed pixels from the image. Assuming this, the value for the fraction of pixels with timing information is $\eta = 3N_{\mathrm{P_{cl}}}/N_\mathrm{P}$ for this intermediate scenario. This results in values of a few percent: $\eta < 0.05$.

Scenario 3: read-out with waveform sampling for all pixels. All pixels of the camera are read out with full waveform information, i.e. $\eta = 1$, for this extreme scenario.

The values of the event sizes and data rates for each kind of telescope and for the whole array are displayed in table 2.8. For clarification purposes, the uncertainties in this and the following tables are not shown. As for the trigger rates, the statistical uncertainty is $\lesssim 5\%$ and the systematic uncertainty is 20% for the γ-ray data rates and 10% for the proton data rates. In addition, since the proton rates are interpreted in the following

[15] These numbers are only approximate: the camera FoV reduction was not taken into account for the calculation and besides, this number could change if a different image cleaning is applied.

			Scenario 1		Scenario 2		Scenario 3	
tel type	$N_{T_{tr}}$	$N_{P_{cl}}$	$S_{im/ev}$ (kB)	$\mathcal{R}_d$ (MB/s)	$S_{im/ev}$ (kB)	$\mathcal{R}_d$ (MB/s)	$S_{im/ev}$ (kB)	$\mathcal{R}_d$ (MB/s)
γ-ray showers								
LST	1.6	11	4.4	0.021	5.5	0.026	67	0.32
MST	1.8	8.4	3.4	0.0033	4.3	0.0042	51	0.049
SST	0.74	8.1	2.7	0.00075	3.6	0.001	41	0.011
total			18	0.18	25	0.23	270	2.8
proton showers								
LST	0.78	14	4.4	11	5.7	14	67	170
MST	1.8	9.3	3.4	3.4	4.4	4.4	51	51
SST	0.64	11	2.7	0.74	3.8	1	41	11
total			14	160	23	210	210	2500

Table 2.8.: Expected event sizes and data rates for γ-rays and protons for the candidate array E. The first column indicates the telescope type. $N_{T_{tr}}$ is the mean number of triggered telescopes of this type in the simulations. $N_{P_{cl}}$ is the average number of pixels that survive the image cleaning for images of each type of telescope. The last six columns give the telescope image size (in kB) and date rate (in MB/s) that is expected in scenarios 1, 2 and 3. Note that the event sizes and data rates for LST, MST and SST telescopes refer to the mean values of *one* telescope of its type in the case of stereoscopy. The numbers listed in the *total* row account for the total event size and data rate for the *central* array trigger. The total data rates for γ-rays and protons for each scenario are highlighted in red. The statistical uncertainty in the numbers is $\lesssim 5\%$ and the systematic uncertainty is between 20% and 30% (the details are given in the main text). For the results for the rest of the candidate arrays, refer to table A.16 in appendix A.

as the total rates of the system, another source of systematical uncertainty applies: the contribution of cosmic ray showers initiated by helium or heavier nuclei. This effect is not taken into account in the simulations and can be as large as 20% to 30% for the trigger rates, and hence for the data rates and data volumes (Aharonian et al. [1999] and the figure 5.11 from Schlenker [2001]), increasing the overall systematical uncertainty to 22% - 32%.

Comparing the values of the table for γ-rays and protons it is clear that the majority of the data rate of the system comes from the protons, because of the huge differences of the trigger rates. In general, while protons have slightly larger images (the number of important pixels is bigger), γ-rays trigger more telescopes on average. These effects are consequences of the fact that showers and images of protons are more scattered than that of γ-rays, resulting in smaller event sizes for protons.

Comparing the scenarios, for the simple scenario of storing integrated charge or the intermediate one (scenarios 1 and 2, respectively), the data rates are of the same order of

magnitude of a few 100 MB/s, whereas the extreme case of scenario 3, where digitization of all pixels is done, generates data rates of one order of magnitude bigger (a few GB/s). In comparison, assuming a mean value of 2.5 triggered telescopes per event, H.E.S.S. has a typical event size of only 9.4 kB and a data rate of 2.75 MB/s.

In the case of a *local* array trigger, the values of the mean data rates of each telescope of a kind are already given in table 2.8. The amount of data to be read out and merged across the whole array can be estimated as

$$\mathcal{R}_\mathrm{d} = \sum_i N_\mathrm{T}^i \langle \mathcal{R}_\mathrm{tr} \rangle_i \, \langle S_\mathrm{im} \rangle_i \,, \quad i = \mathrm{LST,\ MST,\ SST,\ MST_{LFoV}} \tag{2.10}$$

where S_im represents the size of an image in a telescope. The values are in the same order of magnitude of the total values calculated for the case of the *central* array trigger in table 2.8.

In the case of *no* array trigger, the values of the total data rates are calculated using the equation 2.10. The values for the image sizes are overestimated, since they are taken from the values of the stereoscopic case, but in monoscopic mode, as for *no* array trigger, the highest rate comes from small showers that produce small images in the camera. The resulting data rates are a factor 2 higher, than for the case of a *central* array trigger.

2.4.4. Data volumes

Once the data rates have been estimated, the data volumes can be calculated. An assumption has to be made here about the duty cycle of the observatory. For this study a duty cycle of 15% is assumed. For comparison, 19% represents the available time for observations at night under moonless conditions. This is representative for the H.E.S.S. observation strategy. Of course it is also possible to perform observations under moon conditions at the expenses of a higher energy threshold, as done in MAGIC and VERITAS. In this case the values in this subsection need to be corrected to represent the corresponding duty cycle[16], which can be as high as 40%. The values of the data volumes of the whole array in the case of a *central* array trigger for different observation periods are displayed in table 2.9. After 15 years of CTA, the data volume could be as high as 10 PB for the simple scenario, or 160 PB for the extreme one.

Following the trend shown for the data rates, in the case of a *local* array trigger the data volumes are of the same order of magnitude and in the case of *no* array trigger the data volumes are a factor of 2 higher.

For single telescopes, in the case of stereoscopy (i.e. for a *central* or *local* array trigger), the values of the data volumes for a 12 h night observation[17] amount to 0.5 - 7 TB for each LST, 0.2 - 2 TB for each MSTs and 0.03 - 0.5 TB for each SST. The ranges account for the different read-out scenarios. These numbers represent the local (i.e. close to

[16] Notice also, that the MC sample analyzed in this study did not represent the observations under moon conditions, where i.e. the high voltages of the PMTs are higher because of the increased rate of NSB, due to the moon light.

[17] In this case, a 100% duty cycle is assumed.

	Scenario 1	**Scenario 2**	**Scenario 3**
1 day	2 TB	2.6 TB	30 TB
1 month	61 TB	79 TB	910 TB
1 year	0.71 PB	0.93 PB	11 PB
15 years	11 PB	14 PB	160 PB

Table 2.9.: Expected data volumes in the candidate array E assuming a duty cycle of 15% for the stereoscopic array trigger. Each column contains the values of the indicated read-out scenario. The statistical uncertainty in the numbers is $\lesssim 5\%$ and the systematic uncertainty is between 20% and 30% (the details are given in the main text in subsection 2.4.3). For the results for the rest of the candidate arrays, refer to table A.17 in appendix A.

the telescope) disk space needed in the case of a distributed array trigger. As already mentioned, figure 2.11 shows that the local disk space for this case can be reduced for telescopes of a certain kind that are far away from the array center, since the trigger rate decreases for longer distances to the array center.

In the case of *no* array trigger, the values of the data volumes (and accordingly local disk space) for a 12 h night observation[17] amount to 0.9 - 13 TB for each LST, 0.3 - 5 TB for each MST and 0.1 - 1.5 TB for each SST. The ranges account for the different read-out scenarios.

2.5. Summary and discussion

2.5.1. Comparison of candidate arrays

In this subsection, the results for the case of a *central* array trigger are summarized and compared for all the candidate arrays defined for the CTA production-1 MC simulations (Bernlöhr et al. [2013]).

Figure 2.12 shows the trigger rates for each simulated candidate array and for both γ-rays and protons for the case of a *central* array trigger. Comparing the values for both kinds of particles, the resulting signal to noise ratio is quite similar for all cases ($\mathcal{O}(10^{-3})$): note the different scale for the protons (blue points, left scale in kHz) and for the γ-rays (red points, right scale in Hz). Only the subarray HESS has a higher signal to noise ratio of $\sim 1/400$. The main reason for this is the reduced FoV of the subarray HESS: since the simulated signal emission is point-like, but the background is diffuse, a smaller FoV implies a smaller background rate, whereas the signal rate remains unchanged.

The figure shows that most of the southern site candidate arrays have a similar trigger rate between 9 and 13 kHz, only the candidate arrays A and B (tuned to have the best performance at low energies) have a higher rate on the order of 15 kHz. The northern site candidate arrays have a lower rate of the order of 6 kHz, and the H.E.S.S.-like subarray has a rate of about 400 Hz.

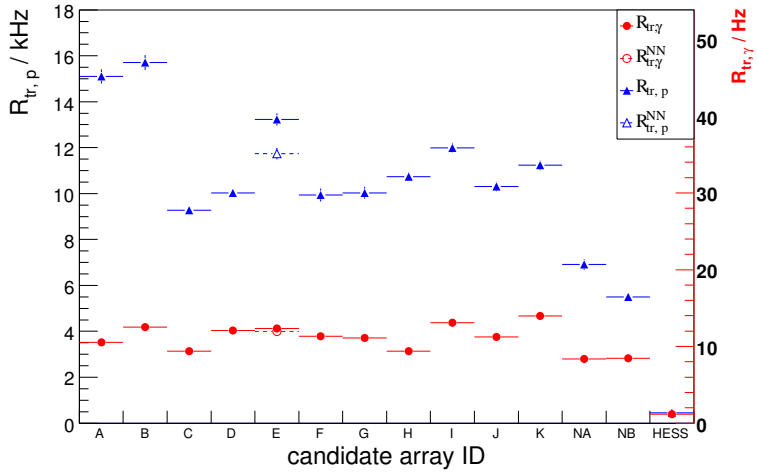

Figure 2.12.: Trigger rates for the simulated CTA production-1 southern site candidate arrays (A-K), northern site candidate arrays (NA, NB) and a subset of 4 MSTs organized as a H.E.S.S.-like telescope array (designated as subarray HESS). The blue triangles represent *BESS*-proton trigger rates, and the red circles represent 1-Crab-unit-γ-ray trigger rates. Note also the different scale for the protons (left scale in kHz) and for the γ-rays (right scale in Hz). For the case of the candidate array E, the dashed open markers indicate the values for a next-neighbors trigger system. The error bars represent 1σ statistical uncertainties.

For the case of the candidate array E, a next-neighbor array trigger was simulated, as mentioned at the beginning of section 2.4 and depicted in figure 2.8. The results for this trigger, marked as dashed lines in figure 2.12, show that a 10% reduction in the proton background is achieved, while keeping most of the γ-ray signal (only 3% is lost).

Figure 2.13 shows the data rate for each simulated candidate array as a vertical shaded band for the case of a *central* array trigger. The band covers the range of values between the simple read-out scenario 1 and the extreme scenario 3 described in subsection 2.4.3. The values range from $\mathcal{O}(100$ MB/s) for the simple scenario to $\mathcal{O}(1000$ MB/s) for the extreme scenario. The values for the intermediate scenario (scenario 2) are of the order of a few 100 MB/s, as denoted by the markers on the same plot. For the subarray HESS, the values are 2 orders of magnitude lower.

In this case, the next-neighbor array trigger from the candidate array E reduces the data rate by 5%, when compared to the normal stereoscopic trigger.

Table 2.10 shows the data volumes for each of the sites and for the whole observatory assuming a 15% duty cycle for the case of a *central* array trigger. Using the candidate array E as an example for the southern site array, the data rate ranges from $\sim$ 200 MB/s for the simplest read-out scenario, to $\sim$ 2500 MB/s for the extreme scenario. For the northern site array (the candidate array NA is used as example), the values are lower:

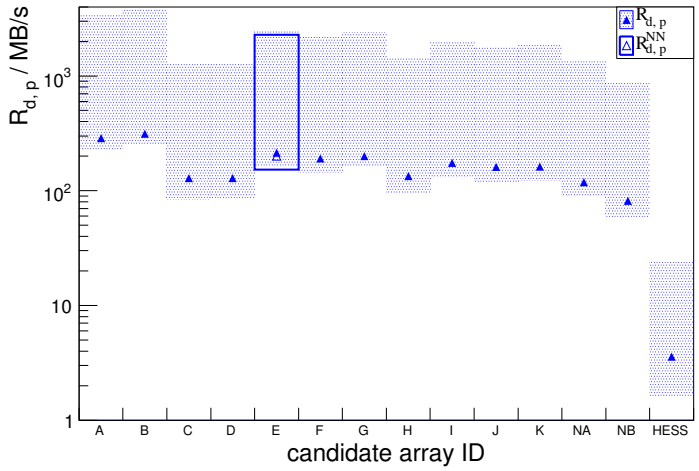

Figure 2.13.: Data rates for the simulated CTA production-1 southern site candidate arrays (A-K), northern site candidate arrays (NA, NB) and a subset of 4 MSTs organized as a H.E.S.S.-like telescope array (designated as subarray HESS). For each candidate array, the shaded area represents the range of data rates expected from the simplest read-out scenario (lower boundary) to the extreme case (upper boundary). The triangles indicate the values for the intermediate scenario (see text for details on each scenario). For the case of the candidate array E, an empty box and an open triangle indicate the range of values for a next-neighbors triggering system.

$\sim$ 100 MB/s for the simple scenario and $\sim$ 1400 MB/s for the extreme scenario. The event sizes range from $\sim$ 20 kB to $\sim$ 250 kB for the southern site candidate array and from $\sim$ 15 kB to $\sim$ 220 kB for the northern site candidate array. These values, and the corresponding data volumes are displayed in the table. The total data volume expected after 15 years of operation amounts to $\sim$ 20 PB for the simple scenario and $\sim$ 260 PB for the extreme scenario.

2.5.2. Implications for the data acquisition and archival system

The array data rates of a few hundred MB/s implied by the simplest read-out scenario shown in table 2.10 could be transferred to a central point using current Gigabit Ethernet lines, where a medium size computing farm could process them. of the Data rates of a few GB/s ($\sim$ 20 Gb/s), as for the extreme scenario, could be more challenging, but are still possible with current technologies, for example using several parallel 10 Gb/s Ethernet lines and several 10 Gb/s switches, link aggregation or InfinyBand. In a few years from now, also new technologies, like 40-100 Gb/s Ethernet lines should be well tested and could be an option for CTA. As a matter of fact, the ATLAS experiment (ATLAS Collaboration [2016]) at LHC (LHC Team [2016]) is currently performing event

	CTA North	CTA South	CTA
trigger rate $\mathcal{R}_{\mathrm{tr}}$	$\sim 7\,\mathrm{kHz}$	$\sim 13\,\mathrm{kHz}$	$\sim 20\,\mathrm{kHz}$
event size S_{ev}	15-220 kB	20-250 kB	15-250 kB
data rate $\mathcal{R}_{\mathrm{d}}$	100-1400 MB/s	200-2500 MB/s	300-4000 MB/s
data volume V_{d} per month	40-520 TB	74-930 TB	120-1500 TB
data volume V_{d} per year	0.5-6.1 PB	0.9-11 PB	1.5-20 PB
total data volume V_{d} (15 years)	6.5-92 PB	13-165 PB	20-260 PB

Table 2.10.: Estimated trigger rates, event sizes, data rates and data volumes for the southern and northern sites and for the complete CTA Observatory. The candidate arrays NA and E from the CTA production-1 simulations are selected as examples for the northern and southern arrays respectively. The entries are given in the form of ranges, covering the values from the expectations using the simplest case (store only integrated signal) to the extreme one (1 GHz sampling rate for all pixels in the camera). A duty cycle of 15% is assumed. For comparison, 19% represents the available time for observations at night under moonless conditions. The statistical uncertainty in the numbers is $\lesssim 5\%$ and the systematic uncertainty is between 20% and 30% (the details are given in the main text in subsection 2.4.3).

building at a rate of ~ 2 kHz for events of ~ 1.5 MB, which implies a data rate of ~ 3 GB/s (ATLAS Collaboration [2010]), and some of the technologies mentioned are being considered for its Phase 2 high luminosity upgrade around 2020.

Another possibility under discussion is a decentralized read-out system, where the data is stored locally, either at the telescopes or in a distributed system, where several farms are in charge of a few close-by telescopes, as could be the case for a *local* or *no* array trigger. In these cases, event merging would be performed offline. As for the trigger, the possibilities of having a distributed (*local*) array trigger system or not having an array trigger system at all are also under consideration. These ideas have been briefly discussed in terms of the dead time of the instrument at the end of subsection 2.4.2. In addition, the ideas of triggering at least some of the telescopes on NSB[18] and reading out non-triggered telescopes are being considered. These last two options would increase the trigger and data rates beyond the values calculated in this work.

In the case of a *local* array trigger, the data rates per telescope depend not only on the read-out scenario but also on the telescope type and its distance to the center of the array, since the trigger rates decrease with the distance, as shown in figure 2.11. The telescope data rates can be as high as 170 MB/s for each LST in scenario 3, as shown in table 2.8. The total array data rate remains roughly the same as that for the *central* array trigger.

In the case of *no* array trigger, the data rates for each telescope depend only on the

[18]This implies lowering the PMT thresholds of the telescopes in order to increase the γ-ray trigger efficiency, at the cost of an increased NSB trigger rate, on the order of the cosmic ray trigger rate, or even higher.

telescope type and are roughly a factor 2 higher than for the *local* trigger. The same applies for the total array data rates.

The cases of a *local* or *no* array trigger can represent a challenge for the online analysis, since the data would be distributed across the whole array. Still, online event building could be performed. In this case, local machines would perform a rough parametrization of the images of the cameras, and transfer the information to a central point, in order to merge and reconstruct the events for the online analysis.

A down-scaling of the data rates could be possible by using algorithms or electronics that perform some sorting of the data, i.e. the identification of the peak signal in the PMT, the identification of the important read-out regions in the camera, or the filtering of the most obvious background events. As an example, some preliminary studies show that some camera electronics concepts can identify and read out only the important region around the core of the image (Vorobiov et al. [2011]). These studies show that in general only up to 20%[19] of the camera needs to be read out (depending on the energy of the events) in order to get the full image, and a much smaller fraction in the case of NSB events. This fraction is larger than the one assumed in this work for scenario 2, where only a few percent of the camera is read out with waveform sampling, and the rest with integrated charge.

On top of the data transfer system, some considerations should be made about the characteristics of the cluster that should read out and process the information, completing the data acquisition system. Especially on the speed and capacity of the disks and the amount and speed of CPUs needed to process the data, but this is beyond the scope of this study. For more details on the data acquisition system of CTA, refer to Wegner et al. [2012] and CTA Consortium [2013].

As for the data volume, it is possible to store the amount of data of a few PB/month shown in table 2.10, but some filtering to suppress the most obvious background events could be applied, in order to reduce the disk space needed by a factor of 10. As comparison, the ATLAS experiment at LHC has a trigger rate $\sim$ 200 Hz after event building, a data rate of $\sim$ 350 MB/s (ATLAS Collaboration [2010]), which corresponds to a data volume of $\sim$ 300 TB/month, assuming a duty cycle of 1/3.

To conclude, the numbers presented in this work depend very much on the technology (i.e. camera electronics) and trigger logics that will be chosen for the final CTA configuration, so they are not final and should be used with care.

[19] The fraction of the area of the camera that needs to be read out is 10% for the low energy events, which are the most numerous, and 20% for the high energy events.

3. Supernova remnants as acceleration sites of cosmic rays

At the end of their life cycle, some stars explode in what is known as a *supernova* (SN) explosion, one of the brightest and most violent events in the universe, competing in luminosity with entire galaxies for a short period of time (from several weeks to several months). As a result of the explosion, most of the material (depending on the SN type, all the material) forming the star is ejected, and a fast shock wave is formed. The shock wave expands into the space, sweeping up and shocking material from the ambient medium: either the interstellar medium (ISM) or the surrounding circumstellar medium (CSM, gas blown by the progenitor star). The expanding material ejected from the progenitor star during the explosion, together with the material swept up and shocked in its expansion is know as the *supernova remnant* (SNR). The SNR is bounded by the expanding shock wave. In addition, depending on the SN type, a compact object can also remain after the explosion.

The Earth atmosphere is continuously bombarded by a constant and largely isotropic flux of charged particles from outer space known as cosmic rays (CRs). Although they were first discovered by Viktor Hess in 1912 (Hess [1912]) more than 100 yr ago, the origin of CRs still remains a mystery. Traditionally, SNRs are considered as the sources of Galactic CRs. This general belief, although supported by evidence and theoretical calculations, has not yet been proven. Nevertheless, particle acceleration up to PeV energies[1] is believed to occur in SNR shocks, making them valuable laboratories for investigating numerous physical processes.

This chapter describes the current knowledge on SNRs and their γ-ray emission mechanisms and introduces the concepts necessary to discuss the results presented in the subsequent chapters 4 and 5. First, an introduction to stellar evolution is presented in section 3.1, focusing on the advanced stages of stars that can lead to an SN explosion and the formation of an SNR. Then, a brief introduction about CRs and the motivation for the belief that SNRs are the source of Galactic CRs are presented in section 3.2, followed by the classifications of SNe and SNRs in section 3.3 and the description of SNR evolution and morphology in section 3.4. The particle acceleration mechanisms and γ-ray emission models relevant for SNRs, and a brief description of γ-ray absorption mechanisms are presented in sections 3.5, 3.6 and 3.7 respectively. The chapter ends with some concluding remarks in section 3.8.

[1] A CR with an energy of 1 PeV can produce a collision with a proton in the ISM with an energy of ~ 1.4 TeV in the center of mass frame. As a comparison, the best particle accelerator ever built, the Large Hadron Collider (LHC, LHC Team [2016]) is designed to produce collisions at energies up to 14 TeV in the center of mass frame.

3.1. Stellar evolution

Stars are formed by the collapse of gas clouds (known as molecular clouds) in the interstellar medium. They are often formed in so called binary systems, in which two gravitationally bound stars rotate around each other. About half of the stars in the Milky Way are part of a multiple (typically binary) star system.

The whole life of a star can be summarized as a competition against the gravitational force that tries to condense all the stellar gas (mostly hydrogen (60% to 90%) and helium (10% to 40%)[2]) into a singularity. To prevent this collapse, the star needs to provide pressure to compensate the pressure exerted by the gravitational force.

The evolution of a star strongly depends on its mass. It is therefore useful to introduce an appropriate mass unit: the solar mass unit $M_\odot$ as the mass of the Sun ($M_\odot \sim 2 \times 10^{30}\,\mathrm{kg}$). The type of processes a star undergoes, its internal structure and its evolution timescale can be expressed in terms of its mass. For instance, massive stars evolve much faster than low mass stars. In this respect, since the evolution of low mass stars (below $0.8\,\mathrm{M}_\odot$) such as *brown dwarfs* or *red dwarfs* is not relevant for this work, they will not be discussed in the following.

Prior to its birth, the collapse of the material in the so called protostar produces an increase in the pressure and temperature of the gas that induces several transitions in the gas, such as the dissociation of the molecular hydrogen into atomic hydrogen and the ionization of the atomic hydrogen. The protostellar phase duration varies depending on the mass, but for a Sun-like star it is $\sim 10^7\,\mathrm{yr}$.

During its regular life cycle, the star compensates the gravitational pull by providing energy from the nuclear fusion of hydrogen to form helium in its hot ($\sim 10^7\,\mathrm{K}$) and dense core. Not all the energy is used to provide pressure. Since a star radiates and emits neutrinos, it looses energy, and needs to continuously provide new energy to prevent the collapse.

After a long time ($\sim 10^9\,\mathrm{yr}$ for a Sun-like star) the hydrogen of the core is exhausted and the core starts to collapse. The temperature rises allowing the burning of hydrogen in a shell around the helium core. While this process occurs close to the core, the outer layers of the star slowly expand to form a red giant star. For a Sun-like star this process takes $\sim 1.5 \times 10^9\,\mathrm{yr}$.

Eventually, the temperature in the core reaches $10^8\,\mathrm{K}$ and helium to carbon and oxygen fusion starts, either in a gradual way for high mass stars, or in a violent event known as helium flash for low mass stars; the boundary being at $\sim 2\,\mathrm{M}_\odot$. At this point, the star has a core of burning helium and a surrounding layer of burning hydrogen, surrounded in an envelope of non-burning material. In a Sun-like star helium burning takes $\sim 3.5 \times 10^9\,\mathrm{yr}$.

Depending on the mass of the star, several cycles of nuclear reactions burning heavier elements in each cycle (H, He, C, O, Si) can take place: stars with larger masses experience larger gravitational pulls, that increase the temperature in the core to higher

[2]The mass fractions of elements in stars depend on the type of star and vary during its evolution. More details are given in Padmanabhan [2001].

values, enabling the fusion of heavier elements. Each cycle occurs faster than the previous one, forming successive layers of different burning materials (the so called onion-like structure), until a core of iron is formed by the fusion of silicon. Since iron fusion is not an exothermic process, further nuclear reactions are not possible to maintain the gravitational pressure and prevent further collapsing of the star. The result is similar even if the mass of the star in not large enough to produce all nuclear reaction cycles: a non burning core of a certain element (the remainder of the last supported nuclear reaction) forms that cannot prevent gravitational collapsing via nuclear reactions.

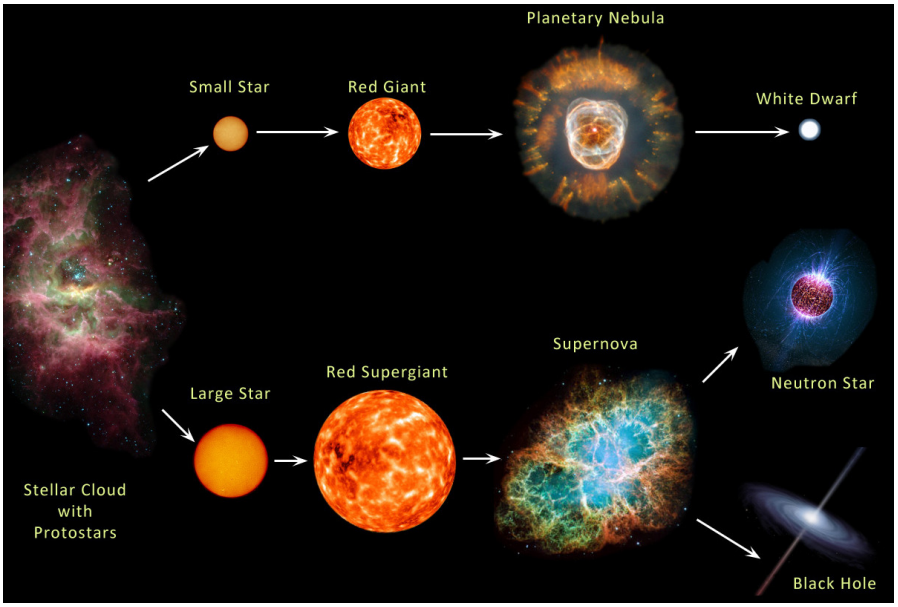

Figure 3.1.: Stellar evolution (not to scale). Figure taken from Earth Blog [2013].

Advanced evolutionary stages of stars (see figure 3.1) prevent further collapse by pressure coming from degenerate matter, typically electrons, as is the case for *white dwarf stars*, or neutrons, as is the case for *neutron stars*. If the mass is large enough so that gravity overcomes fermionic degeneracy pressure, a singularity known as *black hole* is formed. These three states (white dwarf, neutron star and black hole) are very stable and, undisturbed, they can effectively exist for an indefinite amount of time. A brief description of each of these states is given in the following:

White dwarf : white dwarfs are the relics of evolved Sun-like stars ($0.8\,M_\odot$ to $4\,M_\odot$). They are carbon and oxygen stars that do no longer have fusion reactions and prevent gravitational collapsing via electron degeneracy pressure. White dwarfs form in a slow process after the helium ignition: first the outer layers of the star are gently (non explosively) ejected as a planetary nebula exposing the helium burning core, then the core forms a white dwarf when the helium is consumed. White dwarfs are stars with sizes of a planet ($\sim 10^4\,$km) but masses similar to the Sun. The maximum mass possible for a white dwarf is the Chandrasekhar mass

($\sim 1.44\,M_\odot$): above this mass, electron degeneracy pressure cannot compensate the gravitational pull.

Neutron star : neutron stars are the relic of evolved massive stars ($4\,M_\odot$ to $8\,M_\odot$) that prevent gravitational collapsing via neutron degeneracy pressure. The outer layers of the star are ejected as an SNR in a violent SN explosion, while electron capture by the protons of the nuclei of the core occurs, forming neutrons and releasing neutrinos, via inverse β decay. Neutron stars are stars with a diameter the size of a city ($\sim 10\,km$) but a matter density similar to the nuclear density. The maximum mass possible for a neutron star is the Tolman-Oppenheimer-Volkoff mass ($\sim 3\,M_\odot$): above this mass, neutron degeneracy pressure cannot compensate the gravitational pull.

The neutron star can form a *pulsar* (PSR) and a *pulsar wind nebula* (PWN). A pulsar is a fast rotating neutron star whose rotation axis and magnetic field axis are misaligned. The rotating magnetic field creates an electric field that accelerates particles (protons and electrons) close to the neutron star surface. These particles radiate producing highly beamed electromagnetic radiation in a cone around the magnetic field axis. If the line of sight falls within the cone, pulsating radiation with a very precise period can be detected. Moreover, a pulsar can power a pulsar wind, a wind of relativistic particles (likely electrons and positrons), carrying away rotational kinetic energy from the pulsar (pulsar spin-down energy). The pulsar wind, interacting with the surrounding supernova material and later with the interstellar medium produces radiation, forming a pulsar wind nebula.

Black hole : for objects denser than neutron stars no physical force can compensate the gravitational pull, and hence matter collapses into a singularity. The boundary of a black hole is defined by its event horizon: inside it the gravitational force is so strong that the escape velocity is greater than the speed of light, so any matter or radiation that crosses the event horizon will fall into the singularity. Since black holes cannot be observed directly, a good way to gather evidence of such objects is in binary systems via the kinematical effects suffered by the companion star due to the presence of the black hole.

Following the neutron star formation process mentioned before, some supernova models predict that, in very massive stars (above $8\,M_\odot$), the proto-neutron star in the core further accretes matter producing a black hole before the outer layers are expelled in the supernova explosion.

In binary systems it is common that matter transfer occurs from one star to its companion. Indeed if the radius of a star is large enough for the star to overflow the Roche lobe[3] of its companion (for instance during a giant phase of the parent star), the matter is no longer bounded to the parent star but flows to its companion forming an accretion disk. This process is of importance for some types of supernova explosions.

[3]The Roche lobe is the region around a star in a binary system within which orbiting material is gravitationally bound to that star.

Further details about stellar evolution can be found in Longair [2011] chapter 2.

3.2. Cosmic rays

As already mentioned, CRs are charged particles from outer space that arrive at the Earth with a constant and largely isotropic flux.

As observed on top of the atmosphere, most of the CRs (98%) consist of nuclei, and among them protons are the most numerous group (almost 90%). The remaining 2% are electrons.

The spectrum of cosmic rays is well described by a power-law over about 12 decades in energy, with small deviations. The most remarkable feature is the so known *knee*: a spectral break at $E \sim 3\,\mathrm{PeV}$, which is believed to mark the maximum energy of CRs of Galactic origin (i.e. formed within the Milky Way). The spectral index at energies lower than the knee is ~ 2.7 and ~ 3.1 at higher energies (see Blümer et al. [2009] for an overview). Other features, such as the so called *second knee* or the *ankle* are not relevant for this work and therefore not discussed in the following. The CR spectrum is shown in figure 3.2.

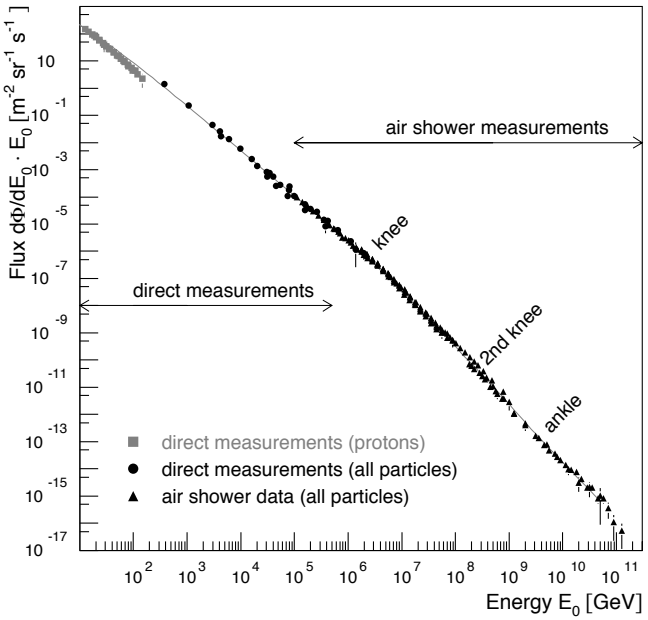

Figure 3.2.: Cosmic ray spectrum. The spectral breaks known as *knee* (at $E \sim 3\,\mathrm{PeV}$), *second knee* (at $E \sim 400\,\mathrm{PeV}$) and *ankle* (at $E \sim 4\,\mathrm{EeV}$) are indicated. Figure taken from Blümer et al. [2009].

Since CRs are charged particles, they get deflected and isotropized by ambient magnetic fields before reaching the Earth, so a direct identification of their origin is not

possible, except perhaps at the highest energies (Pierre Auger Collaboration [2007]).

Further details about CRs can be found in Longair [2011] chapter 15.

3.2.1. SNRs and the energy budget of Galactic CRs

Traditionally, SNRs are considered as the sources of Galactic CRs. This supposition is based on simple energy considerations by Ginzburg and Syrovatskii [1964] (also summarized in Weekes [2003]).

It is well established that the energy density of CRs is $\epsilon_{\mathrm{CR}} \sim 10^{-12}\,\mathrm{erg\,cm^{-3}}$. This energy density is distributed in the whole Galaxy (including the halo), a volume of $V_{\mathrm{MW}} \sim 10^{68}\,\mathrm{cm}^3$. Using an escape time of $\tau_{\mathrm{esc}} \sim 10^7\,\mathrm{yr}$ for CRs leaving the Galaxy, the CR power is calculated as

$$L_{\mathrm{CR}} = \frac{\epsilon_{\mathrm{CR}} V_{\mathrm{MW}}}{\tau_{\mathrm{esc}}} \sim 3 \times 10^{41}\,\mathrm{erg\,s^{-1}}. \tag{3.1}$$

The canonical SN explosion energy is $E_{\mathrm{SN}} = 10^{51}\,\mathrm{erg}$ and the conversion factor of explosion energy into acceleration of charged particles within the SNR is typically $\theta \sim 10\%$. Since a Galactic SN occurs every $\Delta t_{\mathrm{SN}} \sim 30\,\mathrm{yr}$ on average, the total power into CRs is

$$L_{\mathrm{SNR}} = \frac{\theta E_{\mathrm{SN}}}{\Delta t_{\mathrm{SN}}} \sim 10^{41}\,\mathrm{erg\,s^{-1}}. \tag{3.2}$$

Both numbers (L_{CR} and L_{SNR}) agree in the order of magnitude, showing that SNRs are plausible candidates for the origin of the Galactic CRs. In contrast, other type of objects tested in the above mentioned references are either not energetic enough or not recurrent enough to provide the estimated Galactic CR power.

3.3. SN and SNR classifications

The physical properties of SNRs depend on the nature of the SN explosion and the evolution in the ambient medium.

SNe are classified according to optical spectroscopy: the presence or absence of a certain element in the spectrum defines a certain type. For instance type I SNe are characterized by the absence of H lines in the optical spectrum, while type II do have H lines in the spectrum. A diagram of the SN classification is shown in figure 3.3.

SNe can also be grouped into two main categories, depending on the underlying explosion mechanism:

Core-collapse SNe : at the end of their life cycle, massive stars (with a mass of $8\,\mathrm{M}_\odot$ or more) have successive layers of material undergoing fusion, with heavier elements towards the center. The innermost element is iron, resulting from the fusion of silicon. Iron nuclei cannot fuse, since the process is endothermic, therefore the stability of the iron core has to be maintained by electron degeneracy pressure. Since more iron is produced from the silicon fusion, the mass of the iron core

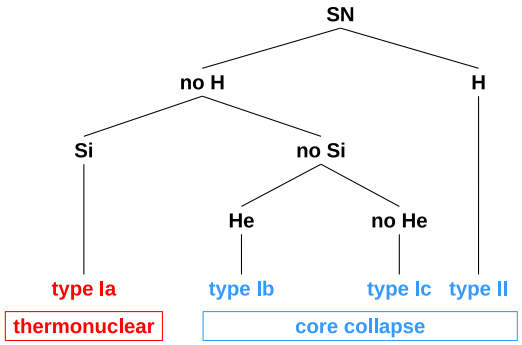

Figure 3.3.: Supernova classification, according to optical spectroscopy and the explosion mechanism.

increases until it reaches the Chandrasekhar limit. At this point, the electron degeneracy pressure is not sufficient to balance the gravitational force any longer, and the core collapses until the conditions for inverse β decay are reached. At this point, electron capture by the protons of the iron nuclei occurs ($e^- + p \rightarrow \nu_e + n$), forming neutrons and releasing neutrinos. When the density of the core reaches nuclear values, neutron degeneracy pressure prevails and stops the collapse of the core, forming a stable structure know as neutron star. This process occurs in a fraction of a second. Meanwhile, the outer layers of the star, that have started collapsing, reach the surface of the newly created neutron star and a shock is produced that ejects the outer layers in a violent event. The total (gravitational) energy released in the process is $\sim 10^{53}$ erg, from which $\sim 1\%$ ($\sim 10^{51}$ erg) is transferred into the kinetic energy of the ejected material, and the rest is released as kinetic energy of the escaping neutrinos formed in the electron capture processes. The expanding material forms a shock and the neutron star remains as compact relic of the progenitor star. This is the case of SNe of types, Ib, Ic and II (all except type Ia).

Some deviations from this process are possible. For instance, in very massive stars (above $8\,M_\odot$), it is believed that the SN explosion does not occur directly when the proto-neutron star is formed, but shortly after: the core continues to accrete matter until a black hole is formed and then the SN explosion occurs. In less massive stars (about $4\,M_\odot$), the fusion of silicon to produce iron might not take place because the necessary densities and temperatures are not reached, in which case, the SN explosion occurs at an earlier fusion stage, for instance at the stage of ignition of the oxygen core.

Thermonuclear SNe : in a binary system of a white dwarf star and an expanding star (i.e. a red giant), it is common that matter transfer from the expanding star to its white dwarf companion occurs, when the former overflows the Roche lobe of the latter. In which case, the white dwarf accretes mass and contracts until the

Chandrasekhar limit is reached. Beyond this limit, the white dwarf destabilizes and should collapse forming a neutron star. It is believed, that before this process takes place, carbon and oxygen fusion reactions start, producing enough thermonuclear energy to disrupt the star. In this process, all the stellar material is ejected and no compact relic is left behind. This is the case for SNe of type Ia. Since the SN explosion occurs at a well-defined mass (the Chandrasekhar limit), the energy of the explosion is always the same $E_{\mathrm{SN}} \sim 10^{51}\,\mathrm{erg}$, making type Ia SNe a standard candle to measure distances of galaxies.

From the description it is clear that, independent of the type of explosion, the energy released in the ejected material is constant, therefore, it is commonly assumed that the typical energy of an SN is $E_{\mathrm{SN}} = 10^{51}\,\mathrm{erg}$.

SNRs can be classified according to their morphology:

Shell-type SNRs : material is ejected in all directions, forming an expanding ring-like structure.

Plerions : the SNR is filled by the outflow of a pulsar. Plerions are also known as pulsar wind nebulae.

Composite : both structures are visible: the expanding shell and the filling plerion.

In the following, unless otherwise specified, only shell-type SNRs are discussed.

Further details about SN and SNR classification can be found in Longair [2011] chapter 13.

3.4. SNR evolution

The properties of shell-type SNRs are very similar to those of a very hot gas sphere expanding supersonically. In the following, the assumption of an expansion into a homogeneous medium is made. From the SN explosion of the progenitor star to the merging of the SNR with the surrounding medium, four different stages can be identified in the evolution of an SNR. The four evolutionary stages of an SNR are presented in the following and in figure 3.4:

Free expansion : the energy of the SN explosion results in the heating and ejection of the material of the envelope of the star. This creates a highly supersonic expanding sphere of hot gas (the ejected material). Because of the supersonic nature of the expansion, a shock front is formed ahead of the sphere. The expansion of the sphere (also known as the contact discontinuity) causes the accumulation, compression and heating of material from the surroundings (either the ISM or the CSM) between the contact discontinuity and the shock front, also known as the swept-up material. This hot material is able to radiate photons up to X-ray energies, becoming the visible shell, characteristic of shell-type SNRs. The dynamics in this phase are characterized by a constant velocity of the sphere.

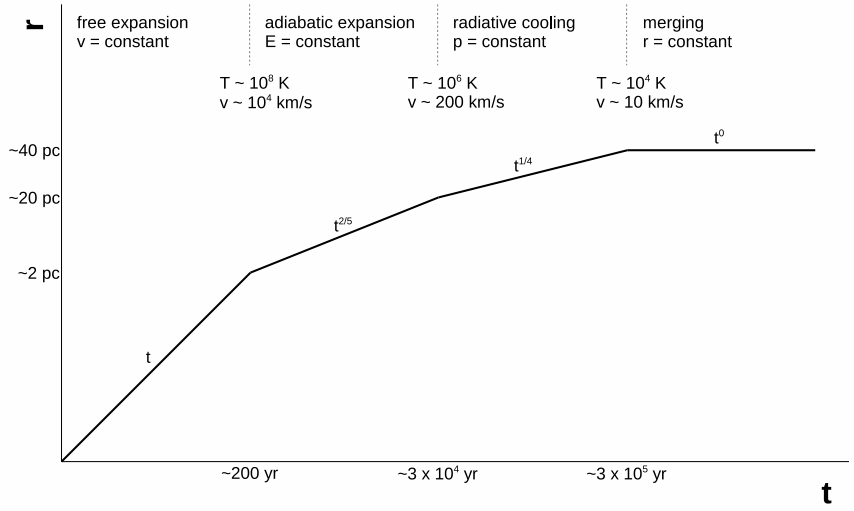

Figure 3.4.: Supernova remnant evolution. Figure inspired by a similar figure in Padmanabhan [2001].

Adiabatic expansion : after a couple 100 yr, when the mass of the swept-up material reaches the same order of magnitude as the mass of the ejected material, the expansion of the sphere starts to decelerate. The ejected material in the interior is thus decelerated, starting with the outer layers (i.e. close to the contact discontinuity). This causes a supersonic movement of the inner ejected material into the outer ejected material provoking a second shock moving inwards (the reverse shock) and hence the reheating of the ejected material. This hot material is able to radiate photons up to X-ray energies, becoming part of the visible shell. The dynamics in this phase are characterized by the adiabatic blast-wave similarity solution of Sedov [1993].

Radiative cooling : after a few 1000 yr, when the temperature of the material behind the shock front drops below 10^6 K, radiative cooling in the form of line emission of heavy elements becomes important. The deceleration of the sphere increases and the shell becomes more compact so the pressure balance is kept.

Merging : after some 10^5 yr, the expansion of the sphere eventually becomes subsonic and the SNR disperses in the medium, loosing its identity.

The most important phases for particle acceleration are the free and adiabatic expansion stages. The visible shell is formed during these two phases. In the adiabatic expansion stage, the morphology of the SNR is similar to the one depicted in figure 3.5. The figure actually shows the morphology of a composite SNR. In the case of shell-type SNRs, the central (dark) pulsar wind and PWN, and eventually even the pulsar, are not present. A typical density profile of this stage, with the different fronts and

discontinuities, is shown in figure 3.6.

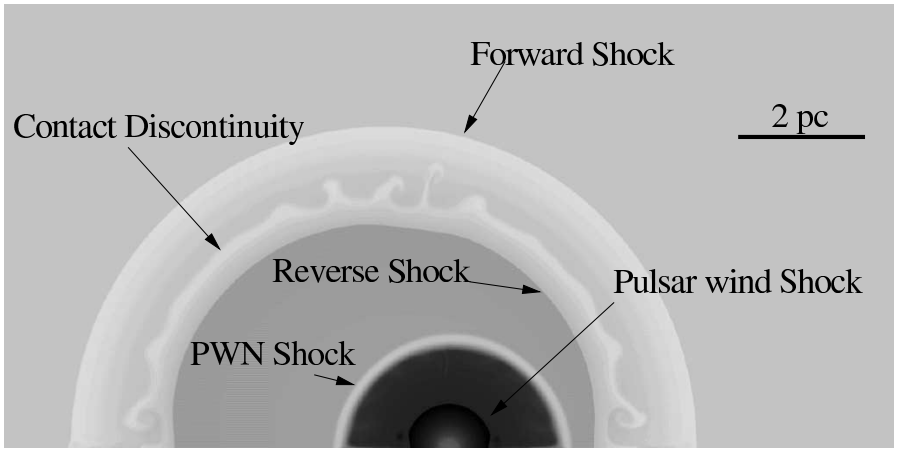

Figure 3.5.: Morphology of a composite SNR. Logarithmic gray-scale plot of the density distribution for an age of 1000 yr. Figure taken from van der Swaluw et al. [2004].

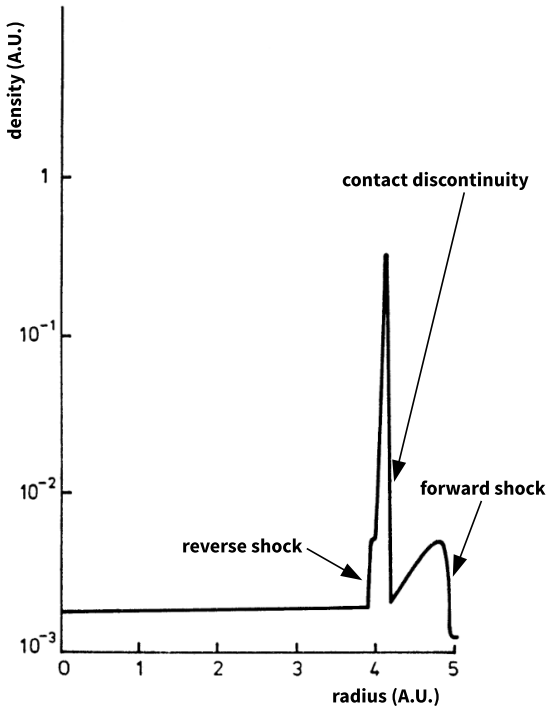

Figure 3.6.: SNR density profile for an SNR of age $\sim$ 100 yr entering the adiabatic expansion phase. The region between the forward and reverse shocks forms the visible SNR shell. Figure modified from a similar figure by Gull [1975].

Further details about SNR evolution can be found in Longair [2011] section 16.7 and in Reynolds [2008] section 3.

3.5. Particle acceleration in SNRs

The mechanisms of acceleration of particles are very complex and not yet fully understood. Nevertheless, non-linear diffusive shock acceleration (DSA) models applied to SNRs predict particle populations in the form of power-laws with a maximum particle acceleration energy similar to the energy of the knee of the measured spectrum of CRs (shown in figure 3.2).

The accelerated particles in SNRs are mostly protons and electrons from ionized H nuclei. The Fermi acceleration mechanism (magnetic mirroring of particles) predicts particle spectra in the form of power-laws. The first order Fermi acceleration mechanism, in the framework of magneto-hydrodynamical models applied to the case of particle acceleration in strong shock waves (known as DSA), predicts a spectral index of 2, and a certain maximum energy for the spectrum (10^5 GeV/nucleon), which is actually below the knee of the CR spectrum. The addition of non linear effects and propagation in the Galaxy allows for a spectral softening and a maximum energy of accelerated particles matching the spectrum of CRs up to the knee.

CRs with energies above the ankle are believed to have extragalactic origin, with the region between the knee and the ankle as transition region from Galactic to extragalactic origin. Indeed, if other (extragalactic) sources are considered, the spectrum above the knee can also be reconciled with the observations.

A more detailed overview of the acceleration mechanisms is given in Longair [2011] chapter 17. Some of the still unresolved problems of the theory involve the particle injection mechanism to start the acceleration and the particle escape process once they are accelerated as pointed out by Reynolds [2008].

3.6. γ-ray emission models

Since the particles accelerated at the shock fronts of SNRs are charged, they are deflected by the magnetic fields in space. An indirect method to measure them is necessary in order to track their sources. One successful method is to search for photons resulting from the interactions of the charged particles with the medium.

Accelerated particles can radiate energy in the form of photons via several mechanisms. The main radiation processes relevant for high energy γ-rays are Bremsstrahlung, synchrotron emission and inverse Compton scattering for electrons, and π^0 decay after proton-proton collisions. The former three are commonly referred to as *leptonic* processes, and the latter as *hadronic* process.

Each of these processes is briefly[4] introduced in the following. Table 3.1 summarizes

[4]Further details about γ-ray emission models can be found in Longair [2011] part II, in Reynolds [2008] section 5 and in Weekes [2003] appendix A.

the main phenomenological properties of each interaction. Figures 3.7a and 3.7b show the approximate shapes of the spectra of photons emitted by these processes[5]. From the figure it is clear that the shape of the hadronic and leptonic curves at TeV energies are very similar, making the identification of such processes based only on VHE γ-ray data very hard.

interaction	crit. parameters	char. E_γ	diff. spectrum
Bremsstrahlung	N_e, n	E_e	E_γ^{-p}
synchrotron	N_e, B	$3\gamma^2 eB\hbar \sin\alpha/(2m_e)$	$E_\gamma^{-(p+1)/2}$
IC	N_e, $n_{\rm ph}$	$\gamma_e^2 h\nu$ (Thomson) $\gamma_e h\nu$ (Klein-Nishina)	$E_\gamma^{-(p+1)/2}$
π^0 decay	N_p, n	$m_{\pi^0}c^2/2$	$E_\gamma^{-4/3(p-1/2)}$

Table 3.1.: Phenomenological properties of the γ-ray emission processes. For each interaction the following is shown: the critical parameters, the characteristic γ-ray energy E_γ and the shape of the γ-ray differential spectrum in the power-law regime (see the equation 1.1 in section 1.1). In the differential spectrum column p represents the spectral index of the parent particle population. Details are given in the text.

3.6.1. Bremsstrahlung

Charged particles are deflected in the presence of the electric field of a nucleus. As a result of the deflection they emit electromagnetic radiation. In astrophysics this process is important in the case of relativistic electrons emitting γ-rays in the presence of atomic or molecular material. The critical parameters of the process are the number of electrons N_e and the medium density n. The characteristic energy of the photons is $E_\gamma \simeq E_e$: the γ-rays have energies similar to the incident electrons. The shape of the Bremsstrahlung γ-ray spectrum matches that of the parent particle population. If p and Γ represent the spectral index of particles (electrons in this case) and γ-rays respectively, then $\Gamma \simeq p$.

Further details about Bremsstrahlung emission in an astrophysical context can be found in Weekes [2003] section A.4 and in Longair [2011] chapter 6 and section 16.2.2.

3.6.2. Synchrotron emission

Charged particles are deflected in the presence of magnetic fields. As a result of the deflection they emit polarized electromagnetic radiation. In astrophysics this process is observed in the case of ultrarelativistic electrons emitting photons in a large range of energies (from radio to X-rays) in the presence of the magnetic fields of cosmic sources. The critical parameters of the process are the number of electrons N_e and the ambient magnetic field B. The characteristic energy of the photons is given by the critical frequency $\omega_{\rm c}$ (frequency at which the maximum power of a single electron is emitted)

[5]The Bremsstrahlung spectrum is not shown because it is not relevant for this work.

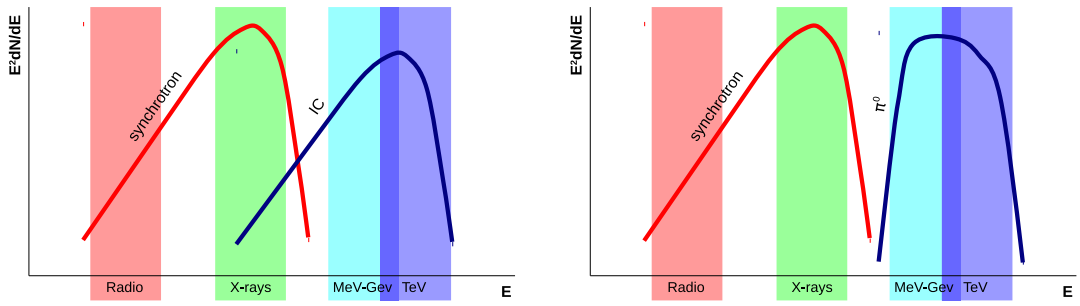

(a) Leptonic SED (b) Hadronic SED

Figure 3.7.: Approximate shapes of the spectral energy distributions (SED) of the main emission processes relevant for γ-ray astronomy. The shaded areas highlight the typical wavelengths of observations: radio, X-rays and γ-rays, the latter at two different energy bands: MeV − GeV from satellites and GeV − TeV from ground-based Cherenkov telescopes. The left figure shows the leptonic model. In the leptonic scenario, typically the same electron population is responsible for the synchrotron and the IC emissions (and the Bremsstrahlung). The Bremsstrahlung spectrum is not shown because it is not relevant for this work. The right figure shows the hadronic model. In the hadronic scenario, the lower energy peak is still due to leptonic processes.

as $E_\gamma = \hbar\omega_c = 3\gamma^2 eB\hbar \sin\alpha/(2m_e)$, where γ is the electron Lorentz factor, and α the angle between the electron velocity vector and the magnetic field lines. The γ-ray index depends on the electron index as $\Gamma = (p+1)/2$.

Further details about synchrotron emission in astrophysical context can be found in Weekes [2003] section A.7 and in Longair [2011] chapter 8 and sections 9.6 and 16.2.4.

3.6.3. Inverse Compton scattering

A high-energy charged particle can upscatter a low energy photon, transferring a large fraction of its energy to the photon. In astrophysics this process is observed in the case of relativistic electrons upscattering ambient photons. In the case of γ-ray astronomy this effect is especially important in the case of cosmic microwave background (CMB) photons upscattered to γ-ray energies. Other local fields specific to each source are also possible, for instance photon fields due to a nearby star. The critical parameters of the process are the number of electrons N_e and the density of the radiation field $n_{\rm ph}$. The characteristic energy of the photons is $\gamma_e^2 h\nu$ in the Thomson regime (incident photon energy much less than the rest mass of the electron), and $\gamma_e h\nu$ in the Klein-Nishina regime. The γ-ray index depends on the electron index as $\Gamma = (p+1)/2$.

Further details about inverse Compton emission in astrophysical context can be found in Weekes [2003] section A.2 and in Longair [2011] sections 9.3 and 16.2.5.

3.6.4. π^0 decay

The most frequent hadronic interaction in astroparticle physics is proton-proton collision. In the case of accelerated protons interacting with ambient hydrogen nuclei, the most frequent reaction is the production of pions (the lightest type of meson): π^+, $\pi^-$and π^0. At high energies, each kind of pion is produced with approximately the same probability. These particles are unstable: the charged pions decay into leptons and neutrinos, and the neutral pions rapidly decay into two γ-rays in 99% of the cases (the π^0 lifetime is 8.5×10^{-17} s). These γ-rays are hence tracers of the initial particle population. In the rest frame of the π^0, the energy of the resulting photons is given by the rest mass of the π^0 as $E_\gamma = m_{\pi^0}c^2/2$. The critical parameters of the process are the number of protons N_p and the medium density n. The γ-ray spectrum resulting from hadronic interactions is usually flatter than the spectrum resulting from leptonic interactions, with an index of $\Gamma = 4/3(p - 1/2)$ and has a rapid drop bellow $E_\gamma = 67.5\,\mathrm{MeV}$ (half of the rest mass of the π^0). In the typical representation of $E^2\mathrm{d}\Phi/\mathrm{d}E$ vs. E (E and $\mathrm{d}\Phi/\mathrm{d}E$ representing respectively the γ-ray energy and the γ-ray differential spectrum), a characteristic spectral break appears at $E_\gamma \simeq 200\,\mathrm{MeV}$.

Further details about π^0 decay emission in astrophysical context can be found in Weekes [2003] section A.5 and in Longair [2011] chapter 10.

3.7. γ-ray absorption

γ-rays can be absorbed on their path through space by pair production either in matter or photon fields. This effect can be important in some particular cases (i.e. dense matter or photon fields close to the corresponding source). Another typical case is the absorption of VHE γ-rays from distant galaxies (typically active galactic nuclei, AGNi) by diffuse extragalactic background light (accumulated radiation in the universe due to star formation and contributions of AGNi). Neither case is important for the results presented in this work, so no further details are given.

Further details about photon absorption processes in astrophysical context can be found in Weekes [2003] section A.6 and in Longair [2011] chapter 9.

3.8. Conclusions

It has been discussed that SNRs are plausible candidates for the acceleration sites of Galactic CRs. It has also been discussed that particle acceleration takes place in the strong shocks present in SNRs, and that theoretically the shape of the resulting spectra match the shape of the spectrum of CRs.

A definite answer to the question whether the particles accelerated in SNRs are indeed the Galactic CRs, and hence SNRs the long sought origin of CRs, is not possible at present. Nevertheless, since CRs consist mostly of protons, an important support for this hypothesis would be achieved if the measured photon spectra of SNRs could

be unambiguously identified as being of hadronic origin, and the properties of the derived parent particle population (spectrum shape, fraction of total energy in accelerated particles relative to the SN explosion, maximum energy of accelerated particles) would match the properties and requirements of the spectrum of CRs. Since hadronic processes produce photons only at γ-ray energies, γ-ray observations of SNRs are instrumental for solving the enigma of the origin of CRs.

4. H.E.S.S. observations of RX J0852.0−4622

This chapter presents detailed analysis results of the γ-ray observations of the SNR RX J0852.0−4622 with the H.E.S.S. experiment. First, an overview about the current understanding of SNR RX J0852.0−4622 is given in section 4.1. The H.E.S.S. experiment is introduced in section 4.2. The H.E.S.S. observations on RX J0852.0−4622 are presented in section 4.3. The analysis techniques used for deriving the results are reviewed in section 4.4. The H.E.S.S. data sets used for the morphology analysis of RX J0852.0−4622 are listed in appendix C. The results of the morphology analysis of RX J0852.0−4622 are presented in sections 4.5, 4.6, 4.7 and 4.8. These results include the spatial morphology (skymaps and skymap projections), the spectral morphology for the search of spectral variations across the SNR and flux upper limits estimations for the possible TeV PWN towards PSR J0855−4644. The chapter concludes with a discussion of the morphology results in section 4.9. Due to its extension, the spectrum of the entire RX J0852.0−4622 region is presented in the subsequent chapter 5.

4.1. Introduction

RX J0852.0−4622, listed as SNR G266.2−1.2 in Green's SNR catalog (see Green [2009]), is a supernova remnant (SNR) towards the direction of the constellation Vela. Its projection on the sky overlaps with the much larger Vela SNR, for this reason, it is commonly known as "Vela Junior".

RX J0852.0−4622 was first discovered in the late 90s during the all-sky survey performed by *ROSAT* at X-ray energies (see Aschenbach [1998]). Since then, it has been observed in a variety of wavelengths, ranging from radio (see Combi et al. [1999]) to VHE γ-rays (see Aharonian et al. [2007]). At VHE it has been resolved as a shell-type SNR, with an apparent diameter of 2°.

Further details like the type of the SN explosion in which RX J0852.0−4622 originated, its age and distance are subject to controversy, due to the complexity of the region, and many scenarios have been proposed (see Iyudin et al. [2007] and references therein for more details). This is mostly due to the presence of the Vela SNR, that makes it difficult to isolate the emission from RX J0852.0−4622 in some wavelengths.

4.1.1. Origin

Observations of RX J0852.0−4622 using X-ray data from *ASCA* (see Slane et al. [2001]) detected the presence of a central compact object (CCO) candidate, that could be a neu-

tron star, suggesting a core collapse SN as the origin for the SNR. Further observations in radio wavelengths (see Reynoso et al. [2006]) indicated that the CCO candidate could be a planetary nebula unrelated to RX J0852.0−4622, so the possibility of a thermonuclear SN cannot be ruled out.

4.1.2. Age and distance

Observations by *COMPTEL* in the direction of RX J0852.0−4622 (see Iyudin et al. [1998]) detected the presence of ^{44}Ti, a radioactive isotope typically created in SN explosions with a relatively short half-life (∼60 yr). This observation suggests that the SNR should be quite young (680 yr) and nearby (200 pc distance), i.e. closer than the Vela SNR (290 pc).

Subsequent measurements using X-ray data from *ASCA* implied a larger distance and age for the remnant. The detection of a Ca line in the X-ray spectrum of the northwestern part of the shell reported by Tsunemi et al. [2000] implies an age of up to 1000 yr. The measured column density[1] values in the direction of RX J0852.0−4622 using X-ray data reported by Slane et al. [2001] are higher than those for the Vela SNR, suggesting that RX J0852.0−4622 could be behind the Vela SNR, and thus as far as 1 kpc to 2 kpc.

Later X-ray observations with *Chandra* of the northwestern rim by Bamba et al. [2005] revealed thin filaments. By using a correlation of the roll-off frequency of the spectra of the filaments to the age of the remnant, the authors derived a distance range of 260 pc to 500 pc and an age range of 420 yr to 1400 yr.

More recent estimates by Katsuda et al. [2008] using the expansion of the northwestern rim of the remnant using X-ray data from *XMM-Newton* suggest an age range of 1700 yr to 4300 yr and a distance of 750 pc. Similar studies recently conducted with *Chandra* X-ray data from the years 2003 to 2008 place a lower limit on the distance to the remnant at 500 pc (Allen et al. [2015]) and an age range of 2400 yr to 5100 yr. Another recent estimate of the *XMM-Newton* X-ray column density by Acero et al. [2013b] yields an upper limit of the distance of 900 pc. The latter two results are in agreement with the distance measurement by Katsuda et al. [2008]. Therefore, the distance of 750 pc is assumed in this work for RX J0852.0−4622.

4.1.3. Properties

The properties of RX J0852.0−4622 are summarized in table 4.1. The coordinates in the table are given according to equatorial coordinates referred to the mean equinox for the year 2000. Unless otherwise specified, all coordinates in this work will follow this convention.

[1] The column density is a measurement of the amount of gas towards a certain direction in the sky. Comparing with a model of the distribution of gas in the Galaxy, distances can be estimated: between two measurements, a larger column density means a larger distance to the source, since more gas lies between the observer and the source. The column density can be measured using the distortion of the spectrum in X-ray data, since the gas can absorb radiation, especially at low X-ray energies.

SN type: core-collapse or thermonuclear explosion
R.A. = 08h52m
Dec. = $-46°22'$
$t = 2.4\,\mathrm{kyr}$ to $4.3\,\mathrm{kyr}$
$d = 750\,\mathrm{pc}$
$d_{\mathrm{GC}} = 8.5\,\mathrm{kpc}$
$D_\phi = 2°$
$D_{750} = 26\,\mathrm{pc}$

Table 4.1.: Properties of RX J0852.0−4622: supernova explosion type, coordinates in right ascension (R.A.) and declination (Dec.) according to equatorial coordinates referred to the mean equinox for the year 2000, age t, distance d, distance to the Galactic center (GC) d_{GC} assuming a Sun-GC distance of 8.5 kpc as in HESS Collaboration [2016a] and a Sun-RX J0852.0−4622 distance of 750 pc, angular diameter D_ϕ and diameter assuming a distance of 750 pc D_{750}. The information is taken from the Green's SNR catalog (Green [2009]). The distance and age estimates are taken from Katsuda et al. [2008] and Allen et al. [2015] (see main text for discussion).

4.1.4. γ-ray observations

In γ-rays, emission coming from the northwestern part of the rim was first detected by CANGAROO Katagiri et al. [2005] in the VHE regime. Further observations with the H.E.S.S. experiment (Aharonian et al. [2005] and Aharonian et al. [2007]) have shown a 2° extended emission covering the whole area of the SNR, with a spatially resolved shell morphology. This makes RX J0852.0−4622 one of the largest objects in the VHE sky. The spectrum of the emission, using a limited energy range an data set, was well described by a simple power law and the spatial distribution of the VHE emission correlates very well to the X-ray emission. The name of RX J0852.0−4622 in the H.E.S.S. catalog (HESS Collaboration [2016], HESS Collaboration [2016b]) is HESS J0852−463.

The *Fermi* collaboration has reported an analysis of RX J0852.0−4622 Tanaka et al. [2011]. An extended emission at the nominal position of the SNR with roughly the same size as the H.E.S.S. source was detected. The shell morphology could not be resolved and the emission was well described by a power-law spectrum, in the energy range of a few GeV up to a few hundred GeV. The *Fermi* spectrum connects well with the H.E.S.S. points but a change in the spectral index is observed between the measurements of both experiments.

4.1.5. Nature of the γ-ray emission

The γ-ray emission has been interpreted in the framework of both hadronic and leptonic scenarios, without a definite answer so far.

The calculations by Katagiri et al. [2005] preferred a hadronic scenario with a relatively

high density, typical of an interaction with a molecular cloud, for which there is no confirmation.

The measurements by Aharonian et al. [2005] suggested either a leptonic scenario with a low magnetic field (several μG) or a hadronic scenario with density $1\,\mathrm{cm}^{-3}$, both values similar to the ISM conditions.

A more detailed modeling by Aharonian et al. [2007] showed that both scenarios had difficulties for the case of a close-by SNR, but it could be possible to explain the emission with both leptonic and hadronic models for the case of a distant SNR. In the case of a leptonic model, a low magnetic field ($\sim 6\,\mu$G) is required.

Including GeV data, Tanaka et al. [2011] conclude that both scenarios face problems: the leptonic case implies a low magnetic field ($\sim 10\,\mu$G) and the hadronic scenario a rather high fraction of the explosion energy converted into accelerated particles if the density is as low as $0.01\,\mathrm{cm}^{-3}$ as indicated by the density upper limit from Slane et al. [2001].

Recent X-ray results by Kishishita et al. [2013] using *XMM-Newton* observations of the northwestern rim of RX J0852.0−4622 have revealed a softening of the spectrum of the remnant from the rim towards the interior of the remnant. The authors interpret the softening in the framework of a synchrotron-cooling mechanism in which the cut-off energy of the electrons decreases gradually towards the interior of the remnant. In addition, the observed profile is well explained using a simple spectral evolution model including synchrotron losses and a magnetic field strength in the post-shock flow of less than several tens of μG. They conclude that if the derived magnetic field is representative for the rest of the SNR, the γ-ray emission could be accounted for by IC emission of the same electron population responsible for the synchrotron emission.

More recent X-ray observations with *Suzaku* (Takeda et al. [2016]) reveal a hard X-ray component in the northwestern rim of RX J0852.0−4622. X-rays are reported with a spectral index of 3.15 in the energy range from 12 keV to 22 keV.

4.1.6. X-ray PWN

Recent X-ray observations Acero et al. [2013b] have revealed a pulsar wind nebula (PWN) with an extension of 150 arcsec on the rim of RX J0852.0−4622 around the energetic radio pulsar PSR J0855−4644. The properties of the pulsar are listed in table 4.2.

Since its discovery in the Parkes multibeam pulsar survey (see Kramer et al. [2003]), the estimate of the distance to PSR J0855−4644 has been revised a few times. The original estimates of 9.9 kpc and 3.9 kpc used the dispersion measure, using the models by Taylor & Cordes from 1993 (Taylor and Cordes [1993]) and Cordes & Lazio from 2002 (Cordes and Lazio [2002]) respectively. The dispersion measure models the electron distribution in the Milky Way. As pointed out by Acero et al. [2013b], these estimates are conservatively high due to the oversimplistic model of the Vela region used by the models mentioned before.

A more recent estimate from Redman and Meaburn [2005] using also the dispersion measure yields an upper limit on the distance of the pulsar of 750 pc. Another study by Acero et al. [2013b] measuring the column density of the pulsar and RX J0852.0−4622

using X-rays data from *XMM-Newton* revealed that both are at similar distances and gave an upper limit of 900 pc.

Since all these recent measurements are consistent with the distance of 750 pc derived for RX J0852.0−4622 by Katsuda et al. [2008], the distance of 750 pc is assumed in this work for both the remnant and the pulsar.

R.A.	$= 08\text{h}55\text{m}36.18\text{s}$
Dec.	$= -46°44'13.4''$
P	$= 65\,\text{ms}$
τ_c	$= 140\,\text{kyr}$
d	$\sim 750\,\text{pc}$
$\dot{E}$	$= 1.1 \times 10^{36}\,\text{erg/s}$

Table 4.2.: Properties of PSR J0855−4644: coordinates in right ascension (R.A.) and declination (Dec.) according to equatorial coordinates referred to the mean equinox for the year 2000, spin period P, characteristic age τ_c, distance d, and spin-down power $\dot{E}$. The information is from the ATNF pulsar catalog Manchester et al. [2005]. The distance estimate is from Katsuda et al. [2008] (see main text for discussion).

It has been discussed in the literature whether PSR J0855−4644 could be the relic of the progenitor star of RX J0852.0−4622 (Redman and Meaburn [2005], Acero et al. [2013b]). Although they are situated at a similar distance, an association seems unlikely due to the age difference and the large speed ($\sim 3000\,\text{km/s}$) needed by PSR J0855−4644 in order to travel from the SNR geometrical center to its current position.

4.1.7. Motivation for this work

RX J0852.0−4622 is one of only five SNRs whose shell morphology has been resolved in γ-rays. The other objects of this group are RX J1713.7−3946 (see H.E.S.S. Collaboration [2016]), SN 1006 (see Acero et al. [2010]), HESS J1731−347 (see H.E.S.S. Collaboration [2011]) and RCW 86 (see H.E.S.S. Collaboration [2016]). Moreover, the properties of RX J0852.0−4622 and RX J1713.7−3946 are similar: both are young (age $\mathcal{O}(10^3\,\text{yr})$), nearby (distance $< 1.5\,\text{kpc}$), very extended (diameter $\gtrsim 0.5°$), bright (γ-ray flux larger than 50% of the flux of the Crab nebula in the same energy band), and the emission at X-ray and radio wavelengths is highly non-thermal. RX J0852.0−4622 being such a unique object, the detailed study of its properties is crucial for the understanding of the processes that occur in SNRs. In particular, it is a very interesting object for studying the mechanisms that accelerate particles up to TeV energies and the origin of cosmic rays.

Since the last H.E.S.S. publication (Aharonian et al. [2007]), the amount of data available for RX J0852.0−4622 has doubled, motivating a re-analysis of this source. In particular, with more statistics, more detailed studies of the spectrum and the spectral

and spatial morphology of the source can be performed. The term *spectral morphology* is used in this work to refer to the spatially-resolved spectroscopy of the source, i.e. the spectral analysis of different regions in which the source under study can be divided. In the following, the results of the analysis using the complete H.E.S.S. data set are presented and interpreted in terms of the nature of the γ-ray emission. In addition, the same observations can be used to investigate a possible emission of the PWN associated with PSR J0855−4644 in the TeV regime.

4.2. The H.E.S.S. experiment

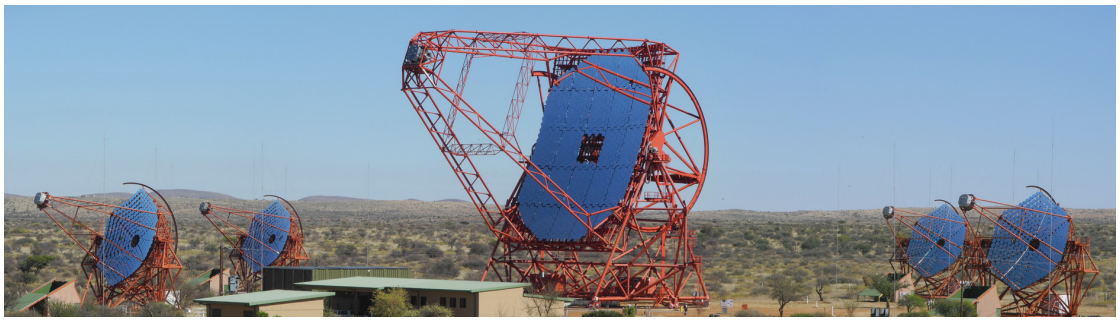

Figure 4.1.: The H.E.S.S. telescope system as of September 2012 at the official inauguration of the new 28 m telescope.

H.E.S.S. is an array of five Cherenkov telescopes situated in the Khomas Highland of Namibia at an altitude of 1800 m above sea level. In its initial phase, during which the data discussed in this work were taken, it consisted of four 13 m diameter telescopes sensitive in the energy range of 100 GeV to 100 TeV. In 2012 a fifth 28 m telescope was added to the center of the array, that allows to lower the threshold of the instrument to several tens of GeV. The four 13 m telescopes have a Davies-Cotton design and are similar in characteristics to the planned CTA Davies-Cotton MSTs presented in section 2.1, whereas the 28 m telescope has a parabolic design similar to the planned CTA LSTs discussed in the same section. A recent picture of the H.E.S.S. telescope system is shown in figure 4.1. In the following, the discussion concentrates on the initial phase of H.E.S.S., in which only the four 13 m telescopes were available.

The four H.E.S.S. telescopes are arranged in a square array of 120 m side length, optimized for having maximum sensitivity at the nominal energy threshold of 100 GeV. The system is able of detecting a point source with a flux level of 1% of the Crab nebula flux in the same energy range in 25 hours at low zenith angles. Its wide field of view (5° diameter), angular resolution (0.1° per event) and energy resolution (15% to 20% per event) make it very suitable for spectral and morphological analysis of very extended sources like RX J0852.0−4622.

Each telescope is equipped with a camera consisting of 960 PMTs facing the mirrors that focus the Cherenkov light emitted by particle showers induced by γ-rays and cosmic

rays entering the Earth atmosphere. The cameras record the images of these showers using a trigger system similar to the one described in section 2.2. More details about the H.E.S.S. trigger system are given in Funk et al. [2004], and about the IACT technique in section 1.3.

More details about the performance of H.E.S.S. in its initial phase are given in Aharonian et al. [2006a] and references therein. For details of the new telescope, please visit HESS Collaboration [2016c].

4.3. Observations

H.E.S.S.observations are performed at night during astronomical darkness, i.e. when the geometrical center of the sun is at least 18° below the horizon and the moon is below the horizon. This ensures the best observing conditions for the cameras to record the faint and brief glow of Cherenkov light coming from particle showers.

The standard observation technique of H.E.S.S. consists in observing the target not by pointing the telescopes directly to it, but slightly offset from it in the so called wobble mode. Since the acceptance of the cameras (system) is rotationally symmetric for rotations around the camera center (pointing position), this observation technique allows for a background estimation directly in the same field of view. This is especially important for flux measurements. By alternating the sign of the wobble offset angle in both R.A. and Dec coordinates at regular intervals, the region around the target is observed homogeneously.

The data used for the analysis of RX J0852.0−4622 were taken between 2004 and 2009. It is composed of data taken in different modi:

- Pointed observations on RX J0852.0−4622 with wobbling positions both within and outside the shell[2].
- Pointed observations on nearby sources: the Vela pulsar, the Vela X nebula and the RCW 38 cluster.
- Scan observations of the Galactic Plane.

The bulk of the observations targeting RX J0852.0−4622 were performed between 2004 and 2006. The analysis of the data up to the end of 2005 has already been published (Aharonian et al. [2005], Aharonian et al. [2007]), but since the last publication the RX J0852.0−4622 data set has roughly doubled[3].

After data taking the raw data is processed in order to correct for different effects involving the observation conditions. For instance, data taken under unstable weather or detector conditions is discarded, the observation time is corrected for the dead time of the instrument and the photo-electron to pixel intensity calibration is performed. This

[2]The majority of the observations usable for the spectral analysis of the whole SNR are targeted at an offset of 1.1° from the nominal center of RX J0852.0−4622.

[3]The data set gain is estimated using the value of the exposure normalized to an offset of 0.7°.

last step takes into account possible inhomogeneities of the PMT responses across the camera. In order to correct for these effects, the performance of the camera is regularly monitored. Other effects, like optical efficiency degradation are corrected at a later stage during the analysis.

Each part of the analysis uses a different data set that is presented at the beginning of the corresponding section. The individual run lists are given in appendix C. The common data revision tag is **production-12-03**.

4.4. Analysis techniques

The results presented in this and the following chapter have been obtained using analysis methods that roughly follow the techniques discussed in Aharonian et al. [2006a]. The largest difference is that this work uses a forward-folding technique with a likelihood fit for spectrum derivation and flux measurements instead of the least-squares method used in the mentioned publication. A schematic view of the steps of the analysis process is shown in figure 4.2.

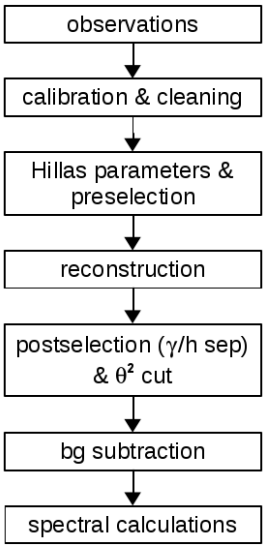

Figure 4.2.: Steps of a typical `Hillas` analysis.

Once the raw data have been filtered and calibrated, the camera images are cleaned to suppress most of the pixels fired due to NSB (see section 1.3.1) instead of the Cherenkov light of a particle shower. Next, the cleaned image is parametrized, obtaining the Hillas parameters (see Hillas [1985]). Images produced by γ-rays have an elliptical shape and are elongated. Images of hadronic showers are more scattered and wider.

At this point a preselection of the images is applied in order to discard poorly reconstructed images. For instance, images too close to the camera edge are not considered for

the analysis. Another important preselection criterion is a cut on the image amplitude (also known as image size). The image amplitude measures the amount of light recorded by the camera and is proportional to the energy of the primary particle. Images that are too faint are discarded. In addition, the requirement that an event has at least two telescope images available is applied. This ensures a stereoscopic view of the particle shower, which improves significantly the quality of the reconstructed properties of the primary particle. This ensemble of requirements is referred to as preselection cuts.

Following the preselection cuts, the properties of the primary particle producing the particle shower are derived using the Hillas parameters of the camera images.

The direction is reconstructed by projecting all images into a common camera plane. The intersection of the major axes of the camera images is the projected direction of the primary particle.

The impact point of the primary particle on the ground, if it had not interacted in the atmosphere, is calculated by intersecting the major axes of the images in the plane perpendicular to the pointing direction of the telescope system. The impact point gives information about the distance of the center of the Cherenkov light pool to the telescope system.

The energy is reconstructed for each telescope using MC data. Simulated events are used to create lookup tables of the energy as a function of the image amplitude and the impact parameter. The image amplitude is proportional to the energy of the primary particle. The impact parameter is a measure of the distance of the shower to the telescope. The impact parameter breaks the ambiguity produced by low-energy close-by showers and high-energy far-away showers leaving the same amount of light in the telescope.

At this point, the effect of optical efficiency degradation of the telescopes is corrected for. With time, the optical efficiency of the telescopes worsens, so the shower images become fainter. If this effect is not corrected for, the energy scale of the results is shifted. For this reason, a correction is applied to the amplitude of the image of each telescope, according to the optical efficiency of the corresponding telescope at the moment of the data taking and to the optical efficiency simulated for the MC used for filling the lookup tables used for the energy reconstruction. The optical efficiency of the telescopes is monitored using images of muons. Therefore the optical efficiency correction is commonly referred to as muon correction. More details about the muon correction is given in the appendix sections E.1 and E.2.

The energy of the primary is thus given by the average of the reconstructed energy for each telescope, using the image amplitudes corrected for optical efficiency degradation.

Once the properties of the primary particle are known, selection cuts are applied for the γ-hadron (short: γ/h) separation. These are simple cuts applied to variables describing the shape of the images in order to reject hadron-like showers in favor of γ-like ones. As mentioned above, the Hillas images of γ-rays tend to be narrower than hadronic ones. The most important variables for γ/h separation are the width and length of the Hillas ellipses[4]. These cuts are referred to as postselection cuts, in contrast to the preselection

[4]The cut is actually applied to the so called mean reduced scaled parameters and not to the parameters

cuts applied before event reconstruction.

Following the γ/h separation, the events are classified as being inside or outside the region of interest defined in the sky (also known as *on*-source region, short: *on* region) by means of the θ^2 cut. θ is defined as the angular distance between the direction of the shower and the test position (center or centroid of the region of interest, depending on its shape). In this sense, the θ^2 cut defines an *on* region in the sky with a circular shape, centered on the test position and with radius $\sqrt{\theta^2}$.

The ensemble of preselection cuts, post selection cuts and θ^2 cut are commonly referred to as selection cuts. In H.E.S.S. they are optimized at the same time in order to maximize detection significance for certain types of sources with certain flux and spectral characteristics[5]. Typically three types of cuts are defined:

- Standard: optimized for detection of typical sources with 10% of the flux of the Crab nebula and a similar spectrum (i.e. power-law-like with spectral index of $\Gamma \sim 2.3 - 2.6$).
- Hard: optimized for detection of weak sources with 1% of the flux of the Crab nebula and a hard spectrum (i.e. power-law-like with spectral index of $\Gamma \sim 2.0$).
- Loose: optimized for detection of strong sources with a similar flux to the Crab nebula and a soft spectrum (i.e. power-law-like with spectral index of $\Gamma \sim 3.0$).

The hard cuts configuration selects telescope images with more than 200 photoelectrons (p.e.) This stringent selection loses significance by increasing the energy threshold of the analysis on the one hand, but enhances the angular resolution on the other hand.

The standard cuts configuration selects telescope images with more than 80 p.e. In contrast to hard cuts, this configuration has an analysis threshold closer to the detector threshold, increasing the statistics and the significance of the results at the expense of a worse angular resolution.

The loose cuts configuration selects telescope images with more than 40 p.e. This configuration has the smallest analysis threshold. Since the spectrum of RX J0852.0−4622 is not soft, this configuration is not appropriated for the study of this source, therefore it is not used in this work.

In the γ/h separation step a large number of hadronic events are rejected. But there is still a background of γ-like hadronic showers that cannot be suppressed. Moreover, electromagnetic showers induced by primary leptons are almost indistinguishable from γ induced showers. Hence, not all events inside the *on* region are γ-rays and the background has to be modeled in order to extract the signal. Background showers are isotropically distributed in direction. Since the acceptance of the cameras is rotationally symmetric around the camera center, this results in background showers being distributed, to a good approximation, with a radial dependence around the center of the field of view.

themselves, as detailed in Aharonian et al. [2006a].

[5]Recently, new sets of selection cuts have been optimized for other criteria (i.e. maximized angular resolution) but they are not used in this work.

This dependence needs to be taken into account for the estimation of the exposure normalization α between the *on* region (region of interest) and the *off* region (region used for extracting the background). There are several methods for background estimation in use within H.E.S.S. (see Berge et al. [2007]). In this work, the two standard methods are used:

- The ring method from Berge et al. [2007]. In this method the background is estimated from a ring of a certain thickness around the test position. Considering that the acceptance of the system is not flat across the field of view, but rather rotationally symmetric for rotations around the pointing position, α is the ratio of the areas of the *on* and *off* regions, corrected for the exposure gradient. This method is applicable to any position within the field of view, allowing the creation of maps of the sky (short: skymaps). In contrast, due to the acceptance correction, the systematic error for flux calculations increases, so this method is not the best suited for spectral analysis.

- The reflected region method from Berge et al. [2007]. This method requires observations in wobble mode as explained in section 4.3. In this configuration, the background is estimated by simply taking several non-overlapping *off* regions with the same shape as the *on* region, mirrored with respect to the center of the field of view at different rotation angles. Since the acceptance of the system is rotationally symmetric for rotations around the pointing position (i.e. the center of the field of view), the exposure normalization α is just the inverse of the number of *off* regions used. Since no acceptance correction has to be performed, the systematic errors are smaller than those connected to the ring background method, making the reflected region background method a good method for calculating fluxes, and hence the derivation of spectra. In contrast, this method does not allow the production of maps, since no *off* regions are possible for the area close to the center of the field of view.

  The offset angle for the wobble mode observations is chosen as a compromise between having the source as close as possible to the center of the field of view, where the instrument acceptance is highest, and having space to place several *off* regions to accurately determine the background.

If there are known sources close to the test position, an exclusion region that encompasses their emission is defined in order to prevent background regions to be created on top of these sources and hence a contamination of the background. In the case of the ring method, if the ring overlaps with an exclusion region, it is truncated and the corresponding exposure correction is included. In the case of the reflected region method, if a reflected region at a certain position overlaps with any exclusion region, no *off* region is created at that position. The two methods described allow background determination within the same field of view where the region of interest is defined. Therefore no dedicated observations are necessary for the background estimation. This results in a reduction of the systematic error and an optimization of the observation time.

The background estimation provides the number of events in the *off* region N_{off} and the *on* to *off* exposure normalization α. So together with the number of events in the *on* region N_{on}, the signal in the on region (also known as γ-ray excess, short: excess) S is estimated as

$$S = N_{\mathrm{on}} - \alpha N_{\mathrm{off}}. \tag{4.1}$$

The significance of the excess ς is calculated using the likelihood ratio method from Li and Ma [1983]. In the mentioned reference, a comparison between the likelihoods of the null hypothesis (H_0: excess originated by the background) and the alternative hypothesis (H_1: excess originated by a new source) is performed. Calling L_0 and L_1 the likelihoods of the null and the alternative hypotheses correspondingly, the significance is calculated as

$$\begin{aligned}\varsigma &= \sqrt{2\log\frac{L_1}{L_0}} \\ &= \sqrt{2\left\{N_{\mathrm{on}}\log\left[\frac{1+\alpha}{\alpha}\left(\frac{N_{\mathrm{on}}}{N_{\mathrm{on}}+N_{\mathrm{off}}}\right)\right] + N_{\mathrm{off}}\log\left[(1+\alpha)\left(\frac{N_{\mathrm{off}}}{N_{\mathrm{on}}+N_{\mathrm{off}}}\right)\right]\right\}}.\end{aligned} \tag{4.2}$$

This definition of the significance does not take into account the number of trials, i.e. the number of attempts using different *on* regions in order to find a significant signal. Therefore, the significance as defined in the equation 4.2 is referred to as pre-trials significance, as opposed to the post-trials significance, which is corrected for the number of trials. In H.E.S.S. an exhaustive search for sources along the central part of the Galactic plane has been performed (Aharonian et al. [2006b], HESS Collaboration [2016b]), hence the detection significance of every new source within the searched region has to be corrected for the number of trials of the Galactic plane scan. RX J0852.0−4622 is located in the area searched but since its detection has long been claimed (Aharonian et al. [2005]) no correction is necessary. Therefore, and unless otherwise specified, the significances reported in this work are significances estimated with the equation 4.2 without trial correction.

At this point in the analysis, with the background subtracted and excess and significance defined, a wide variety of possibilities opens. For instance, skymaps and profiles can be derived for a spatial morphology analysis or flux measurements and spectrum estimates can be performed for a spectral analysis. Each step is introduced in the corresponding section of the analysis results except for the forward-folding method with likelihood fit used for spectrum calculations and the likelihood ratio test used to compare the results from different spectral models. Due to the extension of the description of these two methods, they are described in sections 4.4.3 and 4.4.4 respectively.

The set of analysis techniques described in this section are referred to as `Hillas`-momentum analysis (short: `Hillas` analysis). Although formally the name only applies to the event reconstruction and the γ/h separation. Indeed parts of the analysis described here (like the background subtraction and spectrum determination) are independent of the technique used for event reconstruction and γ/h separation, so they are shared

among all available analysis techniques within H.E.S.S. For more details on the `Hillas` analysis please refer to Hillas [1985], Hofmann et al. [1999], Aharonian et al. [2006a] and references therein. A more updated view of the lookups used for event reconstruction and instrument performance characterization is given in Gast [2012].

4.4.1. Analysis techniques for extended sources

The point spread function (PSF) characterizes the angular resolution of the analysis: in order to be able to claim any hint of structure in the region analyzed the structure has to be larger than the PSF. The PSF is the probability density function of reconstructing a primary photon at a certain offset from its true location. For the determination of the PSF, MC simulations of point sources at different zenith and offset angles are used[6]. The PSF is estimated, for a particular set of observations, by averaging over the livetime available at each pair of zenith and offset angles. The angular resolution of H.E.S.S. does not vary much with energy and can be treated as energy independent. Nevertheless, the PSF is estimated as a function of the energy and then it is averaged over the energy range of the observations weighted by the spectrum of the source[7]. More details about the treatment of the PSF in H.E.S.S. are given in Gast [2012].

Typically, the PSF can be characterized by the sum of two or three one-dimensional Gaussian functions of the offset from the true location in the field of view. The 68% containment radius of the PSF is interpreted as the angular resolution of the instrument. For H.E.S.S. this value is typically of the order of 0.1°, but differs from analysis to analysis and can be smaller than the indicated value. Recent studies of the PSF carried out within H.E.S.S. (HESS Collaboration [2016b]) have discovered a systematic error of 0.03° in the width of the PSF and hence the angular resolution.

Any emission (or feature) larger than the 68% radius of the PSF is considered as extended; if it is smaller, it is considered as pointlike. The analysis of extended sources is very similar to the analysis of pointlike sources, but special attention is required for the choice of the *on* region and the selection cuts.

The sets of selection cuts defined in the previous section, in particular the θ^2 cut, are defined and optimized for both pointlike and extended sources. In the case of the analysis of an extended source, the θ^2 cut is replaced with the specific value required for the particular analysis. Moreover, the definition of arbitrarily shaped *on* regions, as for instance a segment of a ring, is also possible.

In the case of spectral analyses, in order to get correct flux measurements at the nominal H.E.S.S. systematic error level, the *on* region must be one of the following:

Pointlike in the case of a pointlike source. In the case of the analysis of a pointlike region, the effective areas are corrected in order to take into account the signal that falls outside the *on* region due to the PSF tail.

[6] Another possibility (not used in this work) is to use real data from a point source and compare it to MC simulations.

[7] Actually, it is typically weighted by a power-law with a customizable spectral index that should describe the emission of the source. The actual spectral shape of the source may differ and be more complex. Since the PSF does not strongly depend on the energy for H.E.S.S., this is a good approximation.

Extended fully encompassing the complete source up to where the signal drops to zero. In the case the analysis of an extended region, the effective areas are estimated supposing all signal falls within the *on* region.

Extended encompassing a region of constant brightness of a very extended source. This option assumes that the flux left outside the *on* region due to the PSF tails is equal to the flux left inside it but originating in the region outside the *on* region. This is a reasonable supposition for a small region in a large source.

In the first case, selection cuts for pointlike emission should be used for the analysis, with an optimized value of the θ^2 cut. In the other two cases, selection cuts for extended emission should be used, with a user-defined θ^2 cut.

4.4.2. Systematic errors

The systematic error of the angular resolution is given by the 0.03° uncertainty in the determination of the PSF discovered in H.E.S.S. internal studies (HESS Collaboration [2016b]).

The systematic uncertainties of spectral measurements are determined for this work in section 5.3 and listed in section 5.3.1. A summary is presented here. The error on flux measurements is 25%. The error on spectral index measurements is 0.2 for spectral indices in the range from 1.5 to 2.2. The error on energy cut-off measurements is 20%. These uncertainties are slightly larger than the typical H.E.S.S. values given in Aharonian et al. [2006a] and do not represent the general trend of H.E.S.S. measurements.

4.4.3. Forward-folding technique

In order to generate a spectrum, a forward-folding method with a likelihood fit similar to the one described by Piron et al. [2001] is used. The events from the corresponding data set are arranged in an a priori defined three-dimensional fine grid according to their zenith angle, offset angle and reconstructed energy. A bin of such a grid is identified by the corresponding subindices i_z, i_o and i_e. The method uses a certain model for the differential flux $(\mathrm{d}\Phi/\mathrm{d}E)^\mathrm{model}$, where E is the true γ-ray energy, and folds this function with the response functions of the instrument (namely the effective area A_eff and the energy migration matrix R) and the observation time T_on to derive the predicted number of excess events S in a certain bin of the three-dimensional grid as follows:

$$S^\mathrm{model}_{i_\mathrm{z},i_\mathrm{o},i_\mathrm{e}} = T_\mathrm{on} \int_{\tilde{E}^\mathrm{min}_{i_\mathrm{e}}}^{\tilde{E}^\mathrm{max}_{i_\mathrm{e}}} \mathrm{d}\tilde{E} \int_0^\infty \mathrm{d}E \left(\frac{\mathrm{d}\Phi}{\mathrm{d}E}\right)^\mathrm{model} A_\mathrm{eff}(\bar{\theta}_{i_\mathrm{z}}, \bar{\theta}_{i_\mathrm{o}}, E)\, R(\bar{\theta}_{i_\mathrm{z}}, \bar{\theta}_{i_\mathrm{o}}, E \to \tilde{E}). \quad (4.3)$$

$R\,\mathrm{d}\tilde{E}$ represents the probability of reconstructing an energy in the interval $[\tilde{E}, \tilde{E} + \mathrm{d}\tilde{E}]$ for a true energy E. R takes into account the energy resolution and the energy bias of the instrument. Both, R and A_eff depend on the zenith and offset angles and are calculated at the angle $\bar{\theta}_{i_\mathrm{z}}$ corresponding to the angle of the average of the cosine of the zenith angle ($\bar{\theta}_{i_\mathrm{z}} = \mathrm{acos}\langle\cos\theta_{i_\mathrm{z}}\rangle$) and the angle $\bar{\theta}_{i_\mathrm{o}}$ corresponding to the average offset

angle of the three-dimensional bin. The method uses a likelihood function L built from the Poisson distributions of the measured number of *on* and *off* events (respectively N^{on} and N^{off}) in each of the three-dimensional bins as follows

$$L(\vec{x}) = \prod_{i_\mathrm{z},i_\mathrm{o},i_\mathrm{e}} \mathcal{P}(N^{\mathrm{on}}_{i_\mathrm{z},i_\mathrm{o},i_\mathrm{e}})\, \mathcal{P}(N^{\mathrm{off}}_{i_\mathrm{z},i_\mathrm{o},i_\mathrm{e}}). \tag{4.4}$$

The likelihood function can be written to depend only on the spectral parameters $\vec{x}$ of the model with the help of the previous equation 4.3. Varying the fit parameters in an iterative process the likelihood is maximized to get the best fit parameters $\vec{x}_{\mathrm{fit}}$ and their covariance matrix. In this sense, the predicted number of events is compared to the measured value in order to get the fit parameters. Once the fitted spectral function $(\mathrm{d}\Phi/\mathrm{d}E)^{\mathrm{fit}}$ is obtained, the flux points are calculated. The energy E of the point for a certain bin i_e is defined as the energy for which the fitted spectrum is equal to its average over the bin. Calling the differential flux $\phi = \mathrm{d}\Phi/\mathrm{d}E$, the energy is calculated as:

$$\phi^{\mathrm{fit}}(E_{i_\mathrm{e}}) = \langle \phi^{\mathrm{fit}} \rangle_{i_\mathrm{e}}. \tag{4.5}$$

The differential flux ϕ and its error $\delta\phi$ in each three-dimensional bin are calculated from the numbers of measured and predicted excess events as

$$\phi_{i_\mathrm{z},i_\mathrm{o},i_\mathrm{e}} = \frac{S_{i_\mathrm{z},i_\mathrm{o},i_\mathrm{e}}}{S^{\mathrm{fit}}_{i_\mathrm{z},i_\mathrm{o},i_\mathrm{e}}}\, \phi^{\mathrm{fit}}(E_{i_\mathrm{e}}), \quad \delta\phi_{i_\mathrm{z},i_\mathrm{o},i_\mathrm{e}} = \frac{\delta S_{i_\mathrm{z},i_\mathrm{o},i_\mathrm{e}}}{S^{\mathrm{fit}}_{i_\mathrm{z},i_\mathrm{o},i_\mathrm{e}}}\, \phi^{\mathrm{fit}}(E_{i_\mathrm{e}}) \tag{4.6}$$

where $S^{\mathrm{fit}}_{i_\mathrm{z},i_\mathrm{o},i_\mathrm{e}}$ is the result of inserting $\vec{x}_{\mathrm{fit}}$ into the equation 4.3. These values are then averaged over zenith and offset angle in order to get the final values for the flux and its error for each energy bin. Finally, the residuals can be calculated by comparing the points to the fitted model.

This technique is not implemented in the same way in all analysis chains used within the H.E.S.S. collaboration[8]. The main difference occurs for `HAP-HD` (the one extensively used for this work), where the technique is not fully implemented. In this case, the folding of the model with the migration matrix in the equation 4.3 is not done. Instead, the folding with the effective areas is done in reconstructed energy $\tilde{E}$ and the spectrum is restricted to energies where the bias is low (less than 10%). For this reason, the minimum energy of the spectrum with `HAP-HD` tends to be slightly larger than for other analysis chains.

4.4.4. Likelihood ratio test

In the case of several models fitted to the data with a likelihood maximization technique, in order to select the best suited model for describing the data a statistical test based on the likelihood ratio test is used. This test is also used to assess whether a more complicated model is statistically motivated.

[8]The analysis chains used within the H.E.S.S. collaboration are presented and discussed in more detail in subsection 4.4.5.

The likelihood ratio test compares the likelihoods of 2 hypotheses: the null hypothesis H_0 and the alternative hypothesis H_1. Each hypothesis can have a certain number of parameters that can be tuned within certain ranges. A requirement for the test to be valid is that H_0 is "nested" in H_1, meaning that a combination of the parameters for H_1 should return H_0, where the parameters are not on the limit of their ranges. The test statistic is built as the logarithm of the ratio of likelihoods L of H_1 and H_0 multiplied by 2

$$\Lambda = 2 \log \frac{L_1}{L_0} = -2 \left(\log L_0 - \log L_1 \right). \tag{4.7}$$

According to Wilks' theorem (see Wilks [1938]), under the assumption of a large number of samples, the test statistic from the likelihood ratio test follows a χ^2 distribution with a number of degrees of freedom NDF equal to the difference in the number of free parameters NFP between the more complex model and the simpler one:

$$\mathrm{NDF} = \mathrm{NDF}_1 - \mathrm{NDF}_0 = \mathrm{NFP}_1 - \mathrm{NFP}_0. \tag{4.8}$$

Such a χ^2 can be used to derive the probability p_0 of the null hypothesis H_0 (probability that the simpler model is preferred). The opposite $1 - p_0$ represents the probability p that the more complex fit is preferred, which can be translated into a significance in terms of Gaussian standard deviations. The minimum value in order to reject the null hypothesis is chosen to be 3σ for this study.

4.4.5. Analysis chains

In this work, the term *analysis chain* refers to a certain software framework, with specific implementations of one or several analysis methods (such as the `Hillas` analysis). It comprises the whole analysis process, form basic data handling to the production of high-level analysis results, such as skymaps and flux measurements.

Before performing an analysis a decision has to be made regarding the most suited analysis chain and analysis method. The remaining chains and methods can be used to crosscheck the results of the main analysis.

There are different analysis chains available within H.E.S.S. Each of them has several analysis methods implemented. The most common analysis chains are described and compared to each other in table 4.3, concentrating on the implementation of the `Hillas` analysis provided by each software chain[9]. The two main chains are `Paris Analysis` (short: `Paris`) and `HAP-HD` (`HAP` stands for H.E.S.S. Analysis Package and `HD` for Heidelberg). Each of them has an independent calibration and an independent high-level analysis software, though the base software for storing and reading the data and the coordinate system classes is the same: `SASH` (Storage and Analysis Software at H.E.S.S.). A third analysis chain that has overlaps with both of the previous chains is used as well: `HAP-FR` (`FR` stands for France). This chain shares the framework of the high-level

[9] More advanced analysis methods than the `Hillas` analysis presented at the beginning of this section are available. Since they are only barely used in this work, they are briefly presented later in this subsection.

analysis and some of its code with HAP-HD and the calibration with Paris Analysis. Though the different analysis chains tend to have independent software implementations from each other (this is quite accurate at least for the two different software frameworks HAP and Paris Analysis), they share many of the methods, so they appear gray shaded in the table. For instance, all chains share the forward-folding technique with likelihood fit as a spectrum derivation method, but each one has its own implementation.

	HAP-HD	HAP-FR	Paris
calibration	HD	Paris	Paris
base software	SASH	SASH	SASH
framework (interface)	HAP	HAP	Paris Analysis
reconstruction method	Hillas	Hillas	Hillas
MC (i.e. lookup tables)			
selection cuts			
γ/h separation method			
bg method			
spectrum method	forward-folding	forward-folding	forward-folding

Table 4.3.: Most common analysis chains used within H.E.S.S. Shadowed areas denote common (overlapping) features or code between the different chains. The table concentrates on the Hillasanalysis implementation of each chain. References to the more sophisticated analysis chains used within H.E.S.S. are given in the main text.

Each analysis chain has an alternative implementation of a more advanced analysis technique, involving an independent γ/h separation method and eventually also an independent event reconstruction method and selection cuts. HAP-HD and HAP-FR use the multi-variate analysis based on boosted decision trees within the ROOT data analysis framework (see ROOT Team [2016]) with customized parameters in order to perform the γ/h separation. Each chain has its own implementation: TMVA Ohm et al. [2009] for HAP-HD, and Paris MVA Becherini et al. [2011] for HAP-FR. Paris Analysis uses a likelihood minimization technique to compare the raw telescope images to the predictions of a semi-analytical model, producing an event reconstruction and γ/h separation method independent of the Hillas analysis discussed in this section. This likelihood minimization method is referred to as the Model Analysis de Naurois and Rolland [2009].

These sophisticated methods (TMVA, Paris MVA, Model Analysis) are most powerful for the detection of faint sources since they have a better γ/h separation at low energies than the Hillas analysis. At medium to high energies the performance of the sophisticated methods is similar to the Hillas analysis. Moreover, the sophisticated methods have not been fully optimized for very extended source, and therefore are not best suited for the analysis of RX J0852.0−4622. Therefore the Hillas analysis method (more robust than the sophisticated methods) is chosen for the analysis presented in this work. Since the sophisticated analysis techniques are only barely used in this work, no further

details are given about them.

Another analysis method used in the past for analyzing RX J0852.0−4622 is the so called `Model 3D`. This method uses the camera images to fit the parameters of a three dimensional model of an air shower, producing an event reconstruction and γ/h separation method independent of the `Hillas` analysis discussed in this section. More details are given in Lemoine-Goumard et al. [2006]. This method, no longer in use within H.E.S.S., shared the calibration of the `Paris Analysis` framework.

The analysis chain used for this work is `HAP-HD`: the `HAP` framework implemented at the MPIK in Heidelberg. The analysis software is based on the version **hap-12-03-pl03** and the instrument response tables version **32** are used. The data revision tag is **production-12-03**. Unless otherwise specified, all results in the following sections are derived with the `Hillas` analysis implemented in the `HAP-HD` analysis chain (short: `HAP-HD-Hillas` or just `HAP-Hillas`).

4.5. Results

The data available from observations targeted around RX J0852.0−4622 are analyzed using the analysis techniques mentioned above.

The *on*-source region (short: *on* region) selected for the analysis is a circle centered at the nominal position of RX J0852.0−4622 (in right ascension and declination according to equatorial coordinates referred to the mean equinox for the year 2000: R.A: 8h52m Dec: $-46°22'$), with a radius of 1.0°. This region is sometimes referred to as *whole SNR* region. To avoid any contamination of the source and/or the nearby Vela X pulsar wind nebula, the regions of the sky detailed in table 4.4 are excluded for the analysis, in particular for the determination of the background from the *off*-source regions (short: *off* regions).

shape	R.A.	Dec.	radius	name
circle	133.000°	−46.3700°	1.10°	Vela Junior
circle	128.857°	−45.7254°	0.85°	Vela X main
circle	129.985°	−45.1368°	0.60°	Vela X central
circle	130.800°	−44.7000°	0.60°	Vela X tail

Table 4.4.: Exclusion regions used for the analysis of RX J0852.0−4622. The coordinates refer to the center of the corresponding circular region.

Many of the results presented in this and the subsequent chapter 5 are being summarized for publication in HESS Collaboration [2016a]. The aim of the work presented here is to describe the results in more detail, giving more comprehensive explanations in particular for the systematic checks performed.

4.6. Spatial morphology analysis

In this section of the analysis, the increased data set available on RX J0852.0−4622 is used to derive skymaps, morphological profiles (skymap projections) and morphological fits.

The data set for this analysis is selected according to the following criteria:

- Only data taken under favorable weather conditions and stable detector performance are selected.
- Only data taken at pointings up to 3.0° around the center of the SNR are considered.
- Only data taken when at least three telescopes were active are used.

After data quality selection, 169 runs remain with a livetime of 71.8 h. The actual run list can be found in the appendix in table C.1.

For this analysis, a hard γ/h separation cut selection is applied to the data in order to have an improved angular resolution. The background is estimated with the ring method using a ring with inner radius of 1.5° and thickness of 0.3°. The inner ring radius is chosen to be much larger than the radius of the *on* region to avoid contamination of the background with signal events, and the thickness is chosen to have an area of the ring approximately as large as that of the *on* region.

Table 4.5 summarizes the event statistics. With 32σ, the signal in the *on* region is highly significant.

$\langle\theta_{\mathrm{zen}}\rangle$	$\langle\theta_{\mathrm{az}}\rangle$	$\langle\theta_{\mathrm{off}}\rangle$	t / h	N_{on}	N_{off}	α	excess	significance
29°	191°	1.4°	71.8	24348	12731	1.35	7102	32.0σ

Table 4.5.: Statistics used in the spatial morphology analysis: mean zenith and azimuth angles of the observations ($\langle\theta_{\mathrm{zen}}\rangle$ and $\langle\theta_{\mathrm{az}}\rangle$ respectively), mean offset angle $\langle\theta_{\mathrm{off}}\rangle$, the livetime t, number of events in the signal (*on*) region N_{on}, number of events in the background (*off*) region N_{off}, exposure normalization (ratio of *on* to *off* exposures) α, number of excess counts in the *on* region and significance of the signal in the *on* region in number of Gaussian standard deviations σ.

The left panel of figure 4.3 shows the significance map using a 0.1° correlation radius of the region with 3° radius around RX J0852.0−4622. The correlation radius is the radius of the region around each bin in the skymap used to estimate the significance. A highly significant emission is seen as an almost perfect ring coincident with the shell of RX J0852.0−4622.

The central panel of figure 4.3 shows the residuals map, i.e. the significance map after removing the signal from the exclusion regions. No significant structure is visible.

The right panel of figure 4.3 shows, for the spatial morphology analysis, the significance distribution for the whole skymap without the three Vela X exclusion regions in green,

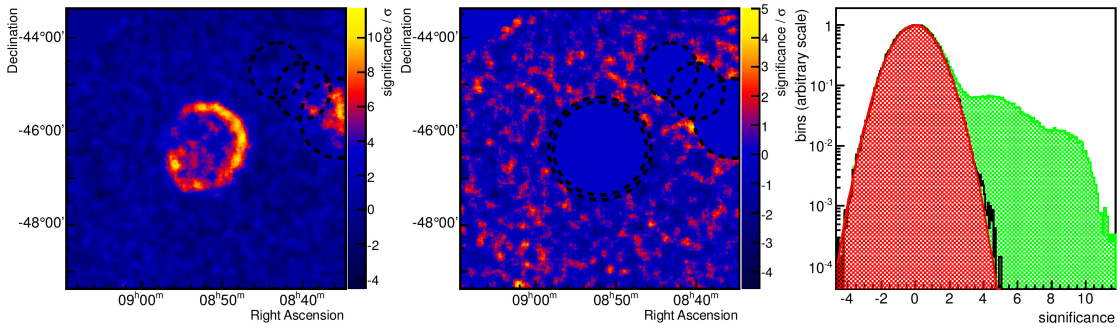

Figure 4.3.: Significance maps and distributions of the data set used for the morphological analysis. The black dashed circles on the maps indicate the exclusion regions. Left: significance map using a 0.1° correlation radius of the region with 3° radius around RX J0852.0−4622. Center: residual significance map of the map on the left panel, when excluding the regions from table 4.4. Right: significance distribution for the significance map on the left panel after excluding the Vela X regions (green histogram and area), significance distribution for the residual map on the center panel (black histogram) and fit of the residual significance distribution to a Gaussian distribution (red curve and area).

the distribution for the background region in black and a fit of the latter to a Gaussian distribution in red. The fit shows, as expected, that the background distribution can be well described by a Gaussian distribution of mean 0 and width 1 (i.e. a normal distribution), meaning that the exclusion regions selected for the analysis (shown in table 4.4) are sufficient to avoid contamination by the signal.

The properties of the data set presented in table 4.5 are used to determine the specific PSF for this analysis as explained in section 4.4.1. In particular, the zenith angle versus offset distribution of the data is used to weight the PSF of the instrument. For the energy average of the function describing the PSF a power-law spectrum with an index of 2.25 is assumed, which is very similar to the value published in Aharonian et al. [2007]. The resulting PSF can be characterized by a triple Gaussian function of the distance with a 68% containment radius of 0.076°. This number, which is affected by the systematic error of the H.E.S.S. PSF (0.03°), defines the angular resolution of the spatial morphology analysis [10] . The PSF is shown as an inset in figure 4.4. The effect of the systematic uncertainty on the width of the PSF is studied further below in this section, when estimating the shell thickness from the fit of the radial profile.

Figure 4.4 shows the excess map corrected for the gradient of exposure across the field of view and smoothed with a Gaussian function with a width of 0.075° (similar to

[10]The angular resolution of the morphological analysis of this work (0.076°) is worse than the one reported for the morphological analysis of Aharonian et al. [2007] (0.06°) because no additional cut restricting the number of telescopes participating in a specific event (multiplicity cut) was applied. This favors γ-ray efficiency at the expense of a somewhat worse angular resolution.

the analysis PSF width). From the figure it is clear that RX J0852.0−4622 is a largely extended source for H.E.S.S., with most of the signal coming from an almost perfectly circular thin shell. The *on* region is chosen to be tight: it barely encompasses the 5σ significance contour. It is chosen like this because, the source being so large ($\sim$ 16% of the H.E.S.S. field of view surface), a larger *on* region makes the determination of *off* regions within the same field of view quite difficult, especially for the reflected region background method used for the spectrum calculations in chapter 5. Nevertheless, the number of γ-rays left outside the *on* region is expected to be small compared to the signal inside it.

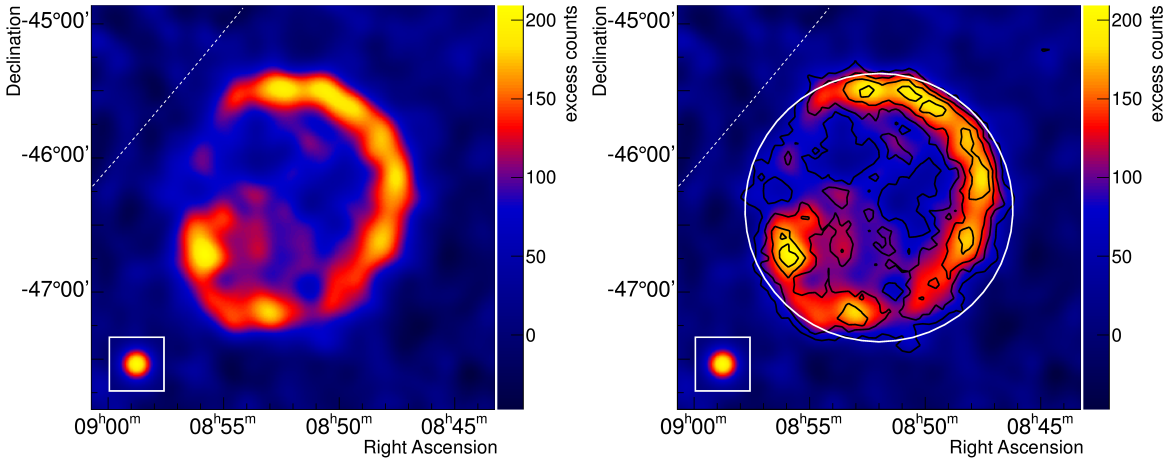

Figure 4.4.: Excess maps. Left: exposure corrected excess map smoothed with a Gaussian function of width 0.075°. The white dashed line shows the position of the Galactic plane. The inset shows the PSF of the analysis at the same scale for comparison. Right: the same as in the left panel, but additionally the boundary of the *on* region is shown as a white circle and the significance contours at 3, 5, 7 and 9σ are shown in black.

Since the emission is extended, the morphology can be studied in more detail. For this purpose, the contents of the skymap are projected in different ways. In order to have uncorrelated bin errors the raw counts map (the so called *on* map) corrected for the gradient of exposure across the FoV is used, instead of the excess map. The use of the *on* map ensures the use of uncorrelated Poissonean errors. However, the smoothed map is shown in the figures for better visibility. The profiles have been normalized for the solid angle covered in the sky.

The bin contents n of the projections are calculated as

$$n = \frac{\sum_{x,y} \frac{N_{\mathrm{on}\,x,y}}{\epsilon_{x,y}}}{\sum_{x,y} A_{x,y}}, \tag{4.9}$$

and the errors σ_n, assuming the exposure correction ϵ without error, as

$$\sigma_n = \frac{\sqrt{\sum_{x,y} \frac{N_{\mathrm{on}\,x,y}}{\epsilon^2_{x,y}}}}{\sum_{x,y} A_{x,y}}. \tag{4.10}$$

In both cases, A represents the solid angle covered by the skymap bins and x, y refer to the angular coordinates of the skymap bins combined to produce one profile bin.

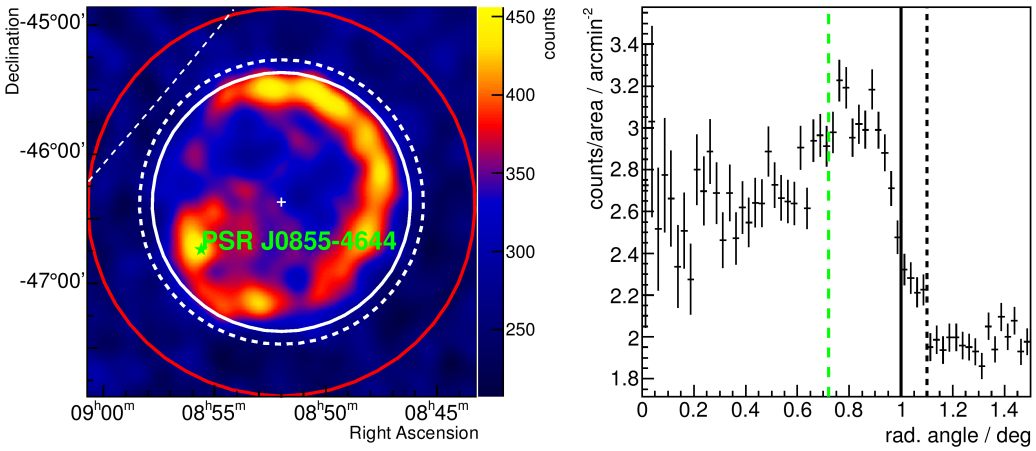

Figure 4.5.: Radial profile. Left: *on* map smoothed with a Gaussian function of width 0.075°. The white dashed line shows the position of the Galactic plane. The red circle marks the radial profile extraction region. The white solid circle marks the *on* region and the dashed white circle the exclusion region chosen for RX J0852.0−4622. The green star marks the position of PSR J0855−4644. Right: radial profile extracted from the region indicated in red in the skymap in the left panel. The projection of the position of PSR J0855−4644 is marked by a dashed green vertical line. The black solid and dashed lines denote the extension of the *on* and exclusion regions respectively.

The radial profile (i.e. skymap projection along the radial coordinate) of the 1.5° radius circular region around the center of the RX J0852.0−4622 remnant is shown in figure 4.5. The histogram shows a shell-like shape, with a peak at around 0.8°. A green line at 0.72°

denotes the projection of the position of PSR J0855−4644 within the profile, showing that it is located within the shell of the TeV emission. A black solid line at 1.0° marks the radius of the *on* region selected for the analysis of RX J0852.0−4622. It can be seen that a few bins outside the *on* region still have a small signal ($\sim 0.2\,\mathrm{counts/arcmin^2}$) above the background ($\sim 2.0\,\mathrm{counts/arcmin^2}$), and that the emission would be fully encompassed by a circular region extending up to 1.1° (black dashed line). This radius has been adopted for the exclusion region of RX J0852.0−4622 (as indicated in table 4.4) in order to avoid background contamination, but not for the *on* region (as already mentioned when discussing the significance contours further above). Nevertheless, the effect is very small and does not affect the results significantly. The number of γ-rays left outside the *on* region is small ($\sim 4\%$) compared to the signal inside and its systematic uncertainty, so the contribution is neglected in the following.

In order to determine the morphology of the source, four different models are tested against the radial profile of figure 4.5: a disk, a Gaussian function and a solid sphere projected onto a plane to test the hypothesis of morphology without a shell structure, and the projection of a uniformly emitting shell onto a plane to test for the shell morphology[11]. Using r as the radial angle coordinate, the models can be written as follows:

1. Disk:
$$f(r) = N \begin{cases} 1 & \text{if } r \leq r_{\mathrm{out}} \\ \\ 0 & \text{if } r > r_{\mathrm{out}} \end{cases} \tag{4.11}$$
N represents the normalization factor, and r_{out} the radius of the disk.

2. Gaussian:
$$f(r) = N e^{\frac{-r^2}{2r_{\mathrm{out}}^2}} \tag{4.12}$$
N represents the normalization factor, and r_{out} the width of the Gaussian.

3. Shell:
$$f(r) = N \begin{cases} \dfrac{1}{r_0}\left(\sqrt{r_{\mathrm{out}}^2 - r^2} - \sqrt{r_{\mathrm{in}}^2 - r^2}\right) & \text{if } r \leq r_{\mathrm{in}} \\ \\ \dfrac{1}{r_0}\sqrt{r_{\mathrm{out}}^2 - r^2} & \text{if } r_{\mathrm{in}} < r \leq r_{\mathrm{out}} \\ \\ 0 & \text{if } r > r_{\mathrm{out}} \end{cases} \tag{4.13}$$
N represents the normalization factor, r_0 the reference radius, and r_{in} and r_{out} the inner and outer radii of the shell respectively.

The latter (shell) model is used twice: once with the fixed parameter $r_{\mathrm{in}} = 0$ to emulate a filled sphere, and once with all parameters (r_{in}, r_{out}, N) free for testing the shell

[11] Actually the functions describing all models should be projected onto a sphere (the celestial sphere), but for the extension of the source (2° in diameter) the projection onto a plane is a good approximation.

morphology. In both cases the reference radius r_0 is set to 1°.

The test is performed by fitting the result of the convolution of each of the models $f(r)$ (plus a constant C to take into account the background level) with a function $g(r)$ representing the PSF of the instrument to the data points of the radial profile. For simplicity, the PSF is modeled as a Gaussian function of width equal to the 68% containment radius of the actual PSF of the analysis (0.076°). None of the models are nested within each other: the complex one - shell - cannot be reduced to any of the simple ones - disk, Gaussian or even sphere. The shell model cannot be reduced to the sphere model since $r_{\mathrm{in}} = 0$ is at the boundary of the physical range of the parameter. Therefore the models cannot be tested against each other. However, each model is tested against the data via the χ^2 probability of the fit. The convolution of each model $f(r)$ (plus the constant C) with the PSF $g(r)$ is calculated as

$$((f + C) \otimes g)(r) = \int_0^r (f(r') + C)g(r - r')\mathrm{d}r'. \tag{4.14}$$

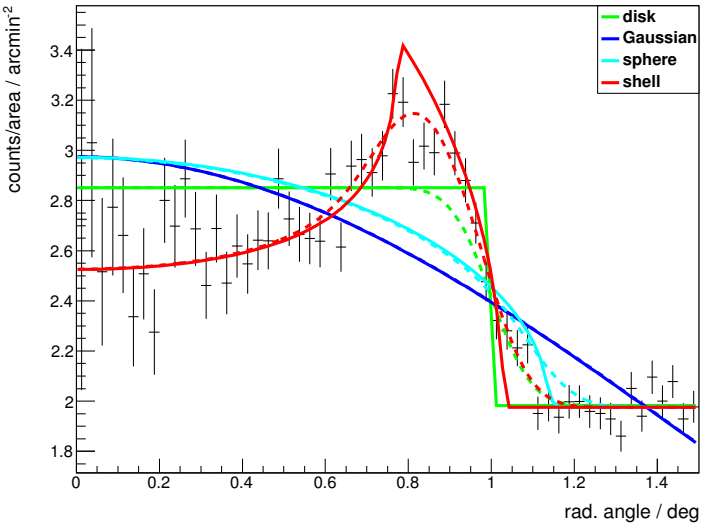

Figure 4.6.: Radial profile from figure 4.5, together with the fitted functions (dashed lines) and their corresponding model functions (solid lines) for the four tested morphologies: disk, Gaussian, filled sphere and shell. The fitted functions are the convolution of the models with a Gaussian PSF, to take into account the angular resolution of the data, plus a constant, to take into account the background level.

The fitted functions and the models are shown in figure 4.6. The parameters and the χ^2 values of the fits are shown in tables 4.6 and 4.7 respectively.

All three-parameter models have difficulties in describing the morphology of the source: all fits (disk, Gaussian and sphere) get very poor p-values, so they are ruled out. With

model	$N/\,\mathrm{arcmin}^{-2}$	$r_{\mathrm{in}}/\,^\circ$	$r_{\mathrm{out}}/\,^\circ$	$C/\,\mathrm{arcmin}^{-2}$
disk	0.87 ± 0.03	n.a.	1.002 ± 0.008	1.982 ± 0.017
Gaussian	2.97 ± 0.03	n.a.	1.52 ± 0.03	0.00 ± 0.18
sphere	0.87 ± 0.03	0 (fixed)	1.141 ± 0.012	1.975 ± 0.018
shell	2.17 ± 0.22	0.777 ± 0.018	1.030 ± 0.013	1.975 ± 0.017

Table 4.6.: Radial profile fit parameters for each of the models mentioned in the text. The quoted errors represent 1σ statistical uncertainties. In the case of the shell and filled sphere models the reference radius r_0 is chosen to be 1°.

model	χ^2	NDF	NFP	p-value
disk	173	57	3	1.4×10^{-13}
Gaussian	509	57	3	8.1×10^{-74}
sphere	346	57	3	5.3×10^{-43}
shell	64.2	56	4	0.21

Table 4.7.: Results of the χ^2 test for the radial profile morphology fits. For each fitted model the χ^2, the number of degrees of freedom NDF, the number of free parameters NFP and the probability of the test p are shown.

a 21% χ^2 fit probability the only model that can describe the profile satisfactorily is the projected shell, so it is concluded that the TeV emission comes from a shell-like structure.

The derived shell thickness is $\sim 0.25^\circ$, and the ratio of the thickness to the outer radius $\sim 25\%$, both quite similar but slightly higher than the values from paper 2 (see Aharonian et al. [2007]) of $\sim 0.2^\circ$ and 18.3% for thickness and ratio respectively. This is due to the fact that the present work derives the radial profile using the whole SNR, whereas the mentioned publication used only the northern region. Therefore, the publication derived the thickness only for the northern rim which is somewhat thinner than the southern region of the remnant, as can be observed in the skymaps of figure 4.4. This can be due to the presence of PSR J0855−4644, which lies slightly outside the inner boundary of the shell (0.06° away from it) and cannot be resolved as a separate contribution. Future experiments with a better angular resolution, such as CTA, might help in the separation of both contributions.

Comparing the ratio of the thickness to the outer radius obtained from the fit results of the shell morphology ($\sim 25\%$) to that of the density profile in figure 3.6 ($\sim 20\%$), the fit value is larger by 5%. This can be due to either the presence of PSR J0855−4644, or to the fact that RX J0852.0−4622 is older than the $\sim 100\,\mathrm{yr}$ used in the derivation of the density profile, so the shell has had more time to evolve and become wider.

The results of this section confirm that the emission from RX J0852.0−4622 comes mostly from a thin shell with a width of $\sim 0.25^\circ$. This number is affected by the systematic error of the H.E.S.S. PSF (0.03°).

Indeed, decreasing the PSF width by 0.03° in the fit yields a value for the shell thickness of $\sim 0.30^\circ$ and for the ratio of the thickness to the outer radius of $\sim 39\%$.

Correspondingly, the increase of the PSF width by 0.03° yields a value of the shell thickness of $\sim$ 0.08° and for the ratio of the thickness to the outer radius of $\sim$ 8%. These values can be interpreted respectively as upper and lower limits on the shell thickness and on the ratio of the thickness to the outer radius.

It is remarkable that the shell width quickly drops when increasing the PSF width. This is due to the fact that the PSF width, increased by its systematic error, is similar to the width of the emission maximum in the radial profile. Hence, in the fit, a large fraction of the width of the peak in the convoluted function is assigned to the PSF and only a small fraction to the intrinsic shell width.

The azimuthal profile (i.e. skymap projection along the azimuthal coordinate) of the ring region between the radial angles 0.6° and 1.0° around the center of RX J0852.0−4622 is shown in figure 4.7[12]. The azimuthal profile is derived in analogy to the radial profile. The azimuth angle is defined anticlockwise, starting at the vertical line on the top of the ring region shown in the map. Two periods separated by a dashed gray line are displayed. A green line at 121° denotes the projection of the position of PSR J0855−4644 within the profile.

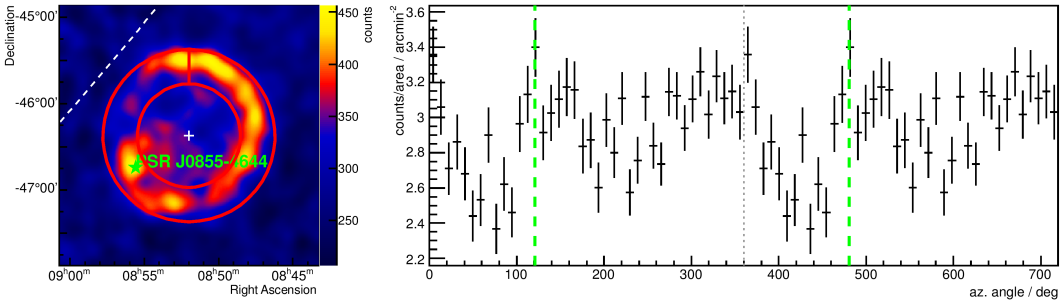

Figure 4.7.: Azimuthal profile. Left: *on* map smoothed with a Gaussian function of width 0.075°. The white dashed line shows the position of the Galactic plane. The red ring marks the azimuthal profile extraction region. The red vertical line denotes the origin of the azimuthal angle, which increases in the anticlockwise direction. The green star marks the position of PSR J0855−4644. Right: azimuthal profile extracted from the region indicated in red in the skymap on the left panel. For better visibility two periods separated by a dashed gray line are shown. The projection of the position of PSR J0855−4644 is marked by a dashed green vertical line.

The azimuthal profile shows that the emission is not homogeneous along the shell. In general, the NW rim (with its plateau approximately ranging from 270° to 380°) is brighter than the SE part of the shell. The emission of the NW rim region is quite

[12]The results from this plot have been independently crosschecked by Fabio Acero with the `Model Analysis` of the `Paris Analysis` analysis chain and are in agreement with them. A preliminary version of this study has been published on Paz Arribas et al. [2011].

uniform, whereas two emission maxima appear towards the S ($\sim 160°$) and SE ($\sim 120°$) directions. The latter is coincident with the position of the pulsar PSR J0855−4644. The former has been found to be coincident with the Fermi source 2FGL J0853.5−4711 (one of the three pointlike sources in the 2FGL Fermi catalog[13] associated with RX J0852.0−4622 as indicated in Lande et al. [2012] and Nolan et al. [2012]) and very close to the radio source PMN J0852−4712 (see Wright et al. [1994]). Not much information is available in the literature about this source.

The morphology displayed in the γ-ray maps is also seen in radio and X-ray maps (see Stupar et al. [2005]), where most of the emission comes from the northwestern rim of the shell, with some local enhancements towards the south. In the case of the X-ray map an enhancement is also seen towards the direction of PSR J0855−4644.

4.7. Spectral morphology analysis

Due to the increased data set available with respect to the last publication (see Aharonian et al. [2007]) the spectral morphology of the remnant can be studied. For this reason, and because of the shell morphology revealed in the spatial morphology analysis in section 4.6, the *on* region used for the whole SNR is split into a central region of 0.6° radius (region 0) and 6 equally sized segments of a ring centered at the center of the remnant and inner and outer radii 0.6° and 1.0° respectively (regions 1 to 6). These regions are indicated in white in figure 4.8.

A particular run selection is performed for each of the regions and for the whole SNR. The data sets for this analysis are selected according to the following criteria:

- Only data taken under favorable weather conditions and stable detector performance are selected.
- For the analysis of the whole SNR region only data taken at pointings from 1.0° up to 1.25° around the center of the SNR are considered.
- For the analysis of each region only data taken at pointings up to 1.5° around the centroid of the region are considered.
- Only data taken when all four telescopes were active are used.

After data quality selection, the amount of data differs for each region. It spans from 38 runs for region 6 (livetime of 16.1 h) to 73 runs for region 0 (livetime of 31.1 h). For the analysis of the whole SNR region 65 runs with a total livetime of 27.7 h are available. The actual run lists can be found in the appendix in table C.2.

Using the regions described above as *on* regions and the same exclusion regions as for the spatial morphology studies in section 4.6, a spectral analysis is performed for each of the regions and the whole SNR using a standard γ/h separation cut selection in order to improve the statistics with respect to the spatial morphology analysis.

[13] Subsequent *Fermi* catalogs (i.e. the 3FGL catalog) model RX J0852.0−4622 as an extended source, so no counterpart is found in them.

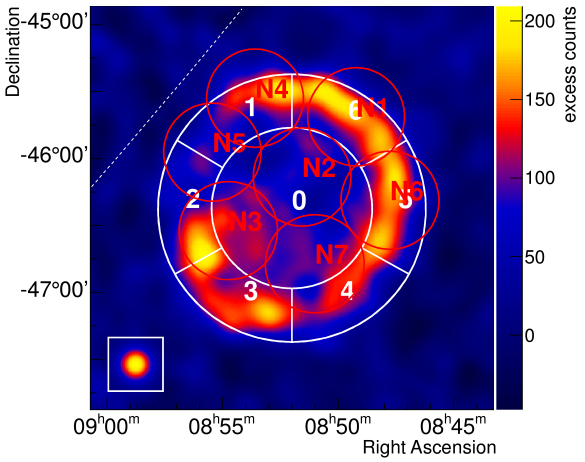

Figure 4.8.: Smoothed exposure corrected excess map from figure 4.4 together with the regions used for the spectral morphology analysis of RX J0852.0−4622. The boundaries of the H.E.S.S. regions used for the spectral morphology analysis are marked with white lines, and the ones for the *ASCA* regions in red.

The background is estimated with the reflected region method. In the case of the analysis of the whole SNR, since the *on* region for RX J0852.0−4622 is so large (1° radius), most observation runs only have space for one reflected *off* region in the field of view. Moreover, since the exclusion regions for RX J0852.0−4622 and Vela X are quite large, it is not possible to place suitable *off* regions for some of the runs when using the reflected region background method, and hence, not all runs can be used for the spectral analysis. Table 4.8 summarizes the event statistics for each region.

Following the discussion in section 1.1, the spectrum of the majority of the VHE sources can be characterized locally by a featureless power-law spectrum given by

$$\frac{\mathrm{d}\Phi}{\mathrm{d}E} = \Phi_0 \left(\frac{E}{E_0} \right)^{-\Gamma}, \tag{4.15}$$

where Φ is the photon flux, E the photon energy, Φ_0 the flux normalization, E_0 the reference energy and Γ the spectral index. The spectrum from some sources can deviate from a pure power-law, and can be characterized by a more complex model. In order to keep the study simple, the energy band of the spectral analyses is limited to the range between 0.5 TeV and 7.0 TeV. The reason for the low energy cut is the low statistics close to the threshold energies. The motivation for the high energy cut is to avoid the possible curvature on the spectrum of the remnant: the spectrum of RX J0852.0−4622 shows an indication of a curvature at high energies as already noticed by Aharonian et al. [2007].

region	$\langle\theta_{\mathrm{zen}}\rangle$	$\langle\theta_{\mathrm{az}}\rangle$	$\langle\theta_{\mathrm{off}}\rangle$	t / h	N_{on}	N_{off}	α	excess	significance
0	32°	205°	1.1°	28.2	41718	87906	0.4	3712	15.6σ
1	30°	202°	0.89°	15.4	7863	30971	0.2	890	9.4σ
2	31°	198°	1.0°	23.8	10639	46454	0.2	844	7.6σ
3	32°	198°	0.85°	16.6	8282	27705	0.3	1031	10.5σ
4	33°	203°	0.87°	15.6	7398	19040	0.3	840	8.7σ
5	31°	198°	1.1°	27.5	12155	52959	0.2	1580	13.6σ
6	31°	205°	0.89°	14.8	7487	15986	0.4	1067	10.9σ
whole SNR	32°	207°	1.2°	19.9	77396	69652	1	7744	20.2σ

Table 4.8.: Statistics used in the spectral morphology analysis for each region: region name, mean zenith and azimuth angles of the observations ($\langle\theta_{\mathrm{zen}}\rangle$ and $\langle\theta_{\mathrm{az}}\rangle$ respectively), mean offset angle $\langle\theta_{\mathrm{off}}\rangle$, livetime t, number of events in the signal (*on*) region N_{on}, number of events in the background (*off*) region N_{off}, exposure normalization (ratio of *on* to *off* exposures) α, number of excess counts in the *on* region and significance of the signal in the *on* region in number of Gaussian standard deviations σ.

The data sets presented in table 4.8 are used to derive spectra with the forward-folding technique described in section 4.4.3 using a power-law model with reference energy $E_0 = 1\,\mathrm{TeV}$ in the energy range from 0.5 TeV to 7.0 TeV.

The spectral indices of all regions and of the whole SNR are shown in table 4.9a and in figure 4.9a[14]. A fit of the spectral indices of all regions to determine the weighted average index yields a value of $\Gamma_{\mathrm{fit}} = 2.14 \pm 0.04_{\mathrm{stat}} \pm 0.24_{\mathrm{syst}}$. This fit result, though not completely accurate, since the data sets of the regions are correlated because the *off* regions used for background estimation partially overlap[15], is fully compatible with the index of the whole SNR ($\Gamma_{\mathrm{SNR}} = 2.14 \pm 0.05_{\mathrm{stat}} \pm 0.24_{\mathrm{syst}}$), showing that the index remains the same within the whole SNR. Region 2 shows a slightly harder spectrum ($\Gamma_2 = 1.86 \pm 0.15_{\mathrm{stat}} \pm 0.21_{\mathrm{syst}}$) but the index is still compatible with that of the whole SNR at 1.8σ. All indices are affected by the systematic error of 0.2 explained in section 4.4.2.

A similar measurement of the spectral morphology has been performed for X-ray data from *ASCA*. The *ASCA* spectral analysis results have been provided by Junko S. Hiraga. The analysis has been performed on the data recorded in a series of 7 pointings with the GIS camera, which is sensitive in the 0.7 keV to 10 keV energy band, in order to cover most of the SNR (see Tsunemi et al. [2000] for more details on the pointing strategy). The *ASCA* pointings are shown in red in figure 4.8. The *ASCA* spectral indices are shown in table 4.9b.

[14] The results from this plot have been crosschecked by Nukri Komin with the `Model Analysis` of the `Paris Analysis` chain. A preliminary version of this study has been published in Paz Arribas et al. [2011].

[15] In order to estimate the correlation and its influence in the measurement, a simulation involving multiple use of *off* events would be necessary; this is beyond the scope of this work.

(a) H.E.S.S. spectral index

region	index
0	$2.11 \pm 0.08_{\mathrm{stat}} \pm 0.23_{\mathrm{syst}}$
1	$2.26 \pm 0.14_{\mathrm{stat}} \pm 0.25_{\mathrm{syst}}$
2	$1.86 \pm 0.15_{\mathrm{stat}} \pm 0.21_{\mathrm{syst}}$
3	$2.26 \pm 0.12_{\mathrm{stat}} \pm 0.25_{\mathrm{syst}}$
4	$2.20 \pm 0.14_{\mathrm{stat}} \pm 0.24_{\mathrm{syst}}$
5	$2.16 \pm 0.09_{\mathrm{stat}} \pm 0.24_{\mathrm{syst}}$
6	$2.11 \pm 0.11_{\mathrm{stat}} \pm 0.23_{\mathrm{syst}}$
fit	$2.14 \pm 0.04_{\mathrm{stat}} \pm 0.24_{\mathrm{syst}}$
whole SNR	$2.14 \pm 0.05_{\mathrm{stat}} \pm 0.24_{\mathrm{syst}}$

(b) *ASCA* spectral index

region	index
N1	$2.79 - 0.09_{\mathrm{stat}} + 0.09_{\mathrm{stat}}$
N2	$2.72 - 0.29_{\mathrm{stat}} + 0.32_{\mathrm{stat}}$
N3	$2.45 - 0.13_{\mathrm{stat}} + 0.13_{\mathrm{stat}}$
N4	$2.60 - 0.11_{\mathrm{stat}} + 0.12_{\mathrm{stat}}$
N5	$2.27 - 0.25_{\mathrm{stat}} + 0.56_{\mathrm{stat}}$
N6	$2.70 - 0.14_{\mathrm{stat}} + 0.16_{\mathrm{stat}}$
N7	$2.72 - 0.17_{\mathrm{stat}} + 0.15_{\mathrm{stat}}$
fit	$2.66 \pm 0.05_{\mathrm{stat}}$
whole SNR	$2.65 \pm 0.15_{\mathrm{stat}}$

Table 4.9.: Spectral morphology of the remnant. Left: the spectral index of each of the H.E.S.S. regions denoted in white in figure 4.8 are presented. The spectral index of the whole SNR and the weighted average of the indices of the 7 regions are also indicated. The errors represent 1σ statistical and systematic errors. Right: the spectral index of each of the *ASCA* regions denoted in red in figure 4.8 are presented. The spectral index of the whole SNR and the weighted average of the indices of the 7 regions are also indicated. The errors represent 90% confidence level (C.L.) statistical errors. The values for each region have been provided by Junko S. Hiraga. The value for the whole SNR is the value used in Aharonian et al. [2007].

The spectral fit for each region has been performed using 3 components: 2 thermal components for the Vela and Vela Junior SNRs respectively and one component in the form of a power-law for the non-thermal emission of Vela Junior. The analysis of the central region N2 excludes the overlapping areas with the surrounding regions and the region around the point source seen by *ASCA* close to the center of the remnant.

The indices of the non-thermal component of the spectra derived for the different pointings of the *ASCA* satellite, together with the H.E.S.S. spectral indices, are shown as function of the azimuthal angle in figure 4.9b[16]. As for the H.E.S.S. data, the weighted average value is fitted to the *ASCA* spectral indices[17], yielding a value of $2.66 \pm 0.05_{\mathrm{stat}}$ (error at the 90% C.L.). The χ^2 test ($\chi^2/\mathrm{NDF} = 14.9/6$, p-value of 0.0213) for the *ASCA* data shows that the X-ray indices are still marginally compatible with a constant, hence no significant spectral variation is measured across the SNR.

In the case of the X-rays, the index close to the region 2 from the H.E.S.S. analysis is also slightly harder than for the rest of the remnant.

[16]The errors on this plot are given at the 90% C.L., because the *ASCA* results were provided only at that C.L.

[17]The fit was performed using errors converted to 1σ C.L. in order to have a correct value of the fit probability. Afterward, the fit error was converted back to 90% C.L. for consistency with the coverage with which the data was originally provided.

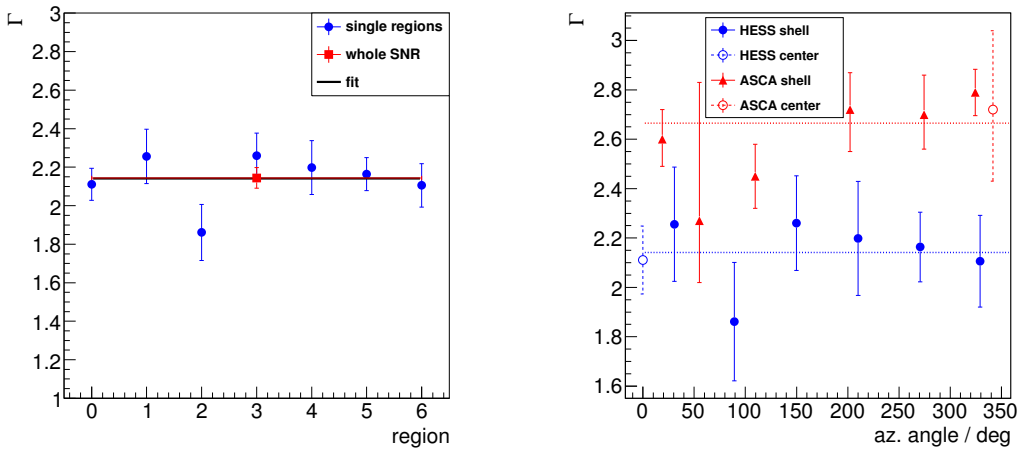

(a) H.E.S.S. spectral index

(b) H.E.S.S. and *ASCA* spectral index

Figure 4.9.: Spectral morphology of the remnant. Left: the spectral index of each of the H.E.S.S. regions denoted in white in figure 4.8 (blue points) are presented. The red point represents the equivalent measurement for the whole SNR. The black line represents the weighted average of the blue points. The error bars represent 1σ statistical errors. Right: the spectral indices for the H.E.S.S. (blue points) and *ASCA* (red points) regions shown in figure 4.8 are presented as a function of the azimuthal angle of the centroid of each region. The error bars are statistical errors given at the 90% confidence level (C.L.). The horizontal lines represent the weighted average values fitted to the H.E.S.S. and *ASCA* points. The definition of the azimuthal angle is the same as for the azimuthal profile shown in figure 4.7.

4.8. Upper limit on the VHE emission from the PWN associated with PSR J0855−4644

The existence of the X-ray PWN associated to PSR J0855−4644 (Acero et al. [2013b]) and the enhancement seen at its direction in the azimuthal profile in figure 4.7 suggest that some of the emission seen around the pulsar could be due to the PWN.

According to the pulsar population study published in Carrigan et al. [2008], pulsars with $\dot{E}/d^2 > 10^{34}\,\mathrm{erg\,s^{-1}\,kpc^{-2}}$ are very likely detected as PWNe in γ-rays by H.E.S.S. In the case of PSR J0855−4644, using the values from table 4.2, $\dot{E}/d^2 = 2.0 \times 10^{36}\,\mathrm{erg\,s^{-1}\,kpc^{-2}}$, which corresponds to a detection probability in γ-rays of more than 70%, according to the mentioned population study.

Since the pulsar emission overlaps with the emission of the shell of RX J0852.0−4622 in γ-rays, it is not possible to disentangle, with the current angular resolution, the possible

PWN contribution from the shell of the SNR. In addition, the 2D morphological fit of the region using several components is complicated, since the emission of the shell is not uniform in this area, as shown by the azimuthal profile in figure 4.7. This kind of fit has been tested with several combinations of source morphology types (i.e. shell and pointlike, or shell and Gaussian, or shell and 2 Gaussians) and yields no meaningful result. For this reason, flux measurements of the TeV emission from the PWN associated to PSR J0855−4644 are not possible and only upper limits can be derived. In order to do this, an assumption about the possible morphology of the PWN associated to PSR J0855−4644 in the TeV domain has to be adopted.

PWNe tend to be much more extended in the TeV γ-ray domain than in the X-ray regime, since γ-rays are tracers of lower energy particles, which have a much larger cooling time and hence have more time to diffuse further away (i.e. Mattana et al. [2009]). For pulsars older than $\sim$10 kyr the size of the TeV PWN can be up to $100-1000$ times larger than the size of the X-ray PWN (see Kargaltsev and Pavlov [2010]) due to particle propagation up to large distances from the pulsar through diffusion/advection processes and/or proper motion of the pulsar itself. The extension of the PWN in X-ray data is 150 arcsec (see Acero et al. [2013b])[18]. In this work three possible morphologies are adopted for the possible TeV emission:

Region A : pointlike emission situated at the position of PSR J0855−4644. This region is characterized by the extension of the H.E.S.S. PSF, which is taken into account by a cut on θ^2 (i.e. square of the *on* region radius). This cut is $0.0125\,\mathrm{deg}^2$ in the case of standard cuts.

Region B : extended encompassing the H.E.S.S. 5σ contour around PSR J0855−4644. A circular region centered on R.A: 133.85° Dec: -46.65° with an extension of 0.3° is a good approximation to the 5σ contour.

Region C : extended encompassing the H.E.S.S. 3σ contour around PSR J0855−4644. A circular region centered on R.A: 133.50° Dec: -46.75° with an extension of 0.6° is a good approximation to the 3σ contour.

The regions are shown in figure 4.10. The γ-ray fluxes from each of these regions can be interpreted as upper limits on the TeV flux of the PWN associated to PSR J0855−4644.

The data set for this analysis is selected according to the following criteria:

- Only data taken under favorable weather conditions and stable detector performance are selected.
- Only data taken at pointings up to 2.5° around PSR J0855−4644 are considered.
- Only data taken when all four telescopes were active are used.

[18]The extension of the X-ray PWN is approximately of the same size as the marker used for the position of PSR J0855−4644 in figures 4.5, 4.7 and 4.10.

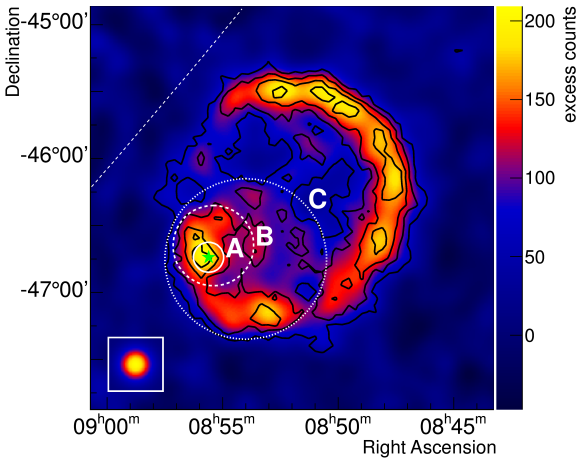

Figure 4.10.: Smoothed exposure corrected excess map from figure 4.4 together with the regions used for the spectral analysis of the possible TeV PWN associated to PSR J0855−4644. The H.E.S.S. significance contours at 3, 5, 7 and 9σ are shown in black. The boundaries of the regions around the position of PSR J0855−4644 (marked by the green star) used for the flux upper limit determinations are marked with white lines: solid for region A, dashed for region B and dotted for region C.

After data quality selection, 83 runs remain with a livetime of 35.4 h. The actual run list can be found in the appendix in table C.3.

Using regions described above as *on* regions, the spectral analysis of the possible TeV PWN associated to PSR J0855−4644 is performed using the standard γ/h separation cut selection and the reflected region background method used for the spectral morphology analysis in section 4.7.

Since the exclusion regions for RX J0852.0−4622 and Vela X are quite large, it is not possible to find suitable *off* regions for some of the runs when using the reflected region background method, and hence, not all runs can be used for the spectral analysis. Table 4.10 summarizes the event statistics for each region.

The data sets presented in table 4.10 are used to derive spectra with the forward-folding technique described in section 4.4.3. Analogously as for the spectral morphology analysis in section 4.7, the spectra are derived using a power-law model with reference energy $E_0 = 1\,\mathrm{TeV}$ in the energy range from 0.5 TeV to 7.0 TeV in order to avoid possible threshold and curvature effects in the spectra. The resulting spectra are then integrated in the mentioned energy range in order to yield the integral fluxes that should be interpreted as upper limits of the TeV flux of the PWN associated to PSR J0855−4644. These flux upper limits correspond to 2%, 7% and 27% of the flux of the whole SNR in

region	$\langle\theta_{\mathrm{zen}}\rangle$	$\langle\theta_{\mathrm{az}}\rangle$	$\langle\theta_{\mathrm{off}}\rangle$	t / h	N_{on}	N_{off}	α	excess	significance
A	31°	197°	1.3°	34.2	1760	26418	0.056	275	6.8σ
B	31°	197°	1.2°	34.2	12042	62348	0.17	1329	11.6σ
C	31°	199°	1.2°	32.9	44264	87343	0.46	4270	17.3σ

Table 4.10.: Statistics used in the PWN analysis for each region: region name, mean zenith and azimuth angles of the observations ($\langle\theta_{\mathrm{zen}}\rangle$ and $\langle\theta_{\mathrm{az}}\rangle$ respectively), mean offset angle $\langle\theta_{\mathrm{off}}\rangle$, livetime t, number of events in the signal (*on*) region N_{on}, number of events in the background (*off*) region N_{off}, exposure normalization (ratio of *on* to *off* exposures) α, number of excess counts in the *on* region and significance of the signal in the *on* region in number of Gaussian standard deviations σ.

the same energy range, for regions A, B and C correspondingly. In addition the energy fluxes in the extrapolated energy range from 1.0 TeV to 30.0 TeV are also calculated by integrating in energy. The values are shown in table 4.11.

region	$F^{\mathrm{UL}}_{0.5-7}/10^{-12}\,\mathrm{cm}^{-2}\,\mathrm{s}^{-1}$	$F^{\mathrm{E,UL}}_{1-30}/10^{-12}\,\mathrm{erg}\,\mathrm{cm}^{-2}\,\mathrm{s}^{-1}$
A	$1.23 \pm 0.22_{\mathrm{stat}} \pm 0.31_{\mathrm{syst}}$	$2.5 \pm 0.8_{\mathrm{stat}} \pm 0.6_{\mathrm{syst}}$
B	$3.73 \pm 0.42_{\mathrm{stat}} \pm 0.93_{\mathrm{syst}}$	$9.6 \pm 1.7_{\mathrm{stat}} \pm 2.4_{\mathrm{syst}}$
C	$14.7 \pm 0.9_{\mathrm{stat}} \pm 3.7_{\mathrm{syst}}$	$32 \pm 3_{\mathrm{stat}} \pm 8_{\mathrm{syst}}$

Table 4.11.: Flux upper limits for the 0.5 TeV to 7.0 TeV energy range $F^{\mathrm{UL}}_{0.5-7}$ and energy flux upper limits for the energy range extrapolated to 1.0 TeV to 30.0 TeV $F^{\mathrm{E,UL}}_{1-30}$ on the TeV emission of the PWN associated to PSR J0855−4644, depending on its extension (see the regions defined in figure 4.8). The values given under $F^{\mathrm{UL}}_{0.5-7}$ ($F^{\mathrm{E,UL}}_{1-30}$) are the fluxes (extrapolated energy fluxes) of the corresponding regions with their 1σ statistical and systematic uncertainties and should be read as upper limits to the VHE emission of the PWN, since the contribution from the SNR cannot be easily subtracted.

4.9. Discussion

Regarding the spectral morphology of RX J0852.0−4622, a constant index is found across the whole SNR in the energy range from 0.5 TeV to 7.0 TeV, compatible with the average value of $2.14 \pm 0.04_{\mathrm{stat}} \pm 0.24_{\mathrm{syst}}$. A similar trend is observed for the *ASCA* X-ray measurement, for which the average index is $2.66 \pm 0.05_{\mathrm{stat}}$ at the 90% C.L. This homogeneous spectral morphology suggests that the particle acceleration and subsequent γ-ray emission processes are similar across the whole SNR. This indicates similar SNR shock properties and properties of the ambient medium in which the shock was formed and is expanding.

Comparing the average spectral indices for γ-rays and X-rays, the values differ by

0.52 ± 0.09 at the 90% C.L. In the framework of a very simple leptonic model, in which the same population of electrons with a power-law energy distribution in a homogeneous magnetic field would be responsible for both the synchrotron and the inverse Compton emissions, the same photon index is expected for both components. The difference observed here could be explained by the fact that the measurements are performed at the cut-off region for both the X-ray and the γ-ray spectra.

Recent X-ray results by Kishishita et al. [2013] using *XMM-Newton* observations of the northwestern rim of RX J0852.0−4622 have revealed a softening of the spectrum from the rim towards the interior of the remnant (more details in section 4.1.5). Due to the larger PSF of H.E.S.S. and the lower statistics, such a detailed study of the change of the spectrum in the rim is not possible in the VHE band.

As for the case of RX J1713.7−3946 (see Abdo et al. [2011]) more detailed spectra of the whole SNR in γ-rays with H.E.S.S. and *Fermi* would be very useful for revealing the nature of the emission.

Regarding the spatial morphology of the remnant, the upper limits on the energy flux of a possible VHE emission from the PWN associated to PSR J0855−4644are between 3 and $30 \times 10^{-12}\,\mathrm{erg\,cm^{-2}\,s^{-1}}$, depending on the PWN extension in the VHE regime (see table 4.11). The flux upper limits represent 2%, 7% and 27% of the flux of the whole SNR in the same energy range, for regions A, B and C correspondingly. The fluxes for regions A and B ($\lesssim 7\%$) are well covered by the flux systematic error of 25% determined for the RX J0852.0−4622 region. In the case of region C, the flux upper limit is slightly larger than the systematic error. However, region C covers a large fraction of the SNR shell and its interior, so a large fraction of the flux is expected to be due to RX J0852.0−4622, ergo the fraction corresponding to the PWN should be smaller than the systematic error.

Mattana et al. [2009] derived phenomenological laws relating pulsar properties (spin-down luminosity $\dot{E}$ and characteristic age τ_c) to the X-ray and γ-ray emissions of PWNe. These laws are based on the correlation found between the γ-ray and X-ray luminosities of old PWNe ($\tau_c > 1\,\mathrm{kyr}$). Such PWNe are believed to have a constant γ-ray luminosity, but a X-ray luminosity decaying with time since they are older than the decay time of the X-rays injected by the pulsar ($t_{\mathrm{dec}\,X} = \mathcal{O}(1 - 10\,\mathrm{kyr})$). However, these laws are not applicable to PSR J0855−4644 due to its large τ_c (140 kyr). At this age, the γ-ray luminosity is no longer constant, but decaying with time because the age exceeds the decay time of the γ-rays injected by the pulsar ($t_{\mathrm{dec}\,\gamma} = \mathcal{O}(10 - 100\,\mathrm{kyr})$).

By using the equations 4 and 6 from Mattana et al. [2009] to predict the γ-ray energy flux of the PWN, using the X-ray energy flux between 2 keV and 10 keV of $0.88 \times 10^{-12}\,\mathrm{erg\,cm^{-2}\,s^{-1}}$ from Acero et al. [2013b], the prediction for the γ-ray energy flux in the 1 TeV to 30 TeV range is $2.1 \times 10^{-10}\,\mathrm{erg\,cm^{-2}\,s^{-1}}$ and $1.9 \times 10^{-9}\,\mathrm{erg\,cm^{-2}\,s^{-1}}$ (if using equations 4 and 6 respectively), several orders of magnitude larger than the upper limits derived in this work.

In addition, the energy fluxes derived using Mattana et al. [2009] indicate an energy flux at least 2.6 times larger than the energy flux of the Crab nebula in the same energy range. Since the VHE flux of the entire RX J0852.0−4622 SNR is roughly of the same

order as the VHE flux of the Crab nebula (Aharonian et al. [2005]), this means that the flux of the VHE emission of the PWN associated to PSR J0855−4644 should be much larger than the flux observed in the whole region surrounding the pulsar, which is not possible. Moreover, such a large flux is in contradiction with the upper limits derived in this work.

The figure 1 (B) of Kargaltsev and Pavlov [2010] shows that the ratio of the γ-ray to X-ray luminosities remains constant for pulsars with very large age ($\log(\tau_c/\mathrm{yr}) > 4.5$) instead of growing with time as for younger pulsars. PSR J0855−4644 falls into the first category, therefore, the γ-ray energy flux predicted by Mattana et al. [2009] is too large.

5. Spectral analysis of RX J0852.0−4622 with H.E.S.S. and outlook with CTA

The increased data set on RX J0852.0−4622 allows for a deeper study of the spectral properties of this source (more details in section 4.1.7). The results of the spectral analysis of the whole SNR are presented in this chapter. First, the strategy for the spectral analysis using different analysis chains is presented in section 5.1. The H.E.S.S. data sets used for the spectral analysis of RX J0852.0−4622 are listed in appendix C. The process used for the derivation of the spectrum for a specific analysis chain is presented in section 5.2. The spectral results for all analysis chains are presented in appendix D. The final spectrum used for the discussion of the results is presented in section 5.3. A comparison of the spectral results derived in this work to the results of previous H.E.S.S. publications is presented in section 5.4. A description of the muon efficiency correction and its effects on the spectral reconstruction is presented in appendix E. The H.E.S.S. spectrum is compared to the *Fermi* measurement in section 5.5. The H.E.S.S. spectral results are discussed in the framework of leptonic and hadronic emission models in section 5.6. Finally, the chapter concludes with an overview of the capabilities of CTA with respect to the detection of spectral energy cut-offs, using RX J0852.0−4622 as a test case in section 5.7.

5.1. Spectral analysis strategy

For the results in this chapter, different analysis chains available within the H.E.S.S. collaboration are used. The motivation for this is the large extension of the source (1°in radius), compared to the typical sources analyzed by H.E.S.S. (mostly $< 0.2°$ in radius, many are point-like). This enforces a large *on* region for spectrum extraction that integrates any systematic effect on flux measurements across a large area. For this reason three analyses are used in order to compare the results and eventually quantify the systematic error from the differences in the obtained results.

The different analysis chains are described in section 4.4.5 and table 4.3. In order to make the comparison as homogeneous as possible, all analyses share the same parameters in terms of run list, exclusion regions, analysis method, selection cuts, background model and spectrum method, as shown in table 5.1.

Each of the analysis chains is used to derive a spectrum, which will be used for deciding upon the final spectrum of the remnant. For the purpose of readability, further discussions about spectrum derivation in this and the subsequent section 5.2 will concentrate on the so called `HAP-HD` analysis chain results. The results of all analysis chains are

	HAP-HD	HAP-FR	Paris
software version	**hap-12-03**	**hap-11-02**	**paris-0-8-24**
DST production version	**production-12-03**	**hap1208a**	**Prod26**
base software	SASH	SASH	SASH
framework (interface)	HAP	HAP	Paris Analysis
run list			
reconstruction method	Hillas	Hillas	Hillas
on and exclusion regions			
selection cuts	std full encl.	std full encl.	std full encl.
bg method	reflected region	reflected region	reflected region
spectrum method	forward-folding	forward-folding	forward-folding

Table 5.1.: Analysis chains used for the spectral analysis of the whole RX J0852.0−4622 SNR. Shadowed areas denote common (overlapping) features or code between the different chains. The DST production version of HAP-FR has a different tag than that of Paris Analysis but uses the detector calibration from the Paris Analysis chain, therefore they appear as shaded in the table.

compared in appendix D. The HAP-HD analysis chain has been selected as example for the spectrum derivation, for being the most familiar one to the author. Moreover, this analysis chain has been used extensively for systematic checks in the spectral analysis presented in this work.

The data set for this analysis is selected according to the following criteria:

- Only data taken under favorable weather conditions and stable detector performance are selected.
- Only data taken at pointings from 1.0° up to 1.25° around the center of the SNR are considered.
- Only data taken when all four telescopes were active are used.
- Only data tagged as good in both calibrations (HD and Paris) are accepted.

After data quality selection, 60 runs remain with a livetime of 25.5 h. The actual run list can be found in the appendix in table C.4.

Using the same *on* and exclusion regions as for the spatial morphology studies in section 4.6, the spectral analysis is performed using the standard γ-hadron separation cut selection and the reflected region background method used for the spectral morphology analysis from section 4.7.

Similar to figure 4.3, a ring background method is run on the 60 runs selected for the spectrum analysis, in order to check if the exclusion regions are sufficient and if the background regions are not contaminated by signal.

The left panel of figure 5.1 shows the significance map using a 0.1° correlation radius of the region with 3° radius around RX J0852.0−4622.

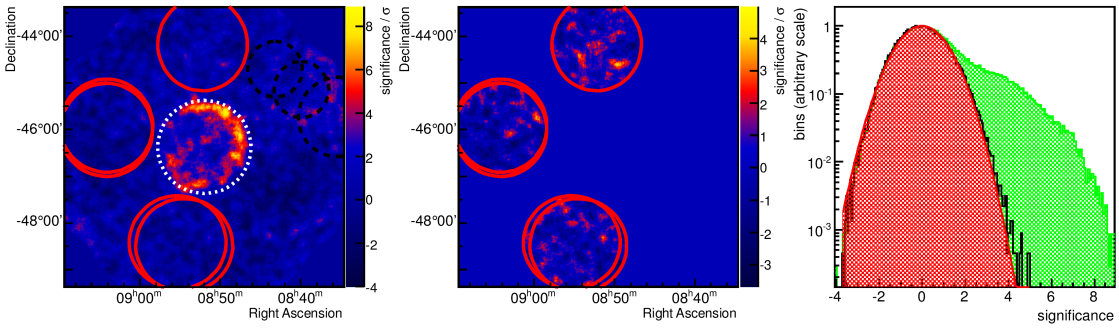

Figure 5.1.: Significance maps and distributions of the data set used for the spectral analysis. The maps and distributions have been produced using the ring background method. The red solid circles on the maps mark the *off* regions defined by the reflected region background method, the white dashed circle indicates the *on* region and the black dashed circles the exclusion regions. Left: significance map using a 0.1° correlation radius of the region with 3° radius around RX J0852.0−4622. Center: residual significance map of the map on the left panel, inside the *off* regions defined by the reflected region background method. Right: significance distribution for the significance map on the left panel after excluding the Vela X regions (green histogram and area), significance distribution for the residual map on the center panel (black histogram) and fit of the residual significance distribution to a Gaussian distribution (red curve and area).

The central panel of figure 5.1 shows the residuals map for the *off* regions. No significant structure is visible.

The right panel of figure 5.1 shows the significance distribution for the whole skymap without the three Vela X exclusion regions in green, the distribution for the *off* regions in black and a fit of the latter to a Gaussian distribution in red. The fit shows, as expected, that the background distribution can be well described by a normal distribution, meaning that the *off* regions selected for the analysis correctly describe the background.

Due to the large size of the *on* region (1.0° in radius) and the presence of Vela X, no *off* regions can be found west of RX J0852.0−4622. This makes all observation runs pointed towards this side unusable for spectrum calculations. As a result, from the 60 runs selected for this analysis, only 42 are used, with a total livetime of 17.7 h. Table 5.2 summarizes the event statistics used in the analysis performed with the reflected region background method. With 19.1σ, the signal in the *on* region is highly significant. A comparison with the other analysis chains, given in the appendix in table D.1, shows that all analysis chains show similar numbers, except for `Paris Analysis`, for which the statistics is a bit lower: `Paris Analysis` has 5000 excess events compared to 6500 from `HAP-FR` or 7000 from `HAP-HD`.

$\langle\theta_{\rm zen}\rangle$	$\langle\theta_{\rm az}\rangle$	$\langle\theta_{\rm off}\rangle$	t / h	$N_{\rm on}$	$N_{\rm off}$	α	excess	significance
32°	208°	1.2°	17.7	70691	63693	1	6998	19.1σ

Table 5.2.: Statistics used in the spectral analysis: mean zenith and azimuth angles of the observations ($\langle\theta_{\rm zen}\rangle$ and $\langle\theta_{\rm az}\rangle$ respectively), mean offset angle $\langle\theta_{\rm off}\rangle$, livetime t, number of events in the signal (*on*) region $N_{\rm on}$, number of events in the background (*off*) region $N_{\rm off}$, exposure normalization (ratio of *on* to *off* exposures) α, number of excess counts in the *on* region and significance of the signal in the *on* region in number of Gaussian standard deviations σ.

5.2. Spectral results

At TeV energies, the spectrum of the majority of the VHE sources can be characterized by a featureless power-law spectrum (more details in sections 1.1 and 4.7). Since the spectrum of RX J0852.0−4622 shows an indication of a curvature at high energies as already noticed in Aharonian et al. [2007][1], more complex models are tested as well: a curved power-law and a power-law with an exponential cut-off. The three models with their corresponding parameters are defined in table 5.3. In the case of the power-law with exponential cut-off, the parameter $\lambda = 1/E_{\rm cut}$ is used for the fit for having a more Gaussian-like error distribution than $E_{\rm cut}$.

model	formula	NFP	fit parameters
PL	$\mathrm{d}\Phi/\mathrm{d}E = \Phi_0(E/E_0)^{-\Gamma}$	2	Φ_0, Γ
CPL	$\mathrm{d}\Phi/\mathrm{d}E = \Phi_0(E/E_0)^{-\Gamma-\beta\log(E/E_0)}$	3	Φ_0, Γ, β
ECPL	$\mathrm{d}\Phi/\mathrm{d}E = \Phi_0(E/E_0)^{-\Gamma}\exp(-E/E_{\rm cut})$	3	Φ_0, Γ, $\lambda = 1/E_{\rm cut}$

Table 5.3.: Spectrum models. For each model the formula (differential flux), the number of free parameters (NFP) and the fit parameters are shown. The models are power-law (PL), curved power-law (CPL, also known as logarithmic parabola, LP) and power-law with exponential cut-off (ECPL).

The data set presented in table 5.2 is used to derive spectra with the forward-folding technique described in section 4.4.3 for all three models mentioned above. The spectral points together with the fitted models are displayed in figure 5.2. The spectral points have been rebinned in order to avoid large fluctuations due to low statistics in the excess between neighboring bins that introduce artificial structures in the spectrum. The spectra have been limited to the energies where the rebinned points had positive significance. This is the range between 0.35 TeV and 30 TeV[2]. The residuals shown in the figure illustrate that the power-law with exponential cut-off model has overall a smaller deviation from the flux points than the other models. This trend is also observed for all

[1] The analysis from the publication didn't show a significant curvature because of lack of statistics.

[2] Please notice the smaller minimum energy for the other 2 analysis chains ($\simeq 0.3$ TeV) in the appendix in table D.2, which is due to the better implementation of the forward-folding technique (more details in section 4.4.3).

analysis chains, the results of which are presented in the appendix in figures D.1, D.2 and D.3.

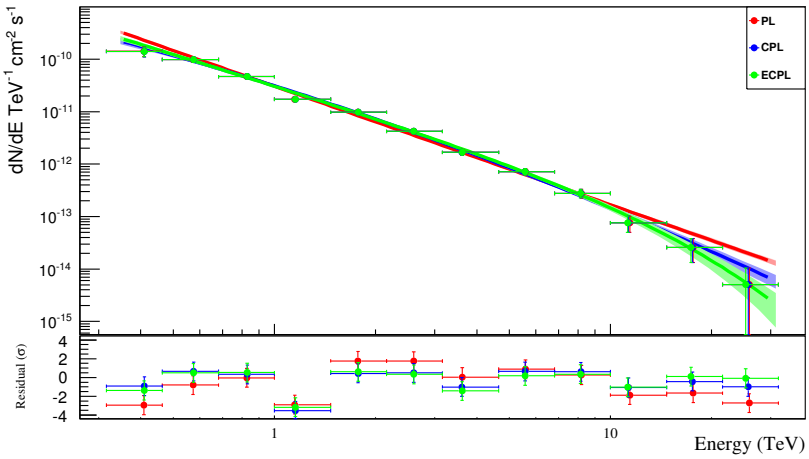

Figure 5.2.: Forward-folding spectra derived for the models listed in table 5.3. The upper pad shows the spectral points together with the spectral fit and its 1σ uncertainty band in the form of a shaded area. The lower pad shows the residuals of the spectral points relative to the fit.

The results of the fits are presented in table 5.4. The p-values from the table, calculated for each model from the difference between the derived flux points and the fitted model, are used as a measurement of the goodness of the fit. The p-values show that, with a goodness of fit of 18%, the power-law with exponential cut-off model shows the best agreement with the flux points. The fit parameters of all analysis chains are shown in the appendix in table D.3. All chains show similar parameters for each model with some differences. `HAP-HD` tends to have softer spectra than the rest: the comparison of the spectral indices obtained for `HAP-HD` for each model to that of the remaining chains shows a deviation ranging from $\sim 2\sigma$ to 2.5σ, depending on the model. `Paris Analysis` tends to have lower flux normalizations than the rest: in this case, the deviation ranges from $\sim 2.5\sigma$ to 3.5σ, depending on the model. There is some spread in the curvature parameters (β or E_{cut}) across all chains, but the relative errors are also a bit larger than for the other parameters: the spread is a 1.9σ effect for β and a 1.1σ effect for E_{cut}.

Since the data set used for this analysis slightly differs from the one used for the whole SNR in the spectral morphology analysis in section 4.7, the spectra of both data sets have been compared to each other and found to be in very good agreement with each other.

5.2.1. Statistical test for curvature in the spectrum

Looking at the residuals of the fits and the p-values interpreted as goodness of fit estimates, the power-law with exponential cut-off is the best model for describing the data.

model	Φ_0 / cm^{-2}s^{-1}TeV^{-1}	Γ	β	E_{cut} / TeV	p-value
PL	$(30.6 \pm 1.2)\,10^{-12}$	2.26 ± 0.04	n.a.	n.a.	1.3×10^{-4}
CPL	$(31.3 \pm 1.3)\,10^{-12}$	2.01 ± 0.08	0.14 ± 0.04	n.a.	0.11
ECPL	$(33.6 \pm 1.7)\,10^{-12}$	1.94 ± 0.09	n.a.	10.3 ± 3.2	0.18

Table 5.4.: Fit parameters for the spectrum for each of the models listed in table 5.3. In the case of the power-law spectrum with exponential cut-off, E_{cut} is shown instead of the fitted parameter $\lambda = 1/E_{\mathrm{cut}}$. The p-values of the fits are calculated from the difference between the derived flux points and the fitted model. The quoted errors represent 1σ statistical uncertainties. In all cases the reference energy E_0 is chosen to be 1 TeV.

Of course, a more complex model tends to fit the data more accurately due to the use of more parameters. In order to check if the extra parameters significantly improve the fit, a statistical test is needed.

In order to select the best suited model for describing the data a statistical test based on the likelihood ratio test described in section 4.4.4 is used.

In this case, the hypotheses to test are the different fit models listed in table 5.3, being H_0 the power-law model hypothesis and H_1 either the curved power-law or the power-law with exponential cut-off model hypothesis. By choosing $\beta = 0$ or $\lambda = 1/E_{\mathrm{cut}} = 0$ correspondingly[3], both models fall back into the power-law model, fulfilling the nested hypotheses requirement.

The results of this test are shown in table 5.5. The power-law model is rejected at the 3.8σ level by the curved power-law model, and with 4.3σ by the power-law with exponential cut-off model. The significances of rejection of the power-law model are even higher (above 5σ) for the alternative analysis chains, the results of which are presented in the appendix in table D.4. Since the power-law with exponential cut-off model shows the highest significance, and this is confirmed using the alternative analysis chains, in the following this model will be chosen as the model describing the data best.

model	$\log L$	NFP	p-value	significance
PL	−25.794	2	n.a.	n.a.
CPL	−18.381	3	99.988%	3.8σ
ECPL	−16.613	3	99.998%	4.3σ

Table 5.5.: Results of the likelihood ratio test for the hypothesis of the existence of a curvature in the spectrum. For each fitted model the logarithm of the likelihood L, the number of free parameters NFP, the probability of the test p and the equivalent significance in Gaussian standard deviations are shown. The test results refer to the comparison of the more complex models (i.e. CPL or ECPL) with respect to the simpler model (i.e. PL).

[3]Remember that for the power-law with exponential cut-off model λ is used for the fit instead of E_{cut}. Both, β and λ are allowed to take both positive and negative values for the fit.

5.3. Final spectrum derivation and studies of systematics

Figure 5.3a shows the best spectrum for each analysis chain, i.e. the spectrum derived using the power-law with exponential cut-off model. The fluxes have been multiplied by E^2 in order to show the differences between the spectra more clearly. Since the three spectra have been derived using the same data set, they are correlated and direct comparison can lead to wrong conclusions and should be done with care. However, it is worth mentioning the largest differences between the spectra. The figure shows that at high energies ($E > 2\,\mathrm{TeV}$) the three spectra have very similar results: the fitted curves are very close to each other. This is not the case at low energies ($E \lesssim 2\,\mathrm{TeV}$), where the curves diverge.

At this point, it is possible to derive the error contours of pairs of fit parameters for each analysis chain, using the probability density function of a pair of parameters and then computing the contours at a certain confidence level away from the fit parameters. Gaussian errors are assumed for the derivation of the probability density function. If $\tilde{\vec{x}}$ represents the fit parameters of a certain analysis chain and C its covariance matrix, then the probability that the actual system has the parameters between $\vec{x}$ and $\vec{x} + \mathrm{d}\vec{x}$ is given by $f(\vec{x})\,\mathrm{d}\vec{x}$ with the following probability density function

$$f(\vec{x}) = \frac{1}{(2\pi)^{N/2}\sqrt{|C|}} e^{-\frac{1}{2}(\vec{x}-\tilde{\vec{x}})^T C^{-1} (\vec{x}-\tilde{\vec{x}})}, \tag{5.1}$$

where N is the number of parameters in the fit (3 in this case). The graphical representation of the two-dimensional contours of a three-dimensional Gaussian probability density function is ellipses.

Figure 5.3b shows the error contours for pairs of fit parameters for each analysis chain. The contours have been derived at 1σ, 2σ and 3σ. In the figure it is clear that the error contours from `HAP-FR` (blue ellipses) tend to be in the middle between the `HAP-HD` and the `Paris Analysis` contours. They also tend to be slightly smaller, showing a smaller statistical uncertainty.

A priori, all three spectra are valid, and there is no reason for ruling out any of them. A criterion is needed to decide which is the best one and at the same time to quantify the dispersion among them. This is done by comparing to the weighted average of all three spectra, taking into account the correlation of the results.

Applying the method of the weighted average between different measurements i of a certain set of parameters $\vec{x}$, the best set of parameters $\bar{\vec{x}}$ describing the data and the dispersion around them can be calculated. If $\vec{x_i}$ represents the fit parameters of a certain analysis chain i and C_i its covariance matrix, then the parameters $\bar{\vec{x}}$ of the average spectrum can be calculated as

$$\bar{\vec{x}} = \left(\sum_i C_i^{-1} \right)^{-1} \sum_i C_i^{-1} \vec{x_i}. \tag{5.2}$$

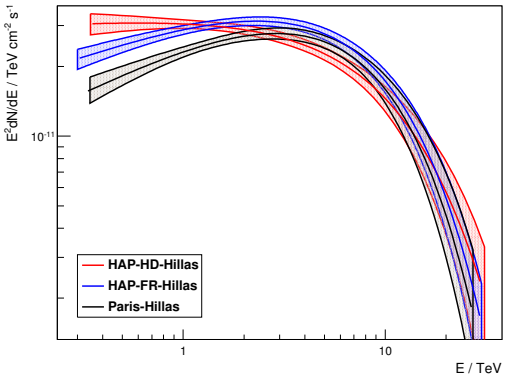

(a) Spectrum crosscheck

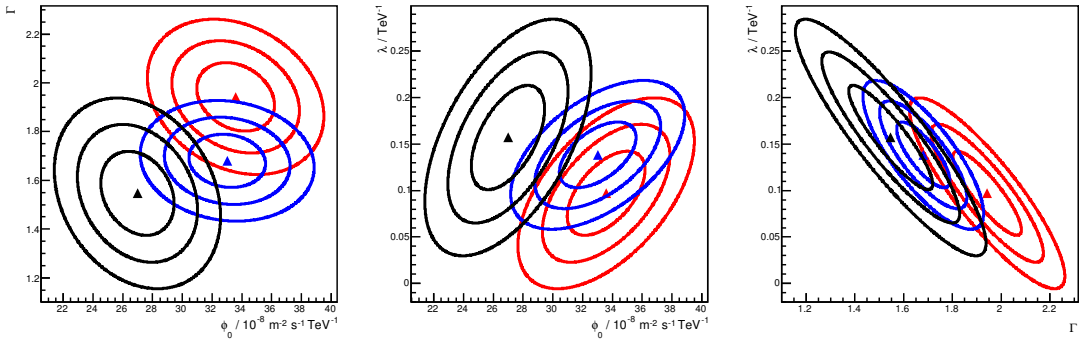

(b) Spectrum crosscheck fit error contours

Figure 5.3.: The top figure shows the spectral fit functions and 1σ statistical uncertainty bands for all three analysis chains, when selecting a power-law with exponential cut-off model to describe the data. The fluxes have been multiplied by E^2 in order to show the differences more clearly. The three bottom figures show the 1σ, 2σ and 3σ confidence level contours for the parameters of the spectra shown in the upper figure: left: index vs. normalization, middle: inverse of the cut-off energy vs. normalization and right: inverse of the cut-off energy vs. index. The legend in the top figure applies to the bottom figures. Since the three spectra have been derived using the same data set, they are correlated and direct comparison can lead to wrong conclusions and should be done with care.

The statistical covariance matrix of the average spectrum is then

$$C_{\mathrm{stat}}(\bar{\vec{x}}) = \left(\sum_i C_i^{-1} \right)^{-1} n, \tag{5.3}$$

where the factor n is a penalization factor for the fact that the averaged measurements

(spectra) are not statistically independent from each other. The exact correlation between each spectrum is very difficult to calculate. Since they all share the same data set, the conservative approach of full correlation will be assumed. In such a case $n = 3$ is the number of measurements (spectra) used for calculating the average[4]. The dispersion of the parameters of each measurement (spectrum) around the average ones can be used as systematic covariance matrix:

$$C_{\mathrm{syst}\,ij} = \Big(\langle (x_i - \bar{x}_i)(x_j - \bar{x}_j) \rangle \Big)_{ij} . \tag{5.4}$$

In analogy to figure 5.3a, figure 5.4a shows the best spectra of all analysis chains together with the average spectrum, the fit parameters of which have been derived using the equation 5.2). The green band represents the 1σ statistical uncertainty on the average spectrum, which is derived using the equation 5.3. It is clear that the average spectrum is very close to the `HAP-FR` spectrum, while the `HAP-HD` and the `Paris Analysis` spectra show correspondingly a higher and lower flux at low energies ($E \lesssim 2\,\mathrm{TeV}$). For clarity the systematic uncertainty band is not shown in this figure, but in figure 5.4b as a dark green band, together with the statistical uncertainty band. This comparison shows that the systematic error, derived using the equation 5.4, dominates at low energies ($E < 2\,\mathrm{TeV}$), while the statistical error dominates at high energies ($E > 10\,\mathrm{TeV}$).

In analogy to figure 5.3b, figure 5.4b shows the error contours for pairs of the fit parameters for each analysis chain together with the contours of the average spectrum (both statistical and systematic uncertainty). The values from the `HAP-FR` spectrum (blue solid ellipses) are very compatible to that of the average spectrum. The dispersion of the fit parameters of all three analysis chains is $\sim 10\%$ for the flux normalization, $\sim 10\%$ for the spectral index and $\sim 20\%$ for the cut-off energy.

In the following, the `HAP-FR` spectrum will be chosen as the best curve representing the spectrum of RX J0852.0−4622 for several reasons:

- It is none of the extreme ones.
- It is very close to the average spectrum.
- The forward-folding technique is fully implemented within the software framework and is well maintained and documented[5].

Its data points and parameters are thus used to represent the values of the final spectrum of the source and their errors as the statistical uncertainties of the final spectrum.

The event statistics used to derive the final spectrum are summarized in table 5.6. he values are slightly different from the values shown in table D.1 under the `HAP-FR` row, because of the energy range limitation imposed for the derivation of the spectrum.

[4] The average spectrum and the correlation factor will not have any direct effect on the final result, since the average spectrum itself will not be used, but only the dispersion of each measurement around the mean in order to estimate the systematic uncertainty.

[5] The software comes as an instrument independent root-based module called `START` (SpecTrAl Reconstruction Tools).

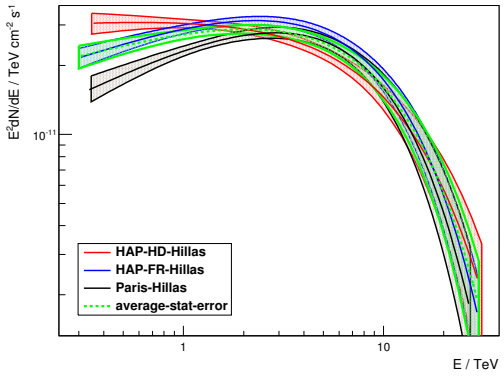

(a) Spectrum average

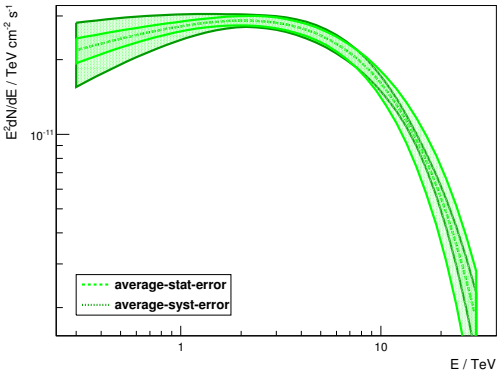

(b) Spectrum average stat and syst errors

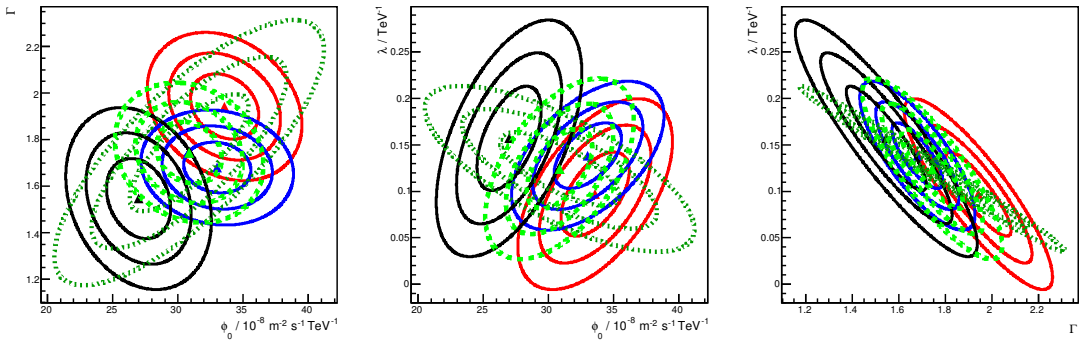

(c) Spectrum average fit error contours

Figure 5.4.: The top left figure shows the spectral fit functions and 1σ statistical uncertainty bands for all three analysis chains and the average spectrum, when selecting a power-law with exponential cut-off model to describe the data. The fluxes have been multiplied by E^2 in order to show the differences more clearly. The top right figure shows the 1σ statistical and systematic uncertainty bands of the average spectrum from the left figure. The three bottom figures show the 1σ, 2σ and 3σ confidence level contours for the parameters of the spectra shown in the two upper figures: left: index vs. normalization, middle: inverse of the cut-off energy vs. normalization and right: inverse of the cut-off energy vs. index. The legends in the top figures apply to the bottom figures. Since the three spectra used to compute the average have been derived using the same data set, they are correlated and direct comparison can lead to wrong conclusions and should be done with care. In this figure the error bands and ellipses of the spectra of the three analysis chains are not meant to be compared directly among each other but to that of the average spectrum.

$\langle\theta_{\rm zen}\rangle$	$\langle\theta_{\rm az}\rangle$	$\langle\theta_{\rm off}\rangle$	t / h	$N_{\rm on}$	$N_{\rm off}$	α	excess	significance	$E_{\rm th}$ / TeV
32°	208°	1.2°	17.4	40568	34065	1	6503	23.8σ	0.23

Table 5.6.: Statistics used in the derivation of the final spectrum: mean zenith and azimuth angles of the observations ($\langle\theta_{\rm zen}\rangle$ and $\langle\theta_{\rm az}\rangle$ respectively), mean offset angle $\langle\theta_{\rm off}\rangle$, livetime t, number of events in the signal (*on*) region $N_{\rm on}$, number of events in the background (*off*) region $N_{\rm off}$, exposure normalization (ratio of *on* to *off* exposures) α, number of excess counts in the *on* region, significance of the signal in the *on* region in number of Gaussian standard deviations σ and energy threshold of the analysis $E_{\rm th}$.

The overall systematic error in the flux calculations due to the use of different analysis chains is calculated in several steps:

1. Calculation of the average spectrum from the fit parameters of the spectra from all analysis chains weighted by their covariance matrices (equation 5.2).

2. Calculation of the systematic covariance matrix as the dispersion of the fit parameters of the spectra from all analysis chains around the average values (equation 5.4).

3. Calculation of the integral flux in the whole energy range (0.3 - 30 TeV) with its systematic error.

4. The systematic errors of flux measurements are calculated from the relative systematic error on the integral flux from the previous step, which is $\sim 15\%$[6].

Hence the total systematic error of flux measurements can be accounted for by adding 15% to the typical H.E.S.S. systematic error of 20% quoted in Aharonian et al. [2006a], which is mostly due to uncertainties in the modeling of the atmosphere in the Monte Carlo simulations. Under the supposition that both uncertainties are statistically independent, the addition of both effects in quadrature results in a total systematic error on the flux of RX J0852.0−4622 of 25%.

The systematic uncertainties in the final spectrum are calculated in a two step process:

1. The systematic error estimated from the differences related to the choice of the analysis chain: the uncertainties in flux points, fit parameters and integral fluxes are calculated using the covariance matrix calculated via the equation 5.4.

2. The typical H.E.S.S. systematic error quoted in Aharonian et al. [2006a]: 20% uncertainty on the flux measurements (flux points, spectrum normalization and integral fluxes) and 0.1 in the spectral index is added in quadrature to the uncertainties calculated in the step 1.

[6]The dispersion around the mean is energy dependent as shown by the dark green band in figure 5.4b: below 2 TeV the systematic error is almost 20%, while above 2 TeV is slightly above 5%.

The final spectrum with statistical and systematic uncertainties in the spectral points is shown in figure 5.5. The spectral points are given in table 5.7, the spectral parameters and the integral fluxes in table 5.8, and the results of the curvature test in table 5.9.

The final spectrum of RX J0852.0−4622 is described by a power-law with an exponential cut-off at 7.2 TeV, rejecting the power-law hypothesis with a significance of 5.8σ. Moreover, a more complicated model to investigate the shape of the cut-off (power-law with sub- or super-exponential cut-off[7]: $\mathrm{d}\Phi/\mathrm{d}E = \Phi_0(E/E_0)^{-\Gamma}\exp(-E/E_{\mathrm{cut}})^{\beta}$) has been tested. The result slightly favors the super-exponential cut-off over the sub-exponential one, but it does not represent a significant improvement compared to the simple exponential cut-off (only 1.4σ), so no further mention of it is made in the following.

At low energies, the uncertainty is dominated by systematics, and at high energies by statistics, the crossing point being at $E \sim 10\,\mathrm{TeV}$.

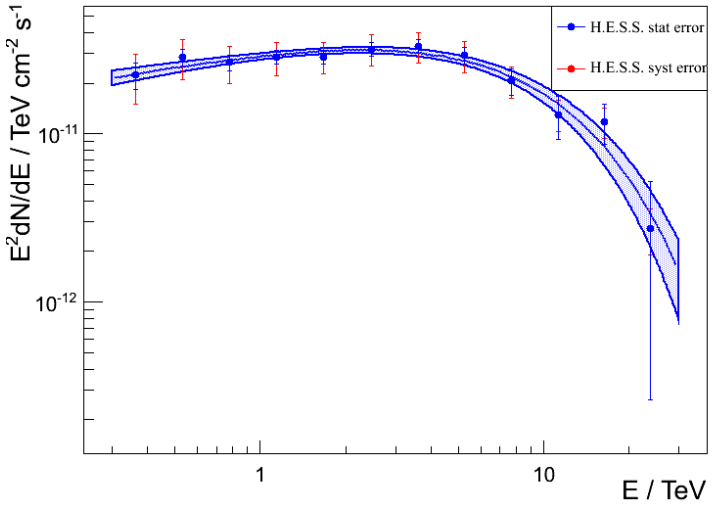

Figure 5.5.: Final spectrum with statistical and systematic errors. The spectral points with 1σ statistical (blue) and systematic (red) error bars are shown together with the spectral fit and its 1σ statistical uncertainty band in the form of a shaded area. The fluxes have been multiplied by E^2.

The final spectrum presented in this section will be referred to as *current spectrum* in the following, as opposed to other H.E.S.S. spectra from previous publications.

5.3.1. Systematic errors in spectral measurements

Based on the studies of systematics from this section, the following convention is adopted for the systematic error of further measurements of H.E.S.S. spectral parameters of the

[7]The name of the model depends on the value of the parameter β: it is called *sub-exponential* if $\beta < 1$ and *super-exponential* if $\beta > 1$.

E/ TeV	$\mathrm{d}\Phi/\mathrm{d}E/\,\mathrm{cm}^{-2}\mathrm{s}^{-1}\mathrm{TeV}^{-1}$	excess	significance
0.362	$(1.71 \pm 0.31_{\mathrm{stat}} \pm 0.57_{\mathrm{syst}})10^{-10}$	820	5.5σ
0.532	$(1.01 \pm 0.11_{\mathrm{stat}} \pm 0.27_{\mathrm{syst}})10^{-10}$	1300	9.1σ
0.780	$(4.37 \pm 0.46_{\mathrm{stat}} \pm 1.09_{\mathrm{syst}})10^{-11}$	1100	9.6σ
1.15	$(2.18 \pm 0.20_{\mathrm{stat}} \pm 0.49_{\mathrm{syst}})10^{-11}$	950	11σ
1.68	$(1.02 \pm 0.10_{\mathrm{stat}} \pm 0.22_{\mathrm{syst}})10^{-11}$	740	11σ
2.46	$(5.29 \pm 0.48_{\mathrm{stat}} \pm 0.11_{\mathrm{syst}})10^{-11}$	620	11σ
3.60	$(2.55 \pm 0.24_{\mathrm{stat}} \pm 0.53_{\mathrm{syst}})10^{-12}$	470	11σ
5.26	$(1.06 \pm 0.13_{\mathrm{stat}} \pm 0.22_{\mathrm{syst}})10^{-12}$	290	8.5σ
7.71	$(3.47 \pm 0.62_{\mathrm{stat}} \pm 0.75_{\mathrm{syst}})10^{-13}$	150	5.7σ
11.3	$(1.03 \pm 0.30_{\mathrm{stat}} \pm 0.22_{\mathrm{syst}})10^{-13}$	72	3.5σ
16.4	$(4.40 \pm 1.17_{\mathrm{stat}} \pm 0.90_{\mathrm{syst}})10^{-14}$	54	3.8σ
23.7	$(4.86 \pm 4.43_{\mathrm{stat}} \pm 1.49_{\mathrm{syst}})10^{-15}$	12	1.1σ

Table 5.7.: Final spectrum points: mean energy of the bin E, differential flux $\mathrm{d}\Phi/\mathrm{d}E$ with 1σ statistical and systematic uncertainties, excess and significance.

$$
\begin{aligned}
\boldsymbol{E_0} &= 1\,\mathrm{TeV} \\
\boldsymbol{\Phi_0} &= (33.0 \pm 1.7_{\mathrm{stat}} \pm 7.3_{\mathrm{syst}})\,10^{-12}\,\mathrm{cm}^{-2}\mathrm{s}^{-1}\mathrm{TeV}^{-1} \\
\boldsymbol{\Gamma} &= 1.68 \pm 0.07_{\mathrm{stat}} \pm 0.19_{\mathrm{syst}} \\
\boldsymbol{E_{\mathrm{cut}}} &= (7.2 \pm 1.2_{\mathrm{stat}} \pm 1.4_{\mathrm{syst}})\,\mathrm{TeV} \\
\boldsymbol{E_{\mathrm{min}}} &= 0.3\,\mathrm{TeV} \\
\boldsymbol{E_{\mathrm{max}}} &= 30\,\mathrm{TeV} \\
\boldsymbol{\Phi(E > 1\,\mathrm{TeV})} &= (27.2 \pm 1.1_{\mathrm{stat}} \pm 5.7_{\mathrm{syst}})\,10^{-12}\,\mathrm{cm}^{-2}\mathrm{s}^{-1} \\
\boldsymbol{\Phi(0.3\,\mathrm{TeV} < E < 30\,\mathrm{TeV})} &= (84.4 \pm 4.4_{\mathrm{stat}} \pm 21.1_{\mathrm{syst}})\,10^{-12}\,\mathrm{cm}^{-2}\mathrm{s}^{-1}
\end{aligned}
$$

Table 5.8.: Fit parameters and integral fluxes for the final spectrum of RX J0852.0−4622. The parameter E_{cut} is shown instead of the fitted parameter $\lambda = 1/E_{\mathrm{cut}}$. The reference energy for the fit E_0 is chosen to be 1 TeV. The integral fluxes above 1 TeV and in the fitted range (0.3 TeV, 30 TeV) represent respectively $\sim 130\%$ and $\sim 65\%$ of the flux of the Crab nebula in the same energy ranges. The quoted errors represent 1σ statistical and systematic uncertainties.

RX J0852.0−4622 region within this work:

- Systematic errors on flux measurements are given using a relative error of 25%, as derived for the integral flux of the whole SNR in the whole energy range.
- Systematic errors on spectral indices are given using the 10% relative error from the dispersion covariance matrix of the average, added in quadrature to the H.E.S.S. systematic error of 0.1 in the spectral index as in Aharonian et al. [2006a]. This yields a value of ~ 0.2 for spectral indices in the range from less than 1.5 to 2.2.
- Systematic errors on energy cut-offs are given using the 20% relative error from the dispersion covariance matrix of the average spectrum.

model	$\log L$	NFP	p-value	significance
PL	276921	2	n.a.	n.a.
ECPL	276938	3	99.9999994%	5.8σ

Table 5.9.: Results of the likelihood ratio test for the final spectrum for the hypothesis of the existence of a curvature in the spectrum. For each fitted model the logarithm of the likelihood L, the number of free parameters NFP, the probability of the test p and the equivalent significance in Gaussian standard deviations are shown. The test result refers to the comparison of the more complex model (i.e. ECPL) with respect to the simpler model (i.e. PL).

5.4. Comparison with the published spectra

When comparing the actual spectrum of RX J0852.0−4622 to the spectrum in the last H.E.S.S. publication (see Aharonian et al. [2007]), a difference in the flux of $\sim 70\%$ is visible, regardless of the model used for the reconstruction of the spectrum or the chain used for the analysis. This is well beyond the systematic error quoted in the paper (20%), and beyond the systematic error derived in this work (25%). Furthermore, the flux levels in the last publication (also known as Paper 2) are compatible with those of the first publication (see Aharonian et al. [2005], also known as Paper 1).

These discrepancies are illustrated in figure 5.6a, where the current spectrum is shown together with the spectra from the mentioned publications. The fluxes have been multiplied by E^2 in order to show the differences more clearly. The spectrum from Paper 1 lies slightly above that from Paper 2, but the two spectra are still compatible. In contrast, the current spectrum yields a larger flux.

The discrepancies can be accounted for if the published results were not corrected for mirror reflectivity degradation of the telescopes (the so called muon efficiency correction). Some evidence supporting this hypothesis is given in the appendix in section E.4.

A recent check (October 2013) of the muon efficiencies of the runs used for the analysis revealed that the correction can be important: the muon efficiency used in the MC data for reconstructing the events is ~ 0.11, whereas the muon efficiency measured from the data used for the analysis in Paper 1 is ~ 0.09. The result is an average muon correction[8] of ~ 1.16 for the data set used for the spectral analysis on Paper 1, which represents an energy displacement of the flux points of the spectrum of 16% towards higher energies. The same procedure applied to the analysis from Paper 2, yields a displacement of 35% in the flux points of the spectrum.

When correcting this effect in the flux points of the spectra from both publications using the simplified approach explained in the appendix in section E.1, the differences with respect to the final spectrum derived in this work are canceled, as illustrated in figure 5.6b. In order to apply the correction, the run-by-run average muon correction of the corresponding data set presented in table 5.10 is used as the factor for the energy

[8] Details on how the muon correction is performed and how it can affect the spectrum are given in the appendix sections E.1 to E.3.

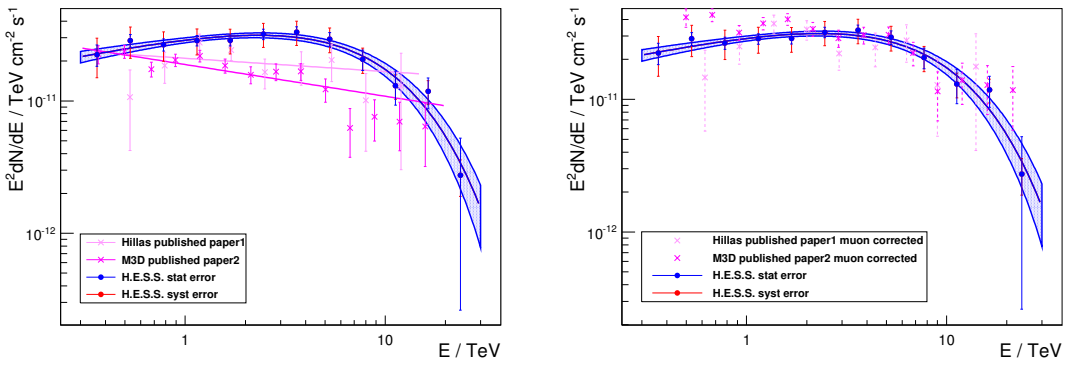

(a) Spectrum: final vs. published

(b) Spectrum: final vs. corrected

Figure 5.6.: The left figure shows the final spectrum derived in this work together with the two spectra from the H.E.S.S. publications Aharonian et al. [2005] labeled as "Paper 1" and Aharonian et al. [2007] labeled as "Paper 2"). The fluxes have been multiplied by E^2 in order to show the differences more clearly. The right figure shows the same final spectrum together with the spectral points from the two publications after correcting properly for the muon efficiency. All error bars and uncertainty bands represent 1σ statistical uncertainties.

shift of the flux points. The average muon correction for each data set is calculated in a two-step procedure. First, the muon correction of each run is estimated as the average of the muon correction of all telescopes in that run. In a second step, the total muon correction is calculated as the runwise average of the muon correction of each run in the corresponding data set run list. Of course, the muon correction of the current data set is already applied in the correct way (following the approach shown in the appendix in section E.2) to the data of the analysis of this work; in particular to the data used to derive the final spectrum. Therefore, no further correction is necessary in this case.

data set	$\langle \mu_{\mathrm{corr}} \rangle$
Paper 1	1.16
Paper 2	1.35
current work	1.42

Table 5.10.: Average muon corrections $\langle \mu_{\mathrm{corr}} \rangle$ derived for each of the indicated data sets using the `HD` calibration data base. The actual data sets used can be found in the appendix in tables C.4 and C.5. The actual run list of Paper 2 could not be recovered, so an approximate run list was used.

This result leads to the conclusion that the fluxes in the publications are underestimated and the current results show the correct flux level.

5.5. Comparison with the *Fermi* spectrum

The *Fermi* collaboration has reported the analysis of RX J0852.0−4622 (Tanaka et al. [2011]) using data from the *Fermi*-LAT. The spectrum covers the energy range from a few GeV up to a few hundred GeV and is well described by a power-law function with index $\Gamma = 1.85 \pm 0.06_{\mathrm{stat}}(^{+0.18}_{-0.19})_{\mathrm{syst}}$. The (systematic) uncertainties in the flux measurements are dominated by uncertainties in the effective area calibration of the instrument and the imperfect modeling of the Galactic diffuse emission, visible in GeV γ-rays.

The *Fermi* spectrum connects well to the H.E.S.S. points published in Aharonian et al. [2007] but a break in the spectral index is observed between the measurements of both experiments. Indeed, with an index of $2.24 \pm 0.04_{\mathrm{stat}} \pm 0.15_{\mathrm{syst}}$, the H.E.S.S. spectral index differs from the *Fermi* spectrum by 5.4σ (stat; or 1.6σ syst).

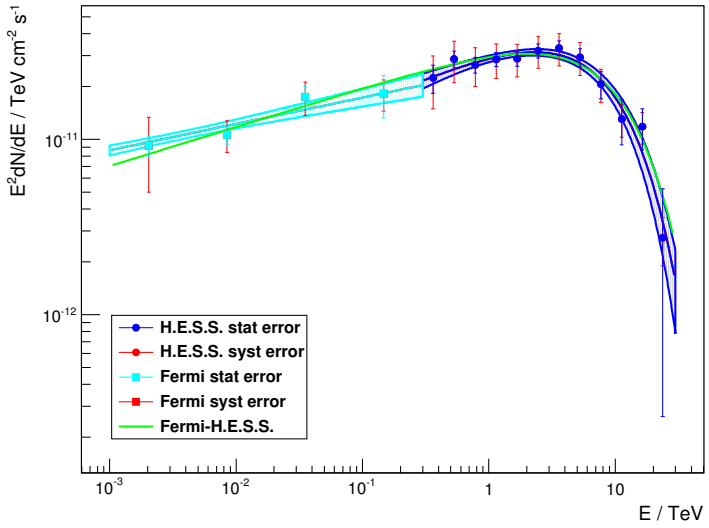

Figure 5.7.: Final spectrum together with the *Fermi* spectrum from Tanaka et al. [2011]. The spectral points with 1σ statistical (light and dark blue lines for *Fermi* and H.E.S.S. respectively) and systematic (red lines in both cases) error bars are shown together with the spectral fits and their 1σ statistical uncertainty bands in the form of shaded areas. In addition the simultaneous fit of the *Fermi* and H.E.S.S. spectral points is also shown. The fluxes have been multiplied by E^2.

The spectrum derived in this work, with its spectral index of $\Gamma = 1.68 \pm 0.07_{\mathrm{stat}} \pm 0.19_{\mathrm{syst}}$ connects very smoothly to the *Fermi* spectrum, as shown in figure 5.7. The difference observed in the spectral index is only 1.8σ (stat; or 0.64σ syst), and can be explained by the systematic errors of the experiments. It is therefore shown that no significant spectral break between the measurements of both experiments exists.

With a smooth connection between both measurements, a simultaneous fit of the

Fermi and H.E.S.S. data points is possible. This assumes that the GeV-TeV spectrum is the same everywhere in the SNR. This assumption is valid for the TeV emission, as shown by the lack of clear spectral variation as shown in section 4.7, and probably also for the GeV emission, since the spectral indices of the pointlike sources in the 2FGL Fermi catalog (Nolan et al. [2012]) associated with RX J0852.0−4622 (2FGL J0848.5−4535, 2FGL J0853.5−4711, 2FGL J0855.4−4625) are compatible with each other. A least-squares fit of the *Fermi*-H.E.S.S. points[9] using all 3 models listed in table 5.3 has been performed. The fit statistics for each model are shown in table 5.11. The χ^2 probabilities, which can be interpreted as measures of the goodness of fit, demonstrate that neither the power-law, nor the curved power-law model are able to describe the data well, whereas the power-law model with exponential cut-off does. It is therefore shown that, with a goodness of fit probability of 84.9%, the power-law model with exponential cut-off is the only valid model describing the broadband γ-ray emission from RX J0852.0−4622.

model	NFP	χ^2/NDF	p-value
PL	2	119/14	1.21×10^{-16}%
CPL	3	42.2/13	6.10×10^{-3}%
ECPL	3	8.01/13	84.3%

Table 5.11.: Results of the χ^2 test for the simultaneous *Fermi*-H.E.S.S. spectral fit. For each fitted model the number of free parameters NFP, the χ^2, the number of degrees of freedom NDF and the χ^2 probability p are shown.

The fit function for the power-law model with exponential cut-off is shown in figure 5.7 and the spectral parameters are presented in table 5.12. The systematic uncertainties in the parameters of the simultaneous fit have been determined by the variation of the fit parameters, when moving the *Fermi* points down (up) and the H.E.S.S. points up (down) by one standard deviation of their respective systematic uncertainties (this mainly tests the systematic uncertainty of the spectral index and the cut-off energy) and by moving all data points down or up simultaneously (which mainly tests the systematic uncertainty of the normalization).

Comparing the parameters of the simultaneous *Fermi*-H.E.S.S. fit (table 5.12) to those of the H.E.S.S. spectrum (table 5.8), the simultaneous fit shows a softer spectrum with a higher energy cut-off. The normalization remains similar. The simultaneous fit shows smaller statistical uncertainties for all parameters, a smaller systematic uncertainty for the spectral index, similar systematic uncertainty in the normalization, and a larger systematic uncertainty in the cut-off energy. Thus, the simultaneous fit is able to better determine the spectral index at the cost of a higher systematic uncertainty in the cut-off energy.

[9]The *Fermi* points are listed in the publication Tanaka et al. [2011]. Since the H.E.S.S. points are model dependent, each fit uses a specific set of points, according to the tested model. The model dependent H.E.S.S. points are given in the appendix in figure D.2; in the case of the power-law model with exponential cut-off, the measured spectral points are listed in table 5.7.

$\boldsymbol{E_0}$	=	$1\,\mathrm{TeV}$
$\boldsymbol{\Phi_0}$	=	$(32.8 \pm 1.5_{\mathrm{stat}} \pm 7.5_{\mathrm{syst}})\,10^{-12}\,\mathrm{cm}^{-2}\mathrm{s}^{-1}\mathrm{TeV}^{-1}$
$\boldsymbol{\Gamma}$	=	$1.777 \pm 0.018_{\mathrm{stat}} \pm 0.104_{\mathrm{syst}}$
$\boldsymbol{E_{\mathrm{cut}}}$	=	$(9.0 \pm 1.0_{\mathrm{stat}} \pm 2.1_{\mathrm{syst}})\,\mathrm{TeV}$
$\boldsymbol{E_{\mathrm{min}}}$	=	$0.001\,\mathrm{TeV}$
$\boldsymbol{E_{\mathrm{max}}}$	=	$30\,\mathrm{TeV}$

Table 5.12.: Parameters of the simultaneous *Fermi*-H.E.S.S. spectral fit of RX J0852.0−4622. The parameter E_{cut} is shown instead of the fitted parameter $\lambda = 1/E_{\mathrm{cut}}$. The quoted errors represent 1σ statistical and systematic uncertainties. The reference energy for the fit E_0 is chosen to be 1 TeV.

5.6. Interpretation

The total flux of RX J0852.0−4622 above 1 TeV is ~ 1.3 times that of the Crab nebula in the same energy range[10], making RX J0852.0−4622 the brightest steady source in the TeV sky. With $\sim 2^\circ$ extension it is also one of the largest TeV sources in the sky. In addition, it has been shown that no spectral break between the measurements of the H.E.S.S. and *Fermi* experiments exists. The combination of the *Fermi* and H.E.S.S. measurements rules out the curved power-law model, demonstrating that the power-law model with exponential cut-off is the only valid model describing the broadband γ-ray emission from RX J0852.0−4622.

Considering the new VHE spectral points derived in this work, together with other multi-wavelength (MWL) data, the nature of the emission of γ-rays can be interpreted within both a leptonic and a hadronic scenario[11], following respectively the calculations by Blumenthal and Gould [1970] and Kelner et al. [2006].

In either case, simple models with one particle population accounting for the emission of the entire region are used. This is motivated by the homogeneous spectral morphology presented in section 4.7. Such models address average properties of the SNR and its surrounding medium. Following the discussion from section 3.5, the spectrum of accelerated particles has the shape of a power-law with a certain maximum energy. In this section it will be assumed that the parent particle spectrum follows a power-law with an exponential cut-off. The intrinsic particle distribution is modeled as

$$N(E) = N_0 \left(\frac{E}{E_0}\right)^{-p} \mathrm{e}^{-E/E_{\mathrm{cut}}}, \tag{5.5}$$

[10] Crab nebula fluxes in this work are calculated using the spectrum from Meyer et al. [2010].

[11] The modeling results derived in this section are derived with a software based on the `modelisation` software package and the fitting classes prepared by Mathieu de Naurois and Nukri Komin. In addition, the results of the leptonic model have been independently crosschecked by Iurii Sushch, yielding similar results.

where $N(E)$ is the differential number of particles at a certain energy E, E_0 the reference energy, N_0 the normalization (number of particles at the reference energy E_0), p the spectral index and E_{cut} the cut-off energy. Due to the uncertainty in the distance measurement, it is convenient to express the normalization as

$$K = \frac{N_0}{4\pi d^2}, \tag{5.6}$$

with K the number of particles per unit area at the reference energy E_0 and d the distance to the object. The total energy in accelerated particles W is calculated as

$$W = \int_{E_{\mathrm{min}}}^{\infty} E\, N(E)\, \mathrm{d}E, \tag{5.7}$$

where E_{min} is the minimum integration energy chosen to be 100 MeV for electrons in the leptonic model and the proton rest mass for the hadronic model.

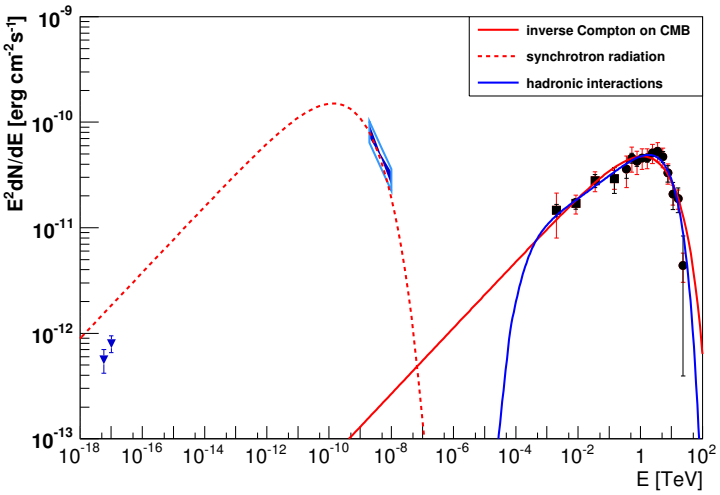

Figure 5.8.: Multi-wavelength spectral energy distribution (SED) with hadronic and leptonic models. The data are: Parkes radio data points from Duncan and Green [2000] (dark blue inverted triangles), *ASCA* X-ray spectral fit from Aharonian et al. [2007] (dark blue filled area for statistical uncertainty band and light blue hollow area for systematic uncertainty band), *Fermi* GeV γ-ray data points from Tanaka et al. [2011] (black/red squares for statistical/systematic uncertainties respectively) and H.E.S.S. TeV γ-ray data points from this work (black/red circles for statistical/systematic uncertainties respectively). The errors shown are the errors given in the corresponding references. The statistical uncertainty for the *ASCA* measurement is given at 90% C.L. The H.E.S.S. points are shown with 1σ statistical/systematic error bars.

parameter	hadronic	leptonic
$\log_{10}(K/\mathrm{TeV}^{-1}\mathrm{m}^{-2})$	$8.892 \pm 0.019_{\mathrm{stat}} \pm 0.116_{\mathrm{syst}}$	$6.89 \pm 0.04_{\mathrm{stat}} \pm 0.18_{\mathrm{syst}}$
p	$1.824 \pm 0.020_{\mathrm{stat}} \pm 0.112_{\mathrm{syst}}$	$2.37 \pm 0.08_{\mathrm{stat}} \pm 0.30_{\mathrm{syst}}$
$E_{\mathrm{cut}}/\mathrm{TeV}$	$77 \pm 10_{\mathrm{stat}} \pm 19_{\mathrm{syst}}$	$40 \pm 9_{\mathrm{stat}} \pm 15_{\mathrm{syst}}$
n/cm^{-3}	1 (fixed)	n.a.
$B/\mu\mathrm{G}$	n.a.	$5.106 \pm 0.020_{\mathrm{stat}} \pm 0.597_{\mathrm{syst}}$
W/erg	$(8.07 \pm 0.34_{\mathrm{stat}} \pm 2.12_{\mathrm{syst}}) \times 10^{49}$	$(7(^{+6}_{-3})_{\mathrm{stat}}(^{+70}_{-6})_{\mathrm{syst}}) \times 10^{48}$

Table 5.13.: Parameters obtained from the SED fits for the leptonic and hadronic scenarios: logarithm of the normalization $\log_{10}K$, spectral index p on the particle distribution, energy cut-off E_{cut} on the particle distribution, density of the interstellar medium n and magnetic field B. In both cases the reference energy E_0 is chosen to be 1 TeV. In addition, the resulting total energy in accelerated particles W for a distance of 750 pc for each scenario is also show. The total energy is calculated above 100 MeV in the case of electrons, and above the rest mass of the proton in the case of protons. The quoted errors represent 1σ statistical and systematic uncertainties.

The MWL data used in this section consist of:

- Parkes radio data points from Duncan and Green [2000]
- *ASCA* X-ray spectral fit from Aharonian et al. [2007]
- *Fermi* GeV γ-ray data points from Tanaka et al. [2011]
- H.E.S.S. TeV γ-ray data points from this work (figure 5.5 and table 5.7).

The various measurements are shown in figure 5.8.

Since the connection between the H.E.S.S. and *Fermi* measurements is so smooth, only γ-ray data (in the GeV and TeV energy regimes) are used to study the parent particle population properties. This approach has the advantage of revealing the properties of the present-time parent particle population without extra assumptions about the SNR evolution, its hydrodynamics, the local magnetic field and energy losses that accelerated particles undergo.

In order to evaluate the systematic uncertainty in the fit parameters and the total energy in accelerated particles the model fit is repeated after shifting the *Fermi* and H.E.S.S. points in an analogous way as for the simultaneous *Fermi*-H.E.S.S. spectral fit in section 5.5.

In order to estimate the value of the total energy W and its statistical uncertainty an MC approach is used: once the parameters of the parent particle population from the equation 5.5 are fitted, random sets of them are simulated within their respective statistical uncertainties. For each set, a value of W is calculated by means of the equation 5.7. If the distribution of W is symmetric (as is the case for the hadronic scenario), W and its statistical uncertainty are calculated as the mean and width from a Gaussian

fit to the distribution. If the distribution is asymmetric (as is the case for the leptonic scenario), W and its asymmetric statistical uncertainty are calculated from the median of the distribution and the 68% quantiles around the median.

5.6.1. Hadronic scenario

In the hadronic scenario, the particle population consists of protons that produce γ-rays via π^0 decay after interacting with other hadrons of the ambient medium. Hadronic processes have been introduced in section 3.6.

In this scenario, the particle population parameters are fitted so that the γ-ray spectrum from π^0 decay matches the GeV and TeV data. The ambient density is left fixed in the fit because the density parameter is inversely proportional to the normalization of the particle spectrum, therefore both parameters are highly anticorrelated. The density is fixed to $1\,\mathrm{cm}^{-3}$ because even if lower densities seem reasonable according to the limit by Slane et al. [2001], the resulting total energy in accelerated particles is too high: $n \lesssim 0.1\,\mathrm{cm}^{-3}$ yields a total energy which is $\gtrsim 80\%$ of the canonical supernova explosion kinetic energy E_{SN} of 10^{51} erg.

The results of the SED model fit are presented in table 5.13 and in figure 5.8. The fitted parameters of the accelerated proton population together with the ambient density and the total energy in accelerated protons are given in the table and the spectrum of the γ-ray emission due to π^0 decay is shown in the figure. The model reproduces the data well with $\chi^2/\mathrm{NDF} = 9.47/13$ (p value of 0.74).

The derived spectral index $p \sim 1.8$ is quite hard, but still in the range between the conventional $p = 2$ and the value of $p = 1.5$ from the test-particle acceleration with strong modified shock approach discussed in Malkov [1999]. The latter (more realistic) case supposes that the accelerated particles modify the SNR shock resulting in a hardening in the spectrum of accelerated particles.

The total energy in accelerated protons is 8% of the canonical supernova explosion kinetic energy, very close to the value of 10% typically required to explain the observed Galactic CR flux. Nevertheless, as stated above, the ambient density assumed for this estimation is larger than expected.

Lower ambient densities might still be possible if the emission is at least partially due to leptonic mechanisms. In this context, RX J0852.0−4622 could accelerate both electrons and protons, but hadrons would escape without producing γ-rays due to the low density of the medium. Another possibility is that, if RX J0852.0−4622 is the result of a core-collapse SN explosion, the explosion energy released into kinetic energy of the ejected material could be somewhat larger than the canonical 10^{51} erg discussed in section 3.3, in which case the hadronic processes could account for the γ-ray emission with a lower ambient density.

5.6.2. Leptonic scenario

In the leptonic scenario, the particle population consists of electrons. These electrons produce low energy synchrotron photons up to hard X-rays due to the ambient mag-

netic field and γ-rays via inverse Compton scattering on ambient photon fields. The most important photon field for γ-ray production is the cosmic microwave background (CMB) photon field. Infrared (IR) and optical radiation fields might also contribute. Nevertheless, according to the interstellar radiation field model by Porter et al. [2006] the contribution of IR and optical radiation fields should be negligible due to the large distance between RX J0852.0−4622 and the Galactic center ($\sim$ 8.5 kpc, see table 4.1 for details). Radiation fields from surrounding stars should also be negligible, since no bright stars are detected in the FoV of RX J0852.0−4622. Therefore, only the CMB photon field is considered in the following. Leptonic processes have been introduced in section 3.6.

Bremsstrahlung processes are neglected in this work because they are not important due to the low density in the ambient medium surrounding RX J0852.0−4622. Bremsstrahlung was studied in Aharonian et al. [2007], yielding no significant contribution.

In this scenario, the fit is performed in two steps. In the first step, the particle distribution parameters are fitted so that the γ-ray spectrum from inverse Compton scattering matches the GeV and TeV data. In the second step, the magnetic field is fitted such that the synchrotron emission produced by the particle population determined in the first step matches the X-ray data[12]. The radio data are not used at all because it is not possible to match at the same time both the X-ray and the radio data in this simple scenario. X-rays are favored over the radio data in the second fit step since the electrons contributing to the X-ray spectrum are in the energy range for which the parent electron population is derived in the first step. The reason is that electrons producing synchrotron emission of keV X-ray photons have similar energies to those producing TeV γ-ray photons via IC scattering: in both processes electrons in the TeV band are necessary. On the contrary, electrons producing synchrotron emission at radio frequencies have much lower energies: in order to produce μeV photons via synchrotron emission electrons in the MeV band are necessary, for which the spectral behavior is not known.

The systematic error on the magnetic field B is estimated by quadratically combining two independent contributions. The first contribution is the change in the fitted value of B due to a change in the spectral parameters of the parent particle population, when systematically shifting the γ-ray data points used for the fit of the parameters of the particle population. This procedure, introduced before in order to derive the systematic uncertainties of the parameters of the particle population themselves, yields a systematic error on B of $\sim 0.4\,\mu$G. The second contribution is the change in the fitted value of B due to variations of the X-ray spectrum within its systematic uncertainty. These variations yield a systematic error on B of also $\sim 0.4\,\mu$G. The quadratic combination of both effects results in a total systematic error on B of $\sim 0.6\,\mu$G.

The results of the SED model fit are presented in table 5.13 and in figure 5.8. The

[12]The fit was performed using errors converted to 1σ C.L. instead of the 90% C.L. with which the data was originally provided. The fit uses 10 points logarithmically equidistant in energy within the range of the measurement (from 2 keV to 10 keV).

fitted parameters of the accelerated electron population together with the fitted ambient magnetic field and the total energy in accelerated electrons are given in the table and the spectra of the γ-ray emissions due to the synchrotron and inverse Compton processes are shown in the figure. The model reproduces the data well with $\chi^2/\mathrm{NDF} = 21.5/13$ (p value of 0.06) for the fit of the γ-ray data used to estimate the parent particle population and with $\chi^2/\mathrm{NDF} = 16.8/9$ (p value of 0.05) for the fit of the X-ray data used to estimate the magnetic field. As for the radio data, looking at the synchrotron curve in figure 5.8, it could be possible that a spectral break occurs at low energies (at $E \sim \mathcal{O}(10^{-4}\,\mathrm{eV})$ in the photon spectrum, which means at $E_e \sim \mathcal{O}(10\,\mathrm{GeV})$ in the electron spectrum). Another possibility is that the radio emission could be produced by a different (older) population of electrons.

The derived magnetic field $B \sim 5\,\mu\mathrm{G}$ is quite low but in agreement with the estimates performed by Kishishita et al. [2013] on the magnetic field of the filamentary structure of the northwestern rim. The magneto-hydro dynamical models suggest that the magnetic field in the SNR responsible for the leptonic emission is similar to the magnetic field in the postshock area of the NW rim. The estimated magnetic field represents the average over the full remnant and does not contradict the existence of regions with significantly amplified magnetic field.

The total energy in accelerated electrons is calculated by integrating the particle spectrum above 100 MeV. The lower limit is chosen to be the energy of electrons with characteristic synchrotron radiation emission in radio frequencies. The total energy in accelerated electrons above 100 MeV is 0.7% of the kinetic energy released in a canonical supernova explosion. Applying the canonical ratio of the number of electron to that of protons in cosmic rays of 1:100, the energy of protons is 100 times that of electrons. This implies that 70% of the explosion energy is transmitted to the acceleration of cosmic rays, a relatively high fraction. This implies that either RX J0852.0−4622 is very efficiently accelerating particles or the canonical ratio does not apply in this case. Indeed, the canonical ratio has been measured locally, but electrons and protons have different mean free paths, so the ratio can differ from its canonical value. As in the hadronic scenario, an explosion energy somewhat larger than the canonical value could also explain the total energy in accelerated particles. In addition, a spectral break at low energies for accommodating the radio data would also lower the total energy estimate. In any case, the total energy in accelerated electrons remains undetermined, since the uncertainties, as shown in table 5.13 are high.

Since the magnetic field has been determined, the effect of synchrotron cooling on the parent electron population can be studied. Following Blumenthal and Gould [1970], the synchrotron energy loss can be integrated to estimate the energy up to which the electrons with maximum energy have been cooled since the SN explosion. This represents the electron break energy $E_{e\,\mathrm{b}}$ above which synchrotron losses become important for the derived present-time electron population. The synchrotron energy loss equation can be written as

$$-\left(\frac{\mathrm{d}E_e}{\mathrm{d}t}\right)_{\mathrm{sync}} = \frac{4}{3}\,\sigma_{\mathrm{T}}\,c\,\gamma^2\,\varepsilon_B, \tag{5.8}$$

where E_e is the electron energy, t the time, $\sigma_{\rm T}$ the Thomson cross section, c the speed of light, γ the electron Lorentz factor and $\varepsilon_B = B^2/2\mu_0$ the magnetic field density, with B being the magnetic field strength and μ_0 the permeability of free space. Integrating the synchrotron energy loss over times since the explosion and over energies between $E_{e\,\rm max}$ (maximum electron energy, assumed to be infinite) and $E_{e\,\rm b}$ (break energy)[13], and adopting an SNR age of 3000 yr, the break energy can be written as

$$E_{e\,\rm b} \simeq 180 \left(\frac{t_{\rm age}}{3000\,\rm yr}\right)^{-1} \left(\frac{B}{5\,\mu\rm G}\right)^{-2} \rm TeV. \tag{5.9}$$

This shows that synchrotron-cooling losses are not important for RX J0852.0−4622, because the break energy above which the losses are important ($E_{e\,\rm b} \sim 180\,\rm TeV$) is much higher than the energy cut-off in the spectrum ($E_{\rm cut} \sim 40\,\rm TeV$). This in turn suggests that the acceleration processes are limited by the age of the SNR, rather than by radiative losses (see Reynolds [2008]).

5.6.3. Conclusions

The detection of non-thermal emission at X-ray and γ-ray energies is a proof of the acceleration of particles up to $\sim 100\,\rm TeV$, since charged particles accelerated to even greater energies are necessary to produce such highly energetic photons (see details in section 3.6). In addition, the observation of polarized radiation at radio frequencies is a proof of acceleration of electrons that produce synchrotron emission. These electrons are responsible for the emission from radio to X-ray frequencies. As for the γ-rays, two scenarios have been presented in this section: a hadronic and a leptonic model. Both scenarios describe the data well and seem plausible, but face some difficulties.

For the hadronic scenario, on the one hand the π^0 decay spectrum matches very well the *Fermi* and H.E.S.S. data but on the other hand the proton spectrum is rather hard with a spectral index $p \sim 1.8$ and the ambient density is higher than that from previous estimates. The hard spectrum is still compatible within values in the literature (Malkov [1999]), but the density is incompatible with the upper limit from Slane et al. [2001].

As for the leptonic scenario, the IC spectrum matches the *Fermi* and H.E.S.S. data, but the synchrotron spectrum does not match at the same time the Parkes radio data and the *ASCA* X-ray measurement. Moreover, the corresponding energy in accelerated cosmic rays is a relatively high fraction of the explosion energy. The difficulties in explaining the radio data suggest an extra break in the electron spectrum at low energies, or else that the radio emission is due to a different electron population. As for the total energy in cosmic rays, it is possible that the canonical ratio of electrons to protons does not apply for RX J0852.0−4622. Also, a spectral break at low energies, as suggested by the radio data, would help reconciling the total energy in cosmic rays with the canonical value. In addition, the low magnetic field derived in this work is consistent with the one derived in

[13] Notice that the energy range of the integral is specified from the maximum energy to a lower energy because it is an energy loss equation and the idea is to measure the energy lost by electrons with maximum energy since the SN explosion.

Kishishita et al. [2013]. This low magnetic field implies that synchrotron-cooling effects are not important in the leptonic scenario.

The results presented in table 5.13 agree with the phenomenological relations of the shape of the γ-ray differential spectrum presented in table 3.1 in section 3.6. Indeed, for the synchrotron and IC emission spectra of the leptonic model, $(p+1)/2 = 1.685$, which is similar to the H.E.S.S. spectral index of $\Gamma = 1.68$. For the π^0 spectrum in the hadronic model, $4/3(p_p - 1/2) = 1.765$, which is the average spectral index between the H.E.S.S. and *Fermi* measurements, and also very close to the spectral index of the simultaneous fit of the *Fermi* and H.E.S.S. spectral points, $\Gamma = 1.777$.

Although the hadronic model seems slightly favored by the larger goodness of fit value (χ^2 fit probability of 74%), the leptonic model cannot be ruled out (χ^2 fit probability of 6%). Potentially a better determination of the cut-off can be crucial for the solution of this ambiguity by putting stronger constrains on both leptonic and hadronic scenarios.

5.7. Outlook with CTA

The future CTA Observatory has been presented in chapter 2. In the previous section 5.6 it has been discussed that more precise cut-off measurements can help in identifying the nature of the γ-ray emission of RX J0852.0−4622. This is also true for SNRs and γ-ray sources in general. In this section an insight in the capabilities of CTA with respect to the detection of spectral features in the form of exponential cut-offs is presented, using RX J0852.0−4622 as a test case. In particular, simulations of the RX J0852.0−4622 spectrum with different cut-off energies are presented in order to evaluate the capabilities of CTA for detecting these features across a large energy range. In addition, the expected improvement for the near future in the measurement of the spectrum of RX J0852.0−4622 is presented, by comparing the performance for such a measurement of H.E.S.S. (current experiment) to that of CTA (future observatory).

According to the population study described in the section 2.1 of Acero et al. [2013a], galactic RX J0852.0−4622-like SNRs should be virtually visible for CTA up to distances of $\sim 10\,\mathrm{kpc}$, and their shell morphologies resolvable for distances up to $\sim 5\,\mathrm{kpc}$, unless obscured by an intermediate object (like a gas cloud or the Galactic center). In addition, if RX J0852.0−4622 is an example of a typical SNR in the Milky Way, this implies that $\sim 30\%$ of the galactic SNRs should be visible and $\sim 10\%$ resolvable. Using the estimate from the authors of $\sim$ 80 SNRs currently emitting TeV γ-rays in the Galaxy, these numbers translate into ~ 24 detectable SNRs and ~ 8 resolvable SNRs for CTA.

5.7.1. Simulation tools

For the work presented in this section, simulations using the official `CTAMacros` (version 6) software tools and the official instrument response function (IRFs) derived with the MC production 1 are used. A description of the tools and the IRFs is given in the section 5 of Bernlöhr et al. [2013]. The implementation of a better shell model in order to accurately simulate shell emission from SNRs within `CTAMacros` has been necessary.

Since these tools are quite rudimentary, no direct comparison of the results of this section to the H.E.S.S. results in this work, which make use of more advanced analysis techniques, is possible. However, the performance of H.E.S.S. can be approximately simulated by using IRFs for a selection of telescopes with similar characteristics as the H.E.S.S. array.

The simulation tools require specific models for the morphology and spectrum of the emission as input. In this case, the emission of an SNR is simulated. The graphical representation of the morphology and spectrum models used for the studies in this section are shown in figure 5.9.

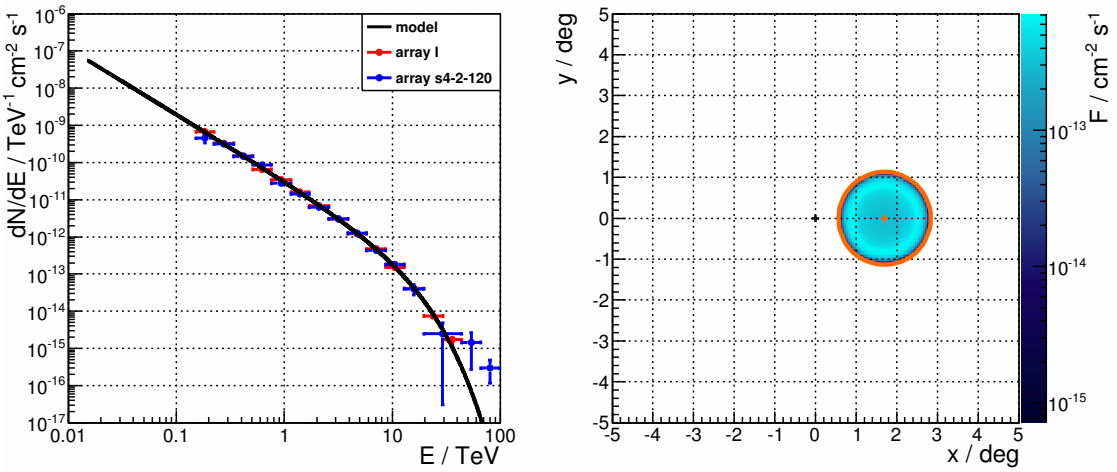

Figure 5.9.: `CTAMacros` simulations. Left: modeled spectrum (black curve) together with the resulting simulated data points for candidate arrays I (red points) and s4-2-120 (blue points). Right: skymap representation of the simulated morphology model. The morphology model has been weighted with the integral over energies of the spectrum model on the left panel such that the color axis (in log scale) represents integral fluxes between 30 GeV and 150 TeV. The simulated observation and target positions are marked with a black and orange cross respectively and the simulated *on* region with an orange circle. The morphology model is restricted to the area inside the *on* region. The x and y coordinates are in the coordinate system of the common camera plane, therefore, the center of the FoV is at coordinate $(0°, 0°)$. The skymap has been simulated for the candidate array I. In the case of candidate array s4-2-120 further parameters are adjusted to match the H.E.S.S. observation and analysis conditions (see main text).

The morphology is modeled by a shell emission convoluted with the expected PSF for CTA as described by the formulas 4.13 and 4.14 from section 4.6. The input parameters for the model are the parameters of the shell fit presented in table 4.6 of the same section. Specifically, $r_{\mathrm{in}} = 0.777°$ and $r_{\mathrm{out}} = 1.030°$. The CTA PSF is modeled by `CTAMacros` as

a simple Gaussian function with a width of 0.035°.

The spectrum is modeled using the parameters of the simultaneous fit of the *Fermi* and H.E.S.S. spectral points presented in section 5.5. The joint spectrum is well described by a power-law with exponential cut-off (see the formula in table 5.3) in the range of 1 GeV to 30 TeV with the parameters from table 5.12. Specifically $E_0 = 1\,\mathrm{TeV}$, $\Phi_0 = 32.8 \times 10^{-12}\,\mathrm{cm^{-2}s^{-1}TeV^{-1}}$, $\Gamma = 1.777$ and $E_{\mathrm{cut}} = 9.0\,\mathrm{TeV}$.

The `CTAMacros` tools simulate the response of one of the possible array configurations for CTA to a γ-ray emission according to the specified morphology and spectrum models. In this section, RX J0852.0−4622 being a southern hemisphere source, the candidate array I is chosen, as one of the multipurpose arrays with a very good performance in the whole energy range relevant for the southern CTA site. The candidate array I has been introduced in the appendix in section A.9.

The instrument response functions used for simulating the array performance are the DESY-20130518 IR files produced by Gernot Maier. Specifically the ones simulating the telescope array at 2000 m altitude and 50 h observation time are used. The altitude is similar to the altitude of the current H.E.S.S. experiment and similar to the altitudes of the site candidates for the southern CTA array. The observation time is of the same order of magnitude as the current H.E.S.S. data set available for spectral analysis and its value can be scaled within the `CTAMacros` tools. For the simulations in this section, an observation time of 20 h is simulated, similar to the livetime for the H.E.S.S. spectral data set presented in table 5.6. Moreover, 20 h is a reasonable observation time for a detailed study of RX J0852.0−4622 with CTA.

Furthermore, the DESY IRFs use MC simulations for 20° zenith angle and off-axis angles ranging from 0° to 5°. For a site situated at the latitude of the H.E.S.S. site, RX J0852.0−4622 is visible every year for $\sim 100\,\mathrm{h}$ between 23° and 25° zenith angle. Since all site candidates for the southern CTA array are at roughly the same latitude as H.E.S.S., 20° zenith angle IRFs are a good approximation for simulating the response of CTA observations of RX J0852.0−4622[14]. And since RX J0852.0−4622 is an extended source, off-axis dependent IRFs are mandatory for a realistic simulation of this source.

The source is simulated with its center at an offset angle of 1.7° from the center of the FoV and a spectrum extraction region of 1.1° is chosen, as shown in the skymap of the right panel of figure 5.9[15]. This allows the creation of three background regions, i.e. a background normalization $\alpha = 1/3$, using the reflected region method described in section 4.4. The simulated bin size for the skymap is 0.05°.

In order to simulate the performance of H.E.S.S. and to be able to compare to that

[14]Notice that the H.E.S.S. data sets for RX J0852.0−4622 analyzed in this work have an average zenith angle of $\sim 30°$ (see tables 4.5, 4.8, 4.10, 5.2). Since no CTA IRFs at 30° zenith angle are available, the 20° zenith angle IRFs are used. This should be a good approximation, since according to Funk et al. [2004] the trigger rate decays slowly for increasing low zenith angles: the decay is $\sim 10\%$ between 20° and 30°.

[15]Notice that the larger FoV of CTA (10°) compared to that of H.E.S.S. (5°) allows a larger offset angle for wobble observations, permitting both, a larger *on* region that fully encompasses the emission from RX J0852.0−4622 and more *off* regions for background extraction, and hence a better background determination.

of CTA, in addition to candidate array I, a study using the candidate array s4-2-120 is performed as an approximation to the H.E.S.S. system. The candidate array s4-2-120 is a subarray of telescopes with similar characteristics as the subarray HESS introduced in the appendix in section A.14. The main difference is the FoV and number of pixels per camera (8° and 1735 pixels for the candidate array s4-2-120 versus 5° and 673 pixels for the subarray HESS). However, for the study using the candidate array s4-2-120, the FoV of the system has been limited within the `CTAMacros` tools to the H.E.S.S. FoV of 5°.

In order to better simulate the H.E.S.S. response when using candidate array s4-2-120, further parameters are adjusted to match those of H.E.S.S. The PSF width used is 0.076° as determined in the morphological analysis from section 4.6. The center of the source is placed at 1.1° offset from the FoV center to match the conditions for the majority of the H.E.S.S. data usable for spectral studies presented in table 5.2. Moreover, to match the spectral analysis parameters discussed in section 4.7, the radius of the spectrum extraction region is set to 1.0° and the background normalization α is set to 1.

As for the case of the subarray HESS used in chapter 2, the comparison of candidate array s4-2-120 and H.E.S.S. is not perfect, since some parameters used in the CTA MC production, like for instance the performance of the PMTs and the camera electronics is improved with respect to that of H.E.S.S. Nevertheless, the results should be similar.

Identifying the responses of candidate arrays I and s4-2-120 with the simulated responses of CTA and H.E.S.S. respectively, the performance of H.E.S.S. and CTA can be compared directly, since all simulations use the same tools.

The resulting spectral points from the simulations are shown in the left panel of figure 5.9. It is remarkable that there are no points below $\sim 100\,\mathrm{GeV}$ for the candidate array I, since CTA should be sensitive at these energies. However, one of the conditions that has to be fulfilled for the points to appear in the spectrum is that the excess in the corresponding bin should be larger than 3% of the background in the same bin, to avoid possible systematic effects in the background. The spectrum being hard (spectral index ~ 1.78), this requirement is not fulfilled for any of the points below $\sim 100\,\mathrm{GeV}$. Since the signal increases linearly with time, but the background only as the square-root of time, longer observation times are necessary in order to get measurements at lower energies.

Comparing both sets of spectral points it is clear that CTA (i.e. candidate array I) is more precise than H.E.S.S. (i.e. candidate array s4-2-120): the error bars, especially at high energies ($E \gtrsim 10\,\mathrm{TeV}$), are much smaller for CTA than for H.E.S.S. In contrast, the spectrum of candidate array s4-2-120 shows points at higher energies ($E \gtrsim 40\,\mathrm{TeV}$) that are not present in that of candidate array I. For these high energy points the excess simulated for the candidate array s4-2-120 is larger than 10 times the expected value, estimated by folding the input spectral model with the migration matrix, the effective areas and the observation time and integrating over the corresponding energy bin. This results in an upper fluctuation in the simulated excess in the case of candidate array s4-2-120, yielding flux points higher than the simulated model.

5.7.2. Results

Spectra of RX J0852.0−4622-like sources are simulated for different values of the energy cut-off (E_{cut}): 5 TeV, 10 TeV, 15 TeV, 20 TeV, 30 TeV, 40 TeV, 50 TeV, 75 TeV, 100 TeV, 150 TeV, 200 TeV. In addition a simple power-law (i.e. $E_{\mathrm{cut}} = \infty$) and a power-law with the actual cut-off from the simultaneous *Fermi* and H.E.S.S. fit shown in table 5.12 ($E_{\mathrm{cut}} = 9.0\,\mathrm{TeV}$) are simulated, the latter twice: for both candidate arrays I and s4-2-120.

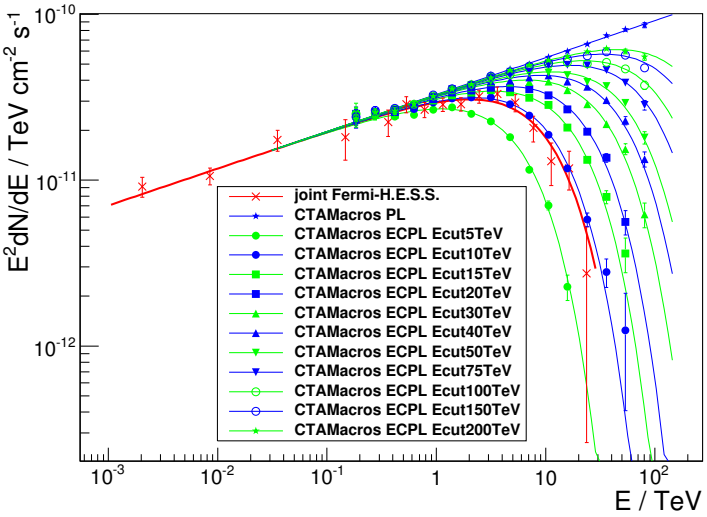

Figure 5.10.: The simulations of the measurements of RX J0852.0−4622-like spectra with CTA for different values of E_{cut} using candidate array I are shown in green and blue colors. The curves represent the models and the data points represent the simulated measurements. The red points represent the *Fermi* and H.E.S.S. points used for the derivation of the simultaneous spectral fit, marked by the red curve. For clarity the points and curves corresponding to the simulations using the same E_{cut} as the joint *Fermi* and H.E.S.S. spectrum for both candidate arrays I and s4-2-120 are not shown. All error bars represent 1σ statistical uncertainty.

The simulated spectra together with the joint *Fermi* and H.E.S.S. spectrum are displayed in figure 5.10. For clarity the spectra for the simulations using $E_{\mathrm{cut}} = 9.0\,\mathrm{TeV}$ for both candidate arrays I and s4-2-120 are not shown in this figure, but in the left panel of figure 5.9. The spectral points resulting from the simulations are fitted using the least-squares method for two different hypotheses: power-law and power-law with exponential cut-off (see the formulas in table 5.3). Then the χ^2 values of both fits are compared to each other using the F-test (see for instance Blobel and Lohrmann [2012]), similarly to the comparison of the likelihoods in the likelihood-ratio test presented in section 4.4.4, in order to assess the significance of the preference of the power-law with

exponential cut-off model versus the simple power-law model.

$E_{\rm cut}^{\rm true}$	F-test sign.	$E_{\rm cut}^{\rm reco}$/TeV	rel. error on $E_{\rm cut}^{\rm reco}$
5 TeV	6.4σ	4.92 ± 0.21	4.2%
10 TeV	7.5σ	9.6 ± 0.4	3.8%
15 TeV	7.3σ	15.2 ± 0.6	3.8%
20 TeV	7.6σ	20.8 ± 0.8	3.9%
30 TeV	7.5σ	31.3 ± 1.2	4.0%
40 TeV	7.3σ	43.7 ± 1.9	4.4%
50 TeV	7.0σ	52.1 ± 2.5	4.8%
75 TeV	6.8σ	74 ± 4	5.6%
100 TeV	6.3σ	100 ± 7	7.1%
150 TeV	5.1σ	148 ± 14	9.5%
200 TeV	5.9σ	176 ± 19	11%
∞ (PL model)	0.53σ	-3000 ± 6000	190%
9.0 TeV (array I)	7.0σ	8.9 ± 0.3	3.7%
9.0 TeV (array s4-2-120)	5.4σ	9.7 ± 1.6	16%

Table 5.14.: F-test significances and reconstructed cut-off energies for the CTA spectrum of each simulation: simulated cut-off $E_{\rm cut}^{\rm true}$, significance of the F-test probabilities of the spectral fits (representing the preference of a power-law model with exponential cut-off versus a simple power-law one), reconstructed cut-off energy $E_{\rm cut}^{\rm reco}$ and relative error in the reconstructed cut-off energy. The quoted errors represent 1σ statistical uncertainties.

The significance of the F-test probabilities of the spectral fits, representing the preference of a power-law model with exponential cut-off versus a simple power-law model, are shown as function of the simulated cut-off energy in table 5.14 and figure 5.11a. The significance of the F-test is $\sim 7.5\sigma$ for cut-offs from 10 TeV up to 40 TeV, and falls logarithmically for higher cut-off energies: as the cut-off approaches energies at the upper edge of the spectrum, not enough data points remain for an accurate estimation of the cut-off energy, and the power-law assumption becomes more and more plausible. Nevertheless, even for cut-off energies above 100 TeV the significance is above 5σ. The limit at high energies is 0.53σ for $E_{\rm cut} = \infty$ (power-law model). For lower energies, the significance also falls: as the cut-off approaches energies at the lower edge of the spectrum, not enough data points remain for an accurate estimation of the spectral index, so even though the probability for a power-law fit is very low, the probability of the fit to a power-law with exponential cut-off also falls.

The comparison of the performances of CTA (candidate array I, blue point) and H.E.S.S. (candidate array s4-2-120, green point) using the same $E_{\rm cut}$ value as that extracted from the simultaneous *Fermi* and H.E.S.S. spectral fit reveals that CTA improves the sensitivity of cut-off detections from $\sim 5.4\sigma$ to $\sim 7.0\sigma$. Notice that the value for array s4-2-120 is very close to the value of 5.8σ obtained from the H.E.S.S. analysis shown in table 5.9.

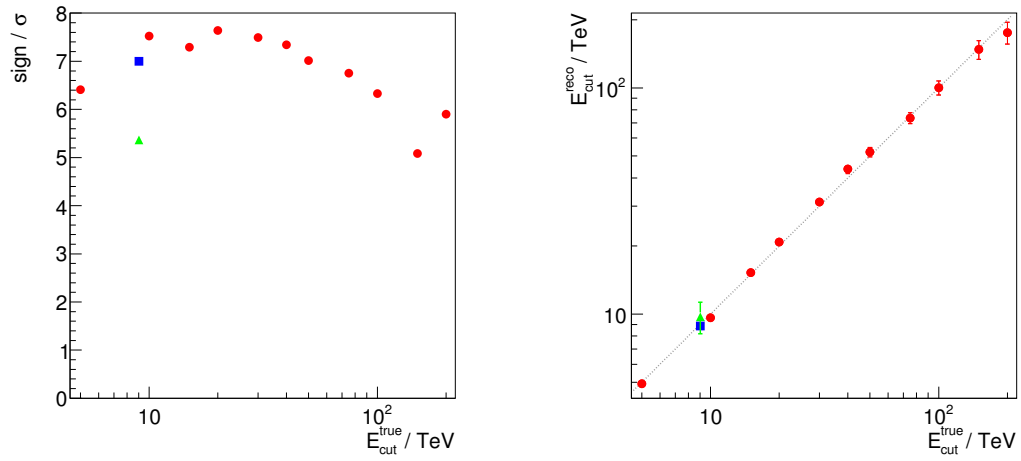

(a) ECPL significance vs. $E_{\mathrm{cut}}^{\mathrm{true}}$

(b) $E_{\mathrm{cut}}^{\mathrm{reco}}$ vs. $E_{\mathrm{cut}}^{\mathrm{true}}$

Figure 5.11.: The left figure shows for each simulation the significance of the fit using the power-law with exponential cut-off model with respect to the simple power-law model as function of the simulated energy cut-off $E_{\mathrm{cut}}^{\mathrm{true}}$. The right figure shows for each simulation the reconstructed energy cut-off $E_{\mathrm{cut}}^{\mathrm{reco}}$ as a function of the simulated energy cut-off $E_{\mathrm{cut}}^{\mathrm{true}}$. The error bars represent 1σ statistical uncertainty. The gray dotted line represents the identity $E_{\mathrm{cut}}^{\mathrm{reco}} = E_{\mathrm{cut}}^{\mathrm{true}}$. In both cases the red points indicate the results of the simulations using candidate array I at the simulated E_{cut} values listed in the main text, and the blue and the green points indicate the results of the simulations using candidate arrays I and s4-2-120 respectively at the same value of E_{cut} as extracted from the simultaneous *Fermi* and H.E.S.S. spectral fit.

In order to illustrate the resolution of the cut-off energies, the reconstructed cut-off energy is shown as a function of the simulated cut-off energy in table 5.14 and figure 5.11b. Even for energies above 100 TeV the cut-off energies are accurately reconstructed. The relative error on the reconstructed cut-off energy is below 5% for $E_{\mathrm{cut}} \leq 50\,\mathrm{TeV}$ and below 10% for $E_{\mathrm{cut}} \leq 150\,\mathrm{TeV}$. Even for $E_{\mathrm{cut}} = 200\,\mathrm{TeV}$ the relative error is only 11%. This represents a large improvement with respect to typical errors of current experiments ($> 15\%$ for energies between a few TeV and 20 TeV). As a comparison, the cut-off energy obtained from H.E.S.S. data for RX J0852.0−4622 in this work is 7.2 TeV with a relative error of 17%.

The comparison of the performances of CTA (candidate array I, blue point) and H.E.S.S. (candidate array s4-2-120, green point) using the same E_{cut} value as that extracted from the simultaneous *Fermi* and H.E.S.S. spectral fit reveals that CTA improves

the resolution of cut-off measurements from $\sim 16\%$ relative error to $\sim 3.7\%$. Notice that the value for array s4-2-120 is very close to the value of 17% obtained from the H.E.S.S. analysis presented in this work.

5.7.3. Conclusions

The simulations of the CTA response for measuring γ-ray spectra for a series of different energy cut-offs for the example of SNR RX J0852.0−4622 have been presented. It is shown that the expected increase in sensitivity and resolution of CTA with respect to current experiments will allow CTA to detect cut-offs of bright extended sources across a large range of energies with a good accuracy. This in turn should help to distinguish between leptonic and hadronic emission scenarios, since the models used to describe the emission of these scenarios present different shapes in the cut-off region.

In the specific case of RX J0852.0−4622, CTA should be able to significantly increase the exponential cut-off detection and reduce the uncertainty in the cut-off energy from $\sim 16\%$ relative error to $\sim 3.7\%$ with a modest observation time of 20 h. The better energy resolution and sensitivity of CTA should also help in the characterization of the shape of the cut-off (i.e. power-law with sub- or super-exponential cut-off: $\mathrm{d}\Phi/\mathrm{d}E = \Phi_0(E/E_0)^{-\Gamma}\exp(-E/E_{\mathrm{cut}})^{\beta}$).

With larger observation times, the lower energy range of RX J0852.0−4622 should be accessible to CTA and hence the obtained spectrum should overlap with the *Fermi* spectrum. This, together with a better energy cut-off determination and studies of the *Fermi* data with deeper exposures and better models for the diffuse background in the Vela region, should help in the identification of the nature of the emission by distinguishing between hadronic and leptonic scenarios. A similar study performed by *Fermi* on two other SNRs (W44 and IC 443) has revealed the characteristic break of the π^0 decay in the γ-ray spectrum (see Ackermann et al. [2013]). Measurements of neutrino detectors like the IceCube Neutrino Observatory (see IceCube Collaboration [2016]), ANTARES (see ANTARES Collaboration [2016]) or the future KM3NeT (see KM3NeT Collaboration [2016]) would also help in this matter, since a clear detection of neutrinos coming from the direction of RX J0852.0−4622 would prove the acceleration of hadrons in the SNR shock. Even if such a detection is challenging, IceCube has already moved a step forward with its measurement of high-energy extraterrestrial neutrinos (see IceCube Collaboration [2013]).

In addition, the improved sensitivity and angular resolution of CTA compared to current experiments should help in separating the contribution of the possible TeV PWN associated to PSR J0855−4644 (discussed in section 4.8) from that of the SNR and/or measure a clear spectral variation across the SNR region. This would enable the modeling of the RX J0852.0−4622 emission in different parts of the remnant and eventually the identification of different particle populations contributing to the overall emission of γ-rays.

Summary

γ-ray astronomy has experienced a fast growth in the last few decades. Cherenkov telescopes are amongst the most successful instruments for the observation of the sky at γ-ray energies.

The next generation of Cherenkov telescope systems is approaching. With its improved sensitivity and angular resolution with respect to current experiments, the CTA Observatory will help in solving many of the puzzles of γ-ray astronomy, particle physics and cosmology. CTA is planned as a two-site observatory with an array of telescopes in each hemisphere, in order to be able to observe the full sky. The improved sensitivity will increase the array trigger rates from a few 100 Hz for current experiments to $\sim 13\,\mathrm{kHz}$, in the case of the more demanding southern array. Depending on the read-out scenario, this implies a data rate of $200 - 2500\,\mathrm{MB/s}$ and a data volume after 15 yr of operation and assuming a duty cycle of 15% of $13 - 165\,\mathrm{PB}$. In addition, single telescope trigger rates are expected as high as $\sim 5\,\mathrm{kHz}$. The design of the trigger system and read-out electronics will be a challenge but should be manageable with existing technologies.

More than 100 yr after their discovery, the origin of cosmic rays is still a mystery. Supernova remnants are the primary source type candidate for Galactic cosmic rays. Since cosmic rays consist mostly of protons and astrophysical hadronic processes produce photons only at γ-ray energies because of the large rest mass of the proton, γ-ray observations of supernova remnants are instrumental for solving the enigma of the origin of CRs.

Observations of the supernova remnant RX J0852.0−4622 in γ-rays with H.E.S.S. reveal a 2° diameter extended emission from a thin shell of $\sim 0.25^\circ$ width. No spectral variation is found across the supernova remnant in either γ-rays or X-rays. The azimuthal profile reveals an emission enhancement towards the direction of the pulsar PSR J0855−4644, that coincides with the shell emission from RX J0852.0−4622. The emission from the pulsar cannot be separated from the emission from the supernova remnant and, though the spectrum of the region around the pulsar shows an indication of a hardening with respect to that of its surroundings, it is still compatible with that of the rest of the supernova remnant.

The H.E.S.S. spectrum of the whole RX J0852.0−4622 region is found to be curved. It is best described by a power-law model with an exponential cut-off at 7.2 TeV, although a curved power-law model cannot be ruled out using solely the TeV data. The revised flux, using the correct muon efficiency corrections, makes RX J0852.0−4622 the brightest steady source above 1 TeV with ~ 1.3 times the flux of the Crab nebula in the same energy range. The smooth connection to the *Fermi* measurement allows a simultaneous fit of the GeV and TeV spectral points that serves to rule out the curved power-law model. In addition, the smooth GeV-TeV connection allows a straightforward modeling

using solely γ-ray data in order to derive the properties of the parent particle population responsible for the non-thermal broadband SED emission in leptonic and hadronic scenarios. Although it results in a larger than expected ambient medium density, the hadronic model describes the data better than the leptonic model. Nevertheless, a leptonic origin of the emission cannot be ruled out. In the leptonic scenario, the magnetic field of $\sim 5\,\mu$G necessary to describe the X-ray measurement as synchrotron emission of the electron population is compatible with other results in the literature. For such a low magnetic field, synchrotron losses are negligible. In addition, in the leptonic scenario, an additional spectral break in the electron spectrum would help in accommodating the radio measurement.

Precise measurements of energy cut-offs in the spectra of γ-ray sources can help to distinguish between hadronic and leptonic emission models. The analysis of simulated data shows that CTA should be able to significantly improve the detection of energy cut-offs over a large energy range with respect to that of current experiments. In the specific case of RX J0852.0−4622, CTA should easily improve the accuracy of the measured energy cut-off in the spectrum by a factor 5. This would help to better characterize the shape of the cut-off, which in turn would help in identifying the nature of the γ-ray emission.

A. Appendix: expected trigger rates, data rates and data volumes for all CTA-UTRA3 candidate arrays

This appendix is dedicated to the results of the calculations of the trigger rates, data rates and data volumes for all CTA-UTRA3 candidate arrays. First, each candidate array is presented in a separate section (sections A.1 to A.14). The appendix ends with a summary of the results of all candidate arrays together in section A.15.

A.1. Candidate array A

This is a precision array designed to have a high telescope multiplicity, with focus on a few hundred GeV.

A.1.1. Array layout

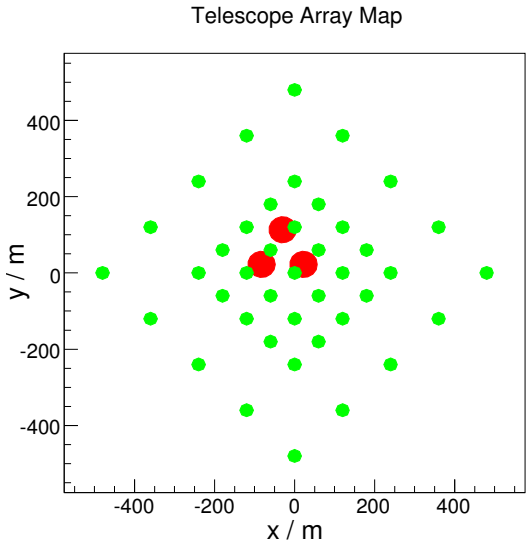

Figure A.1.: Telescope map for the candidate array A. Each circle represents a telescope on the ground. The sizes of the circles are scaled to represent the size of the mirror dishes of the telescopes scaled by a factor three in radius for better visibility. Each color represents a different telescope type.

	N_T	Φ_FoV / °	N_P
LST	3	4.9	2587
MST	41	8	1735

Table A.1.: Particularities of the different telescopes of the candidate array A: number of telescopes of each kind, diameter of the field of view covered by the camera and number of pixels.

A.2. Candidate array B

This is a precision array designed to have a high telescope multiplicity, with focus on a few hundred GeV.

A.2.1. Array layout

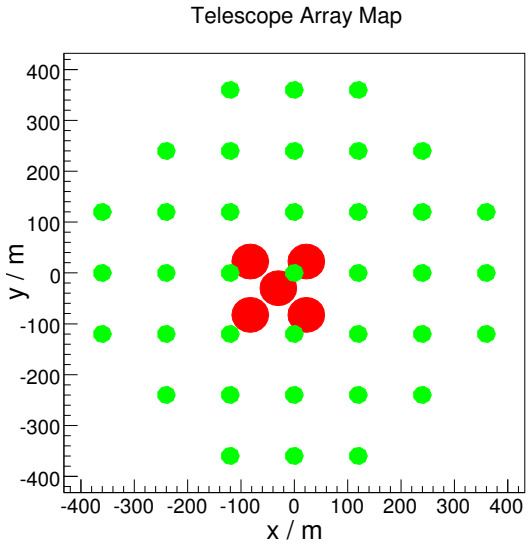

Figure A.2.: Telescope map for the candidate array B. Each circle represents a telescope on the ground. The sizes of the circles are scaled to represent the size of the mirror dishes of the telescopes scaled by a factor three in radius for better visibility. Each color represents a different telescope type.

	N_T	Φ_FoV / °	N_P
LST	5	5	2713
MST	37	8	1735

Table A.2.: Particularities of the different telescopes of the candidate array B: number of telescopes of each kind, diameter of the field of view covered by the camera and number of pixels.

A.3. Candidate array C

This is a large area array designed for having the best performance at multi TeV energies.

A.3.1. Array layout

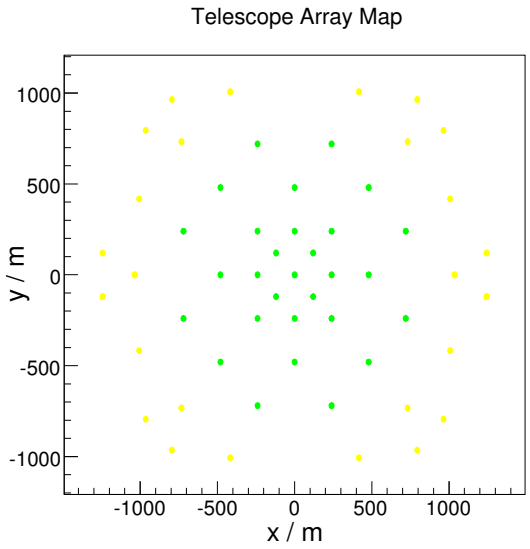

Figure A.3.: Telescope map for the candidate array C. Each circle represents a telescope on the ground. The sizes of the circles are scaled to represent the size of the mirror dishes of the telescopes scaled by a factor three in radius for better visibility. Each color represents a different telescope type.

	N_T	Φ_FoV / °	N_P
MST	29	8	1735
$\mathrm{MST_{LFoV}}$	26	10	1393

Table A.3.: Particularities of the different telescopes of the candidate array C: number of telescopes of each kind, diameter of the field of view covered by the camera and number of pixels.

A.4. Candidate array D

This is a large area array designed for having the best performance at multi TeV energies.

A.4.1. Array layout

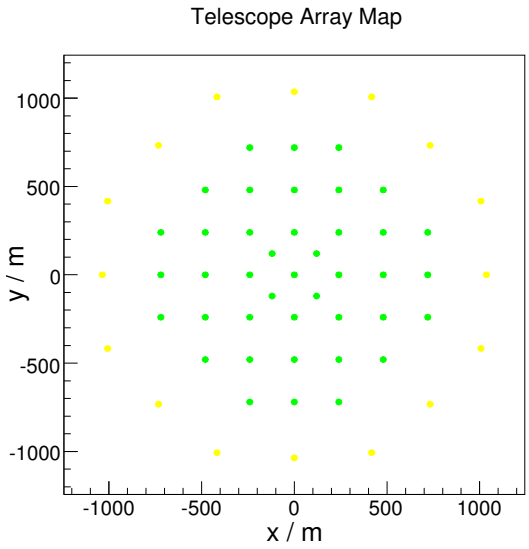

Figure A.4.: Telescope map for the candidate array D. Each circle represents a telescope on the ground. The sizes of the circles are scaled to represent the size of the mirror dishes of the telescopes scaled by a factor three in radius for better visibility. Each color represents a different telescope type.

	N_T	Φ_FoV / °	N_P
MST	41	7.4	1483
$\mathrm{MST_{LFoV}}$	16	10	1393

Table A.4.: Particularities of the different telescopes of the candidate array D: number of telescopes of each kind, diameter of the field of view covered by the camera and number of pixels.

A.5. Candidate array E

This is a multipurpose array, with a good sensitivity and angular resolution across the whole energy range.

A.5.1. Array layout

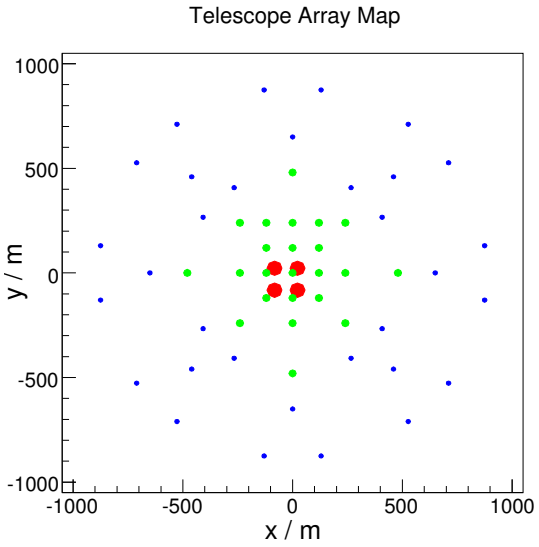

Figure A.5.: Telescope map for the candidate array E. Each circle represents a telescope on the ground. The sizes of the circles are scaled to represent the size of the mirror dishes of the telescopes scaled by a factor three in radius for better visibility. Each color represents a different telescope type.

	N_T	Φ_FoV / °	N_P
LST	4	4.6	2275
MST	23	8	1735
SST	32	10	1393

Table A.5.: Particularities of the different telescopes of the candidate array E: number of telescopes of each kind, diameter of the field of view covered by the camera and number of pixels.

A.6. Candidate array F

This is a low-energy array, with the best sensitivity and energy resolution at low energies.

A.6.1. Array layout

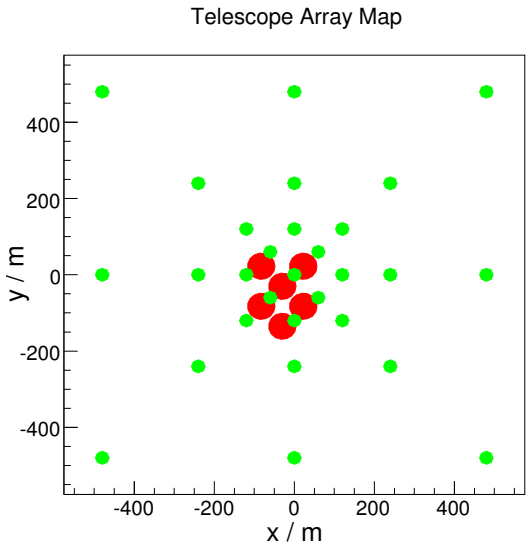

Figure A.6.: Telescope map for the candidate array F. Each circle represents a telescope on the ground. The sizes of the circles are scaled to represent the size of the mirror dishes of the telescopes scaled by a factor three in radius for better visibility. Each color represents a different telescope type.

	N_T	Φ_FoV / °	N_P
LST	6	4.8	2479
MST	29	6.3	1069

Table A.6.: Particularities of the different telescopes of the candidate array F: number of telescopes of each kind, diameter of the field of view covered by the camera and number of pixels.

A.7. Candidate array G

This is a low-energy array, with the best sensitivity and energy resolution at low energies.

A.7.1. Array layout

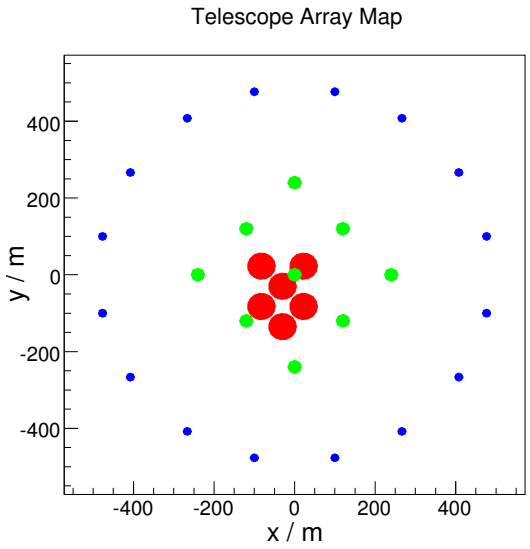

Figure A.7.: Telescope map for the candidate array G. Each circle represents a telescope on the ground. The sizes of the circles are scaled to represent the size of the mirror dishes of the telescopes scaled by a factor three in radius for better visibility. Each color represents a different telescope type.

	N_T	Φ_FoV / °	N_P
LST	6	5	2713
MST	9	8	1735
SST	16	10	1393

Table A.7.: Particularities of the different telescopes of the candidate array G: number of telescopes of each kind, diameter of the field of view covered by the camera and number of pixels.

A.8. Candidate array H

This is a multipurpose array, with a good sensitivity and angular resolution across the whole energy range.

A.8.1. Array layout

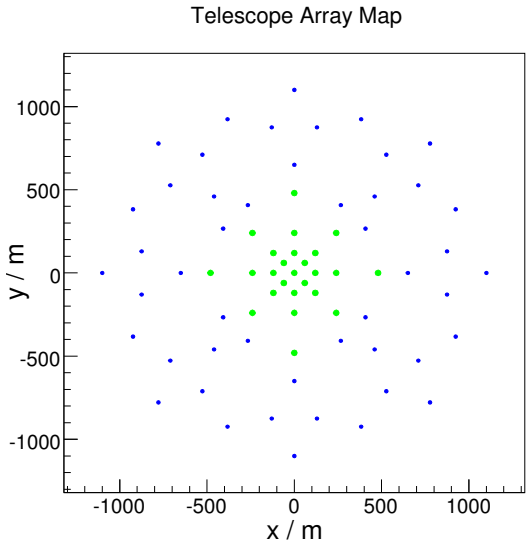

Figure A.8.: Telescope map for the candidate array H. Each circle represents a telescope on the ground. The sizes of the circles are scaled to represent the size of the mirror dishes of the telescopes scaled by a factor three in radius for better visibility. Each color represents a different telescope type.

	N_T	Φ_FoV / °	N_P
MST	25	7	1333
SST	48	10	1393

Table A.8.: Particularities of the different telescopes of the candidate array H: number of telescopes of each kind, diameter of the field of view covered by the camera and number of pixels.

A.9. Candidate array I

This is a multipurpose array, with a good sensitivity and angular resolution across the whole energy range.

A.9.1. Array layout

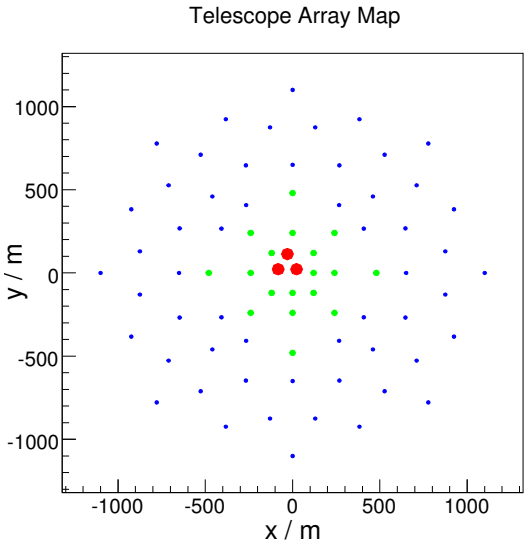

Figure A.9.: Telescope map for the candidate array I. Each circle represents a telescope on the ground. The sizes of the circles are scaled to represent the size of the mirror dishes of the telescopes scaled by a factor three in radius for better visibility. Each color represents a different telescope type.

	N_T	Φ_FoV / °	N_P
LST	3	4.9	2587
MST	18	8	1735
SST	56	9	1135

Table A.9.: Particularities of the different telescopes of the candidate array I: number of telescopes of each kind, diameter of the field of view covered by the camera and number of pixels.

A.10. Candidate array J

This is a multipurpose array, with a good sensitivity and angular resolution across the whole energy range.

A.10.1. Array layout

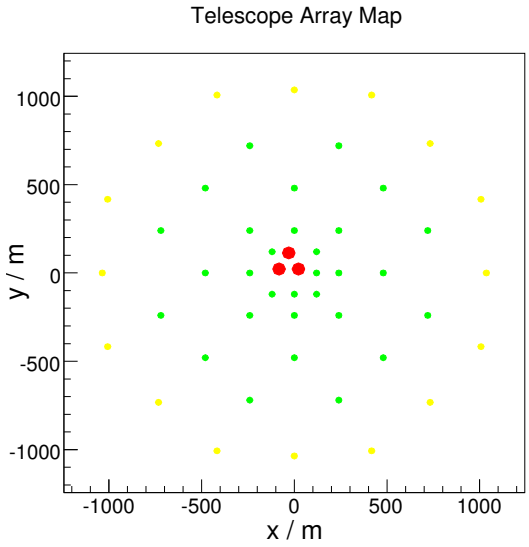

Figure A.10.: Telescope map for the candidate array J. Each circle represents a telescope on the ground. The sizes of the circles are scaled to represent the size of the mirror dishes of the telescopes scaled by a factor three in radius for better visibility. Each color represents a different telescope type.

	N_T	Φ_FoV / °	N_P
LST	3	4.9	2587
MST	30	8	1735
$\mathrm{MST}_\mathrm{LFoV}$	16	9	1135

Table A.10.: Particularities of the different telescopes of the candidate array J: number of telescopes of each kind, diameter of the field of view covered by the camera and number of pixels.

A.11. Candidate array K

This is a multipurpose array, with a good sensitivity and angular resolution across the whole energy range.

A.11.1. Array layout

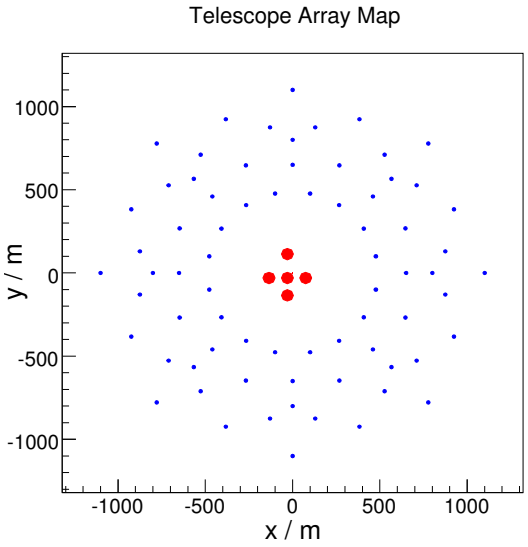

Figure A.11.: Telescope map for the candidate array K. Each circle represents a telescope on the ground. The sizes of the circles are scaled to represent the size of the mirror dishes of the telescopes scaled by a factor three in radius for better visibility. Each color represents a different telescope type.

	N_T	Φ_FoV / °	N_P
LST	5	5	2713
SST	72	9.5	1261

Table A.11.: Particularities of the different telescopes of the candidate array K: number of telescopes of each kind, diameter of the field of view covered by the camera and number of pixels.

A.12. Candidate array NA

This is a northern array with focus on low energies.

A.12.1. Array layout

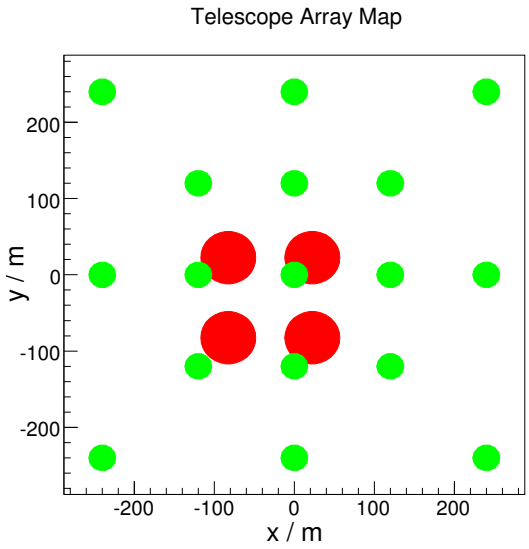

Figure A.12.: Telescope map for the candidate array NA. Each circle represents a telescope on the ground. The sizes of the circles are scaled to represent the size of the mirror dishes of the telescopes scaled by a factor three in radius for better visibility. Each color represents a different telescope type.

	N_T	Φ_FoV / °	N_P
LST	4	5	2713
MST	17	6	955

Table A.12.: Particularities of the different telescopes of the candidate array NA: number of telescopes of each kind, diameter of the field of view covered by the camera and number of pixels.

A.13. Candidate array NB

This is a northern array with focus on low energies.

A.13.1. Array layout

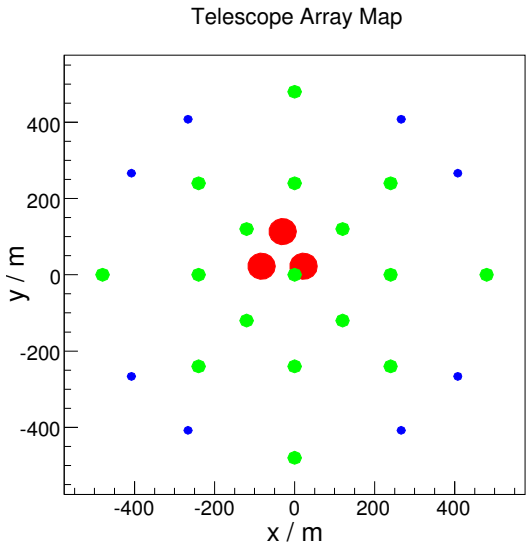

Figure A.13.: Telescope map for the candidate array NB. Each circle represents a telescope on the ground. The sizes of the circles are scaled to represent the size of the mirror dishes of the telescopes scaled by a factor three in radius for better visibility. Each color represents a different telescope type.

	N_T	Φ_FoV / °	N_P
LST	3	4.9	2587
MST	17	6	955
SST	8	8	889

Table A.13.: Particularities of the different telescopes of the candidate array NB: number of telescopes of each kind, diameter of the field of view covered by the camera and number of pixels.

A.14. Candidate array HESS

This is a subarray selected for the study of the performance of the array in case of array splitting for the observation of multiple targets at the same time.

A.14.1. Array layout

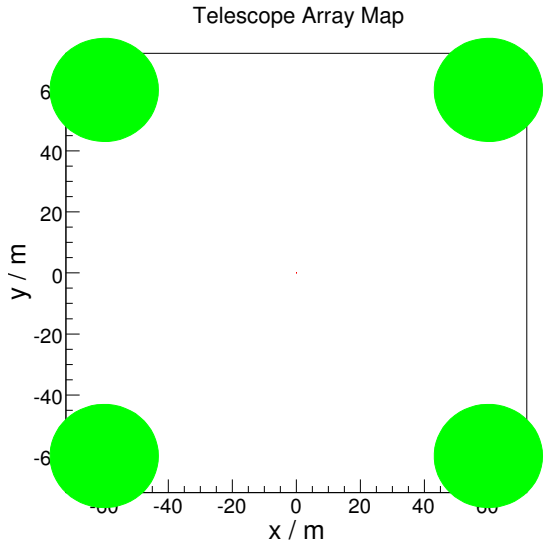

Figure A.14.: Telescope map for the candidate array HESS. Each circle represents a telescope on the ground. The sizes of the circles are scaled to represent the size of the mirror dishes of the telescopes scaled by a factor three in radius for better visibility. Each color represents a different telescope type.

	N_T	Φ_FoV / °	N_P
MST	4	5	673

Table A.14.: Particularities of the different telescopes of the candidate array HESS: number of telescopes of each kind, diameter of the field of view covered by the camera and number of pixels.

A.15. Results

A.15.1. Trigger rates

array	$\mathcal{R}_{\mathrm{tr}_\gamma}$ / Hz	$\mathcal{R}_{\mathrm{tr}_\mathrm{p}}$ / kHz	E_{th_γ} / GeV
A	10.52 ± 0.12	15.1 ± 0.3	$26.7^{+3.2}_{-2.9}$
B	12.52 ± 0.13	15.7 ± 0.3	$21.2^{+2.6}_{-2.3}$
C	9.40 ± 0.08	9.28 ± 0.15	106^{+13}_{-12}
D	12.06 ± 0.10	10.03 ± 0.17	106^{+13}_{-12}
E	12.32 ± 0.12	13.2 ± 0.3	$33.7^{+4.1}_{-3.7}$
$\mathrm{E_{NN}}$	11.94 ± 0.12	11.7 ± 0.3	$33.7^{+4.1}_{-3.7}$
F	11.32 ± 0.13	9.9 ± 0.3	$21.2^{+2.6}_{-2.3}$
G	11.11 ± 0.13	10.0 ± 0.3	$21.2^{+2.6}_{-2.3}$
H	9.37 ± 0.09	10.74 ± 0.20	106^{+13}_{-12}
I	13.09 ± 0.12	11.99 ± 0.21	$26.7^{+3.2}_{-2.9}$
J	11.24 ± 0.11	10.31 ± 0.21	$26.7^{+3.2}_{-2.9}$
K	13.99 ± 0.13	11.23 ± 0.21	$21.2^{+2.6}_{-2.3}$
NA	8.36 ± 0.11	6.91 ± 0.23	$33.7^{+4.1}_{-3.7}$
NB	8.45 ± 0.10	5.49 ± 0.17	$26.7^{+3.2}_{-2.9}$
HESS	1.15 ± 0.03	0.45 ± 0.04	106^{+13}_{-12}

Table A.15.: Expected array trigger rates for γ-ray and proton showers and energy threshold for γ-rays for all candidate arrays for the case of a *central* array trigger. The errors on the trigger rates are 1σ statistical errors, the error on the energy threshold represents the limits of the bin where the maximum of the differential trigger rate is found.

A.15.2. Data rates

			Scenario 1		**Scenario 2**		**Scenario 3**	
tel type	$N_{\mathrm{T_{tr}}}$	$N_{\mathrm{P_{cl}}}$	$S_{\mathrm{im/ev}}$ (kB)	$\mathcal{R}_\mathrm{d}$ (MB/s)	$S_{\mathrm{im/ev}}$ (kB)	$\mathcal{R}_\mathrm{d}$ (MB/s)	$S_{\mathrm{im/ev}}$ (kB)	$\mathcal{R}_\mathrm{d}$ (MB/s)
array A								
LST	0.57	14	5.1	14	6.4	18	76	210
MST	3.1	8.2	3.4	3.8	4.4	4.9	51	57
total			20	230	33	290	300	3400
array B								
LST	1	12	5.3	17	6.4	20	79	250
MST	2.6	8.3	3.4	3.7	4.4	4.8	51	55
total			21	250	33	310	310	3800

array C								
MST	1.8	13	3.4	1.9	4.6	2.6	51	29
MST_{LFoV}	0.84	33	2.7	0.82	5.6	1.7	41	12
total			10	84	21	130	150	1300
array D								
MST	2.5	13	2.9	1.7	4.2	2.5	43	26
MST_{LFoV}	0.3	35	2.7	0.53	5.7	1.1	41	8
total			10	86	20	130	150	1300
array E								
LST	0.78	14	4.4	11	5.7	14	67	170
MST	1.8	9.3	3.4	3.4	4.4	4.4	51	51
SST	0.64	11	2.7	0.74	3.8	1	41	11
total			14	160	23	210	210	2500
array E_{NN}								
total			14	150	25	200	220	2300
array F								
LST	1.8	12	4.8	14	6	18	73	220
MST	1.9	9.1	2.1	1.4	3.3	2.2	31	21
total			16	150	30	190	240	2200
array G								
LST	1.9	12	5.3	16	6.4	20	79	240
MST	0.91	9	3.4	3.4	4.4	4.4	51	50
SST	0.48	11	2.7	0.82	3.8	1.1	41	12
total			16	160	26	200	240	2400
array H								
MST	1.9	11	2.6	2.1	3.7	3	39	32
SST	1.2	12	2.7	0.72	3.9	1	41	11
total			11	95	20	130	160	1400
array I								
LST	0.58	14	5.1	12	6.4	15	76	170
MST	1.3	11	3.4	2.9	4.5	3.8	51	43
SST	1.1	12	2.2	0.55	3.4	0.84	33	8.3
total			11	130	21	170	170	1900
array J								
LST	0.68	14	5.1	12	6.4	15	76	170
MST	1.9	12	3.4	2.2	4.6	3	51	33
MST_{LFoV}	0.25	37	2.2	0.38	5.4	0.92	33	5.7
total			12	120	22	160	180	1800

array K								
LST	1	13	5.3	12	6.5	14	79	170
SST	1.9	11	2.5	0.73	3.6	1.1	37	11
total			11	120	19	160	170	1800
array NA								
LST	1.6	13	5.3	15	6.5	18	79	220
MST	1.6	9.4	1.9	1.2	3	2	28	19
total			14	90	28	120	210	1400
array NB								
LST	1.2	15	5.1	11	6.4	14	76	170
MST	1.5	12	1.9	0.94	3.2	1.6	28	14
SST	0.28	13	1.7	0.36	2.9	0.61	26	5.4
total			10	58	22	82	160	870
array HESS								
MST	2.5	18	1.3	0.4	3	0.9	20	6
total			3.8	1.6	15	3.6	56	24

Table A.16.: Expected event sizes and data rates for protons for all candidate arrays. The first column indicates the telescope type. $N_{\mathrm{T_{tr}}}$ is the mean number of triggered telescopes of this type in the simulations. $N_{\mathrm{P_{cl}}}$ is the average number of pixels that survive the image cleaning for images of each type of telescope. The last six columns give the telescope image size (in kB) and date rate (in MB/s) that is expected in the read-out scenarios 1, 2 and 3. Note that the event sizes and data rates for LST, MST and SST telescopes refer to the mean values of *one* telescope of its type in the case of stereoscopy. The numbers listed in the *total* row account for the total event size and data rate for the *central* array trigger. The total data rate for protons for each scenario is highlighted in red. The statistical uncertainty in the numbers is $\lesssim 5\%$ and the systematic uncertainty is between 20% and 30% (the details are given in the main text).

A.15.3. Data volumes

	Scenario 1	**Scenario 2**	**Scenario 3**
array A			
1 day	2.8 TB	3.5 TB	42 TB
1 month	84 TB	110 TB	1300 TB
1 year	0.98 PB	1.2 PB	15 PB
15 years	15 PB	19 PB	220 PB

array B			
1 day	3.1 TB	3.9 TB	47 TB
1 month	93 TB	120 TB	1400 TB
1 year	1.1 PB	1.4 PB	16 PB
15 years	16 PB	21 PB	250 PB
array C			
1 day	1 TB	1.6 TB	16 TB
1 month	31 TB	48 TB	470 TB
1 year	0.36 PB	0.56 PB	5.5 PB
15 years	5.5 PB	8.4 PB	82 PB
array D			
1 day	1.1 TB	1.6 TB	16 TB
1 month	32 TB	48 TB	480 TB
1 year	0.37 PB	0.56 PB	5.6 PB
15 years	5.6 PB	8.4 PB	84 PB
array E			
1 day	2 TB	2.6 TB	30 TB
1 month	61 TB	79 TB	910 TB
1 year	0.71 PB	0.93 PB	11 PB
15 years	11 PB	14 PB	160 PB
array E_{NN}			
1 day	1.9 TB	2.5 TB	28 TB
1 month	56 TB	74 TB	850 TB
1 year	0.66 PB	0.87 PB	9.9 PB
15 years	9.9 PB	13 PB	150 PB
array F			
1 day	1.8 TB	2.4 TB	27 TB
1 month	54 TB	71 TB	810 TB
1 year	0.63 PB	0.83 PB	9.5 PB
15 years	9.5 PB	12 PB	140 PB
array G			
1 day	2 TB	2.5 TB	30 TB
1 month	60 TB	74 TB	900 TB
1 year	0.7 PB	0.87 PB	11 PB
15 years	11 PB	13 PB	160 PB
array H			
1 day	1.2 TB	1.7 TB	18 TB
1 month	35 TB	50 TB	530 TB
1 year	0.41 PB	0.58 PB	6.2 PB
15 years	6.2 PB	8.7 PB	93 PB

array I			
1 day	1.6 TB	2.2 TB	24 TB
1 month	48 TB	65 TB	720 TB
1 year	0.56 PB	0.76 PB	8.5 PB
15 years	8.5 PB	11 PB	130 PB
array J			
1 day	1.5 TB	2 TB	22 TB
1 month	44 TB	60 TB	660 TB
1 year	0.52 PB	0.7 PB	7.7 PB
15 years	7.7 PB	11 PB	120 PB
array K			
1 day	1.5 TB	2 TB	23 TB
1 month	45 TB	60 TB	680 TB
1 year	0.53 PB	0.7 PB	8 PB
15 years	8 PB	11 PB	120 PB
array NA			
1 day	1.1 TB	1.5 TB	17 TB
1 month	33 TB	44 TB	500 TB
1 year	0.39 PB	0.51 PB	5.9 PB
15 years	5.9 PB	7.7 PB	88 PB
array NB			
1 day	0.72 TB	1 TB	11 TB
1 month	22 TB	30 TB	320 TB
1 year	0.25 PB	0.35 PB	3.8 PB
15 years	3.8 PB	5.3 PB	57 PB
array HESS			
1 day	0.02 TB	0.044 TB	0.3 TB
1 month	0.59 TB	1.3 TB	8.9 TB
1 year	0.0069 PB	0.016 PB	0.1 PB
15 years	0.1 PB	0.23 PB	1.6 PB

Table A.17.: Expected data volumes for all candidate arrays assuming a duty cycle of 15% for the stereoscopic array trigger. Each column contains the values of the indicated read-out scenario. The statistical uncertainty in the numbers is $\lesssim 5\%$ and the systematic uncertainty is between 20% and 30% (the details are given in the main text in subsection 2.4.3).

B. Appendix: CTA-UTRA3 candidate array E next-neighboring system

The details of the connection among telescopes for the next-neighbors array trigger are given in this appendix. The first column of table B.1 shows the ID of each telescope belonging to the candidate array E. The second column shows the IDs of the corresponding neighboring telescopes. The position of each telescope listed in the table is shown in figure B.1.

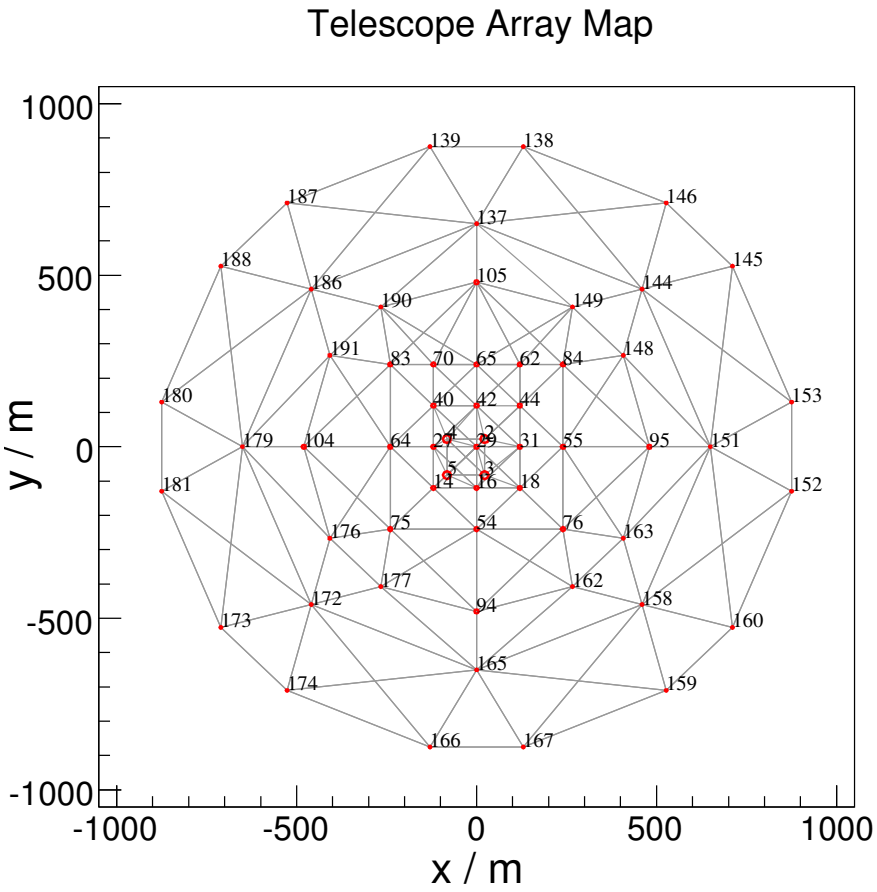

Figure B.1.: Telescope map for the candidate array E. Each circle represents a telescope on the ground. The numbers represent the telescope IDs T_{ID} used in the simulations. The sizes of the circles are scaled to represent the size of the mirror dishes of the telescopes.

T_{ID}	neighbors
187	88 186 139 137
188	87 186 180 179
180	88 181 179 186
181	80 179 173 172
173	81 174 172 179
174	73 172 166 165
166	65 174 167 172
167	66 165 159 158
159	67 160 158 165
160	59 152 158 151
152	60 153 151 158
153	52 151 145 144
145	146 144 153 151
146	137 138 144 145
138	146 137 139 144
139	137 138 187 186
186	137 139 187 188 180 179 191 190
179	186 188 180 181 173 172 176 104 191
172	179 181 173 174 166 165 177 176
165	172 174 166 167 159 158 162 94 177
158	165 167 159 160 152 151 163 162
151	158 160 152 153 145 144 148 95 163
144	151 153 145 146 138 137 149 148
137	144 146 138 139 187 186 190 105
190	105 137 186 191 83 70 65
191	190 186 179 104 64 83
104	191 179 176 75 64 83
176	104 179 172 177 75 64
177	176 172 165 94 54 75
94	177 165 162 76 54 75

T_{ID}	neighbors
162	94 165 158 163 76 54
163	162 158 151 95 55 76
95	163 151 148 84 55 76
148	95 151 144 149 84 55
149	148 144 137 105 65 62 84
105	149 137 190 83 70 65 62 84
70	65 105 190 83 40 42 62
83	70 105 190 191 104 64 40
64	27 40 83 191 104 176 75 14
75	54 14 64 104 176 177 94
54	16 14 75 177 94 162 76 18
76	18 54 94 162 163 95 55
55	95 148 84 44 31 18 76 163
84	148 149 105 62 44 55 95
62	84 149 105 65 42 44
65	62 149 105 190 70 40 42 44
40	70 83 64 27 29 42 65
27	40 64 14 16 29 42
14	27 64 75 54 16 29
16	29 27 14 54 18 31 29
18	31 29 16 54 76 55
31	44 42 29 16 18 55
44	62 65 42 29 31 55 84
42	62 65 70 40 27 29 31
29	42 40 27 14 16 18 31 44
5	4 3 2 14 16 27 29
4	5 3 2 27 40 42 29
3	2 4 5 16 18 31 29
2	3 4 5 29 42 44 31

Table B.1.: Next neighboring telescopes for candidate array E. The numbers represent the telescope IDs T_{ID} used in the simulations.

C. Appendix: H.E.S.S. data sets for RX J0852.0−4622

This appendix is dedicated to the H.E.S.S. RX J0852.0−4622 data sets used in this work.

run num.	run num.	run num.	run num.	run num.	run num.
20000	24834	25413	30921	37164	49672
20046	24841	25414	31301	37165	49673
20048	24842	25415	31313	37185	49695
20076	24844	25441	31314	37186	49696
20102	24877	25442	31315	37210	49697
20104	24879	25506	31317	37211	49698
20126	24890	25507	36688	37213	49722
20128	24891	30151	36689	37239	49777
23693	24894	30152	36704	37241	49795
23694	24926	30198	36705	37243	49796
23698	24948	30199	36730	37245	49813
23699	24949	30201	36731	37291	49814
23700	24970	30485	36748	43833	49815
23705	25025	30490	36749	43957	49831
23706	25247	30491	36752	44036	49850
23707	25249	30525	36753	44151	50339
23709	25281	30526	36774	44195	50340
23821	25296	30528	36775	44386	50341
23822	25318	30529	36798	44435	50353
23846	25319	30530	36799	49320	
23864	25337	30551	36800	49560	
24125	25339	30552	36821	49580	
24126	25340	30553	36823	49581	
24594	25366	30554	36824	49582	
24619	25367	30593	36826	49601	
24719	25368	30594	36827	49602	
24720	25369	30596	36852	49603	
24738	25387	30597	37125	49626	
24740	25389	30893	37148	49630	
24741	25390	30894	37149	49632	

Table C.1.: List of runs used for the spatial morphology analysis.

whole SNR run num.	region 0 run num.	region 1 run num.	region 2 run num.	region 3 run num.	region 4 run num.	region 5 run num.	region 6 run num.
24594	23698	23698	23698	23698	23698	23698	23698
24619	23699	23699	23699	23699	23699	23699	23699
24719	23700	23700	23700	23700	23700	23700	23700
24720	23705	23705	23705	23705	23705	23705	23705
24738	23706	23706	23706	23706	23706	23706	23706
24740	23822	23822	23822	23822	23822	23822	23822
24741	24126	24126	24126	24126	24126	24126	24126
24841	24594	24594	24594	24594	24720	24720	24720
24842	24619	24619	24619	24619	24738	24738	24740
24844	24719	24719	24719	24719	24841	24740	24834
24877	24720	24740	24738	24738	24844	24841	24841
24879	24738	24741	24740	24741	24877	24842	24842
24891	24740	24834	24741	24844	24894	24844	24877
24894	24741	24842	24842	24879	24926	24877	24894
24926	24841	24879	24844	24891	24970	24894	24970
24949	24842	24891	24879	24926	25247	24926	25025
24970	24844	24949	24891	24949	25319	24970	25249
25025	24877	25025	24926	25247	25340	25025	25296
25247	24879	25249	24949	25339	25366	25247	25319
25249	24891	25296	25025	25366	25368	25249	25340
25296	24894	25339	25247	25369	25390	25296	25367
25319	24926	25367	25249	25390	25413	25319	25368
25339	24949	25369	25296	25414	25415	25340	25389
25340	24970	25389	25339	25415	25442	25366	25413
25366	25025	25414	25366	25442	25506	25367	25441
25367	25247	25441	25367	25507	30151	25368	25506
25368	25249	25507	25369	30151	30491	25389	30152
25369	25296	30152	25389	30198	30526	25390	30485
25389	25319	30198	25390	30490	30529	25413	30491
25390	25339	30485	25414	30528	30530	25415	30525
25413	25340	30490	25415	30529	30552	25441	30526
25414	25366	30525	25441	30530	30554	25442	30552
25415	25367	30528	25442	30551	30596	25506	30553
25441	25368	30551	25507	30554	30893	30151	30596
25442	25369	30553	30151	30593	30921	30152	30597
25506	25389	30593	30152	30594	31301	30485	30893
25507	25390	30594	30198	30894	31315	30491	31301
30151	25413	30597	30485	30921	31317	30525	31314
30152	25414	30894	30490	31313	36798	30526	
30198	25415	31313	30525	31315	36799	30529	
30485	25441	31314	30528	31317		30530	
30490	25442	36824	30529	36798		30552	
30491	25506		30530	36799		30553	
30525	25507		30551	36821		30554	
30526	30151		30553	36823		30596	
30528	30152		30554			30597	

(continued ...)

(. . . continued)

whole SNR run num.	region 0 run num.	region 1 run num.	region 2 run num.	region 3 run num.	region 4 run num.	region 5 run num.	region 6 run num.
30529	30198		30593			30893	
30530	30485		30594			30921	
30551	30490		30597			31301	
30552	30491		30894			31314	
30553	30525		30921			31315	
30554	30526		31313			31317	
30593	30528		31314			36689	
30594	30529		31315			36705	
30596	30530		31317			36731	
30597	30551		36798			36749	
30893	30552		36821			36753	
30894	30553		36824			36775	
30921	30554		36826			36798	
31301	30593					37149	
31313	30594					37165	
31314	30596					37186	
31315	30597					37211	
31317	30893					37243	
36798	30894					37291	
	30921						
	31301						
	31313						
	31314						
	31315						
	31317						
	36798						
	36821						

Table C.2.: Lists of runs used for the spectral morphology analysis.

run num.	run num.	run num.
23698	25296	30553
23699	25319	30554
23700	25339	30593
23705	25340	30594
23706	25366	30596
23707	25367	30597
23709	25368	30893
23822	25369	30894
24126	25389	30921
24594	25390	31301
24619	25413	31313
24719	25414	31314
24720	25415	31315
24738	25441	31317
24740	25442	36798
24741	25506	36799
24834	25507	36800
24841	30151	36821
24842	30152	36823
24844	30198	36824
24877	30485	36826
24879	30490	36827
24891	30491	36852
24894	30525	
24926	30526	
24949	30528	
24970	30529	
25025	30530	
25247	30551	
25249	30552	

Table C.3.: List of runs used for the analysis of the PWN.

run num.	run num.	run num.
24619	25319	30528
24719	25339	30529
24720	25340	30530
24738	25366	30551
24740	25367	30552
24741	25368	30553
24841	25369	30554
24842	25389	30593
24844	25390	30594
24877	25413	30596
24879	25414	30597
24891	25415	30893
24894	25506	30894
24926	25507	30921
24949	30198	31301
24970	30485	31313
25025	30490	31314
25247	30491	31315
25249	30525	31317
25296	30526	36798

Table C.4.: List of runs used for the spectral analysis of the whole SNR.

Paper 1 run num.	Paper 2 run num.
18928	24594
18929	24619
18947	24719
18948	24720
18949	24738
18994	24740
18995	24741
18996	24841
	24842
	24844
	24877
	24879
	24891
	24894
	24926
	24949
	24970
	25025
	25247
	25249
	25296
	25319
	25339
	25340
	25366
	25367
	25368
	25369
	25389
	25390

Paper 1 run num.	Paper 2 run num.
	25413
	25414
	25415
	25441
	25442
	25506
	25507

Table C.5.: Lists of runs used for the published spectral analyses for RX J0852.0−4622. The run list labeled "Paper 1" corresponds to the list of ON-source runs used in Aharonian et al. [2005] for the spectral analysis. The run list labeled "Paper 2" corresponds to the list of runs appropriate for spectral analysis according to the Heidelberg calibration taken on RX J0852.0−4622 during 2005: it should be very close to the run list used in Aharonian et al. [2007] for the spectral analysis; the actual run list used in the reference is missing and cannot be recovered.

D. Appendix: H.E.S.S. spectrum crosscheck results for RX J0852.0−4622

This appendix is dedicated to the H.E.S.S. RX J0852.0−4622 results from crosscheck analysis of the spectrum of the whole SNR. For each analysis chain listed in table 4.3, the following results are presented: the event statistics used in the spectral analysis (section D.1), the spectra for each of the tested models as listed in table 5.3 (sections D.2 to D.4) and the results of the likelihood ratio test used to investigate a possible curvature in the spectrum of RX J0852.0−4622 (section D.5).

D.1. Spectral analysis statistics

chain	$\langle\theta_{\mathrm{zen}}\rangle$	$\langle\theta_{\mathrm{az}}\rangle$	$\langle\theta_{\mathrm{off}}\rangle$	t / h	N_{on}	N_{off}	α	excess	significance
`HAP-HD`	32°	208°	1.2°	17.7	70691	63693	1	6998	19.1σ
`HAP-FR`	32°	208°	1.2°	18.0	66333	59831	1	6502	18.3σ
`Paris`	32°	208°	1.0°	17.8	50733	45815	1	4959	16.0σ

Table D.1.: Statistics used in the spectral analysis for each analysis chain: mean zenith and azimuth angles of the observations ($\langle\theta_{\mathrm{zen}}\rangle$ and $\langle\theta_{\mathrm{az}}\rangle$ respectively), mean offset angle $\langle\theta_{\mathrm{off}}\rangle$, livetime t, number of events in the signal (*on*) region N_{on}, number of events in the background (*off*) region N_{off}, exposure normalization (ratio of *on* to *off* exposures) α, number of excess counts in the *on* region and significance of the signal in the *on* region in number of Gaussian standard deviations σ.

D.2. Spectrum figures

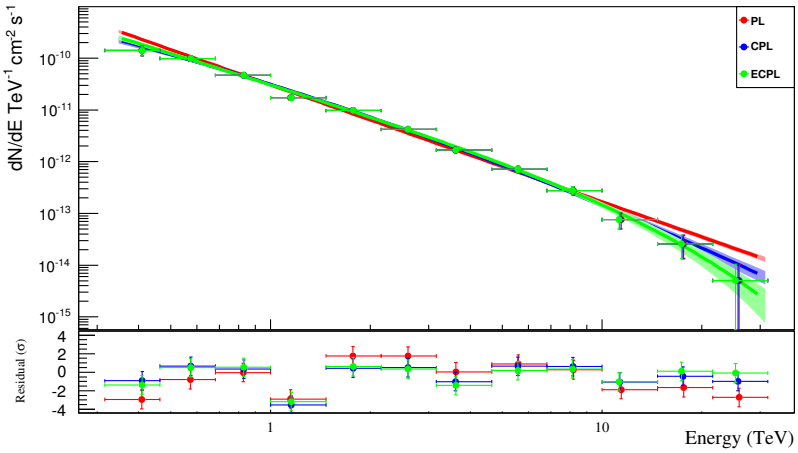

Figure D.1.: Forward-folding `HAP-HD` spectra derived for the models listed in table 5.3. The upper pad shows the spectral points together with the spectral fit and its 1σ uncertainty band in the form of a shaded area. The lower pad shows the residuals of the spectral points relative to the fit.

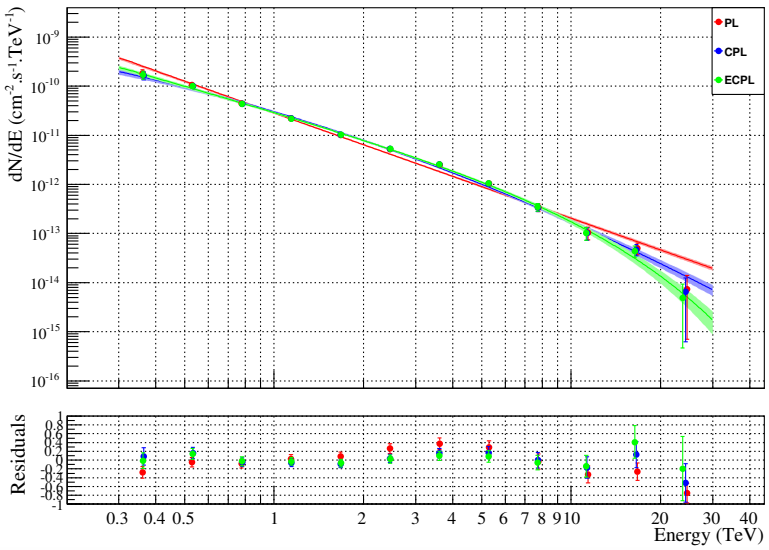

Figure D.2.: Forward-folding `HAP-FR` spectra derived for the models listed in table 5.3. The upper pad shows the spectral points together with the spectral fit and its 1σ uncertainty band in the form of a shaded area. The lower pad shows the residuals of the spectral points relative to the fit.

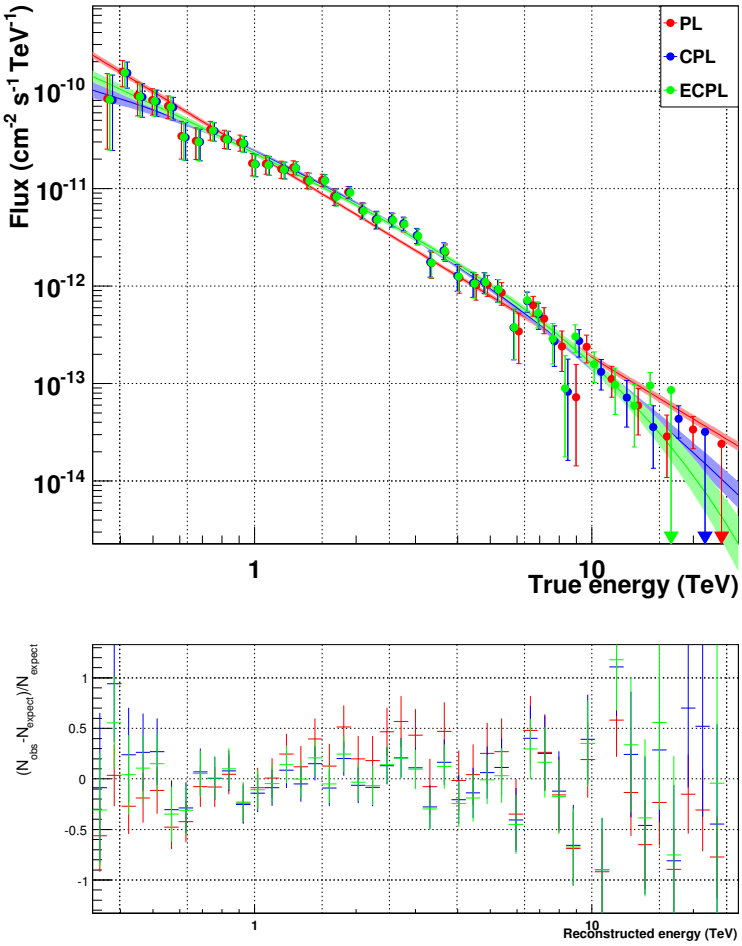

Figure D.3.: Forward-folding `Paris Analysis` spectra derived for the models listed in table 5.3. The upper pad shows the spectral points together with the spectral fit and its 1σ uncertainty band in the form of a shaded area. The lower pad shows the residuals of the spectral points relative to the fit.

D.3. Energy range for the spectral fit

chain	E_{min}/ TeV	E_{max}/ TeV
`HAP-HD`	0.35	30
`HAP-FR`	0.30	30
`Paris`	0.33	27

Table D.2.: Minimum and maximum energies used for deriving the spectra for each analysis chain.

D.4. Parameters of the spectral fit

model	$\mathbf{\Phi_0}$ / $\mathrm{cm^{-2}s^{-1}TeV^{-1}}$	$\mathbf{\Gamma}$	$\boldsymbol{\beta}$	$\boldsymbol{E_{\mathrm{cut}}}$ / TeV	p-value
		HAP-HD			
PL	$(30.6 \pm 1.2)\,10^{-12}$	2.26 ± 0.04	n.a.	n.a.	1.3×10^{-4}
CPL	$(31.3 \pm 1.3)\,10^{-12}$	2.01 ± 0.08	0.14 ± 0.04	n.a.	0.11
ECPL	$(33.6 \pm 1.7)\,10^{-12}$	1.94 ± 0.09	n.a.	10.3 ± 3.2	0.18
		HAP-FR			
PL	$(28.3 \pm 1.1)\,10^{-12}$	2.14 ± 0.03	n.a.	n.a.	1.2×10^{-4}
CPL	$(30.0 \pm 1.3)\,10^{-12}$	1.80 ± 0.07	0.19 ± 0.03	n.a.	0.67
ECPL	$(33.0 \pm 1.7)\,10^{-12}$	1.68 ± 0.07	n.a.	7.2 ± 1.2	0.95
		Paris Analysis			
PL	$(23.1 \pm 1.1)\,10^{-12}$	2.10 ± 0.04	n.a.	n.a.	3.8×10^{-3}
CPL	$(24.0 \pm 1.2)\,10^{-12}$	1.60 ± 0.10	0.26 ± 0.05	n.a.	0.93
ECPL	$(27.0 \pm 1.6)\,10^{-12}$	1.55 ± 0.11	n.a.	6.4 ± 1.5	0.92

Table D.3.: Fit parameters for the spectrum for each of the fitted models for each analysis chain. In the case of the power-law spectrum with exponential cut-off, E_{cut} is shown instead of the fitted parameter $\lambda = 1/E_{\mathrm{cut}}$. The p-values of the fits are calculated from the difference between the derived flux points and the fitted model. The quoted errors represent 1σ statistical uncertainties. In all cases the reference energy E_0 was chosen to be 1 TeV.

D.5. Tests of spectrum curvature

model	$\log L$	NFP	p-value	significance
		HAP-HD		
PL	−25.794	2	n.a.	n.a.
CPL	−18.381	3	99.988%	3.8σ
ECPL	−16.613	3	99.998%	4.3σ
		HAP-FR		
PL	276921	2	n.a.	n.a.
CPL	276935	3	99.999988%	5.3σ
ECPL	276938	3	99.9999994%	5.8σ
		Paris Analysis		
PL	−39.0	2	n.a.	n.a.
CPL	−19.0	3	99.99999997%	6.3σ
ECPL	−19.2	3	99.99999997%	6.3σ

Table D.4.: Results of the likelihood ratio test for each analysis chain for the hypothesis of the existence of a curvature in the spectrum. For each analysis chain: for each fitted model the logarithm of the likelihood L, the number of free parameters NFP, the probability of the test p and the equivalent significance in Gaussian standard deviations are shown. The test results refer to the comparison of the more complex models (i.e. CPL or ECPL) with respect to the simpler model (i.e. PL).

E. Appendix: muon correction and its effect on spectral parameters

In section 5.4, it is mentioned that a flux difference of $\sim 70\%$ is observed between the spectrum derived for RX J0852.0−4622 in this work and the spectra from the previous H.E.S.S. publications (Aharonian et al. [2005] and Aharonian et al. [2007]). It is also shown that the discrepancies can be explained if the reconstructed γ-ray energies in these publications were not corrected for the mirror reflectivity degradation of the telescopes (the so called muon efficiency correction).

In the following, a description of the muon efficiency correction (sections E.1 and E.2) and its effects on the spectral reconstruction (section E.3) is presented. A discussion follows about a software feature in the H.E.S.S. code that could have led in some cases to wrong energy reconstructions and hence wrong flux estimations in the past (section E.4). The appendix finishes with a verification (section E.5) of the relations introduced, when discussing the effects of the muon corrections in spectral reconstruction.

E.1. Muon correction (simplified approach)

Muons produce Cherenkov light in a cone along their trajectory in the atmosphere, leaving a very characteristic ring-shaped signal in the detector. Since they are easily identified, their images are used to measure the mirror reflectivity of the telescopes by comparing their brightness to MC simulations, and hence derive a correction for the energy of the events recorded by the system.

This section will make use of two simplifications: ignore that each telescope has its own correction and assume that the correction can be applied directly to the energy. In practice, the correction is applied telescope by telescope to the amplitude of the images in the cameras in order to reconstruct an energy corrected for the optical efficiency of the telescope.

Supposing that μ_{corr} is the muon correction of the telescope system

$$\mu_{\mathrm{corr}} = \frac{\mu_{\mathrm{eff\,MC}}}{\mu_{\mathrm{eff\,data}}}, \tag{E.1}$$

E_{reco} is the reconstructed energy using an MC sample simulated for an efficiency $\mu_{\mathrm{eff\,MC}}$ ($\propto$ optical efficiency). Approximating that the muon correction can be directly applied to the energy, the corrected energy can be written as

$$E_{\mathrm{corr}} = E_{\mathrm{reco}}\,\mu_{\mathrm{corr}}. \tag{E.2}$$

E.2. Actual muon correction

Each telescope i has its own correction

$$\mu_{\mathrm{corr}_i} = \frac{\mu_{\mathrm{eff\,MC}_i}}{\mu_{\mathrm{eff\,data}_i}}, \tag{E.3}$$

which is applied to the Hillas size (also known as amplitude) parameter S_{im} of the image recorded by its camera, as defined in Hillas [1985], as follows

$$S^{\mathrm{corr}}_{\mathrm{im}_i} = S_{\mathrm{im}_i}\, \mu_{\mathrm{corr}_i}. \tag{E.4}$$

Then the corrected sizes are used to reconstruct a new value of the energy E_{corr}, which is corrected for the mirror reflectivity.

E.3. Changes in the spectrum due to the muon correction

The effect of the muon correction can be regarded as a shift of the measured energy of the γ-rays by a factor $A = \mathrm{const}$. This shift is energy independent, so all distributions participating in the determination of the flux are equally shifted in log scale: they all remain unchanged in shape and move by log(A) in the log(E) scale. Hence, the flux (spectrum) is also shifted (but the shape remains unchanged). Calling ϕ (and ϕ_0) the flux (and flux normalization) when no muon correction is applied and ϕ' (and ϕ'_0) the flux (and flux normalization) when a certain muon correction μ_{corr} is applied, it holds that

$$\phi'(AE) = \phi(E) \tag{E.5}$$

and

$$\frac{\phi'(E)}{\phi(E)} = \frac{\phi'_0}{\phi_0} = B = \mathrm{const.} \tag{E.6}$$

In the particular case of a spectrum following a power-law, since the shape does not change, the index remains the same in both cases, so the equation E.6 is verified

$$\frac{\phi'(E)}{\phi(E)} = \frac{\phi'_0\,(E/E_0)^{-\Gamma}}{\phi_0\,(E/E_0)^{-\Gamma}} = \frac{\phi'_0}{\phi_0} = \mathrm{const.} \tag{E.7}$$

and the equation E.5 yields

$$\phi'_0\,(AE/E_0)^{-\Gamma} = \phi_0\,(E/E_0)^{-\Gamma} \tag{E.8}$$

to find that

$$\frac{\phi'_0}{\phi_0} = A^{\Gamma}. \tag{E.9}$$

The combination of the equations E.9 and E.6 results in

$$B = A^{\Gamma}. \tag{E.10}$$

That is, the shift in energy (factor A) is related to the factor between the fluxes B via the spectral index Γ. So a change in flux can be translated to a shift in energy.

Using the simplified approximation mentioned in section E.1 (specifically the equation E.2), the energy shift factor A can be approximated by the muon correction

$$A \simeq \mu_{\mathrm{corr}}, \tag{E.11}$$

hence the equation E.10 yields

$$B \simeq (\mu_{\mathrm{corr}})^{\Gamma}. \tag{E.12}$$

The procedure developed in this section is also applicable in the general case of two different muon corrections applied to the same data: μ_{corr} and μ'_{corr} corresponding to measured fluxes of ϕ and ϕ' respectively. In this case there is also a shift of the energy scale between both measurements and the equation E.10 is also applicable. Using the simplified approach, the energy shift factor A can be approximated by the ratio of muon corrections

$$A \simeq \mu'_{\mathrm{corr}}/\mu_{\mathrm{corr}}, \tag{E.13}$$

so the final expression (the equation E.10) is

$$B \simeq (\mu'_{\mathrm{corr}}/\mu_{\mathrm{corr}})^{\Gamma}. \tag{E.14}$$

The equations E.11 and E.12 are recovered if $\mu_{\mathrm{corr}} = 1$ (no muon correction) and μ'_{corr} is represented as μ_{corr} for simplicity.

E.4. Muon correction in the old MPIK analysis chain

Extensive checks of the old MPIK analysis code (`wobble chain`[1] from 2006) revealed a problem in the code: a hard-coded reference when checking the MC muon parameters in the data base in order to perform the muon correction[2]. Instead of checking the MC run that is used for the lookup tables employed for the event reconstruction, the software reads the latest MC entry available in the database.

This effect can lead to wrong muon corrections for the reconstructed energies. For instance, if an analysis performed in 2006 reconstructs the events with lookup tables produced with MC phase1 (MC run = 100, mirror reflectivity $\sim 100\%$), this hard-coded reference would produce the energy to be corrected using the latest MC entry of the data base at that time: MC run 101, which corresponds to MC phase1b (mirror reflectivity 70%).[3] This results in a wrongly corrected energy, so the spectrum is shifted in energy, showing a difference in the flux.[4]

The analysis results used to crosscheck the main H.E.S.S. results on RX J0852.0−4622

[1] The so called `wobble chain` framework is the precursor of the current `HAP` framework.

[2] This problem has been solved in more recent versions of `wobble chain` and hence `HAP`.

[3] Details on how the muon correction is used for the energy reconstruction are given in sections E.1 and E.2.

[4] Details on how a shift in the energy can produce a difference in the flux are given in section E.3.

in Aharonian et al. [2007] (using the `Model 3D` analysis chain, short: `M3D`) were derived using the `wobble chain`. It is believed that the crosscheck analysis results are affected by a wrong energy reconstruction as a result of the issue described above. Since the actual analysis result files used for the publication do not exist any longer, the results used for the crosscheck of the paper cannot be traced back fully. Nevertheless, later H.E.S.S. internal results from 2007 show this problem.

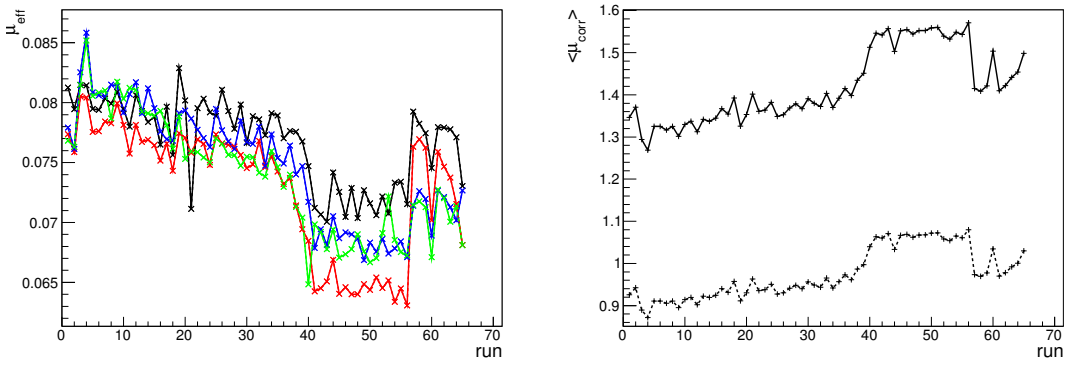

(a) Muon parameters

(b) Average muon corrections

Figure E.1.: The left figure shows the muon efficiencies for the data set used to derive the spectrum for each telescope: black for CT1, red for CT2, blue for CT3 and green for CT4. The right figure shows the average muon correction of the spectrum data set for two different sets of MC simulations: phase1 (MC run 100) with a solid line and phase1b (MC run 101) with a dashed line.

Since the flux differences caused by the use of different muon corrections is independent of the spectral model or the analysis chain used, the results in this section are performed using a power-law model and the MPIK analysis chain: `HAP-HD` for the current results and `wobble chain` for the crosscheck of the results of the previous publication.

Figure E.1a shows the muon efficiencies for the data set used for the spectral analysis of RX J0852.0−4622 as they are at present (October 2013) in the `HD` data base. The differences with the corrections of the MPIK (`wobble chain`) analysis from 2007 are typically less than a few percent, so very similar to the current ones, showing that the muon corrections in `HD` have been very stable in the last years.

Figure E.1b shows the muon corrections that one should apply to the data set used for the spectral analysis of RX J0852.0−4622, when reconstructing the events using lookup tables produced with either MC phase1 (solid line) or MC phase1b (dashed line). The MPIK (`wobble chain`) analysis from 2007 used lookup tables produced with MC phase1, so it should have used the corrections from the solid line, but due to the hard-coded reference in the code, it used the ones from the dashed line (MC phase1b). So instead of using a correction of ~ 1.4 it was using a correction of ~ 1.0. Therefore, the muon correction applied is too small (almost as if no muon correction was applied at all), yielding analysis results, in particular a spectrum, as if derived from the uncorrected

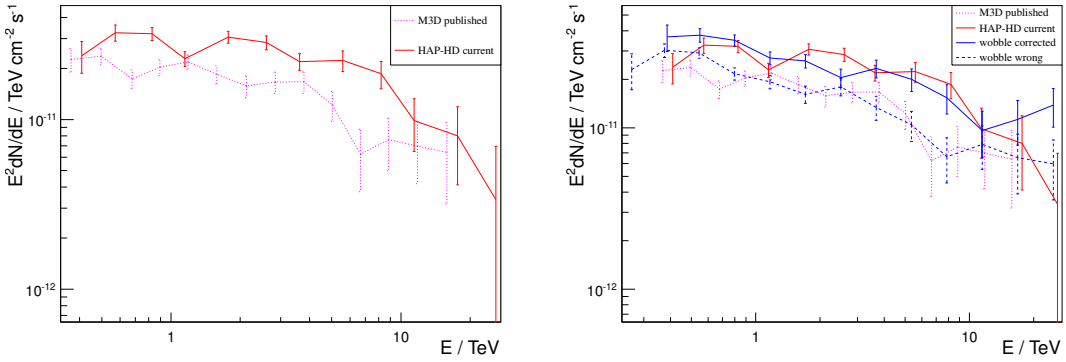

(a) Spectrum: current vs. published

(b) Spectrum: wrong vs. corrected

Figure E.2.: The left figure shows the spectral points for the current `HAP-HD` spectrum and the `Model 3D` spectrum from Aharonian et al. [2007]. The fluxes have been multiplied by E^2 in order to show the differences more clearly. The right figure shows the same as the left figure together with the spectra using the old `wobble chain` software from 2006 (blue points) with the wrong energy reconstruction (dashed blue points) and the corrected one (solid blue points).

energy.

Figure E.2a shows the spectral points for the current `HAP-HD` spectrum and for the published spectrum. A difference in flux is visible between both sets of points. Figure E.2b shows the spectral points for an analysis using reconstruction with lookup tables produced with MC phase1 and the correct muon corrections (blue solid points) and for the same analysis but using the muon corrections of MC phase1b (blue dashed points). The set of blue dashed points (with mixed-up muon corrections) is very well compatible with the published spectral points (magenta dotted points). The set of blue solid points is in very good agreement with the current `HAP-HD` spectrum (red solid points).

The conclusions from this study are:

- The effect of mixed-up muon corrections (compatible with the lack of muon correction) explains the differences between the fluxes of the published and the current spectra.
- The analysis crosscheck using the MPIK analysis chain and data of the publication most probably had this problem. Correcting this effect, the crosscheck is no longer compatible with the `Model 3D` spectrum from the publication, but rather with the current one.
- The analysis of the `Model 3D` spectrum from the publication most probably did not correct the reconstructed γ-ray energies for the mirror reflectivity degradation of the telescopes, yielding a too small flux.

E.5. Verification of the spectral changes and the simplified muon correction method

The equations in section E.3 describe the change in the spectrum due to a change in the muon correction. The validity of the equations can be verified by comparing two spectra derived using the same data and the same MC but two different muon corrections. In addition, if the two spectra use the proper muon correction from section E.2, the energy shift between both can be measured and compared to the shift predicted by the simplified approach from section E.1, and thus verify its validity.

The spectra derived with the old `wobble chain` analysis code from 2006 from section E.4 (more precisely, the spectra depicted with blue lines - solid and dashed - in figure E.2b) match these requirements and can thus be compared to each other in order to test the validity of the relations mentioned above. The comparison of the energies at the same flux in order to estimate A and the fluxes at the same energy in order to estimate B for both spectra (the other parameters are trivial) yields

$$\begin{aligned} A &\sim 1.2 \\ B &\sim 1.5 \\ \Gamma &\sim 2.4 \\ \mu'_{\mathrm{corr}} &\sim 1.3 \\ \mu_{\mathrm{corr}} &\sim 0.9. \end{aligned}$$

Therefore

$$\begin{aligned} \mu'_{\mathrm{corr}}/\mu_{\mathrm{corr}} &= 1.4 \sim A \\ A^{\Gamma} &= 1.5 = B, \end{aligned}$$

verifying to some extent ($\sim 20\%$ accuracy) the relations mentioned in section E.3, specifically the equation E.10 and the hypothesis that the effect of the muon correction can be approximated by an energy shift factor equal to the ratio of muon corrections (equation E.13, derived from the equation E.2).

It is thus shown that the relations describing the spectral change are valid, and also, to some extent, the simplified approach. Hence the spectral points from the two publications after correcting for the muon efficiency presented in figure 5.6b show approximately the correct flux. And therefore, since they agree with the spectrum derived in this work, it is shown that the spectral analysis of this work yields the correct flux level.

References

A. A. Abdo et al. Observations of the Young Supernova Remnant RX J1713.7-3946 with the Fermi Large Area Telescope. *ApJ*, 734:28, June 2011. doi: 10.1088/0004-637X/734/1/28.

F. Acero, A. Bamba, S. Casanova, E. de Cea, E. de Oña Wilhelmi, S. Gabici, Y. Gallant, D. Hadasch, A. Marcowith, G. Pedaletti, O. Reimer, M. Renaud, D. F. Torres, F. Volpe, and CTA Consortium. Gamma-ray signatures of cosmic ray acceleration, propagation, and confinement in the era of CTA. *Astroparticle Physics*, 43:276–286, March 2013a. doi: 10.1016/j.astropartphys.2012.05.024.

F. Acero, Y. Gallant, J. Ballet, M. Renaud, and R. Terrier. A new nearby pulsar wind nebula overlapping the RX J0852.0-4622 supernova remnant. *A&A*, 551:A7, March 2013b. doi: 10.1051/0004-6361/201220799.

F. Acero et al. First detection of VHE γ-rays from SN 1006 by HESS. *A&A*, 516:A62, June 2010. doi: 10.1051/0004-6361/200913916.

B. S. Acharya et al. Introducing the CTA concept. *Astroparticle Physics*, 43:3–18, March 2013. doi: 10.1016/j.astropartphys.2013.01.007.

M. Ackermann et al. Detection of the Characteristic Pion-Decay Signature in Supernova Remnants. *Science*, 339:807–811, February 2013. doi: 10.1126/science.1231160.

F. Aharonian et al. Cosmic ray proton spectrum determined with the imaging atmospheric cherenkov technique. *Phys. Rev. D*, 59:092003, Mar 1999. doi: 10.1103/PhysRevD.59.092003.

F. Aharonian et al. Detection of TeV γ-ray emission from the shell-type supernova remnant RX J0852.0-4622 with HESS. *A&A*, 437:L7–L10, July 2005. doi: 10.1051/0004-6361:200500130.

F. Aharonian et al. Observations of the Crab nebula with HESS. *A&A*, 457:899–915, October 2006a. doi: 10.1051/0004-6361:20065351.

F. Aharonian et al. The H.E.S.S. Survey of the Inner Galaxy in Very High Energy Gamma Rays. *ApJ*, 636:777–797, January 2006b. doi: 10.1086/498013.

F. Aharonian et al. H.E.S.S. Observations of the Supernova Remnant RX J0852.0-4622: Shell-Type Morphology and Spectrum of a Widely Extended Very High Energy Gamma-Ray Source. *ApJ*, 661:236–249, May 2007. doi: 10.1086/512603.

A. Akhperjanian and V. Sahakian. Performance of a 20 m diameter Cherenkov imaging telescope. *Astroparticle Physics*, 21:149–161, May 2004. doi: 10.1016/j.astropartphys.2003.12.010.

J. Aleksić et al. Performance of the MAGIC stereo system obtained with Crab Nebula data. *Astroparticle Physics*, 35:435–448, February 2012. doi: 10.1016/j.astropartphys.2011.11.007.

G. E. Allen, K. Chow, T. DeLaney, M. D. Filipović, J. C. Houck, T. G. Pannuti, and M. D. Stage. On the Expansion Rate, Age, and Distance of the Supernova Remnant G266.2-1.2 (Vela Jr.). *ApJ*, 798:82, January 2015. doi: 10.1088/0004-637X/798/2/82.

ANTARES Collaboration. ANTARES website, 2016. URL `http://antares.in2p3.fr/`.

B. Aschenbach. Discovery of a young nearby supernova remnant. *Nature*, 396:141–142, November 1998. doi: 10.1038/24103.

ATLAS Collaboration. The ATLAS Trigger Monitoring and Operations in proton-proton collisions. Technical Report ATL-DAQ-PUB-2010-003, CERN, Geneva, May 2010. URL `https://cds.cern.ch/record/1267378`.

ATLAS Collaboration. ATLAS website, 2016. URL `http://atlas.ch`.

A. Bamba, R. Yamazaki, and J. S. Hiraga. Chandra Observations of Galactic Supernova Remnant Vela Jr.: A New Sample of Thin Filaments Emitting Synchrotron X-Rays. *ApJ*, 632:294–301, October 2005. doi: 10.1086/432711.

Y. Becherini, A. Djannati-Ataï, V. Marandon, M. Punch, and S. Pita. A new analysis strategy for detection of faint γ-ray sources with Imaging Atmospheric Cherenkov Telescopes. *Astroparticle Physics*, 34:858–870, July 2011. doi: 10.1016/j.astropartphys.2011.03.005.

D. Berge, S. Funk, and J. Hinton. Background modelling in very-high-energy γ-ray astronomy. *A&A*, 466:1219–1229, May 2007. doi: 10.1051/0004-6361:20066674.

K. Bernlöhr. eventio - a machine-independent hierarchical data format and its programming interface. Not published, 2001. URL `ftp://ftp.pw.plock.pl/pub/student/knb/cors/eventio_en.ps`.

K. Bernlöhr. CTA simulations with CORSIKA/sim_telarray. In F. A. Aharonian, W. Hofmann, and F. Rieger, editors, *American Institute of Physics Conference Series*, volume 1085 of *American Institute of Physics Conference Series*, pages 874–877, December 2008a. doi: 10.1063/1.3076816.

K. Bernlöhr. Simulation of imaging atmospheric Cherenkov telescopes with CORSIKA and sim_telarray. *Astroparticle Physics*, 30:149–158, October 2008b. doi: 10.1016/j.astropartphys.2008.07.009.

K. Bernlöhr et al. Monte Carlo design studies for the Cherenkov Telescope Array. *Astroparticle Physics*, 43:171–188, March 2013. doi: 10.1016/j.astropartphys.2012.10.002.

V. Blobel and E. Lohrmann. *Statistische und numerische Methoden der Datenanalyse*. May 2012.

G. R. Blumenthal and R. J. Gould. Bremsstrahlung, Synchrotron Radiation, and Compton Scattering of High-Energy Electrons Traversing Dilute Gases. *Reviews of Modern Physics*, 42:237–271, 1970. doi: 10.1103/RevModPhys.42.237.

J. Blümer, R. Engel, and J. R. Hörandel. Cosmic rays from the knee to the highest energies. *Progress in Particle and Nuclear Physics*, 63:293–338, October 2009. doi: 10.1016/j.ppnp.2009.05.002.

S. Carrigan, J. A. Hinton, W. Hofmann, K. Kosack, T. Lohse, and O. Reimer. Establishing a connection between high-power pulsars and very-high-energy gamma-ray sources. *International Cosmic Ray Conference*, 2:659–662, 2008.

J. A. Combi, G. E. Romero, and P. Benaglia. Radio Detection of the Supernova Remnant RX J0852.0-4622. *ApJL*, 519:L177–L180, July 1999. doi: 10.1086/312120.

J. M. Cordes and T. J. W. Lazio. NE2001.I. A New Model for the Galactic Distribution of Free Electrons and its Fluctuations. *ArXiv Astrophysics e-prints*, July 2002.

CTA Consortium. Design concepts for the Cherenkov Telescope Array CTA: an advanced facility for ground-based high-energy gamma-ray astronomy. *Experimental Astronomy*, 32:193–316, December 2011. doi: 10.1007/s10686-011-9247-0.

CTA Consortium. CTA preliminary technical design report. Not published, 2013.

CTA Consortium. CTA website, 2016. URL `https://www.cta-observatory.org`.

M. de Naurois and L. Rolland. A high performance likelihood reconstruction of γ-rays for imaging atmospheric Cherenkov telescopes. *Astroparticle Physics*, 32:231–252, December 2009. doi: 10.1016/j.astropartphys.2009.09.001.

A. R. Duncan and D. A. Green. The supernova remnant RX J0852.0-4622: radio characteristics and implications for SNR statistics. *A&A*, 364:732–740, December 2000.

Earth Blog. Earth Blog, 2013. URL `http://earthspacecircle.blogspot.com`.

Fermi Collaboration. *Fermi* website, 2016. URL `http://www.nasa.gov/content/fermi-gamma-ray-space-telescope`.

S. Funk, G. Hermann, J. Hinton, D. Berge, K. Bernlöhr, W. Hofmann, P. Nayman, F. Toussenel, and P. Vincent. The trigger system of the H.E.S.S. telescope array. *Astroparticle Physics*, 22:285–296, November 2004. doi: 10.1016/j.astropartphys.2004.08.001.

H. Gast. A new lookup scheme for hap. Internal note (not published), 2012.

V. L. Ginzburg and S. I. Syrovatskii. *The Origin of Cosmic Rays*. Pergamon, 1964.

D. A. Green. A revised Galactic supernova remnant catalogue. *Bulletin of the Astronomical Society of India*, 37:45–61, March 2009.

S. F. Gull. The X-ray, optical and radio properties of young supernova remnants. *MNRAS*, 171:263–278, May 1975. doi: 10.1093/mnras/171.2.263.

D. Haefner et al. New improved Sum-Trigger system for the MAGIC telescopes. In *International Cosmic Ray Conference*, volume 9 of *International Cosmic Ray Conference*, page 246, 2011.

HAWC Collaboration. HAWC website, 2016. URL `http://www.hawc-observatory.org/`.

HEGRA Collaboration. HEGRA website, 2006. URL `http://www.mpi-hd.mpg.de/hfm/HEGRA/HEGRA.html`.

G. Hermann, C. Bauer, C. Föhr, W. Hofmann, and T. Kihm. A Trigger And Readout Scheme For Future Cherenkov Telescope Arrays. In F. A. Aharonian, W. Hofmann, and F. Rieger, editors, *American Institute of Physics Conference Series*, volume 1085 of *American Institute of Physics Conference Series*, pages 898–901, December 2008. doi: 10.1063/1.3076822.

V. F. Hess. Über Beobachtungen der durchdringenden Strahlung bei sieben Freiballonfahrten. *Physik. Zeitschr.*, pages 1084–1091, 1912.

H.E.S.S. Collaboration. A new SNR with TeV shell-type morphology: HESS J1731-347. *A&A*, 531:A81, July 2011. doi: 10.1051/0004-6361/201016425.

HESS Collaboration. H.E.S.S. catalog, 2016. URL `http://www.mpi-hd.mpg.de/hfm/HESS/pages/home/sources/`.

H.E.S.S. Collaboration. H.e.s.s. observations of rx j1713.7−3946 with improved angular and spectral resolution; evidence for gamma-ray emission extending beyond the x-ray emitting shell. A&A forthcoming, 2016.

HESS Collaboration. Acceleration of petaelectronvolt protons in the Galactic Centre. *Nature*, 531:476–479, March 2016a. doi: 10.1038/nature17147.

HESS Collaboration. The H.E.S.S. Galactic plane survey. In preparation, 2016b.

H.E.S.S. Collaboration. Detailed spectral and morphological analysis of the shell type SNR RCW 86. *ArXiv e-prints*, January 2016.

HESS Collaboration. Deeper H.E.S.S. Observations of Vela Junior (RX J0852.0-4622): Morphology Studies and Resolved Spectroscopy. A&A forthcoming, 2016a.

HESS Collaboration. H.E.S.S. website, 2016b. URL `https://www.mpi-hd.mpg.de/hfm/HESS/`.

HESS Collaboration. H.E.S.S. website, 2016c. URL `https://www.mpi-hd.mpg.de/hfm/HESS/pages/about/HESS_I_II/`.

A. M. Hillas. Cerenkov light images of EAS produced by primary gamma. *International Cosmic Ray Conference*, 3, August 1985.

W. Hofmann, I. Jung, A. Konopelko, H. Krawczynski, H. Lampeitl, and G. Pühlhofer. Comparison of techniques to reconstruct VHE gamma-ray showers from multiple stereoscopic Cherenkov images. *Astroparticle Physics*, 12:135–143, November 1999. doi: 10.1016/S0927-6505(99)00084-5.

IceCube Collaboration. Evidence for High-Energy Extraterrestrial Neutrinos at the IceCube Detector. *Science*, 342:1242856, November 2013. doi: 10.1126/science.1242856.

IceCube Collaboration. IceCube website, 2016. URL `https://icecube.wisc.edu/`.

A. F. Iyudin, V. Schönfelder, K. Bennett, H. Bloemen, R. Diehl, W. Hermsen, G. G. Lichti, R. D. van der Meulen, J. Ryan, and C. Winkler. Emission from ^{44}Ti associated with a previously unknown Galactic supernova. *Nature*, 396:142–144, November 1998. doi: 10.1038/24106.

A. F. Iyudin, V. Aschenbach, V. Burwitz, K. Dennerl, M. Freyberg, F. Haberl, and M. D. Filipovic. Multiwavelength Appearance of Vela Jr.: Is it up to Expectations? In *ESA Special Publication*, volume 622 of *ESA Special Publication*, page 91, 2007.

O. Kargaltsev and G. G. Pavlov. Pulsar-wind nebulae in X-rays and TeV γ-rays. *X-ray Astronomy 2009; Present Status, Multi-Wavelength Approach and Future Perspectives*, 1248:25–28, July 2010. doi: 10.1063/1.3475228.

KASCADE Collaboration. KASCADE website, 2014. URL `http://www-ik.fzk.de/KASCADE_home.html`.

H. Katagiri et al. Detection of Gamma Rays around 1 TeV from RX J0852.0-4622 by CANGAROO-II. *ApJL*, 619:L163–L166, February 2005. doi: 10.1086/427980.

S. Katsuda, H. Tsunemi, and K. Mori. The Slow X-Ray Expansion of the Northwestern Rim of the Supernova Remnant RX J0852.0-4622. *ApJL*, 678:L35–L38, May 2008. doi: 10.1086/588499.

S. R. Kelner, F. A. Aharonian, and V. V. Bugayov. Energy spectra of gamma rays, electrons, and neutrinos produced at proton-proton interactions in the very high energy regime. *Physical Review D*, 74(3):034018, August 2006. doi: 10.1103/PhysRevD.74.034018.

T. Kishishita, J. Hiraga, and Y. Uchiyama. Nonthermal emission properties of the northwestern rim of supernova remnant RX J0852.0-4622. *A&A*, 551:A132, March 2013. doi: 10.1051/0004-6361/201220525.

KM3NeT Collaboration. KM3NeT website, 2016. URL `http://www.km3net.org/home.php`.

M. Kramer, J. F. Bell, R. N. Manchester, A. G. Lyne, F. Camilo, I. H. Stairs, N. D'Amico, V. M. Kaspi, G. Hobbs, D. J. Morris, F. Crawford, A. Possenti, B. C. Joshi, M. A. McLaughlin, D. R. Lorimer, and A. J. Faulkner. The Parkes Multibeam Pulsar Survey - III. Young pulsars and the discovery and timing of 200 pulsars. *MNRAS*, 342:1299–1324, July 2003. doi: 10.1046/j.1365-8711.2003.06637.x.

J. Lande, M. Ackermann, A. Allafort, J. Ballet, K. Bechtol, T. H. Burnett, J. Cohen-Tanugi, A. Drlica-Wagner, S. Funk, F. Giordano, M.-H. Grondin, M. Kerr, and M. Lemoine-Goumard. Search for Spatially Extended Fermi Large Area Telescope Sources Using Two Years of Data. *ApJ*, 756:5, September 2012. doi: 10.1088/0004-637X/756/1/5.

M. Lemoine-Goumard, B. Degrange, and M. Tluczykont. Selection and 3D-reconstruction of gamma-ray-induced air showers with a stereoscopic system of atmospheric Cherenkov telescopes. *Astroparticle Physics*, 25:195–211, April 2006. doi: 10.1016/j.astropartphys.2006.01.005.

LHC Team. LHC website, 2016. URL `http://home.cern/topics/large-hadron-collider`.

T.-P. Li and Y.-Q. Ma. Analysis methods for results in gamma-ray astronomy. *ApJ*, 272:317–324, September 1983. doi: 10.1086/161295.

M. S. Longair. *High Energy Astrophysics*. February 2011.

MAGIC Collaboration. MAGIC website, 2016. URL `http://magic.mppmu.mpg.de/`.

M. A. Malkov. Asymptotic Particle Spectra and Plasma Flows at Strong Shocks. *ApJL*, 511:L53–L56, January 1999. doi: 10.1086/311825.

R. N. Manchester, G. B. Hobbs, A. Teoh, and M. Hobbs. The Australia Telescope National Facility Pulsar Catalogue. *Astron. J.*, 129:1993–2006, April 2005. doi: 10.1086/428488.

F. Mattana, M. Falanga, D. Götz, R. Terrier, P. Esposito, A. Pellizzoni, A. De Luca, V. Marandon, A. Goldwurm, and P. A. Caraveo. The Evolution of the γ- and X-Ray Luminosities of Pulsar Wind Nebulae. *ApJ*, 694:12–17, March 2009. doi: 10.1088/0004-637X/694/1/12.

M. Meyer, D. Horns, and H.-S. Zechlin. The Crab Nebula as a standard candle in very high-energy astrophysics. *A&A*, 523:A2, November 2010. doi: 10.1051/0004-6361/201014108.

P. L. Nolan et al. Fermi Large Area Telescope Second Source Catalog. *ApJS*, 199(2):31, April 2012. doi: 10.1088/0067-0049/199/2/31.

S. Ohm, C. van Eldik, and K. Egberts. γ/hadron separation in very-high-energy γ-ray astronomy using a multivariate analysis method. *Astroparticle Physics*, 31:383–391, June 2009. doi: 10.1016/j.astropartphys.2009.04.001.

T. Padmanabhan. *Theoretical Astrophysics - Volume 2, Stars and Stellar Systems*. July 2001.

M. Paz Arribas. First Monte Carlo studies for the array level trigger system in CTA. Master's thesis, Humboldt Universität Berlin, 2008.

M. Paz Arribas, U. Schwanke, I. Sushch, N. Komin, F. Acero, S. Ohm, and for the H.E.S.S. Collaboration. H.E.S.S. deeper observations on SNR RX J0852.0-4622. In *International Cosmic Ray Conference*, volume 7 of *International Cosmic Ray Conference*, page 140, 2011. URL `http://www.ihep.ac.cn/english/conference/icrc2011/paper/proc/v7/v7_0801.pdf`.

M. Paz Arribas, U. Schwanke, R. Wischnewski, and for the CTA Consortium. Trigger and data rates expected for the CTA observatory. In F. A. Aharonian, W. Hofmann, and F. M. Rieger, editors, *American Institute of Physics Conference Series*, volume 1505 of *American Institute of Physics Conference Series*, pages 781–784, December 2012. doi: 10.1063/1.4772376.

Pierre Auger Collaboration. Correlation of the Highest-Energy Cosmic Rays with Nearby Extragalactic Objects. *Science*, 318:938, November 2007. doi: 10.1126/science.1151124.

F. Piron, A. Djannati-Atai, M. Punch, J.-P. Tavernet, A. Barrau, R. Bazer-Bachi, L.-M. Chounet, G. Debiais, B. Degrange, J.-P. Dezalay, P. Espigat, B. Fabre, P. Fleury, G. Fontaine, P. Goret, C. Gouiffes, B. Khelifi, I. Malet, C. Masterson, G. Mohanty, E. Nuss, C. Renault, M. Rivoal, L. Rob, and S. Vorobiov. Temporal and spectral gamma-ray properties of <ASTROBJ>Mkn 421</ASTROBJ> above 250 GeV from CAT observations between 1996 and 2000. *A&A*, 374:895–906, August 2001. doi: 10.1051/0004-6361:20010798.

T. A. Porter, I. V. Moskalenko, and A. W. Strong. Inverse Compton Emission from Galactic Supernova Remnants: Effect of the Interstellar Radiation Field. *ApJL*, 648: L29–L32, September 2006. doi: 10.1086/507770.

S. Preuß, G. Hermann, W. Hofmann, and A. Kohnle. Study of the photon flux from the night sky at La Palma and Namibia, in the wavelength region relevant for imaging atmospheric Cherenkov telescopes. *Nuclear Instruments and Methods in Physics Research A*, 481:229–240, April 2002. doi: 10.1016/S0168-9002(01)01264-5.

M. P. Redman and J. Meaburn. A possible association of a young pulsar (PSR J0855-4644) with the young Vela supernova remnant RX J0852.0-4622. *MNRAS*, 356:969–973, January 2005. doi: 10.1111/j.1365-2966.2004.08523.x.

S. P. Reynolds. Supernova Remnants at High Energy. *Annual Review of A&A*, 46: 89–126, September 2008. doi: 10.1146/annurev.astro.46.060407.145237.

E. M. Reynoso, G. Dubner, E. Giacani, S. Johnston, and A. J. Green. The interior of the SNR RX J0852.0-4622 (Vela Jr) at radio wavelengths. *A&A*, 449:243–250, April 2006. doi: 10.1051/0004-6361:20054236.

ROOT Team. `ROOT` website, 2016. URL `https://root.cern.ch/`.

T. Sanuki et al. Precise Measurement of Cosmic-Ray Proton and Helium Spectra with the BESS Spectrometer. *ApJ*, 545:1135–1142, December 2000. doi: 10.1086/317873.

S. Schlenker. Simulation Study of the H.E.S.S. Single Telescope Trigger Rate. Master's thesis, Humboldt Universität Berlin, 2001.

M. Schroedter, J. Anderson, K. Byrum, G. Drake, C. Duke, J. Holder, A. Imran, A. Madhavan, F. Krennrich, A. Kreps, and A. Smith. A Topological Trigger System for Imaging Atmospheric-Cherenkov Telescopes. *ArXiv e-prints*, August 2009.

L. I. Sedov. *Similarity and dimensional methods in mechanics*. CRC Press, 10th ed edition, 1993. ISBN 0849393086,9780849393082.

P. Slane, J. P. Hughes, R. J. Edgar, P. P. Plucinsky, E. Miyata, H. Tsunemi, and B. Aschenbach. RX J0852.0-4622: Another Nonthermal Shell-Type Supernova Remnant (G266.2-1.2). *ApJ*, 548:814–819, February 2001. doi: 10.1086/319033.

M. Stupar, M. D. Filipović, P. A. Jones, and Q. A. Parker. Radio continuum observations of the galactic supernova remnant Vela Z (G266.2-1.2). *Advances in Space Research*, 35:1047–1051, 2005. doi: 10.1016/j.asr.2005.02.060.

S. Takeda, A. Bamba, Y. Terada, M. S. Tashiro, S. Katsuda, R. Yamazaki, Y. Ohira, and W. Iwakiri. Suzaku observations of the hard X-ray spectrum of Vela Jr. *ArXiv e-prints*, March 2016.

T. Tanaka, A. Allafort, J. Ballet, S. Funk, F. Giordano, J. Hewitt, M. Lemoine-Goumard, H. Tajima, O. Tibolla, and Y. Uchiyama. Gamma-Ray Observations of the Supernova Remnant RX J0852.0-4622 with the Fermi Large Area Telescope. *ApJL*, 740:L51, October 2011. doi: 10.1088/2041-8205/740/2/L51.

J. H. Taylor and J. M. Cordes. Pulsar distances and the galactic distribution of free electrons. *ApJ*, 411:674–684, July 1993. doi: 10.1086/172870.

TeVCat Team. TeVCat catalog, 2016. URL `http://tevcat.uchicago.edu/`.

H. Tsunemi, E. Miyata, B. Aschenbach, J. Hiraga, and D. Akutsu. Overabundance of Calcium in the Young SNR RX J0852-4622: Evidence of Over-Production of ^{44}Ti. *PASJ*, 52:887–893, October 2000. doi: 10.1093/pasj/52.5.887.

E. van der Swaluw, T. P. Downes, and R. Keegan. An evolutionary model for pulsar-driven supernova remnants. A hydrodynamical model. *A&A*, 420:937–944, June 2004. doi: 10.1051/0004-6361:20035700.

VERITAS Collaboration. VERITAS website, 2016. URL `http://veritas.sao.arizona.edu/`.

H. J. Völk and K. Bernlöhr. Imaging very high energy gamma-ray telescopes. *Experimental Astronomy*, 25:173–191, August 2009. doi: 10.1007/s10686-009-9151-z.

S. Vorobiov, J. Bolmont, P. Corona, E. Delagnes, F. Feinstein, D. Gascón, J.-F. Glicenstein, C. L. Naumann, P. Nayman, A. Sanuy, F. Toussenel, and P. Vincent. NECTAr: New electronics for the Cherenkov Telescope Array. *Nuclear Instruments and Methods in Physics Research A*, 639:62–64, May 2011. doi: 10.1016/j.nima.2010.08.112.

T. C. Weekes. *Very high energy gamma-ray astronomy*. 2003.

P. Wegner et al. Simultaneous operation and control of about 100 telescopes for the cherenkov telescope array. *Journal of Physics: Conference Series*, 396(1):012052, 2012. URL `http://stacks.iop.org/1742-6596/396/i=1/a=012052`.

A. Weinstein. The VERITAS Trigger System. In *International Cosmic Ray Conference*, volume 3 of *International Cosmic Ray Conference*, pages 1539–1542, 2008.

R. White, F. di Pierro, G. Greenshaw, R. Pareschi, R. Canestrari, and for the CTA Consortium. Telescopes for the High Energy Section of the Cherenkov Telescope Array. In *International Cosmic Ray Conference*, volume 9 of *International Cosmic Ray Conference*, page 58, 2011.

S. S. Wilks. The large-sample distribution of the likelihood ratio for testing composite hypotheses. *The Annals of Mathematical Statistics*, 9(1):60–62, 03 1938. doi: 10.1214/aoms/1177732360. URL `http://dx.doi.org/10.1214/aoms/1177732360`.

A. E. Wright, M. R. Griffith, B. F. Burke, and R. D. Ekers. The Parkes-MIT-NRAO (PMN) surveys. 2: Source catalog for the southern survey (delta greater than -87.5 deg and less than -37 deg). *ApJS*, 91:111–308, March 1994. doi: 10.1086/191939.

List of Figures

List of Tables

Acknowledgments

I would like to thank everybody that helped me in doing this work.

First of all I would like to warmly thank Ulli Schwanke, who guided me during the entire process from the beginning in both projects: the CTA technical work and the H.E.S.S. data analysis. He has been also a great help during the process of writing this thesis, always with helpful comments. Without his help this work would not have been possible.

I would like to thank Thomas Lohse and Stefan Schlenstedt for accepting me in their groups at the Humboldt University and DESY respectively, where I learned a great deal about γ-ray astronomy and computing, and for their guidance and support during my PhD. In addition, I thank Stefan Funk for accepting me in his group at SLAC during my short visit to Stanford.

Many thanks also to Iurii Sushch and Nukri Komin, who helped me with the interpretation of the results of the H.E.S.S. analysis: Iurii made many useful suggestions and comments for the discussion of the RX J0852.0−4622 analysis results and Nukri introduced to me the `modelisation` package used for modeling the RX J0852.0−4622 emission. In addition I thank Nukri for introducing to me the `Paris Analysis` framework used for the crosscheck of the H.E.S.S. analysis.

I also thank my colleagues at the Humboldt University and DESY for the fruitful discussions and also for the moments of relax, especially Igor Oya, Matthias Füssling, Matthias Kerschhaggl, Mathew Dalton, Gerrit Spengler, Michael Gajdus, Thomas Murach, Emrah Birsin, Ekrem Oğuzhan Angüner, Michelangelo Giorgi, Arne Schönwald, Susanne Schröder, Anna Franckowiak, Robert Franke, Lucie Gérard, Garteh Hughes, Heike Prokoph, Ralf Wischnewski, Gernot Maier, Arnim Balzer, Eike Middell. In addition, I would like to thank Joshua Lande, former member of Stefan Funk's group at SLAC.

I also thank my colleagues in the CTA consortium and the H.E.S.S. collaboration for the great teamwork towards creating a new experiment and maintaining the current one smoothly working. In this respect, I really appreciate the help I got in moments of confusion especially from Karl Kosack, Dalibor Nedbal, Christopher van Eldik, Stefan Ohm, Raquel de los Reyes, Henning Gast, Vincent Marandon, Mathieu de Naurois, Konrad Bernlöhr, Yvonne Becherini, Joanna Newton (Skilton, when I first met her), Christoph Deil, Emma de Oña Wilhelmi, Abelardo Moralejo.

I would like to thank Veronika Schneider (Fetting, when I first met her) for her work as secretary of the group in the Humboldt University. Her advice in university bureaucracy is invaluable. I also appreciate Olf Epler's work in maintaining the computer cluster at the Humboldt University and promptly solving any unexpected computing problems.

I would like to thank my family for their support an patience: my wife Tais, my son Bruno, my daughter Alisa, my parents Lola and Manolo, my siblings Lolita and Ignacio, including other members *ex officio*: Fran, Naranjo, Lorenzo, and my parents in law Leonid and Natalia.

I also thank the many friends that cheered me up, when I was feeling down: Loles, Ana, Almudena, Stefan, Salva, Matthäus, Christoph, Moty, Anne, David, Farid, Sergio (x2), Laurent, Andrés, Pedro, Miguel, María Eugenia, Melina, Gregg, Camille, Sara, Norma.

Finally, I would also like to thank to the additional people that contributed to this work a way or another but I forgot to mention.

Selbständigkeitserklärung

Ich erkläre, dass ich die Dissertation selbständig und nur unter Verwendung der von mir gemäß § 7 Abs. 3 der Promotionsordnung der Mathematisch-Naturwissenschaftlichen Fakultät, veröffentlicht im Amtlichen Mitteilungsblatt der Humboldt-Universität zu Berlin Nr. 126/2014 am 18.11.2014 angegebenen Hilfsmittel angefertigt habe.

Palo Alto (Kalifornien), den 25.07.2016 Manuel Paz Arribas